Bernard Raymond Becker

164 Words

CPT Conservation and Atmospheric Neutrinos in the MINOS Far Detector

The MINOS Far Detector is a 5400 ton iron calorimeter located at the Soudan state park in Soudan Minnesota. The MINOS far detector can observe atmospheric neutrinos and separate charge current ν_μ and $\bar{\nu}_\mu$ interactions by using a 1.4 T magnetic field to identify the charge of the produced muon. The CPT theorem requires that neutrinos and anti-neutrinos oscillate in the same way. In an fiducial exposure of 5.0 kilo-ton years a total of 41 candidate neutrino events are observed with an expectation of 53.1$\pm$7.6(system.)$\pm$7.2(stat.) unoscillated events or 31.6$\pm$4.7(system.)$\pm$5.6(stat.) events with $\Delta m^2 = 2.4 \times 10^{-3} eV^2$,$sin^2(2\theta) = 1.0$ as oscillation parameters. These include 28 events which can have there charge identified with high confidence. These 28 events consist of 18 events consistant with being produced by ν_μ and 10 events being consistant with being produced by $\bar{\nu}_\mu$. No evidence of CPT violation is observed.

UNIVERSITY OF MINNESOTA

This is to certify that I have examined this copy of a doctoral thesis by

Bernard Raymond Becker

and have found that it is complete and satisfactory in all respects and that any and all revisions required by the final examining committee have been made.

Professor Jon Urheim and Professor Michael DuVernois
(Faculty Advisers)

GRADUATE SCHOOL

CPT Conservation and Atmospheric Neutrinos in the MINOS Far Detector

A THESIS
SUBMITTED TO THE FACULTY OF THE GRADUATE SCHOOL
OF THE UNIVERSITY OF MINNESOTA
BY

Bernard Raymond Becker

IN PARTIAL FULFILLMENT OF THE REQUIREMENTS
FOR THE DEGREE OF
DOCTOR OF PHILOSOPHY

Professor Jon Urheim and Professor Michael DuVernois

February, 2006

CPT Conservation and Atmospheric Neutrinos in the MINOS Far Detector

by Bernard Raymond Becker

Under the supervision of Professor Jon Urheim and Professor Michael DuVernois

ABSTRACT

The MINOS Far Detector is a 5400 ton iron calorimeter located at the Soudan state park in Soudan Minnesota. The MINOS far detector can observe atmospheric neutrinos and separate charge current ν_μ and $\bar{\nu}_\mu$ interactions by using a 1.4 T magnetic field to identify the charge of the produced muon. The CPT theorem requires that neutrinos and anti-neutrinos oscillate in the same way. In an fiducial exposure of 5.0 kilo-ton years a total of 41 candidate neutrino events are observed with an expectation of 53.1$\pm$7.6(system.)$\pm$7.2(stat.) unoscillated events or 31.6$\pm$4.7(system.)$\pm$5.6(stat.) events with $\Delta m^2 = 2.4 \times 10^{-3} eV^2$,$sin^2(2\theta) = 1.0$ as oscillation parameters. These include 28 events which can have there charge identified with high confidence. These 28 events consist of 18 events consistant with being produced by ν_μ and 10 events being consistant with being produced by $\bar{\nu}_\mu$. No evidence of CPT violation is observed.

Acknowledgements

Since a fellow MINOS graduate student has already quoted Dante in the introduction to his thesis[1], I repeat the reference to Dante in the introduction of *my thesis* with some hesitation. Although Caius has chosen a more appropriate reference to Dante then I have, my reference comes way of the great poet (and my favorite poet) T.S. Elliot at the start of his well know poem, *The Love Song of J. Alfred Prufrock*:

S'io credesse che mia riposta fosse

A persona che mia tornasse al mondo

Quseta fiamma staria senza piu scosse

Ma perciocche giammai di questo fondo

Non torno vivo alcun s'i'odo il vero

Senza tema d'infamia ti respondo

Graduate school at times seems to be as much about this as it is anything else and it is only through the people in these acknowledgments that this has ended as well as it has.

It is impossible to underestimate the amount of work it takes to complete a thesis. Likewise it is impossible the amount of help and support I have received to reach this goal.

The very first people I must thank are my two advisor's, Jon Urheim and Micheal DuVernois. The amount of time, help and advice I have received from them is enormous.

I have been quite a handful at times to deal with and they have shown patience dealing with me[1].

The MINOS collaboration has been good to me. There are nearly too many names to list. The most memorable collaborators were those spent time with me at Soudan. This list includes Louie Barrett, Dave Boehnlein, Jeff Nelson, Bob Webb, Andrew Godley, Chris Smith, Brian Rebel, Tass Belias, Sergei Avvakumov, Leo Jenner, Rob Morse, Geoff Pearce, Caius Howcroft, Nathanial Tagg, Nat Longley and Dave DeMuth.

The mine crew at Soudan was instrumental in my activities at Soudan where I spent in total a half year of time. Lab manager Bill Miller and associate manager Jerry Meier run one of the most effective operations I have ever seen in any operation I have been involved in. The difficulty in the task of managing a laboratory full of physicists while running a construction project at the same time cannot be underestimated. Eileen Amos had to deal with my last moment requests for housing at Soudan. Jim Beaty is willing to help you with some technical problem even if it is not his problem and gave me much assistance. Irene and Brian who did most of the actual optical survey measurements on my shifts did some good work and made my job more efficient. Finally, I don't think I can forget either Whitey or Grim who moved scintillator modules down from the deck so we could remap them.

The Minnesota high energy group and the local MINOS group (past and present) in particular has been very instrumental in my development. The MINOS faculty and post-docs have been a very valuable source for knowledge, advice and assistance. In particular, I must thank: Pete Border who came up with the idea for tutorial videos, Hugh Gallagher for all the help I got on the cross sections and statistics, Sue Kashara for all the help with the veto shield and ntuples, David Petyt for his help on physics analysis in general, Peter Litchfield for his general knowledge of neutrino physics and Keith Ruddick for his knowledge of everything.

[1]In particular, the reading and correcting of this thesis!

My family who has been supportive of me. My brother Martin for all the strange and great phone talks we have had over the years. My sister Mary Kay and her husband Luis who had made my life easier than it could have been. My sister Teresa who has always been excited in what I'm doing. My gradmother who has helped me in many ways my entire life. My father. My mother who this thesis is dedicated in memory of. There are not words to describe how much assistance she gave and how much she is missed.

My fellow graduate students who shared the memorable experience *which is graduate school*. There are the graduate students who came before me like Ted Vidnovic, Matt Graham, Steve Giron, Bill Cooley, Andy Ferst, Dave Engerbreston and Long Duong. Then there is 'my' generation, those graduate students who started in the fall of 1999. These include my fellow MINOS collaborators, Ben Speakman, Jeremy Gogos and Dipu Rahman. They also include Emily Maher, Brian Andersson[2], Rick Zelman, Brian Calivia, Paul Way, Jonathan Strand, Sarwa Tan, Lindsey Hillensheim, Ben Bousquet, Tao Qian, Melissa Eblen-Zayas and Selina Li. Then there are those who started after me and include Erik Beall, Justin Hietala, Sujeewa Kumaratunga, Eric Grashorn and Brian Lang. I must also apologize for anyone who got confused on the topic of a certain super-intelligent chimpanzee who happens to be a world class expert on human anatomy and that chimpanzee status on the faculty[3].

The readers of my thesis and committee member for being involved in this whole process. I have known Professors Bob Lysak and Bob Gehrz since I took undergraduate classes from them a decade ago and they have both given useful advice over the years. Professor Mikhail Voloshin who was always willing to answer a question about particle physics. From my oral exam committee I must thank Professor Charles Woodward

[2]Or any of his 10^{75} pseudonyms

[3]In particular to Melissa who had the most horrified expression on her face I have ever seen, in Phys. 5001 over six years ago

who probably prevented me from imploding by asking an easy question at just the right time.

My friends from high school. In particular, the Jordan brothers who have been good friends for 15 years.

Finally, I would like to thank several of my high school instructors who put me on the path I'm now on. My first junior high science teacher David Bassett[4] forced me to learn how to learn and was more influential then he might ever know. My first physics instructor Mark Westlake[5] who first showed me the beauty of physics. My latin instructor John Raiter who I had many remarkable discussions with on a variety of topics over the years.

[4]After writing this, I heard of Mr. Bassett's passing. I now only wish I had taken the time to tell him this.

[5]Look at the inside of your copy. An old promise is kept.

Dedication

This is dedicated in the memory of Mary Ruth Becker

Table of Contents

List of Tables

List of Figures

Chapter 1

Neutrino Physics and the Standard Model

1.1 Introduction

The neutrino was first postulated by Pauli in 1930 to explain beta decay without invoking violation of energy conservation [2]. Almost another quarter century would pass until the first neutrino interaction was observed by Reines and Cowan in 1953 [3]. In 1962 it was discovered that there are more than one kind of neutrino, with the discovery of the ν_μ (versus the $\bar{\nu}_e$ type anti-neutrino discovered earlier) [4]. The third (family) type of neutrino interaction was not observed until recently, when the DONUT (E872) collaboration observed the ν_τ [5].

1.2 The Standard Model

The Standard Model (SM) is the theoretical basis of particle physics. It consists of what at first appears to be three different theories: electromagnetism, weak interaction, and strong interaction (although electroweak unification of electromagnetism and the weak

interaction is significant as we will see). Gravity is not part of the standard model. The standard model has been successful in explaining particle physics. No convincing violation of the standard model has ever been observed[1].

1.2.1 Leptons

In the Standard Model there are three generations of leptons. Each generation consists of a charged lepton and an electrically neutral particle, a neutrino. The leptons undergo electroweak interactions. The three generations of charged leptons are the electron (e), muon (μ) and tau (τ). The three generations of the neutrinos (ν) are the ν_e, ν_μ and ν_τ

1.2.2 Quarks

In the Standard Model there are three generations of quarks. Each generation consists of two quarks. The quarks undergo both electroweak and strong interactions. The first generation of quarks consist of the down (d) and up (u) quark. The second generation consists of the strange (s) and charm (c) quark. The third generation consists of the bottom or beauty (b) and the top or truth (t) quark. Normal matter is made up of only first generation quarks and leptons.

1.2.3 Strong Interaction-QCD

The strong interaction (Quantum Chromodynamics) is mediated by a massless spin-1 boson known as the gluon. The gluon interacts to particles through the particles color charge. There are three color charges, commonly called red, blue and green. This is represented mathematically by the SU(3) group. The quarks all carry color charge and thus interact with gluons. However, unlike the electrically neutral photon in electrodynamics, the gluons (all 8 of them) carry color as well. This leads to a

[1]This depends on exactly what you define the SM to be. As will be seen a non-zero ν mass could be considered evidence for non SM physics. See section 1.3.6

more complex theory. All particles observed in the physical world appear to be color neutral (no net color) and quarks are never observed by themselves. Another important property is called asymptotical freedom which means that the strong force becomes weaker at high energy [6][7]. QCD is a significant part of modern particle physics, but is not at the main point of this thesis, the interested reader can instead reference [12][13].

1.2.4 Electroweak

The Electroweak interaction is unified electrodynamics and weak interaction theory. The electroweak is sometimes called GSW theory for it three creators, Glashow, Salam and Weinberg. Glashow [8] proposed the SU(2)xU(1) symmetry group for the weak interaction. Salam and Ward [9] created a theory of leptons using this symmetry. Weinberg [10] proposed spontaneous symmetry breaking as a mechanism in a theory for leptons. However, the electroweak theory was not shown to be renormalizable (non-divergent) until 't Hooft [11]. In the electroweak theory there are three massive bosons that mediate the weak force, the W^+, W^- and Z^0. In this theory there are two additional quantum numbers, weak-isospin and hypercharge. The leptons and quarks can be examined in terms of these of new quantum numbers. There are left-handed doublets that have weak-isospin of 1/2 and a third component of isospin (τ_3) of $\pm\frac{1}{2}$.

$$\begin{pmatrix}\nu_e\\ e\end{pmatrix}_L, \begin{pmatrix}\nu_\mu\\ \mu\end{pmatrix}_L, \begin{pmatrix}\nu_\tau\\ \tau\end{pmatrix}_L \tag{1.1}$$

$$\begin{pmatrix}u\\ d\end{pmatrix}_L, \begin{pmatrix}c\\ s\end{pmatrix}_L, \begin{pmatrix}t\\ b\end{pmatrix}_L \tag{1.2}$$

There are also a set of singlets with weak-isospin of 0.

$$(e)_R, (\mu)_R, (\tau)_R \tag{1.3}$$

$$(u)_R, (c)_R, (t)_R \tag{1.4}$$

An important point to raise here is that neutrinos have only been observed in left handed states and anti-neutrinos have only been observed in right handed states, which leads to the violation of parity (see Chapter 2). However, in the weak interaction the right handed particles do not interact. This is a consequence of the Vector-Axial (V-A) nature of the interaction [14][15][16]. The V-A behavior means that in the weak interaction one must include a term proportional to $\gamma_\mu(1-\gamma_5)$. This insures the observed behavior of neutrinos.

1.2.5 Overview of SM particles

There are many measured properties of Standard Model particles. Indeed there are more properties than could be possibly written about here. However, Appendix B has an brief overview of some basic properties of the fundamental particles (quarks, leptons and force mediating bosons).

1.3 Neutrino Properties and Interactions in the Standard Model

Experimentally, there are three light neutrinos, the ν_e, ν_μ and ν_τ. This is known because of precise measurements of the Z^0 lineshape. A result from LEP gives $N_v = 3.011 \pm 0.077$ [18] looking at the cross section for events with photon(s) and missing energy. By looking at all the data collected at LEP a value of $N_v = 2.994 \pm 0.012$ [17] can be found. These measurements and other similar measurements are based on looking at the Z^0 and measure the number of neutrinos that have a mass less than $M_Z/2$ and couple to the Z^0.

1.3.1 Standard Model Neutrinos

There are three different possible types of neutrinos, Dirac, Majorana and Weyl. Both Dirac and Majorana neutrinos can be massive while the Weyl neutrino must be massless. The result of these differences in neutrino properties can (in principle) be measured. The question of Dirac versus majorana neutrino is important because it is related to the question of whether a neutrino is its own anti-particle. The other fermions in the SM are known to be Dirac type particles because they are charged and the difference in particle and anti-particle can be seen in the electric charge. This argument does not work for the neutrino.

1.3.2 Helicity and Chirality

Helicity is the projection of spin along the direction of motion of the particle. For spin 1/2 particles (all the leptons and quarks!) this means that the spin can be parallel or anti-parallel (two spin states) with the direction of motion.

$$\lambda = \vec{P} \cdot \vec{S}/|P| \tag{1.5}$$

States which are parallel $\lambda = 1/2$ are called right handed and states which are antiparallel λ = -1/2 are called left handed. Because helicity transform like a pseudoscalar, it flips signs under a parity transformation. This means that in a parity conserving interaction both left and right handed states must be equally involved [19]. However, in general the helicity of a particle depends on the observer. The reason is that it is in general possible to Lorentz boost an observer such that the sign of the momentum flips, while the spin is unchanged, causing the helicity to flip. This means that a particle could be observed as a right handed particle by one observer and a left handed neutrino to a different observer. There is just one exception, Weyl particles.

If a particle is a Weyl particle, then the Hamiltonian commutes with γ_5 and both

can be simultaneously diagonalized. However, ${\gamma_5}^2 = 1$ and thus the two eigenvalues of γ_5 are 1 or -1. A state with an eigenvalue of 1 is said to positive chirality and a state with an eigenvalue of -1 is said to have negative chirality. It is possible to write the Weyl spinor as [69]:

$$\psi = \psi_L + \psi_R \tag{1.6}$$

$$\psi_R = \frac{1}{2}(1 + \gamma_5)\psi \tag{1.7}$$

$$\psi_L = \frac{1}{2}(1 - \gamma_5)\psi \tag{1.8}$$

An important thing to note is that helicity of a particle is always defined, even if the particle is massive. However, a massive particle does not have a well defined chirality because the Hamiltonian only commutes with γ_5 in the massless limit.

1.3.3 Weyl Neutrinos

Weyl neutrino can be represented by a two component spinor. Weyl neutrinos are by definition massless. However, the evidence is currently strong that neutrinos are massive. Even though neutrinos are not massless, the momentum of neutrinos are normally large compared to their mass. Thus, the study of Weyl neutrino properties are relevant. Weyl neutrinos have a definite value of helicity because they travel at the speed of light and there are no frames of reference that can flip the momentum. A Weyl neutrino must have its electric and magnetic dipole moments vanish. A detailed discussion of electromagnetic interactions in all types of neutrinos is given by Mohapatra and Pal [20].

1.3.4 Dirac Neutrinos

Dirac neutrinos are represented by 4 component spinors just like any other lepton or quark in the standard model. A Dirac neutrino is a different particle from Dirac anti-neutrino. In principle a Dirac neutrino can posses a electric and magnetic moment. The magnetic moment (SM) is calculated to be [21]:

$$\mu_\alpha \approx \frac{3eG_F}{8\pi^2\sqrt{2}} m_\alpha \tag{1.9}$$

It is non zero for a massive neutrino. For a mass of the neutrino on the order of an eV this is expected to $\approx 3 \times 10^{-19}\mu_B$, while a limit based on Solar neutrino data from Super-Kamiokande gives a limit of $< 1.5 \times 10^{-10}\mu_B$[22].

1.3.5 Majorana Neutrinos

Majorana neutrinos are represented by a two component spinor. A Majorana [23] neutrinos is the exactly same particle as a majorana anti-neutrino. A Majorana neutrino must have its magnetic and electric dipole moments vanish (in the vacuum) [27]. However, this is not true for Majorana neutrinos in a medium[28]. Unlike the Weyl or Dirac neutrino, a Majorana neutrino has the possibility of participating in neutrinoless double beta decay[24]. The Heidelberg-Moscow double beta decay experiment claimed to observe neutrinoless double beta decay [25] in Ge76, although serious doubts have been raised [26] with regard to this claim.

1.3.6 What is a Standard Model Neutrino?

The standard model was created with massless neutrinos. This means that the SM neutrino is a Weyl particle and thus has no electric or magnetic dipole moment and as will be explained in the next section, cannot undergo neutrino oscillation. In this

sense massive neutrinos are evidence for non-SM physics. On the other hand the massless nature of SM neutrinos are 'put in by hand' by having a theory with only left handed neutrinos and right handed anti-neutrinos (V-A Interactions). This point can be observed by looking at the lepton mass term:

$$M_{lepton} = \frac{\lambda}{2}(\bar{\psi}_R\psi_L + \bar{\psi}_L\psi_R) \tag{1.10}$$

Where λ is a constant. This expression is discussed in some detail by Greiner[29]. However, it is clear that the standard model neutrino must be massless independent of the value of λ as V-A interaction requires.

1.3.7 Neutrino Interactions

Neutrinos undergo two fundamentally different type of interactions depending on whether a $W^{\pm}$ or Z^0 boson is exchanged. These interactions are charged current interactions and neutral current interactions. Both type of interactions can result in neutrino scattering off either leptons or quarks. Charged Current interactions were the interactions observed in the first generation of neutrino experiments. Neutral Current interactions were not observed until 1973 in Gargamelle [30].

Charged Current Interactions

Charged current (CC) interactions occur when a quark or lepton interacts with a $W^{\pm}$. An example of a CC event is shown in figure 1.1. The important point of this example is that a charged lepton is produced. However, another important point of this example is that besides the charged lepton, a hadronic shower can also be produced (and observed) when there are neutrino-nucleon interactions. The charged lepton produced in CC interaction must be from the same generation as the neutrino that produced it. This means that a μ^- must come from a ν_μ not an ν_e or ν_τ.

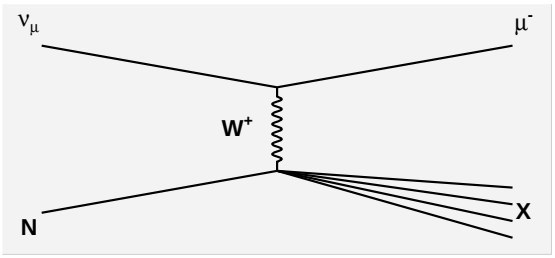

Figure 1.1: This is an example of Neutrino-Nucleon CC scattering. N here is some nucleon and X is some final hadronic state. This type of CC interaction is Deep Inelastic Scattering. There is both a charged muon and a hadronic shower in this event.

Neutral Current Interactions

Neutral Curent (NC) interactions occur when a quark or lepton interacts with a Z^0. All flavors of neutrinos can participate in NC interactions. No (primary) leptons are produced from an NC interaction. In a nucleon-neutrino interaction a NC interaction can be observed from the hadronic shower it produces. An example of a NC process is shown in figure 1.2.

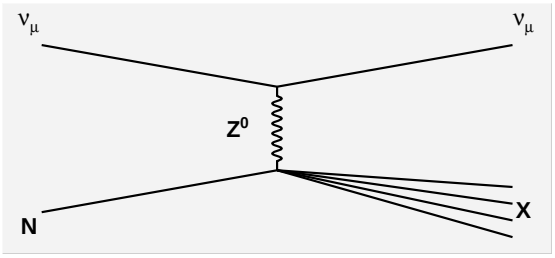

Figure 1.2: This is an example of Neutrino-Nucleon NC scattering. N here is some nucleon and X is some final hadronic state. Unlike CC scattering no charged lepton is produced.

1.4 Properties of Massive Neutrinos

Neutrino oscillations are experimentally the most important consequence of neutrino mass. Many important things can be learned from neutrino oscillation. However, neutrino oscillation cannot be used to distinguish between Dirac and Majorana oscillations [31]. The fundamental cause of neutrino oscillation is that neutrinos are generated in weak (flavor) eigenstates but proprogate in mass eigenstates. These two states are not in general the same. Another way to think of this is that the flavor states are really a linear superposition of mass states. Pontecorvo [32] was the first to discuss the possibility of neutrino oscillation. The interested reader has many sources for example [69][17][20] which discuss neutrino oscillations in detail.

1.4.1 Neutrino oscillation

Two flavor neutrino oscillation is a good example to start to understand neutrino oscillation. In two neutrino oscillation one considers two flavor of neutrinos ν_α,ν_β and two mass states of neutrinos ν_1,ν_2. The mixing is represented by a 2 x 2 Unitary matrix. The equation for this is:

$$\begin{pmatrix} \nu_\alpha \\ \nu_\beta \end{pmatrix} = \begin{pmatrix} cos\theta & sin\theta \\ -sin\theta & cos\theta \end{pmatrix} \begin{pmatrix} \nu_1 \\ \nu_2 \end{pmatrix} \tag{1.11}$$

In the context of neutrino oscillation the angle θ is known as the mixing angle. Notice that if $\theta = 0$, then no mixing takes place. If $\theta = \frac{\pi}{4}$ it is called maximal mixing. As it will be shown below, if no mixing takes place then no neutrino oscillation can occur. If maximal mixing occurs then the amount of oscillation will be the greatest amount possible. To see this, look at the probability that a neutrino ν_α is observed as ν_α after a time t has passed.

$$P_{\nu_{\alpha\alpha}} = |\langle \nu_\alpha(0) | \nu_\alpha(t) \rangle|^2 \tag{1.12}$$

P here is the oscillation probability. The probability that the neutrino has oscillated to a different neutrino is (1-P). Given the form of neutrino mixing and the fact that neutrinos are ultra-relativistic, $E \approx p + \frac{m^2}{2p}$ it is possible to calculate out the oscillation probability is terms of observable quantities (in units where $\hbar = c = 1$).

$$P_{\nu_{\alpha\alpha}} = 1 - sin^2(2\theta) sin^2\Big(\frac{\Delta m^2_{12} L}{4E}\Big) \tag{1.13}$$

In the equation time has been replaced by L which is known as the baseline of the oscillation. $\Delta m^2_{12} = m^2_2 - m^2_1$ is known as the mass difference or simply Δm^2. It is important to realize that $sin(2\theta)$, Δm^2 are the physically important quantities that represent neutrino oscillation while L and E represent the experimental conditions. It is common for this expression to be written is units where L is measured in kilometers, Δm^2_{12} is measured in eV^2, and E is measured in GeV. In this case, the oscillation probability is given as:

$$P_{\nu_{\alpha\alpha}} = 1 - sin^2(2\theta) sin^2\Big(\frac{1.27\Delta m^2_{12} L}{E}\Big) \tag{1.14}$$

This expression also shows the importance of L/E. Since in general the energy and baseline of neutrino oscillations vary with the type (atmospheric, solar, long baseline, ...) of experiment, the parameter space probed by these different neutrino oscillation experiments also varies. For example, atmospheric and long baseline neutrino experiments all measure neutrinos on the order of 1-100 GeV. The baseline in longbaseline experiment is $\approx 10^2 - 10^3$ km while atmospheric neutrinos have a baseline of the order $10 - 10^4$ km. In two flavor neutrino oscillations there are three cases of interest:

$$P_{\nu_{\alpha\alpha}} = 1 - sin^2(2\theta) sin^2\Big(\frac{1.27\Delta m^2_{12} L}{E}\Big) \begin{cases} \approx 1 & \text{for L/E} \ll 1 \\ \approx 1 - sin^2(2\theta) sin^2\Big(\frac{1.27\Delta m^2_{12} L}{E}\Big) & \text{for L/E} \approx 1 \\ \approx 1 - \frac{1}{2} sin^2(2\theta) & \text{for L/E} \gg 1 \end{cases} \tag{1.15}$$

In the first case, the neutrinos have not had enough time to have oscillated. In the second case, the neutrino are undergoing the first oscillation (first dip) and the first rise. In the final case, the neutrinos are undergoing rapid oscillations in L/E space. This suggests that the second case is the best situation to measure neutrino oscillation parameters. In the first and third situation only the total number of observed neutrinos can be measured. Remember that all experiments have a finite energy resolution and the rapid oscillation in L/E becomes smeared out (L is 'smeared' atmospheric neutrino oscillation experiments, for example). However, when L/E$\approx$ 1, both the number and spectrum of L/E can in principle be extracted.

1.4.2 Three flavor oscillation

Even though two flavor oscillation gives a simple and relatively easy to understand example of neutrino oscillation, it must be remembered that there are three SM neutrinos. This means that the physically important model of three flavor oscillation must be understood. Three flavor mixing is parametrized by three mixing angles and a (Dirac) CP violating phase. As with the two flavor case, this can be represented by a unitary matrix U:

$$U = \begin{pmatrix} c_{12}c_{13} & s_{12}c_{13} & s_{13}e^{-i\delta} \\ -s_{12}c_{23} - c_{12}s_{23}s_{13}e^{i\delta} & c_{12}c_{23} - s_{12}s_{23}s_{13}e^{i\delta} & s_{23}c_{13} \\ s_{12}s_{23} - c_{12}c_{23}s_{13}e^{i\delta} & -c_{12}s_{23} - s_{12}c_{23}s_{13}e^{i\delta} & c_{23}c_{13} \end{pmatrix} \tag{1.16}$$

Where $s_{ij} = sin(\theta_{ij}), c_{ij} = cos(\theta_{ij})$ and δ is a CP violating phase [33]. This is clearly more complex than the two flavor case. Besides having three angles instead of one angle there is an imaginary phase that can give rise to CP violation. This matrix is known as PMNS (Pontecorvo-Maki-Nakagawa-Sakata) matrix in recognition of the work of Pontecorvo and Maki, Nakagawa and Sakata [34].

1.4.3 Matter effects

Matter effects are a consequence of the fact that the universe is made of almost exclusively first generation particles. In particular, because of the short lifetimes of the muon and tau, the electron is effectively the only charged lepton in matter. The reason this is significant is that when neutrinos proprogate through matter (for example, atmospheric neutrinos going through the earth or solar neutrinos going through the sun) the neutrinos can have interactions with the matter. However, because there are many electrons in the earth or sun and basically no muons in the earth or sun the interactions are not the same. The important idea is forward coherent scattering, consider $\nu_e + e^- \rightarrow \nu_e + e^-$ can be mediated by a W but the same process cannot happen with ν_μ, ν_τ as there are no μ, τ in normal matter. This was first realized by Wolfenstein [35]. This can cause the observable parameters $(\Delta M^2, sin^2(2\theta))$ to be measured at different values than those that would be observed in vacuum. This is known as the MSW effect (Mikheev-Smirnov-Wolfenstein) to include the contribution of Mikheev and Smirnov [36].

1.5 Evidence for Massive Neutrinos

The evidence for massive neutrinos is neutrino oscillation, in particular, neutrino oscillation of solar and atmospheric neutrinos. This evidence consists of many different experiments measuring different sources and different types of neutrinos. These experiments have different detectors with different fundamental detection technology and different systematic errors. This is important, as it is difficult to imagine a single systematic error or faulty detector technology that can explain the observed results.

1.5.1 Atmospheric neutrino experiments

There are a set of atmospheric neutrino experiments that have shown strong evidence for neutrino oscillations. The three experiments listed below were not the first neutrino experiments, but all made an important contribution to atmospheric neutrino oscillation physics. Atmospheric neutrinos are central to this thesis and are discussed in more detail in chapter 5. The results for the three experiments listed below are presented later in the chapter.

Super-Kamiokande

Super-Kamiokande is a large water cherenkov detector located in the Mozumi mine in the Gifu prefecture Japan. The detector lies under a depth of 2700 meter water equivalent[2] (mwe). It has a total mass of 50 kton and a inner fiducial region of 22.5 kton filled with ultrapure water. The fiducial region has PMT (50 cm) looking inward (to the fiducial region) and pointing out (20 cm) to veto particle both entering and leaving the fiducial region. Both the charge and timing are used for event reconstruction [37]

Soudan2

Soudan2 was a tracking calorimeter located 2341 feet (2090 mwe) underground at the Soudan underground state park in Soudan, Minnesota. The detector had a mass of slightly less than a kiloton (963 tons) and was built in order to search for nucleon decay. The detector consisted of individual 2.7x1xl m modules (224 total). Each module consisted of thin (1.6 mm) sheets of steel that formed a 'honeycombed' pattern in which 7560 1 meter long drift tubes filled with a Argon/CO_2 mixture were placed. The detector was surrounded by a large ($2040m^2$) veto shield that had nearly 4π coverage. The detector had good spatial resolution (0.18 cm resolution in transverse direction)

[2]This means the rock overburden of the detector is equivalent to being under 2,700 meters of water. It is common to use this measure of depth in underground physics.

[38].

MACRO

MACRO was an experiment located in hall B at the Gran Sasso Laboratory (LNGS) in Italy. The average depth of the detector was 3700 mwe. The detector was made of 6 super modules each 12.6x12x9.6 meters in dimension. The purpose of MACRO was to look for monopoles and muons from cosmic point sources. The detector used both streamer tube and scintillator technology. The detector has horizontal and lateral planes of streamer tunes and liquid scintillator. The top and bottom most plane of streamer tubes are separated from the next plane of streamer tubes by a plane of liquid scintillator, while the other horizontal planes are separated by an absorber [41].

1.5.2 Solar Neutrinos

The first persistent sign of possible neutrino oscillation was observed in the solar neutrinos. Solar neutrinos detection was discussed from a theoretical point of view by Bahcall [42] and from an experimental point of view by Davis [43] in two (back to back) Physics Review Letters papers in 1964. Bethe [44] looked at neutrino production in stars 25 years earlier. In particular, Davis and Bahcall considered using $^{37}Cl + \nu_e \rightarrow {}^{37}Ar + e^-$ to look for solar neutrinos although this idea was presented in unpublished form earlier (see references in [42]). This would be used for the Homestake[45] experiment. Over the next 35 years a great deal of work was done on solar neutrino physics, and it became evident that there was a problem, as the number of observed neutrinos was lower than expectations. This was seen with different detectors looking at neutrinos made in different reactions in the sun. Although, neutrino oscillation is a possible explanation of this observed deficit, it is not the only explanation. The deficit could be caused (for example) by a overly simple model of the sun. For a historical review of the experimental situation in the late 1990's, see Mohaptra [20]. If neutrino oscillations are responsible

for the deficit of solar neutrinos, it would be expected that the neutrino oscillate from ν_e to either a ν_μ or a ν_τ. However, since all three active flavors can interact by means of the neutral current, it would be expected that while there would be a ν_e deficit, the NC rate would be consistant with solar model. The SNO experiment [46] did this measurement. SNO is a water cherenkov detector located in a mine near Sudbury Ontario. SNO was able to measure three types of reactions, CC, NC and Elastic Scattering (for example $\nu_e e \rightarrow \nu_e e$). CC interactions are only sensitive to ν_e, while NC was sensitive to all flavors of neutrinos. The ES reaction was mainly sensitive to ν_e, but it also had partial sensitivity to the other flavors. When looking at all three interactions [47], SNO observed that while the NC rate was consistent with the solar model, the non-electron type neutrino rate (ν_μ, ν_τ) was 5.3σ above zero. Since only ν_e are made in the sun, this is strong evidence for neutrino oscillation. Further evidence from an experiment in Japan, KamLAND[48] that used anti-neutrinos from nuclear reactors helped resolve some possible ambiguousness in the solar neutrino results.

1.5.3 Atmospheric Neutrinos

Atmospheric neutrinos are made (in the context of a simple model) when cosmic ray particles interact in the upper atmosphere, produce a secondary shower of mesons which have decays that produce neutrinos[3]. This topic is dealt with in great detail in chapter 5. From an experimental point of view, atmospheric neutrino events can be divided into three different categories based on where the event vertex takes place relative to the detector. Fully and partially contained events have an event vertex that in inside the particle detector, with fully contained events stopping while still completely inside the detector. Upward going muons have an interaction in the material outside the detector. A fully contained event can in general be any flavor of neutrino and be either

[3]For example:$P + {}^{16}_{8}O \rightarrow \pi^+ + X$. Where X is the remnant of the oxygen nucleus. The $\pi^+ \rightarrow \mu + \nu_\mu$ decay chain produces a neutrino. If the μ decays before it hits the ground it produces two neutrinos.

a CC or NC interaction. Partially contained events generally refers to CC induced muons that are produced in the detector but exits the detector. This is because muons travel farther than particles that shower. Upward going muons (as its name suggests) are CC induced muons that are produced in the material (rock for example)below the detector. In general, these muons are also produced above the detector and on the side of detector (Horizontal muons), however, since the background of cosmic ray muons is only coming from above there is no way to tell the difference. It is important to note that the populations of neutrinos (with regard to energy and direction) in the three different categories are not the same, thus the the different categories complement each other.

Atmospheric neutrino experimental results

A wide variety of experiments have shown evidence for oscillation of atmospheric neutrinos. The two experimental results listed here do not form an inclusive list, but rather are meant to illustrate these situation. Super-Kamiokande [37] found evidence of neutrino oscillation by observing a deficit of $\nu_\mu(\bar{\nu}_\mu)$ neutrinos while observing the predicted flux of $\nu_e(\bar{\nu}_e)$ neutrinos. This deficit was observed to be direction (zenith angle) dependent, with the largest amount of deficit coming from neutrinos from the other side of the earth. This results is consistent with $\nu_\mu \rightarrow \nu_\tau$, as the $\nu_e(\bar{\nu}_e)$ result is consistent with no oscillations, the $\nu_\mu(\bar{\nu}_\mu)$ cannot be turning into $\nu_e(\bar{\nu}_e)$. This only leaves $\nu_\mu \rightarrow \nu_\tau$ (assuming the standard picture of neutrinos). Another experiment that showed evidence of neutrino oscillation is Soudan2 [40]. The Soudan2 experiment carried out an unbinned maximal likelihood fit of the atmospheric neutrino data it collected. Like Super-Kamiokande it to observed a deficit of $\nu_\mu(\bar{\nu}_\mu)$ neutrinos. There result was consistent with the Super-Kamiokande result. It should be noted that Soudan2 and Super-Kamiokande are different experiments. They have different active materials, use

different photo-detector technology and used different analysis techniques. This is valuable because it reduces the likehood that a single systematic could fake the neutrino oscillation signal.

1.5.4 Accelerator Based Experiments

The only long baseline experiment that as of the end of 2005 that has published results is K2K[49]. Like other long baseline neutrino experiments K2K has three parts, a neutrino beam, a near detector(s) and a far detector. The baseline distance is 250 km.

1.5.5 Beam

The beam for K2K is produced at the KEK-PS. The beam starts out as a 12 GeV beam of protons (6×10^{12} per spill) that are scattered off an aluminum target. A magnetic horn is used to focus π^+ while defocussing all negatively charged particles. The pions are then allowed to go down a 200 m long decay pipe before hitting a beam dump that is used to stop charged particles. It is important to understand the kinematics of the beam, in order to accomplish this a gas Cherenkov detector is sometimes inserted into the beam line. Downstream of the beam dump a muon monitor is used to understand the spill by spill variation in the beam. The muon monitor is an ionization chamber and a silicon pad detector. The resulting beam is almost entirely (98.2 percent) ν_μ and has an average energy of 1.3 GeV.

1.5.6 Near Detectors

K2K uses two different near detectors. Since the comparison of the neutrino beam at the near and far detector is the experiment, it is important to have the near and far detector as similar as possible. To do this K2K built a 1 kt water cherenkov detector 300 m from target. It uses the same algorithms and same phototubes in the same arrangement as Super-K. It is the neutrinos this detector that will be compared with Super-K neutrinos.

However, K2K uses a second near detector which is a scintillating fiber detector. The purpose of the second detector is to understand the neutrino interactions in the beam.

1.5.7 Far Detector

The far detector for K2K is Super-Kamiokande. The neutrinos from the beam can be separated from atmospheric neutrinos by the use of GPS timing. Because the TOF is known between KEK and Super-K a timing cut of $1.5\mu s$ can be applied. With this cut and other cuts similar to the FC neutrino analysis the background from atmospheric neutrinos is reduced to $\approx 10^{-3}$.

1.5.8 First results

28 FC events were observed in the far detector after the cuts were applied. This is compared to an expectation of $37.8^{+3.5}_{-3.8}$ events with no oscillation. This is based on extrapolating the results in the near detector to the far detector. This shows a deficit of neutrinos. Although, the deficit is small, it must be remembered that additional information is in the energy spectrum.

1.5.9 Neutrino mixing parameters

It is possible to look at all the available data from neutrino experiments and try and determine the most likely form of the PMNS matrix. This requires an three flavor analysis of the different experiments and use solar ,atmospheric, long baseline and reactor experiments. The results [50] are $\Delta m^2_{12} = (6.0 - 8.4)\times 10^{-5} eV^2, \Delta m^2_{12} = (1.8 - 3.3)\times 10^{-3} eV^2, sin^2(\theta_{12}) = (0.25 - 0.36), sin^2(\theta_{23}) = (0.36 - 0.67), sin^2(\theta_{13}) = (\leq 0.035)$ where the values are given in the 2σ range. However, the above analysis does not include any possible effects from CP violation and also use the fact that one mass scale is much bigger than the other to set $\Delta m^2_{12} = 0$ in the long baseline and atmospheric analysis and $\Delta m^2_{13} = \infty$ in the solar and KamLAND analysis.

Chapter 2

CPT Symmetry and the Neutrino

2.1 Charge, Parity and Time Reversal Symmetry

The CPT theorem is an important result in quantum field theory. It is important because although the separate Charge conjugation, Parity or Time reversal symmetries can (and are) violated in nature, the combined CPT symmetry has always been observed to be conserved.

2.2 Discrete Symmetries and CPT

An examination of the separate discrete symmetries is given below. Since the purpose of this section is to understand neutrino physics, only the transformation properties of fermion (Dirac) fields will be considered. The following is based on the presentation by Kim [69] but Gross [71] and Peskin [70] also include a good presentation of the material. Direct comparison of results between these source must be done carefully as the authors use different notations.

2.2.1 Parity

The parity operation can be thought of as an inversion of the spatial coordinates. A Dirac fields transformation under parity is given by:

$$\mathcal{P}\psi(t,\mathbf{x})\mathcal{P}^{-1} = \eta_F\gamma_0\psi(t,-\mathbf{x}) \tag{2.1}$$

where $\eta_F = \pm 1$ is the intrinsic parity of the fermion.

Experimentally, parity is known to be violated in the weak interaction. This was first proposed by Lee and Yang [67] and soon afterwards observed by Wu [68]. The violation of parity in the weak interaction is *maximal*. There is no evidence of parity violation in electromagnetism or the strong interaction.

2.2.2 Charge Conjugation

The charge conjugation operation can be thought of as an exchange of a particle for its anti-particle. A Dirac fields transformation under Charge conjugation is given by:

$$\mathcal{C}\psi(t,\mathbf{x})\mathcal{C}^{-1} = \xi_F\lambda\gamma^2\gamma^0\bar{\psi}(t,\mathbf{x})^T \tag{2.2}$$

where $|\xi_F| = 1$ and ξ_F is a phase and $|\lambda|^2 = 1$.

2.2.3 Time Reversal

The Time reversal symmetry can be thought of as an inversion of time. A Dirac field's transformation under time reversal is given by:

$$\mathcal{T}\psi(t,\mathbf{x})\mathcal{T}^{-1} = \zeta_F\lambda\gamma^1\gamma^3\psi(-t,\mathbf{x}) \tag{2.3}$$

where $|\zeta_F| = 1$ and ζ_F is a phase and $|\lambda|^2$.

The $\mathcal{T}$ operator is not linear, rather it is anti-linear or anti-unitary. This means that it operates like:

$$\mathcal{T}(a|\psi\rangle + b|\phi\rangle) = a^*\mathcal{T}|\psi\rangle + b^*\mathcal{T}|\phi\rangle \tag{2.4}$$

The time reversal symmetry is known to be broken in systems that violate the CP symmetry. Besides being required by CPT invariance this has been directly observed in the kaon system [73].

2.2.4 CP

CP is the combined charge conjugation and parity operation. CP is known to be violated in the quark sector. The first discovery of the CP violation was in the mixing and decay of neutral kaons [72]. More recently, CP violation has been observed in B meson physics [74][75]. However, no evidence of CPT violation has been observed in these systems despite a number of high precision measurements.

2.2.5 CPT

CPT is the combined charge conjugation, parity and time reversal operator. A Dirac field's transformation under $\Theta = \mathcal{CPT}$ is:

$$\Theta\psi(t,\mathbf{x})\Theta^{-1} = \omega\gamma_5\gamma_0\bar{\psi}(-t,-\mathbf{x})^T \tag{2.5}$$

where $|\omega|$=1 and ω is a phase.

2.2.6 CPT Theorem

The CPT theorem states if a Lagrangian density is normal ordered, Hermitian, Lorentz invariant and obeys the normal the spin-statistic relationship (Local), then the combined CPT (in any order of C,P or T) transformation is always a symmetry of the theory. This was proved in the 1950's by Luders,Pauli and Schwinger[58]. Related work was done on the topic [63] at about the same time.

2.3 Implications of CPT and Neutrinos

2.3.1 Implication of CPT for particle physics

There are several important consequences of CPT conservation for particle physics. One significant result is that the mass of a particle and its anti-particle must be the same. The total lifetime of a particle and its anti-particle must be the same, as must the gyromagnatic ratio (g) and the Charge-Mass ratio [61]. Greenberg [62] shows that if particles have different masses compared to anti-particles the theory must be non-local.

2.3.2 Implication of CPT for neutrinos

If CPT, CP or T are violated in neutrino oscillation there will be an observable effect. Although, Pakvasa [64][65] was not the first to publish these results they results will be presented in a modified version of his notation. P here is the probability for oscillation over a distance L and energy E, where α, β=ν_e, ν_μ, ν_τ.

2.3.3 CP violation in neutrinos

CP violation is observed in neutrinos if [59][60]:

$$P_{\alpha\beta}(L,E) \neq P_{\bar{\alpha}\bar{\beta}}(L,E) \tag{2.6}$$

for $\beta \neq \alpha$

2.3.4 T violation in neutrinos

T violation is observed in neutrino oscillation if [60]:

$$P_{\alpha\beta}(L,E) \neq P_{\beta\alpha}(L,E) \tag{2.7}$$

for $\beta \neq \alpha$

2.3.5 CPT violation in neutrinos

CPT violation is observed in neutrinos oscillation if [59]:

$$P_{\alpha\beta}(L,E) \neq P_{\bar{\beta}\bar{\alpha}}(L,E) \tag{2.8}$$

for $\beta \neq \alpha$

or

$$P_{\alpha\alpha}(L,E) \neq P_{\bar{\alpha}\bar{\alpha}}(L,E) \tag{2.9}$$

2.4 Current Bounds on CPT violation

The current bounds on CPT violation depend greatly on the process in question. The bounds can based on a variety of different measurements. These bounds look for differences in particle and anti-particle properties. An example of these bounds is given in table 2.1.

2.4.1 Present Limits on CPT violation om non-neutrino systems

Particle	CPT Test	Method	Bound	Ref.
e	$M = \overline{M}$	e^+ Spectroscopy	$< 8 \times 10^{-8}$	[76]
P	$M = \overline{M}$	Laser Spectroscopy: $He^+\bar{P}$	$< 5 \times 10^{-7}$	[77]
$\pi^{\pm}$	$\tau = \overline{\tau}$	Beam Experiment	$(5.5 \pm 7.1) \times 10^{-4}$	[78]
K^0	$M = \overline{M}$	Beam Experiment	$< 2 \times 10^{-18}$	[79]
e	g_-/g_+	Penning Trap	$1 + (0.5 \pm 2.1) \times 10^{-12}$	[80]

Table 2.1: This shows some limits on CPT violation from some common systems in high energy physics. Notice that the systems include both lepton and quark systems. Also notice that the measurements are done with different experimental methods and test different predictions of the CPT theorem. In the case of CPT conservation the first four example should be zero and the last one should be 1.

As the values in Table 2.1 show, in many systems any CPT violation is small. In comparison, the parity violation in the weak interaction is maximal. Even the value of

CP violation in Kaon systems is larger ($\approx 2.3 \times 10^{-3}$) [72] than least stringent limit presented, while most are much stronger than the observed CP violation in Kaons.

2.4.2 Present Limits on CPT violation in neutrino systems

The limits on CPT violation in neutrinos are not as strong as those for other systems already discussed. In fact the published limits in the Review of Particle Physics are so weak that even large violation of CPT are not ruled out[17]. These limits involve limits on CPT violation that are many orders of magnitude greater than ΔM^2. For example, Clark[87] gives a limit of 450 KeV on the difference between ν_μ and $\bar{\nu}_\mu$. Thus for all practical purposes any limit on this is useful.

2.5 Theoretical possibilities for violation of CPT

Even though CPT violation has never been seen and would require the breaking of a fundamental postulate of nature, CPT violating theories can be written down and prediction of the consequences of this violation made.

2.5.1 Why look for CPT violation in neutrinos

Given both the strong theoretical and experimental limits on CPT violation, the utility of searching for CPT in neutrinos could be questioned. However, it should be remembered that the Standard Model is only as good of a model as the experiments to back up its validity. It is for this reason this search for CPT violation is done. Given the weak limits that exist on CPT violation in neutrinos, an attempt to improve the limit should be made to verify or refute the CPT symmetry as much as possible.

2.5.2 Theories that break CPT

Given the requirements of the CPT theorem, any CPT violating theory must break one of the postulates that go into the CPT theorem. An example of a Lorentz breaking theory is given in the next section.

2.5.3 A CPT violating theory: An Example

An example of CPT violating theory is presented. This theory breaks Lorentz invariance by the supposing the existence of a constant vector (Aether). This model is given in Pakvasa [64] and Barger [65]. The breaking of Lorentz invariance is done by adding a non-Lorentz invariant term to the Lagrangian:

$$\bar{\nu}_L^{\alpha} b_{\alpha\beta}^{\mu} \gamma_{\mu} \nu_L^{\beta} \tag{2.10}$$

where α,β are flavor indices and b is the Lorentz violating vector which is rotationally invariant in the frame where the cosmic microwave background radiation is isotropic.

This means that the energy of neutrinos are eigenvalues of the following matrix:

$$m^2/2p = b^0 \tag{2.11}$$

where b^0 is a hermitian matrix (which will called b for the rest of this example) with the property that for anti-neutrinos $b \rightarrow -b$ except for Majorana neutrinos where b does not flip sign.

This leads to many possible situations. However, only one situation shall be considered here. It will be assumed that the oscillation can be represented by a two flavor model. It is also assumed that the same rotation angle θ diagonalizes both m^2 and b. Furthermore it is assumed that there is no phase difference between the two matrices. With these assumptions, the oscillation probabilities become:

$$P_{\alpha\alpha}(L,E) = 1 - sin^2(2\theta)sin^2\left(\left(\frac{\delta m^2}{4E} + \frac{\delta b}{2}\right)L\right) \tag{2.12}$$

and

$$P_{\bar{\alpha}\bar{\alpha}}(L,E) = 1 - sin^2(2\theta)sin^2\left(\left(\frac{\delta m^2}{4E} - \frac{\delta b}{2}\right)L\right) \tag{2.13}$$

Where $\delta b = b2 - b1$ and $\delta m = m_2^2 - m_1^2$. L is the distance the neutrinos (anti-neutrinos) travel and E is neutrino (anti-neutrino) energy. The difference which is exactly zero if CPT is conserved:

$$P_{\alpha\alpha}(L,E) - P_{\bar{\alpha}\bar{\alpha}}(L,E) = -sin^2(2\theta)sin\left(\frac{\delta m^2 L}{2E}\right)sin(\delta bL) \tag{2.14}$$

The effect of CPT violation in this theory is this phase difference in oscillation of neutrinos and anti-neutrinos.The situation gets more complex in the case where matter effects are taken into account. However, given the number of simplification already made and the general speculative nature of all CPT violating theories the implication of matter effects will not be dealt with here.

2.5.4 A more general CPT framework

The example given above is a limited example of what is possible with neutrions and CPT violation. A more general framework is the SME[1] as applied to neutrinos[66]. In this framework beside the normal terms in the SM Lagrangian, general Lorentz violating terms are added to the Lagrangian. This predicts several possible effects including neutrino-anti-neutrino mixing, sidereal and annual variation in neutrino oscillations. In this sense the Barger model is only a special case of a much more general theory.

[1]Standard Model Extension

Chapter 3

The MINOS Experiment

3.1 Introduction

The MINOS (Main Injector Neutrino Oscillation Search) is a long baseline neutrino oscillation experiment (E875). As with all long baseline neutrino oscillation experiments, the basic idea of MINOS is to make a beam neutrinos (which is understood) detect the beam after it has traveled a relatively short distance and then observe the beam when it has travel a much longer distance. The principle behind this is to eliminate or reduce the systematic uncertainty that exists when 'natural' (solar or atmospheric) neutrinos are used. A second important idea is that if the atmospheric neutrinos experiments have determined the approximate values for the oscillation parameters as these experiments have, then it is possible to tune the experiment with the baseline and energy of neutrino beam to value that maximize the oscillation signature. This tuning in L/E is important to get right. The neutrino energy spectrum can be changed by a reasonable amount. However, the distance between the near detector and far detector never changes. The project as whole is discussed in detail in the technical design report[81] and detector design parameter book[82]. It should be noted that some of the detailed information changed in the time between the completion of the documents and the

final construction. In the situation of a difference, the correct value will be used in this thesis.

3.2 MINOS-Long Baseline Neutrino Experiment

The MINOS experiment can be roughly thought of as three separate parts, a neutrino beam, a near detector and a far detector. There was also a calibration detector that was used to gain understanding of detector response, but was only ran before the main experiment. The neutrino beam and near detector both are located at Fermi National Accelerator Lab (FNAL) in Batavia, Illinois. The far detector is located in Soudan, Minnesota. The distance (baseline) between FNAL and Soudan is 735 km. The neutrino beam is a (nearly) pure beam of ν_μ. Figure 3.1 shows the beam path.

Since the goal of the MINOS experiment is to measure the neutrino spectrum at the near detector and again at the far detector, the near detector and far detector should be as similar as possible. However, this is not always possible. For example, the event rate is obviously much higher at the near detector from a simple flux argument. This for example mean the near detector must be able to handle multiple neutrino events in a short ($\approx \mu s$) time scale while this is not required at the far detector. Even though there some differences, the detectors are still similar. Both the near and far detector are magnetized iron calorimeters. Both use 4 centimeter wide scintillator read out by means of a wavelength shifting fiber connected to clear optical cable. The same design of alternating orthogonal planes of scintillator to gain 3 dimensional tracking is used in both detectors. Figure 3.2 shows the three different detector setups.

3.3 NuMI-Neutrino Beam

The NuMI beamline's[51] importances to the MINOS experiment cannot be understated. Both quantity and quality of neutrinos must be high. Although, the need for

Figure 3.1: This image shows the path of the neutrino beam as seen from above and as seen from the side. The beam is always several or more km underground.

high quantity (many neutrinos) might appear obvious, the importance for high quality neutrinos might not. The 'quality' of the neutrinos here is meant to be understanding of the kinematic distributions of the neutrino spectrum and the flavor of the neutrinos. It should be pointed out that by changing the configurations of the beamline elements the spectrum can change and the elements of the beamline must work with these different configurations. This is only meant to be a brief introduction to the beam and this explanation is simplified. The material for this section is from the technical design handbook[51].

3.3.1 NuMI Beamline

The NuMI beamline consists of both the actual elements which create neutrino beam and the elements which are used to measure properties about the beam from the decay particle produced with the neutrinos. The neutrinos are produced by the decay of mesons, mainly $\pi^{\pm}$ and some kaons. These mesons are made by colliding a beam of protons on a fixed carbon target.

Extraction

The first step in producing the neutrino beam is the extraction of 120 GeV protons every 1.87 seconds from the main injector. This is done with either 5 or 6 batches (depends on the other users of the main injector), each batch has 84 bunches. The bunch spacing is 18.8 ns and depending on the number of batches, the spill is either 8.14 or 9.78 μs long. The maximum number of protons per spill is 4×10^{13} and the maximum total power is 404 kW[1]. During the extraction the protons are bent with magnets and directed towards Soudan. The protons then interact with the target.

Target

The main target is a graphite target that consists of 47 segments. Each segment is 20 mm long and 6.4 mm high. These segments are separated by 0.3 mm. The target is enclosed in an aluminum casing with beryllium windows to allow the beam to enter and exit the airtight target enclosure. There is a water cooling system used to keep the target cool. This is important because of the large amount of energy being dumped in the target. After the target the particles are focused by the two magnetic horns.

[1]The actual power the beam runs at currently is closer to 250 kW

Magnetic Horns

The horns are used to focus or defocus charged particles based on the particle electric charge. This allows you to make a neutrino or anti-neutrino beam. The NuMI beams uses two horns. These horns produce a toroidal magnetic field using an inner and outer conductor. The horns have a parabolic inner conductor and produce a magnetic field with a high pulsed current of 200 kA. If a particle is focused by the first horn it will pass the second horn without being bent. The distance between the horns can be changed allowing the experiment to change the neutrino spectrum. Like the target, the horns must be water cooled.

Decay pipe and absorber

The decay pipe is 675 m long pipe kept at a low pressure (< 1 torr). This is designed to allow the π to decay. The decay pipe starts 50 m after the target, thus the particles have a total distance 725 m to decay. The pipe is 1.98 m in diameter and has windows on either side. The absorber is used to stop the hadrons from beam which did not interact to prevent them irradiating the rock in front decay pipe from both long term use and in the situation when the beam misses the target. It consists of aluminum and steel. However, this will not stop μ which need much more material to stop. These are ranged out with 240 m of rock between the end of the absorber hall and the start of near detector hall.

3.3.2 Beamline instrumentation

The purpose of the beamline instrumentation is to understand the interactions going on in the beam. There are two main reasons for this, first there is the physics goal of understanding the beam spectrum by measuring the flux, energy and angle of the decays particles. Second, there is the diagnostic use of this information. If for example, there is a problem with a component in the beamline, the instrumentation can help

prevent damage from occurring to the beamline. The instrumentation consists of a hadron monitor[52], a muon monitor[53] and beam profile monitor[54]. The hadron and muon monitors are ionization monitors. The beam profile monitor is a secondary emission monitor. This is not an inclusive list of every monitor or sensor in the NuMI hall see the referenced works for more details.

3.3.3 Neutrino beam

The NuMI beamline is designed such that it can be ran with different energy configurations. In particular, three configurations are normally discussed in MINOS. These three configurations are the Low energy (LE), medium energy (ME), and high energy (HE) configurations. The different energy spectrums are shown in figure 3.3:

The different configurations of the beams are useful to study different energy neutrinos being produced by different populations of particles, this help reduce the systematic uncertainties. The beam configuration for the main experimental run (versus these special short systematic runs) is set by the physics goal of trying to maximize the expected signal. If the signal is different than expected, the beam configuration can be changed.

A diagram of a simplified version of the beamline is given in figure 3.4.

3.4 Near Detector

The near detector is much closer to the beam than the far detector. This has several implications for the design of the near detector. First, the overburden of rock is much less than the far detector and thus the rate of cosmic muons is much higher. The rate of neutrino interactions from the beam is also much higher by a simple flux argument. The net result of this is two fold, the near detector can be smaller and the near detector must have electronics that can handle the much higher event rate. Indeed, the near detector must be able to handle many neutrino events per spill. Indeed only the events

vertices in a small fiducial region at the front of the near detector are sufficient to get high statistics.

The near detector[82] has 282 steel planes in a single super module. Unlike the far detector which is uniform in composition, the near detector has different sections. Ignoring the first plane which is only steel, the first 120 planes have scintillator on every plane. The last 161 planes have scintillator on only every fifth plane. This region is known as the spectrometer region and has the purpose to allow the μ^- from CC ν_μ to range out inside the detector. The total mass of the detector is 980 tons, less than 20% of the far detector mass. The near detector has the same 5.94 cm per plane pitch as the far detector and has 1.2 T magnetic field.

The 120 plane fully instrumented region is broken up into a 20 plane veto region in the front, this is done to eliminate rock muons produced when neutrinos interact in the rock in front of the far detector. This is followed by a 100 plane target region and this is followed by the spectrometer. Sometimes the target region is discussed as a separate target and shower region, although this is nothing other then a different definition. It should be noted that fully instrumented means scintillator on every plane, not scintillator covering the entire plane. Every fifth plane in the first 120 planes is fully covered by scintillator, the other 4 planes are only covered near where the beam should interact. The fiducial region is small, only about 25 cm radius around the beam center. The first 120 planes have only one ended readout and have no multiplexing. The spectrometer has 1 to 4 multiplexing versus the 1 to 8 multiplexing done in the far detector. The fiber are readout using M64[84][2] versus the M16 used at the far detector. The rate of cosmic rays has an advantage for the near detector alignment[83] and calibration as there are many more muons to use for these task than are at the far detector. However, the rate of $\approx$ 300 Hz (the cosmic rate at all detectors depend on your reconstruction requirements) is still low enough that the timing eliminates most

[2]The M64 is a single device that can be thought of as 64 independent photo multiplier tubes.

of the background, an requirement it comes from beam eliminate almost all the rest.

The near detector electronics is different from the far detector electronics because the near detector must handle multiple neutrino events in a single spill. Up to 20 neutrino events per spill are expected in the low energy beam and many more in a higher energy beam. In particular there is a possible problem if the events overlap. To deal with this a special purpose ASIC chip, the QIE[81][85][86] chip is used. The QIE runs at 53 MHz and is pipelined so that it has no intrinsic dead time. Even with these special electronics a software algorithm known as slicing is applied to assure that the pulse height is associated with the correct event.

3.5 Far Detector

The Far Detector (FD) is the topic of chapter 4. Thus this is just a brief introduction. The far detector consists of two separate iron calorimeters known as super modules (SM). With the exception that SM1 is 248 planes long and SM2 is 236 planes long they are identical. Each SM is constructed of scintillator-steel sandwich. Each plane has 1 inch of steel and 1 cm of scintillator. The scintillator is constructed in a plane of 8 scintillator modules which each consist of either 20 or 28 4.1 cm wide scintillator strips (192 strips per plane). Each scintillator strip has a single wavelength shifting fiber. This single fiber is read out on both sides by optically summing 8 fibers together and reading out the results on a single M16 PMT pixel. The optical signal is then converted to an electrical signal. The signal was then electronically read out and stored on disk. Both SM have an magnetic field of $\approx 1.4T$. There is a veto shield that covers the top and part of the sides of both detectors. This is only needed for the atmospheric neutrino experiment and not the beam experiment.

3.6 Calibration Detector

The Calibration detector (Caldet) was ran at CERN in Switzerland. The purpose of the Caldet detector was measure the response of the detector when it was placed in a beam of known particles. This really has two purposes. The first purpose is to measure the detector response of electromagnetic shower ($e^{\pm}$), hadronic showers ($\pi^{\pm}$, p, n) and $\mu^{\pm}$. The electromagnetic and hadronic shower response is of particular importance as this is the only real way to calibrate them. This contrasts with the $\mu^{\pm}$ which can be measured in variety of ways at different detectors.

The second purpose is to measure the effect of the different electronics has on the response. This was done by running both near and far detector electronics. Given the differences in the two sets of electronics it is important to make sure there is nothing systematically changing the results. Since Caldet finished its run, the project is well documented in many places[88][89][90]. The reference on Caldet come from these sources. This section is only meant to be a brief introduction.

Caldet ran between 2001 and 2003 in the T7 and T11 beamlines in the PS East Hall at CERN. The CalDet detector was much smaller than either the near detector or far detector. It had only 60 planes each 1m$\times$1m size plates each 2.5 cm (versus the other detectors 2.54 cm) thick steel planes. Unlike the near and far detector, CalDet had no magnetic field. One complication of CalDet that does not effect either of the two other MINOS detectors is that CalDet had to be portable so it could moved. The T7 beamline delivered particles with momentum in the range of 0.2-3.6 GeV, while T11 delivered particles with momentum as high as 10 GeV. Both of these beamlines used aluminum and tungsten enriched targets.

An advantage of the beamlines is that information about the particles ID could be learned from additional instrumentation in beamline. An Cerenkov system and TOF (time of flight) system were used to ID the particles. The configurations of these particle ID instrumentation changed depending on the run (see [89] for details).

However, electrons, pions, muons and protons could be ID (details of this depend of momentum and particle type). Some runs were taken with the detector at an angle with the beam, this is important as the particles in a neutrino interaction will not go perpendicular the plane.

The analysis of CalDet runs did provide much useful information to the MINOS experiment. Knowing the particle ID allows for careful comparison between the MC and data for both the event topology and energy response. Discrepancies were between data and MC found and studied. Some MC packages found to agree better than other (see[88] for details) The energy resolution for hadronic particles and electrons were found. The energy resolution for $\pi^{\pm}$ is given to be[88]: $\frac{56.1\pm0.3}{\sqrt{E}} \oplus (2.1 \pm 1.5)\%$, where E is the energy in GeV and the errors are added in quadrature. Likewise the electron energy resolution is[89]: $\frac{21.42\pm0.06\%}{\sqrt{P}} \oplus \frac{4.1\pm0.2\%}{P}$ where P is momentum is GeV (for these energies P and E are nearly interchangeable).

3.7 Experimental goal

The main experimental goal of the MINOS experiment is make a precise measurement of the oscillation spectrum of ν_μ neutrinos. In particular a precise measurement of the oscillation parameters for $\nu_\mu \rightarrow \nu_\mu$. However, MINOS is not a single measurement experiment. In addition to the $\nu_\mu \rightarrow \nu_\mu$ measurement MINOS will also make a competitive measurement on $\nu_\mu \rightarrow \nu_e$ which probes $sin^2(2\theta_{13})$. θ_{13} is the only mixing angle that has not been measured (only a limit exists[56]). Non-standard neutrino physics can also be probed in the MINOS experiment. What is meant by non-standard neutrino physics in this context is physical process that would to lead to a different oscillation spectrum from the one predicted by neutrino oscillation alone. A study of MINOS physics potential was carried out by the collaboration[55], and some of the results are shown in this section.

3.7.1 $\nu_\mu \rightarrow \nu_\mu$

The high precision measurement of $\nu_\mu \rightarrow \nu_\mu$ is something MINOS can do well. From the atmospheric neutrino experiments the evidence strongly favors $\nu_\mu \rightarrow \nu_\tau$ versus $\nu_\mu \rightarrow \nu_e$ or oscillation to a sterile neutrino. This means that the $\nu_\mu \rightarrow \nu_\mu$ measurement is a disappearance experiment in that less neutrinos will be observed in Soudan than would be extrapolated from the number observed in the near detector. However, this disappearance should be energy dependent. Figure 3.5 show some of the MINOS physics potential.

3.7.2 $\nu_\mu \rightarrow \nu_e$

The search for $\nu_\mu \rightarrow \nu_e$ is significant because of its relevance to $sin^2(2\theta_{13})$. Since, there is only one unmeasured angle (θ_{13}) in the PMNS matrix, any measurement would be important. This measurement is more difficult than the $\nu_\mu \rightarrow \nu_\mu$, because electrons and NC showers look more alike than electrons and muon tracks. An example of what could be done with 25×10^{20} protons on target is shown in figure 3.6.

3.7.3 Non-standard neutrino physics

MINOS has the ability to probe some non-standard neutrino physics. Non-standard neutrino physics in this context means any other physical process that could cause distortions to the $\frac{L}{E}$ not explainable by standard (PMNS) neutrino oscillations. The challenge of this is that many models have been suggested and since they are all non-standard physics, it is not clear which model to give priority to test. Instead of going through each possible model, an example of a possible model will be given. The model is radiative neutrino decay[57]. This process happens when a neutrino decays like: $\nu_h = \nu_l + \gamma$, where by energy conservation $m_{\nu_h} > m_{\nu_l}$ as ν_h is the heavier of the two neutrinos. There are many details to get right if a precise estimate is to be made (see [57][20]), but if only SM interactions are assumed (and the mass of all the neutrinos

are $\leq 1eV$) then the estimated decay time is much larger than the age of the universe ($10^{21}+$ years!). The point is if this would be seen, it would suggest non-SM physics. An example of what (non-SM) neutrino decay would look like is given on the MINOS sensitivity plot.

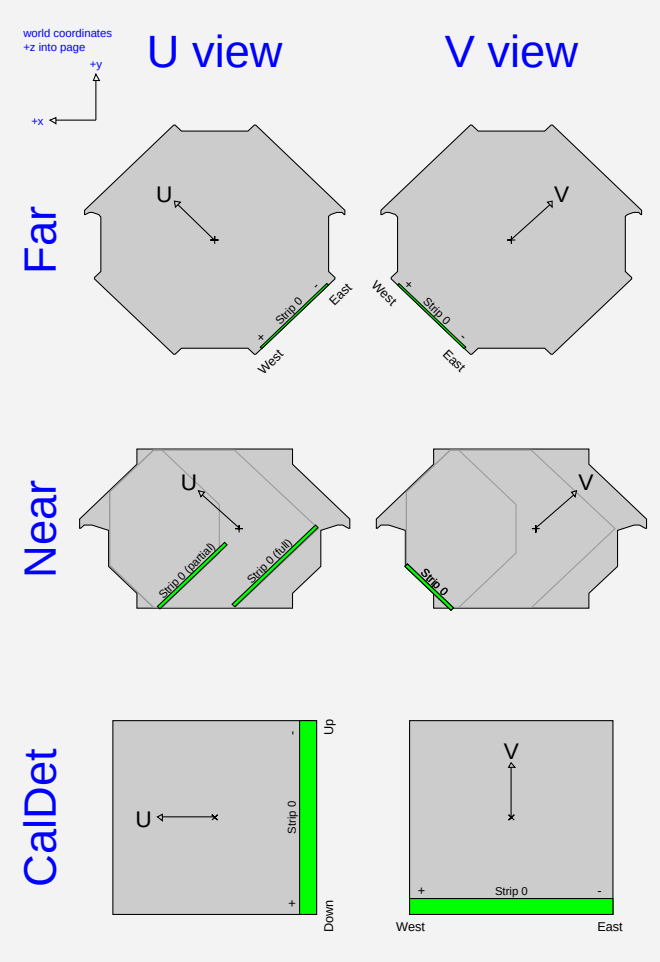

Figure 3.2: This image shows the three different MINOS detectors as they look face on. This shows the shape of each detector and it shows the two orthogonal views of each detector (with what a single strip would look like on the steel plane). The three detectors are not drawn to scale, the far detector is 8 meters across while the near detector is only 1 meter across.

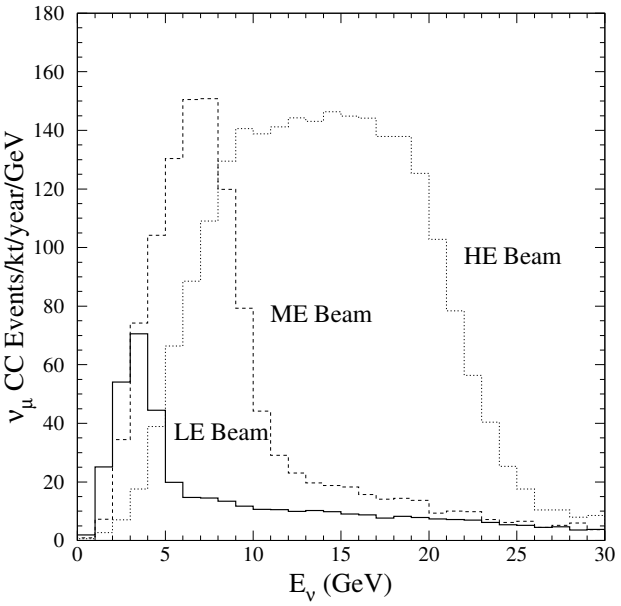

Figure 3.3: This shows the flux of ν_μ CC interaction as seen at the far detector without any neutrino oscillation for the LE,ME and HE beam configurations.[55].

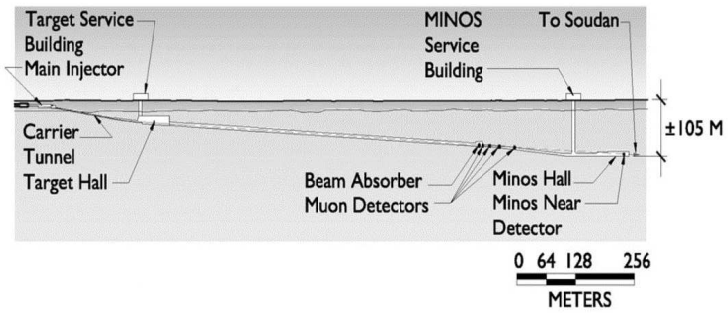

Figure 3.4: This shows the NuMI beamline as seen from the side. The target and near detector hall are clearly visible in the picture as is the buildings above each of them that service the target and near detector.

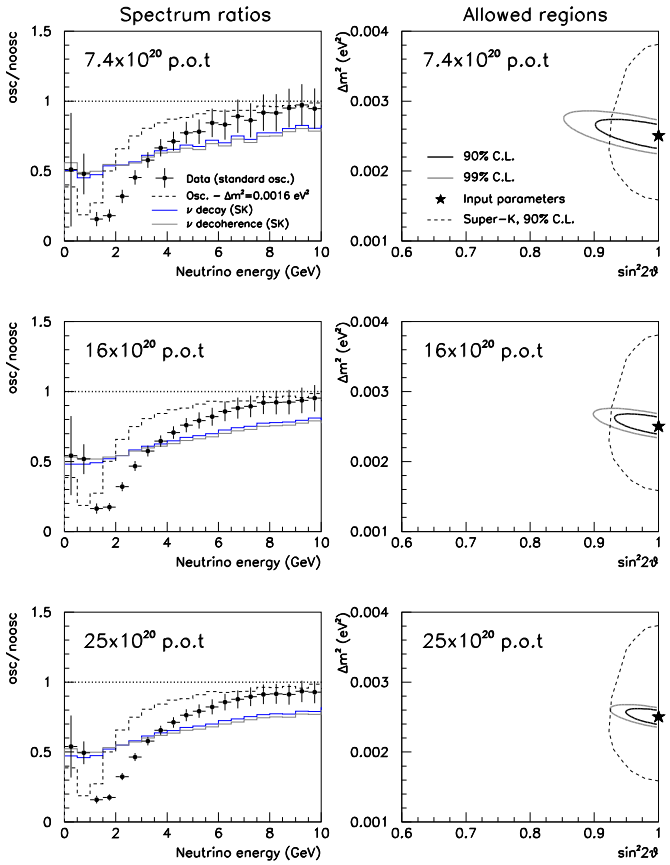

Figure 3.5: This is MC simulation of the sensitivity of the MINOS experiment for $\nu_\mu \rightarrow \nu_\mu$. Each plot on the left shows the spectrum ratio of oscillated to non-oscillated neutrinos observed in the far detector for a variety of oscillation scenarios. Each plot on the right shows the region of $(\Delta m^2, sin^2(2\theta))$ parameter space excluded at 90 and 99 percent confidence levels (C.L). The input value for oscillations in all cases is $(\Delta m^2 = 0.0025 eV^2, sin^2(2\theta) = 1.0)$ which is represented by the star. These are compared with results from Super-K atmospheric neutrino oscillation results at 90 C.L. The top plot is for 7.4×10^{20} protons on target. The middle and bottom plots shows the experiment sensitivity with more total beam.

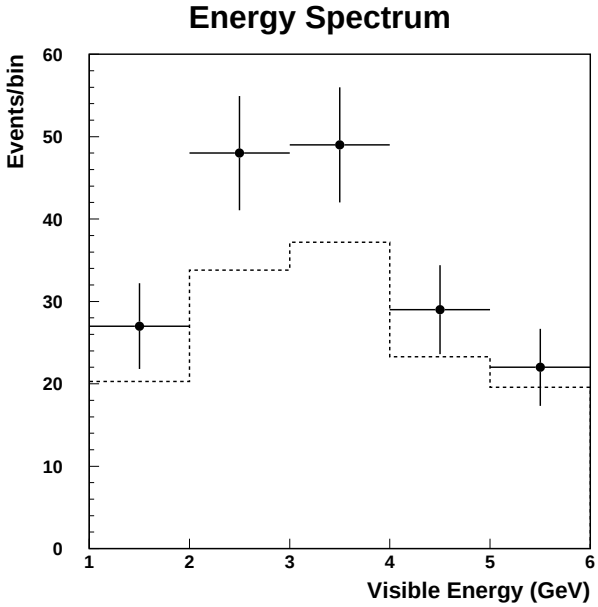

Figure 3.6: This is MC simulation of the signal for $\nu_\mu \rightarrow \nu_e$ in the MINOS experiment. In particular it shows the energy spectrum of the ν_e candidates with the data points and error bars for a signal compared to the no oscillation signal (only background in dashed histogram). The input value for oscillation parameters are $(\Delta m^2 = 0.0025eV^2, sin^2(2\theta_1 3) = 0.067)$. The plot is for 25×10^{20} protons on target.

Chapter 4

The MINOS Far Detector

4.1 Introduction

The far detector serves both it main purpose as the second detector in the long baseline experiment and as an atmospheric neutrino detector. It is this latter purpose that is relevent for this thesis. Even though the MINOS far detector can carry out these two different types of physics, it was designed only for the long baseline experiment. This means that the detector was optimized for neutrinos coming from FNAL, not all directions.

4.2 Far Detector- An Overview

The far detector consists of two nearly identical super modules (SM). SM1 has 248 planes of scintillator. Plane 0 is only steel. Planes 1-248 each has planes of steel and scintillator. SM2 starts at plane 249 (steel only). Planes 250-485 have both steel and scintillator for a total of 236 planes of scintillator. Each scintillator plane consist of 8 scintillator modules with a total of 192 strips. Every strip is read out on both ends. This gives a total of $484 \times 192 \times 2 = 185{,}856$ channels.

It should be noted that the energy deposited by particles interacting in the FD is eventually converted to charge (current). This charge is the fundamental quantity that is measured in the MINOS detectors. In particular, the location of the charge deposition, the time of the charge deposition and the quantity of charge deposition are measured. Every other reconstruction and tracking result is based on measurement of these three quantities.

Another significant comment is that because the entire detector is built underground everything must be brought down from the surface through the shaft. This limits the size of objects that can brought down and means that larger objects (like the steel planes) must be brought down in small pieces and assembled in the lab. This limits objects to a length of slightly longer than 8m and about 2m wide. This limitation sets many of the parameters of the far detector.

Many references exist om the MINOS far detector. For an overview the technical design report[81] and detector design parameter book[82] are good starts but some of the details have changed. A still to be published NIM[98] article will be used when needed. Many NuMI-Notes and some published paper have been written on specific subsystems and these will be used when possible. An diagram of the MINOS FD is shown in figure 4.1.

4.3 Far detector site

The MINOS far detector is located at the Soudan Underground State park (on level 27) in Soudan Minnesota. It is located at 47.820 degrees North and 92.242 degrees West and the physical detector depth is 710 m[99]. The detector is in a hall located next to the Soudan 2 hall[1].

[1]Soudan 2 has been physically removed from the hall.

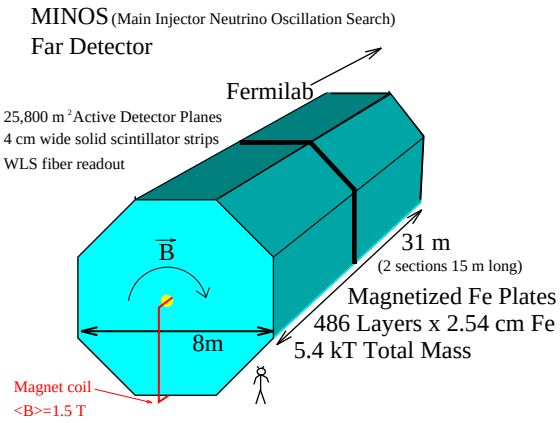

Figure 4.1: This is a diagram of the far detector. Note the two the super modules and the magnetic field return coil sticking out the front of the super module.

4.4 Steel and Magnetics

The far detector consists almost entirely by mass of steel sheets. These sheets serve multiple purposes for the far detector. The steel sheets serve a structural purpose as the scintillator modules are hung from the steel. Given the large fraction of total mass the steel has in the far detector, the steel is the target for the neutrinos. Finally, most of magnetic field generated by the coil is contained to the steel. A detailed discussion of the steel is given in the TDR[81].

4.4.1 Steel planes

The final iron (steel) planes of the MINOS far detector give the MINOS FD its octagon shape. Each of the these planes is 1 inch thick and consists of eight separate sections[2] that were brought down from the surface and welded together in the mine. The steel properties[81] were chosen to be consistent with AISI 1006 low-carbon steel. The carbon

[2]Each section is 1/2 inch thick

content of this steel is between $0.04\% - 0.06\%$ (by weight)[3]. The properties of this steel were chosen to give a high magnetic permability while also giving a high tensile strength.[4] A possible concern for the steel is radioactive contamination as this would increase the singles rate. Thus a specification of no more than 0.15 γ/kg/sec above 0.5 MeV was required. The physical dimensions of the steel also must be kept to tight specifications. For one of the 1/2 inch thick plates the thickness specification was $12.7^{+0.8}_{-0.254}$mm and the width specification was 2000 ± 0.76mm. For any particular steel plane, the eight plates were brought down from the surface placed on a rig known as a strong back and plug welded together with 76 individual welds. Then after the scintillator was placed on the plane the whole plane was lifted and installed. The steel plate rests on the so called ears and is bolted to the previous plates. The distribution of steel mass and the variation of steel mass in the far detector has been studied and is documented[132].

4.4.2 Magnetic coil and cooling tube

The magnetic coil is used to generate the magnetic field by simply running a large current through many cables in the center of the far detector. Because of joule losses in the cables a water based cooling system must be used to keep the system from over heating. This cooling tube consists of two (one for each SM) cooper tubes with pipes running through them, the current carrying cables are ran through the same tube. The current running through the cables is 80 amps and there are 190 turns in the coil. The current can (and has) been reversed, which can change the direction of the magnetic field. The forward field is designed to focus negative particles (μ^- produced from ν_μ) from FNAL.

---

[3]The AISI 1006 standard allows for up to 0.08% percent carbon.

[4]The ultimate tensile strength is specified to be a minimum of 40,000 psi.

4.4.3 Magnetic field

The magnetic field model that is used is based on a FEA simulation. The magnetic field that is used for data and MC are actually not exactly the same. This seems like it could be a problem but is not. The reason that this is acceptable are three fold. First, the same magnetic field used to generate the MC is used to reconstruct the MC. Second, the difference between the two maps is small as will be shown the biggest difference is not in the fiducial volume. Thirdly, the magnetic field maps are basically ideal maps and do not have all the known imperfections of the detector. Figures[100] 4.2,4.3, and 4.4 show the magnetic field for map 201 which is used for MC, map 202 which is used for data and the difference between the two maps. As can be seen from the map the magnetic field near the coil is nearly two Tesla but drops down to 1.5 Tesla a meter away. The magnetic field is more complicated near the start and end of the detector (edge effects) and it clearly grow weaker at large radii from the detector. The physics impact of this is lessened because the fiducial volume is away from the ends and in the more inner part of the detector.

4.5 Scintillator and Module design

Solid plastic scintillator is the active detector element in the MINOS far detector. Each scintillator plane is attached to a steel plane and has 8 scintillator modules. Each scintillator module has either 20 or 28 scintillator strips. The inner four modules ('CalTech Modules') have 20 strips, while the outer 4 modules ('Minnesota modules') have 28 strips. Figure 4.5 shows a diagram of a scintillator plane.

4.5.1 Scintillator strips

Each scintillator strip is 4.1 cm wide and 1 cm thick. The length of the strips are variable although some are as much as 8m in length. The scintillator is an extruded

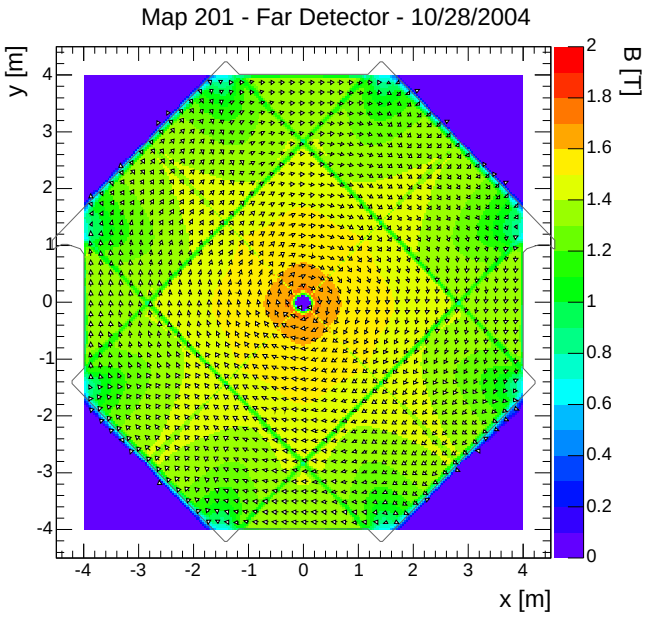

Figure 4.2: This shows the magnetic field map 201 used in the MC. The model has a simple model of the gaps in the steel. The MC is generated and reconstructed with the same map

polystyrene scintillator that consists of Dow 663w clear polystyrene with traces of PPO (3% by weight) and POPOP (0.01% by weight). A coextruded outer layer with TiO_2 is used to reflect light back into the strip. An extruded central groove is used to insert the WLS fiber (there is no outer layer in the groove)[98] and is glued in place.

4.5.2 Scintillator modules

The purpose of the scintillator modules[98][81] is to hold the scintillator strips. This is done using an thin aluminum skin. It is important the scintillator strips do not move in the modules. As mentioned before there are 20 strip and 28 strip wide modules but actually this is simplified picture of reality. The difference between the different types of 28 wide modules is cosmetic. The outer module (refer to figure 4.5) is simply smaller the next module in. The difference between the 20 wide modules is more substantial as

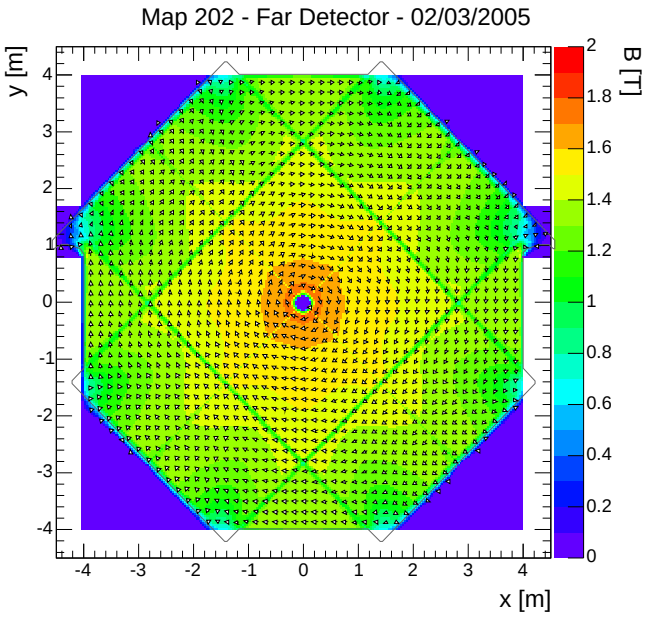

Figure 4.3: This shows the magnetic field map 202 used for the data.

the inner module must have a bypass added as the coil goes through the middle of the detector compared with the next module out. At both ends of all modules there is a manifold and a light injection manifold (LIM) which is simply at the top of the manifold and allows light injections calibration. The purpose of the manifold is to direct the light out of the module to the clear fiber cables through an optical connector. Each module is connected between the manifold and the optical connector by a set of pins and in many cases black plastic and tape to guarantee no light leakage. During all stages of installation and commissioning of the modules light leaks were searched and fixed with electric tape and black plastic sheets. This is important as once the plane goes up it impossible to fix the leak. All modules were mapped to determined the attenuation of the scintillator and this is discussed later in the chapter.

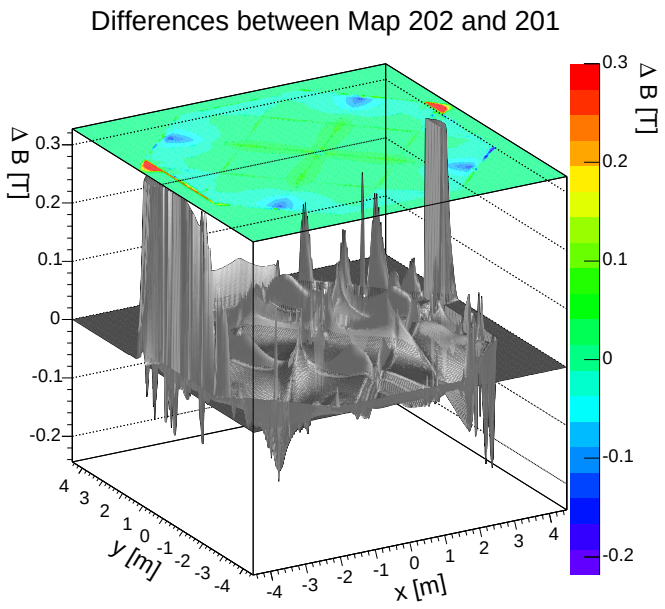

Figure 4.4: This shows the difference between the magnetic field map 202 and 201. The biggest difference is in the ears and not in the fiducial region

4.6 Phototubes and Optical system

The light in the scintillator must be transported from the scintillator to the wavelength shifting fiber to clear fiber so it can be readout by the PMT. MINOS uses optical summing (Multiplexing) to reduce the number of PMT's that must be purchased. Eight clear fibers are read into a single PMT pixel. The PMT then converts the light into a electrical signal. An diagram (or maybe more correctly a cartoon) that shows the interface of the of the scintillator and optical system is shown in figure 4.6.

4.6.1 Wavelength shifting fibers (WLS)

The wavelength shifting fibers[98][81] are responsible for taking light made in the scintillator and transporting it to the clear fiber so it can go to the M16 PMT. The fibers are 1.2 mm diameter double clad polystyrene fibers. The fibers have 170 ppm of Y11

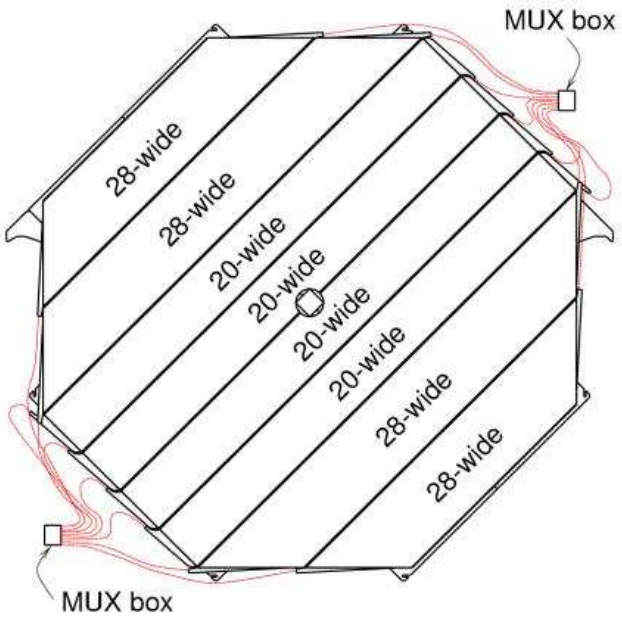

Figure 4.5: This image shows the structure of a scintillator plane. Notice the plane consists of both 20 and 28 strip wide modules.

(K27) fluor produced by Kuraray[98]. The fibers work by absorbing photons from the scintillators and readmitting the photons at a lower energy. In particular blue light enters (420 nm) and the admission is centered around green light (470 nm). A fraction[5] of these photons become trapped (total internal reflection) and propagate to the end of WLS where they are transfered to the clear fiber. An important concern which had to be addresses when designing this system is make sure that the attenuation is not so strong that the light cannot make 8 meters so that the energy deposit is observed on both ends, to this goal, the specification of 5+ m attenuation length was made.

[5]The fraction depends on where the photon is produced but the fraction is low $\approx 5\%$

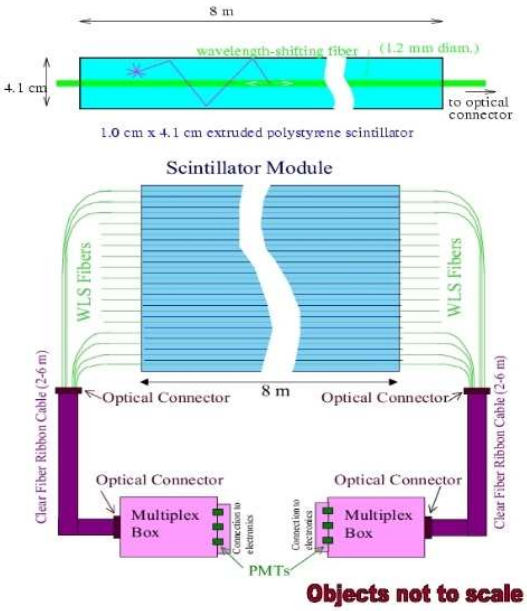

Figure 4.6: This shows how the optical system interfaces with the scintillator.

4.6.2 Clear fibers and Multiplexing

The clear fibers[81] are anywhere between 2 and 6 meters long and have the purpose to transport the light from the WLS to the PMT. In order to reduce the electronics cost, multiplexing[6] is used. This is done by having 8 clear fibers come to one PMT pixel. Since there are 192 strips in a plane this means that only 24 PMT pixels will be used to read the plane out[7], the downside of this is that it is more difficult to determine where the event actually reconstructed[8]. Each strip is read out with another strip 24 strips down. This means that providing no physics event is more than 1 m in the transverse direction the multiplexing should work. Furthermore, by properly picking a

[6]This is maybe more properly called optical summing.

[7]A single side of a plane

[8]This means there are 8 possible solutions for every given plane. The process of determining which solution is real is called demultiplexing or demuxing for short and discussed later in this chapter.

clever pattern for each side of the double ended readout, the process of reconstructing the proper signal can be made less difficult. It should be noted that cross-talk and random noise makes the determination of the physical solution (demultiplexing) more challenging. The place the clear fiber comes together is known as a mux box[81][98]. Each mux box has 3 M16 PMT. Since each PMT reads outs 128 fiber (8×16=128), one mux box reads out 384 fibers which is equivalent to 2 planes. The mux boxes are located on the first and third level of the MINOS detector super-structure. The 128 fibers are mounted into a cookie which is then aligned with high precision (25μm) with the PMT. The PMT are located close to the detector but the magnetic field is actually weak outside the detector in the air and is partially shielded by the mux box.

4.6.3 M16 PMT

The MINOS far detector uses M16[98][81][117] PMT made by Hamamatsu. The M16 is a 12 stage, 16 pixel PMT. The M16 uses a bialkali as the photocathode and has a 1 mm thick borosilicate glass window. The quantum efficiency is 13% at 420 nm although the spectral response goes from 300 to 650 nm with a maximum quantum efficiency at 520 nm. Each pixel is 4 by 4 mm square. The maximum HV that the PMT can be ran at is 1000 volts although 800 volts is more normal. The average gain of the tubes is 10^6. For a large signal (10+ PE) the timing is sub 2 ns. For smaller signals the timing is dominated by the decay spectrum in the fluor in the WLS. The tube should be linear up to 20 PE and below a 3 kHz dark count rate at 1/3 PE threshold.

Performance

The performance[118][119][120][121] of the M16 is well documented. This was tested at test stands located at Texas and in Greece. The test stand results include comparisons over short periods of time to time frames as large as two year. The results show for the most part the M16 behaves in understood ways. For example, the M16 does undergo a

slow (but understood) variation in gain.

Cross Talk

Cross talk in the M16 PMT is well studied and well documented in the MINOS FD (See Jenner and included references[92]). There are two types of cross talk that occur in the M16 PMT, optical and electrical. Optical cross talk occurs when a photon jumps pixels, the amount of ph in this cross talk is higher energy (1+ pe) but is more rare than electrical cross talk which occurs when charge on one pixel is read out on another pixel. The cross talk is observed as hits in pixels adjacent to pixels with activity. The effect of this cross talk on the reconstructed is somewhat minimized as the detector does not readout adjacent strips from adjacent pixels. The vast majority of cross talk is in the (up to) 8 adjacent pixels, which only a tiny amount of cross talk from more distant pixels ($\approx 0.01\%$). The cross talk has been studied at both the lab (PMT test stands) and in CALDET. Software can be used to remove most of the effect of cross talk.

4.7 Electronics and DAQ

The purpose of the electronics[98][122] and DAQ is to take the electrical signal from the PMT and turn it into a machine readable file. This is an important process with many steps. One advantage of the detector and the electronics is that because the detector is the homogeneous in nature the electronics are also homogeneous in nature and there are only a few unique elements. For a detailed look at the electronics see Felt et al.[122]. A diagram of the electronics/DAQ is shown in figure 4.7

4.7.1 VA and VFB

Each M16 is readout to a 32 channel ASIC VA32 HDR11[9], simply known as VA chip[122]. This chip is a CMOS device made on a 0.8μm process and contains both analog and digital circuits. Each channel on the VA chip has a charge sensitive preamp, a shaper, a track and hold stage and an analog output multiplexer. As much as 30 pC of charge can read in a reasonably linear manner from the M16. The VFB (VA front-end board) is the place the VA chips reside. It has support and power circuitry for the VA chips and has another ASIC which compares the 3 VA chips dynode signal against a threshold for time stamping and readout. The VFB is does not operate independently as is controlled by the VARC.

4.7.2 VMM and VARC

The VMM[122] (VA Mezzanine Module) have a 14-bit 10 MHz ADC where the analog multiplexed signal from the VA is digitized. Although the ADC can run at 10 MHz it normally runs at a lower rate. Each VMM has signal from two VFB. Six VMM are placed on a VARC[122][98] (VA readout controller). Three VARC, a timing card and a VME processor share a VME crate. The total detector has 16 VME crates for the 22,000 channels of electronics. The VARC starts the readout process when a dynode trigger from a VFB. The VARC then timestamps the signal and starts the readout process. The timestamps are based on an 640 MHz TDC signal that is cleverly generated from a 80MHz FPGA. This gives MINOS a fundamental time unit of 1.5625 ns. The VARC coordinates the readout (the VA chip could already be busy). There is a 5 μs dead time during the readout period. After the VARC order the readout the signal is digitized in the VMM. The digitized data has pedestal subtraction and is placed in VME memory and is then the responsibility of the DAQ.

[9]This was a modified version of a different chip made by IDE Corp. of Norway

4.7.3 DAQ

The MINOS DAQ system is well documented and for a detailed explanation the interested reader can see other MINOS theses[1][135]. The DAQ system is modular. Every VME has a read out processor (ROP). The ROP takes the data and places it in a 1 second long timeframe. The timeframes are fed to the Branch Readout Processor which in turn feeds the data to the trigger processor. The trigger processors are a local farm of PC that uses the timestamp information to order the data into hits which must have at least 100 clock ticks (156 ns) of no activity between them. If one of these sections of data with a 100 or more clock ticks of separation passes one of the adjustable triggers (normally 4 out 5 planes hit) then the event is readout and is known as a snarl. The readout is done with the Data Collection process. Besides the snarl the previous 30 μs of data is also readout to look for detector deadtime, this is known as the pre-trigger window. After the data is readout it is sent to FNAL and stored on tape. This raw data is where the data analysis begins.

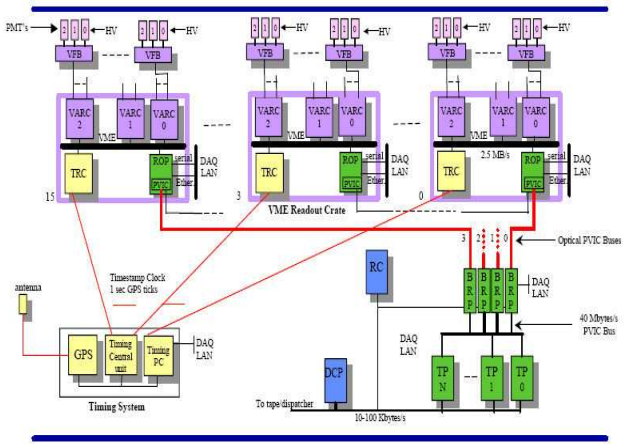

Figure 4.7: This shows an overview of the electronics/DAQ sysetm in the MINOS FD.

4.8 Veto Shield

The veto shield is not required for the long baseline neutrino oscillation (main) part of the MINOS experiment. However, to carry out an atmospheric neutrino experiment using fully or partially contained neutrinos the veto shield must be used. Because the veto shield is not required to carry out the long baseline experiment the detector was not designed with a vetoshield. The vetoshield was began in 2002 and consists of scintillator (20 strip wide non-bypass) modules overlayed on each other. The vetoshield has coverage on the top of the detector and partial coverage on the side of the detector[10]. The vetoshield uses a different type of optical summing compared with scintillator in the main detector in that 8 adjacent strips are optically summed and readout to one pixel of a M16[11]. However, the scintillator does retain the good timing resolution and this nano-second timing resolution is useful in telling the difference between signal and noise. Given the length of the modules is about half that of a SM, the modules are layed across the detector with the modules long axis pointed in the beam direction. The shield is broken up into four sections. Each section has three different regions, a top region which is over the center of the detector, a wing region that covers the area on the left and right of the top region and a wall region[12]. The top region and (almost all) the wing region is double layered and the wall regions are single layered. The shield is designed so that no downgoing particle should be able to enter the detector without going through at least one scintillator module[13]. The setting of the gain on the PMT

[10]The detector is not going to be confused with a 4π steradian shield. On the other hand there is no reason for the shield to offer full coverage either as by far the dominant background is coming from above.

[11]Eight such strips are known as a plank. A complication that can arise is that because 20 modulo 8 is not zero, you are left with the quandary of either not using the PMT pixels efficiently or having some planks split between different scintillator modules. The latter solution was chosen when possible.

[12]The wall region has a upper wall and lower wall.

[13]This is based on geometry. Simply because a particle goes through the shield does not mean it will be vetoed. For example, the particle could enter the shield and still miss the scintillator by going between the scintillator strips. More likely still is an particle enters and does not deposit that much

is not a trivial exercise as it is important to have a high efficiency in tagging events and a low false rejection rate (random noise that mimics a particle going through the shield). An compromise must be reached, to balance both requirements in order to have the best possible result for atmospheric neutrinos. The performance of the shield is discussed in chapter 6 and 9 although both high efficiency and low false rejection can be accomplished. Figure 4.8 and figure 4.9 shows the vetoshields physical appearance and are provided by Sue Kasahara.

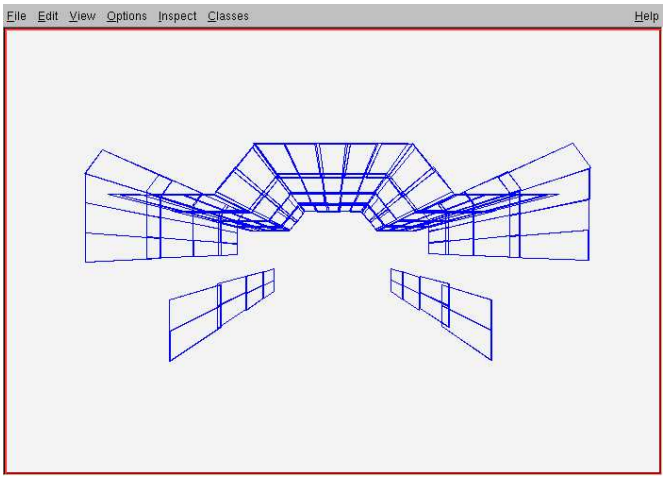

Figure 4.8: This shows how the vetoshield looks without the detector. The most center region is the top region, the regions to the left and right are the wing regions and the distached region on the far left and far right are the wall regions. The top and wing regions have double layers of scintillator and the walls have single layer of scintillator. Image provided by S. Kasahara.

4.9 Calibration and Alignment

There are three things that can be directly measured from the MINOS FD, energy, time and position. All other reconstruction is based on the knowledge of these three

energy because (for example) it clips only a corner of a scintillator strip and is consistent with random noise and thus not vetoed

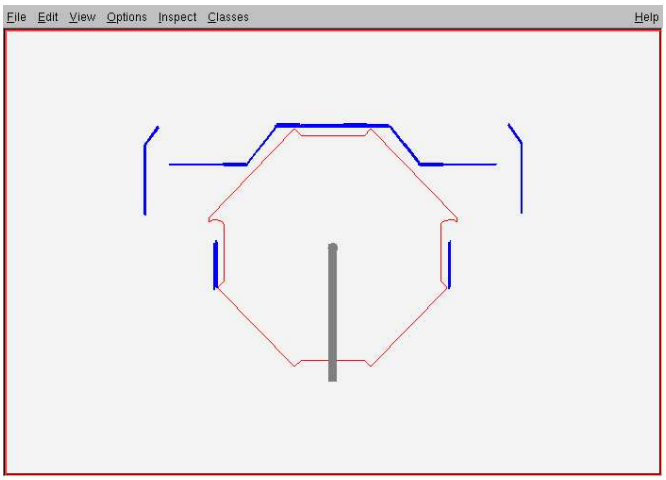

Figure 4.9: This shows how the vetoshield looks with the detector. The most center region is the top region, the regions to the left and right are the wing regions and the distached region on the far left and far right are the wall regions. The top and wing regions have double layers of scintillator and the walls have single layer of scintillator. Image provided by S. Kasahara. The objects in this image are drawn to scale, so a estimate of the total size of the shield can be gained.

quantities. For every hit (called a Digit), the energy, time and position can be estimated. Thus in order to properly understand reconstruction, these three quantities must all be understood. This is done by spatial alignment, energy calibration and timing calibration.

4.9.1 Alignment and Survey

Alignment and survey is the process of determing the spatial location of detector elements. These elements include both structural elements (collar hole for example) and the location of the scintillator. In the end it is the location of the scintillator which is of greatest importance as the scintillator position is important in order to properly reconstruct tracks and showers.

Structural survey

During construction the far detector was surveyed. This survey is based on a coordinate system that defines the origin to be at the center of plane 0. The coordinate system has z running along the detector and x running approximately west-east and y running up and down. From this high precision survey, survey markers (Dijak bolts) were places around the hall and the relative positions were measured with sub-mm precision[123]. A later survey [124] made after the detector was partly constructed shows that rails that supports the detector sags up to 5 mm under load. Besides these two high precision surveys using professional surveyors, the mine crew building the detector made measurements using the Vulcan system from ArcSecond (ArcSecond is a registered trademark of ArcSecond Inc.). These measurements were used both to make modifications (shimming planes) during construction to ensure the detector was as uniform as possible and for post-construction analysis. This post construction analysis [127][128] consisted of looking at both the data for the steel and scintillator. The steel data was used to measure the average pitch of the detector ≈59.49 mm/plane for SMl and ≈59.46 mm/plane for SM2. Another use was to estimate the distance of the gap between super modules (≈110.6 cm). In addition to these measurements, other studies of detector drift were carried out. These values were in general in excellent agreement (mm level) with independent estimates. The scintillator data set was used to get an estimate of the scintillator planes average rotation. The results of this study for SMl[130] are average rotations less than 1 mrad.

Muon alignment

Cosmic ray muons allow for the alignment of far detector[101][102][103] scintillator modules. The alignment done of the far detector is a module by module alignment using long straight muons. A strip by strip alignment is not practical as the statistics at the far detector (unlike the near detector) are too low to make this possible over a reasonable

time frame. However, this can be partially corrected by the module mapper data. Although the module mapper was not designed to measure the scintillator position with great detail, this information can be extracted and strips can be known to better than a mm. The alignment was designed to align modules to a 3 mm specification. In reality, it was found that alignment could be done to be about 800 μm. This was found to improve the tracking quality of the tracks.

4.9.2 Energy Calibration

Energy calibration[98] is process that relates the observed electrical current in the electronics back to the physical process that produced it. The energy calibration for MINOS requires a 5% absolute calibration and 2% near to far detector calibration. The calibrated energy unit for MINOS is known as MEU[14] (muon equivalent unit). The calibration is done in several separate corrections. These are the drift, linearity, strip-strip, attenuation and stopping muon calibrations. The ultimate point is that the stopping muons[15] should be the same in all three detectors and allow for the calibration.

Module Mapping

Module mapping[98] was an important calibration carried out during the construction and installation phase. The module mapping was done in order to understand the response of every strip at different transverse positions along the strips. The mapper used a 5 mCi cesium collimated source. The calibration was reproducible to $\approx$ 1%. From this mapping the attenuation factor of every strip is known. This allows for the flagging of damaged or dead strips[16]. About 1000 modules ($\approx$ 25%) were also

[14]For certain purposes the difference between an MEU and a more common unit like adc is small. This is especially true if the measurement is a ratio of adc counts.

[15]Since stopping muons all range out by definition.

[16]No strip was completely dead

mapped at Soudan. These remapped modules allowed to check if the shipping and handeling had damaged the modules and would also show any variation with time in the modules[17]. Only a fraction of modules showed variation and even these were within the specifications. Figure 4.10 shows the uniformity of the output from modules as measured by the module mapper.

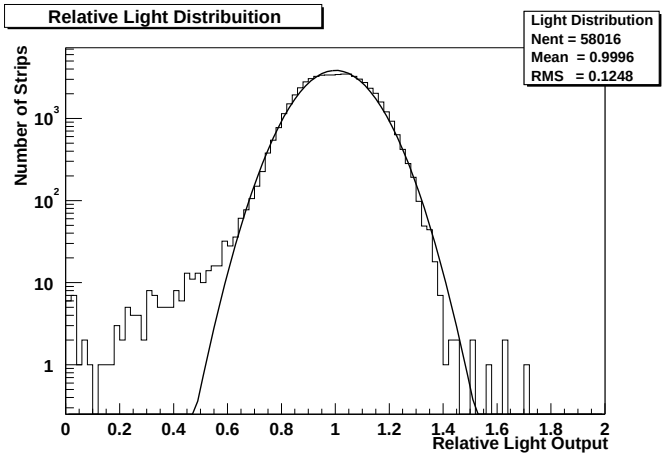

Figure 4.10: This shows the light output from the module mapping. Notice the 12% RMS.[98]

Light and charge Injection

The light injection (LI) calibration[93][94][95][96][97] system is mainly used to measure the gain response of the detector and time dependent (drift) changes to the gain. This is important as the PMT become non-linear at large ph and the channel can drift with variations of temperature and voltage. The light injection system is based on pulsed blue LED that are mounted in boxes 'pulser boxes', these pulser boxes have optical cables that feed the signal into the scintillator modules. Each scintillator module has the optical cable enter at the LIM 'light injection modules'. After entering the LIM

[17]The difference in time it took for a module to mapped and then remapped depended on many details but could be on the order of a year

the pulsed light illuminates the scintillator. A PIN diode is readout during the light injection so the amount of light is measured. Variations in gain on size of 1% can measured using the LI system. For more details the interested reader should look at the references, in particular[93] which provides a good overview. The charge injection[122] is used to look at VA chip gain for a particular channel. It is used to understand non-linearities in the VA chips.

4.9.3 Time Calibration

The timing[98] in the far detector is important as it can be used to separate down and up going events. The timing calibration is determined by looking at muons and comparing the timing difference from the two sides of the detector. By iterating this process over many muons it is possible to calibrate the detector so that the single hit timing RMS uncertainty is 2.6 ns. For much more detail on the timing calibration see Blake[135].

4.10 Data Taking

The data taking process consists of several types of runs with different purposes. The physics runs are runs for the taking of physics data for analysis. There are several types of special runs that can be done including diagnostic and light injection runs. The beam runs are runs for when the neutrino beam is on. It should be noted that the run types evolved over the first couple years of detector operations as more was learned about the detector.

4.10.1 Physics runs

The physics runs are the run type where physics data is taken. By total run time this is most common type run by far. A physics run lasts eight hours[18] A run consists of a set of sub-runs[19] normally 1 hour long. Starting with run 19,847 the LI was interspersed with the data. It should be stated that in an 8 hour run it is easy to get over 100,000 triggers and have only about 10,000 events. This is because the trigger is a loose trigger. The most common trigger is the 4/5 trigger which requires 4 out of 5 planes to have at least 1/3 PE. There is also a weaker energy trigger called E4 designed to find beam NC events and ν_e events and both of these triggers can be used with an or[20].

4.10.2 Special runs

There are many type of special runs. Some special runs are used as a diagnostic for a bad component. Other special runs can be used to test out new software or triggers designs. These special runs are not used for the physics analysis and are normally short runs of less than an hour. Light Injection used to be done in special runs but is not anymore and as in the case with physics runs these special runs have changed over time.

4.10.3 Beam runs

The beam runs are physics runs when the neutrino beam from FNAL is up and running. This data can be selected by the global timing using the GPS system. This data is then separated from the rest of the data and used for analysis. Even if the mechanism for determining when the beam fails, an beam event can be extracted in post processing

[18] This is true provided something does not go terribly wrong. In the case the run crashes, the problem is fixed and a new run starts.

[19] This evolved much over the course of a couple years. The only thing it really changes is the file sizes.

[20] Effectively every event which will pass 4/5 will pass E4 as well

as the time the near detector saw the spill and the far detector trigger time both have GPS timestamps.

4.11 Software-overview

The use of software[98] in MINOS is diverse and the details of it go well beyond the scope of this thesis. In particular the software used for the beam and near detector are not going to be discussed[21], although much of the near detector software is similar. Generally speaking the software is broken up into online and offline software. Several traits are common to all (or almost all) the software. MINOS software is written in object oriented C++. The CERN based data analysis package ROOT[22] is heavily used in the offline and online software. The most commonly used data files, ntuples are root readable files. The minossoft software always has a development release available which is in state of flux and on occasion releases a frozen release. Only frozen releases are used for analysis work. In particular, the work in this thesis is based on R1.14.1.

4.11.1 Offline software

Offline software is generically software ran offline, that is to say software which is not directly related to the running of the detectors in real or near real time. This is not exclusively reconstruction software, although only reconstruction software will be considered in this section. It should also be mentioned that for all the major reconstruction processes multiple algorithms were developed. Some of these algorithms are similar and other are not. The package as a whole is known as minossoft. It is not possible to fully detail in this thesis the work that went into all the packages. However, the following will give terse explanations of particular types of software that were relevant for the

[21] For example, the process of separating different neutrino events during a near detector spill-known as slicing will not be discussed.

[22] http://root.cern.ch

analysis.

Demuxing

Demuxing[125][126] is the process of undoing the optical summing. This process is done before track finding or fitting and must be done correctly for event reconstruction to work. For tracks this is easy as a single double ended hit strip in a plane can be determined by the pattern on the PMT on the opposite end of the detector. Shower reconstruction is a bit more complex as ambiguities must be resolved. This is done by considering the different possibilities[23] and using a χ^2 method to rank the solution on how likely they are. The demuxer uses up and downstream information when possible and uses unambiguous hits when possible to constrain the event. One type of event the demuxer has trouble with is events that overlap in z. The demuxer does have the ability to throw a flag if it determines the demuxed solution to be unlikely.

Track finding and fitting

The tracking software starts the trackfinding process by applying a hough transform to a list of digits. Then it attempts to determine the track direction off timing with regard to Z. This process is used to make track sections which are used to make track clusters and eventually two and then three dimensional tracks. The track fitting software is based on a Kalman filter. The track fitter determines the fitted momentum (and sign) of a track. The track fitter also can change the track by adding or deleting digits to the track. Only after the track fitting is the final track known. If the track fitter cannot come up with a consistent solution it throws a flag.

[23] There are up to 8 possible solutions.

4.11.2 Online software

The online monitoring has the purpose of monitoring the detectors physical components to make sure they are not broken or have not drifted. This includes the monitoring of the slow controls like temperature and pressure, the current and HV monitors for the detector and the electronics, to the DAQ system itself. This also includes looking at physically motivated measurements like the singles rate. Most of this information is monitored by physicists in real or near real time so serious problems (HV trip) can be corrected quickly and more minor problems (low PMT response) at a scheduled time[24]. This information is stored and can be accessed at a later time if needed.

[24] When the beam is off for example

Chapter 5

Cosmic Ray and Atmospheric Neutrinos

5.1 Introduction

Cosmic Rays and the production of atmospheric neutrinos must be studied if neutrino oscillation experiments using atmospheric neutrinos are to be understood. The properties of atmospheric neutrinos (energy distributions and angular distributions) also must be understood in some detail.

5.2 Cosmic Ray Production

The cosmic ray production physics must be understood for two separate (but related) reasons. The cosmic ray showers are the source of atmospheric neutrinos. These same showers are also the source of the backgrounds for atmospheric neutrino events. Thus a carefull evaluation is needed.

5.2.1 Primary cosmic ray particles

The primary cosmic ray particles are responsible for the creation of the airshowers at the energies of interest that produce the (mostly) $\pi^{\pm}$ and $\mu^{\pm}$ that produce atmospheric neutrinos. These primary particles are produced by astrophysical sources and propagate through space until they interact in the upper atmosphere of the earth. About 79 percent of these are free protons and most of the rest being helium.

The differential intensity is given by[17][91]:

$$I_N \approx 1.8E^{-\alpha}\frac{nucleons}{cm^2 \cdot s \cdot sr \cdot GeV} \tag{5.1}$$

Where α is the differential spectral index and has a value of 2.7 for energies between a few GeV and 1000 TeV.

Although, there is much interest in the topic of primary cosmic rays, this is sufficient commentary for purposes of this thesis. For more information see a reference like Gaisser [91].

5.2.2 Airshower and particle production

After a primary interacts in the upper atmosphere it produces secondary particles. These secondary particles then can interact to create more secondary particles, this process forms an airshower. Figure 5.1 shows an airshower. These airshowers have electromagnetic, hadronic and muonic components. For atmospheric neutrino physics the important point is that through the hadronic (mostly π) and muons decays the atmospheric neutrinos are produced as are $\mu^{\pm}$ which are an important background for studying atmospheric neutrinos. The topic of airshower physics is large and goes well beyond the scope of the thesis. For more information see Gaisser [91].

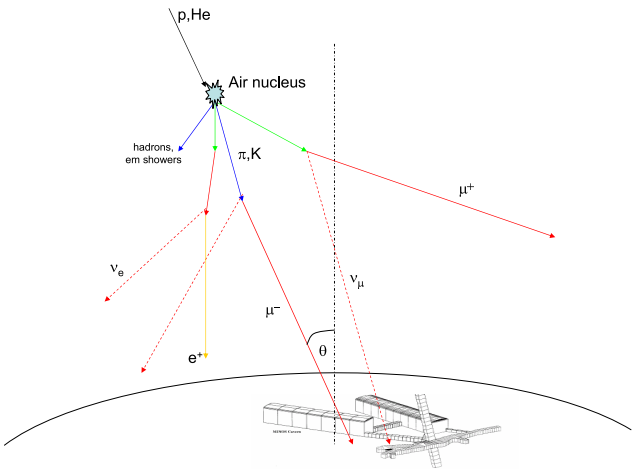

Figure 5.1: This shows the interaction in an airshower. The primary interaction is at the top and the ν and μ are the final products of the reaction. Image provided by E. Beall

5.2.3 Cosmic μ

Cosmic $\mu^{\pm}$ are relevant to study in a deep underground neutrino experiment because if the $\mu^{\pm}$ have a high enough energy they can penetrate many kilometers of rock. If they make it to the detector they are a possible background. The reason $\mu^{\pm}$ can penetrate so far is that they have a relatively long lifetime ($2.19703 \pm 0.00004 \times 10^{-6} s$[17]) and they loose energy relatively slowly. The energy loss at low energy is dominated by (continuous) ionization while at high energy it is dominated by stochastic processes. The topic of muon energy loss is discussed in many sources[91][17]. Using the notation in [17] the energy loss of muon can be represented as:

$$-\frac{dE}{dx} = a(E) + b(E)E \tag{5.2}$$

In this expression a(E) is the ionization energy loss given by Bethe-Bloch formula and b(E) is the energy loss of the stochastic processes (Bremsstrahlung, pair production and photo-nuclear production) and E is the energy in GeV. An important point is that

there is a critical energy where a(E) and b(E)E are equal. For muons in rock the critical energy is $\approx$ 500 GeV [91]. The reason this is significant is that a(E) is approximately constant below the critical energy where it is the main source of energy loss and is equal to about 2 MeV per $g \cdot cm^{-2}$.

The energy spectrum of muons is given at the surface by[91]:

$$\frac{dN_\mu}{dE_\mu} \approx \frac{0.14 E_\mu^{-2.7}}{cm^2 \cdot s \cdot sr \cdot GeV} \times \left\{ \frac{1}{1 + \frac{1.1 E_\mu cos(\theta)}{115 GeV}} + \frac{0.054}{1 + \frac{1.1 E_\mu cos(\theta)}{850 GeV}} \right\} \tag{5.3}$$

5.3 Atmospheric Neutrino Production

The interactions that produce atmospheric neutrinos make several simple predictions that are robust. In particular, this is true for the predicted flavor and particle/anti-particle ratios. The energy and angular spectrums must be also be examined in order to make any sense out of neutrino oscillation measurements.

5.3.1 Two ratios:flavor and particle/anti-particle

The flavor and particle/anti-particle ratios are significant in understanding the atmospheric neutrinos. First, the flavor ratio tells you what flavor the neutrinos have at the time of there production. The ratio of particle/anti-particle is important for CPT physics.

A simple argument

In this section a simple model of the neutrino production in the atmosphere will be presented. Later it will be compared with a more realistic model. In this simple model it will be assumed that all neutrinos come from $\pi^\pm$ and there decay particles. Furthermore, it will be assumed that none of the particles hit the ground before the decays happens. Finally the effects of the earth's magnetic field will be ignored.

$$\pi^{\pm} \rightarrow \nu_{\mu}(\bar{\nu}_{\mu}) + \mu^{+}(\mu^{-}) \tag{5.4}$$

The π decays this way 99.98770$\pm$0.00004[17] percent of the time. While the following decay is also effectively the only decay channel.

$$\mu^{\pm} \rightarrow \bar{\nu}_{\mu}(\nu_{\mu}) + \nu_{e}(\bar{\nu}_{e}) + e^{+}(e^{-}) \tag{5.5}$$

Thus the two ratios can be calculated by simply adding up the neutrinos and the results are:

$$(\nu_e : \nu_{\mu} : \nu_{\tau}) = (1 : 2 : 0) \tag{5.6}$$

for the flavor ratio and

$$(\nu : \bar{\nu}) = (1 : 1) \tag{5.7}$$

for the particle to anti-particle ratio

There are several remarkable things about this model. The flavor ratio is independent of the π^{+}/π^{-} ratio. Secondly, the ratio of ν_{μ} to $\bar{\nu}_{\mu}$ is also independent of the $\pi+/\pi^{-}$ ratio. This model is greatly simplified, however, given that both π and μ have dominant decay modes with nearly all of the decays going through the above modes it should not be unexpected that the results presented above are reasonably accurate.

A more elaborate argument

There are more quantative ways to estimate both the absolute flux and the flavor ratios. Recently, there has been several atmospheric neutrino calculations[105, 106, 108, 107] carried out. Honda suggest that for neutrinos below 10 GeV the systematic uncertainty cannot be larger than about 10% while Battistoni[108] suggests that the FLUKA based hadronic interaction model give an uncertainty of $\approx$ 10% but estimates

a total uncertainty of 17% before the cross-sections are taken into account. A more conservative value of 15% will be chosen for this thesis. However, the flux ratios are somewhat more robust and the flux ratio of has an uncertainty of less than 4%[109] which are much smaller than the cross-section uncertainty.

Production Height

The production height of neutrinos is important to understand for atmospheric neutrino oscillation experiments. The reason for this is that neutrino oscillation depends on the path length of the neutrino. For neutrinos coming from above the detector this is important as it can be as large or larger in general as the distance the neutrino travels through the earth. For neutrino coming from below the horizon the effect is smaller as the the total distance L is dominated by the path length through the earth. A simple parameterization of neutrino production height [111] was developed by Keith Ruddick. In [111] the details of the model of which the parameterization is based and the actual parametrization are documented. Briefly, the model use a uniform production height of 30 km if the cosine of the zenith is less than -0.2 (the path length through the earth dominates), if the cosine of the zenith is bigger than -0.2 then a three parameter model is used. The results of this model are given below. In this toy model the zenith angle distribution is assumed to be uniform and the energy of the event is taken to be uniform either between 0-1 GeV or 0-5 GeV. The production height is shown in figure 5.2 and 5.3.

5.4 Properties of atmospheric neutrinos

Atmospheric neutrinos have several characteristics that can be used to differentiate them from other neutrinos. These properties can be observed from the following histograms. The events in the plots are from run 179 and run 180 and processed with R1.14.1. Run 179/180 are atmospheric neutrino MC files. These distribution show the

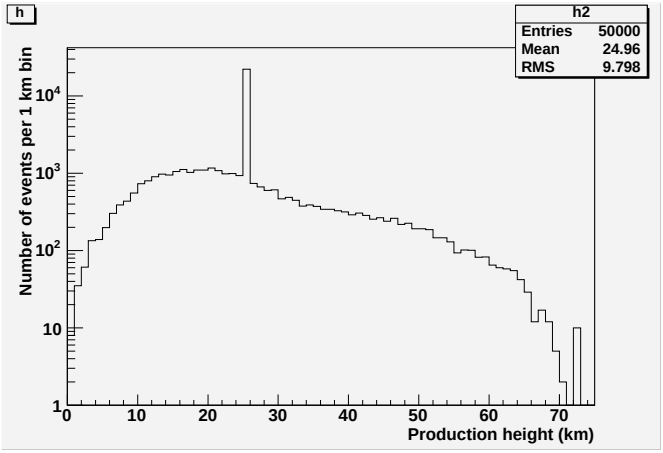

Figure 5.2: This shows the production height of a neutrino using the Ruddick model. The events are chosen from a uniform zenith angle distribution (0-180 degrees) and the energy is drawn from a uniform energy distribution between 0-1 GeV. The peak are events from below a zenith angle of -0.2 where the uncertainty in the production height does not alter the total path length.

truth information for events that passed the filter (based of reconstructed quantities). The filter is discussed in detail in the next chapter, but for this purpose the filter allows all events that reconstruct in the fiducial region with no obvious tracking problems[1]. The summed fiducial exposure for these two runs is about 650 kty (over a century of running!).

Energy Distribution

The true energy distribution of the neutrinos are shown in figure 5.4. It should be remembered that the reconstructed neutrino energy is based on the reconstructed $\mu^{\pm}$ energy and the reconstructed shower energy. It should be noted that this distribution peaks at a relatively low energy and few events have an energy greater than 20 GeV. Since the $\mu^{\pm}$ must have a lower energy than the parent neutrino this distribution

[1]These events are slightly different from the normal post filter data in that no shower requirement is made. This is a tiny difference

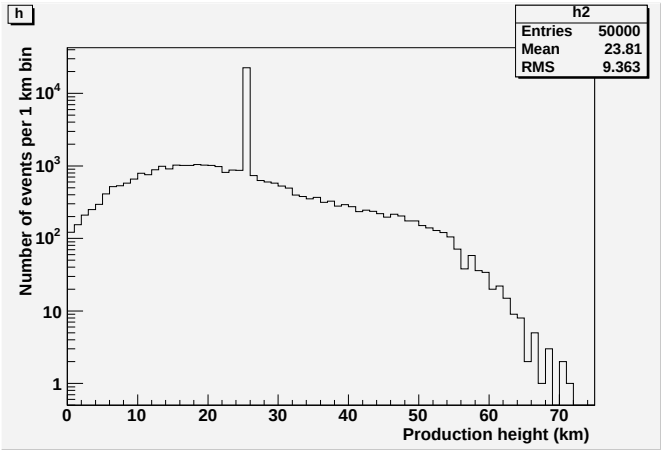

Figure 5.3: This shows the production height of a neutrino using the Ruddick model. The events are chosen from a uniform zenith angle distribution (0-180 degrees) and the energy is drawn from a uniform energy distribution between 0-5 GeV. The peak are events from below a zenith angle of -0.2 where the uncertainty in the production height does not alter the total path length.

suggests that $\mu^{\pm}$ in energy regime of 10 Gev or less must be understood.

Angular Distributions

The angular distributions are important to understand in order to reject background and to measure oscillation parameters. Figure 5.5 shows the true directional cosine in the z direction. $z = \pm 1$ corresponds to a particle going through perpendicular to the planes (forwards or backwards relative to the beam direction) and z=0 is a neutrino going in parallel to the detector planes. As before this is the truth from the neutrino not the muon. If a muon really does go parallel to the detector plane it will not hit enough planes to reconstruct. However, this plot clearly shows that even at this lowest level of reconstruction, a bias exists between events entering parallel and perpendicular to planes.

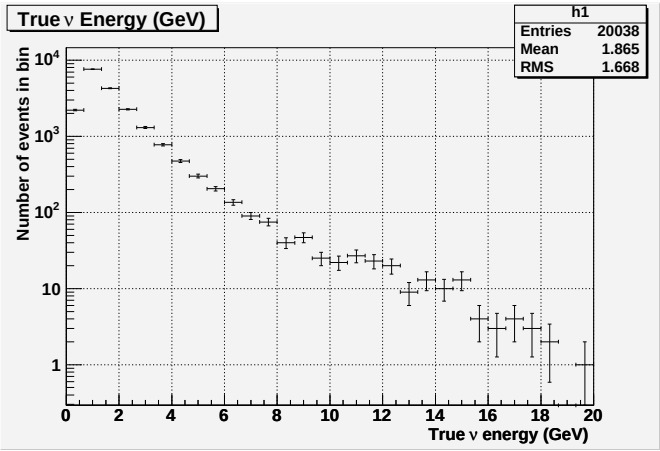

Figure 5.4: This shows the true neutrino energy of R179/180 for all true energies between 0 and 20 GeV. This shows the true neutrino energy of R179/180 for all true energies between 0 and 20 GeV. All the events shown passed the event filter. Not all of the events are CC ν_μ or $\bar{\nu}_\mu$ but the vast majority are.

L/E Distribution

The L/E distribution are an important to study as neutrino oscillation are proportional to L/E. Figure 5.6 shows the true log_{10}(L/E) distribution for the neutrinos in the absence of neutrino oscillations. The true energy distribution is easy to get from the MC. The true L is more difficult to estimate. An simple estimate is given below:

$$L = \sqrt{R^2 cos^2(\theta) + 2Rh + h^2} - Rcos(\theta) \tag{5.8}$$

The neutrino travels depends on the height it was produced. This has to be modeled to get the L distribution correct for the neutrinos coming down. For now it shall be assumed h=25 km. The radius of the earth is approximated as 6380 km in this simple model. The $cos(\theta)$ is calculated by using the true neutrinos directional cosine in y.

This distribution shows two clear peaks. The first peak at low L/E is from down going neutrinos the second peak at higher L/E is from up going neutrinos. The second peak should be suppressed if neutrino oscillation occurs. Recall E changes only 1 order

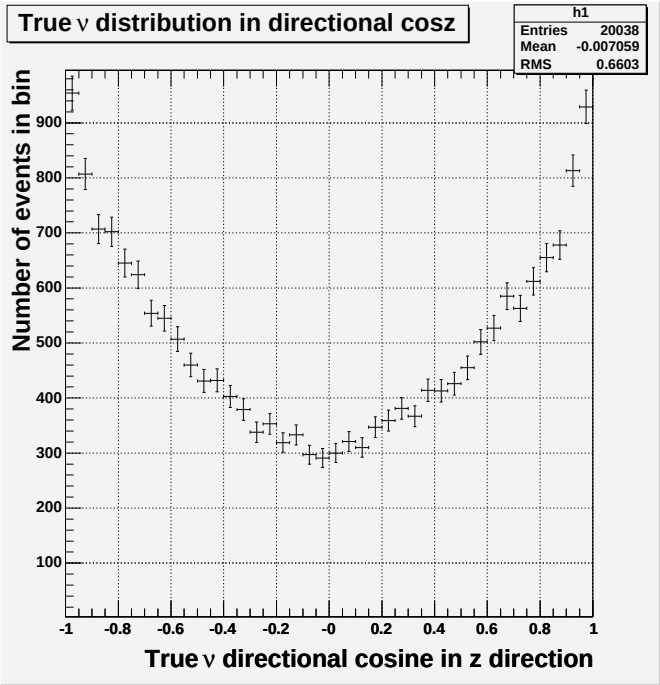

Figure 5.5: This shows the true neutrino directional cosine z of R179/180. All the events shown passed the event filter.

in magnitude while L changes almost three orders of magnitude.

5.5 Cross section and atmospheric neutrinos

The atmospheric neutrinos in MINOS have an average energy ($\approx 1 - 10$GeV) which probes a complex region for cross sections. The fundamental cause of this is that in this energy range three separate physical interactions take place. These interactions are quasi-elastic, resonace production and deep inelastic scattering. In general neutrino-nucleon experiments have a difficult time measuring cross-sections at these energies. The cross-sections are both small and have these multiple physical processes behind them. An excellent overview of neutrino physics in the relevant energy range is found in Gallagher and Goodman[129]. One of the theoretical problems is the question of how

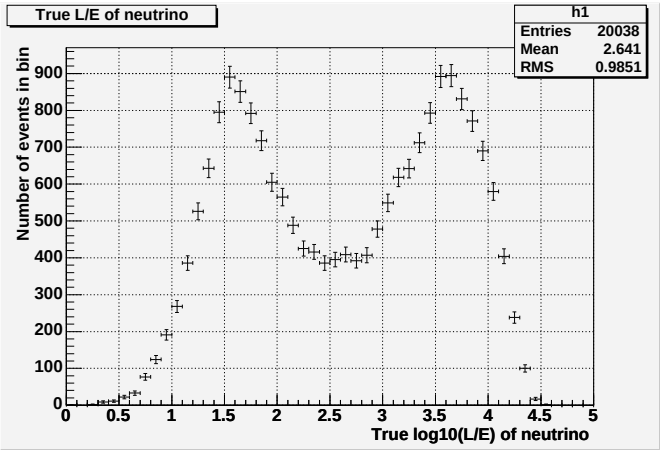

Figure 5.6: This shows the true neutrino $log_{10}(L/E)$ of R179/180. This shows the true neutrino $log_{10}(L/E)$ of R179/180. All the events shown passed the event filter. Notice the two peaks. The second peak should be suppressed if oscillations occur.

to properly add the contributions together in such a way that it neither over or under counts the states.

5.5.1 Quasi-Elastic

Quasi-elastic neutrino-nucleon scattering can be thought of as the scattering of a neutrino off an entire nucleon. At low energies in particular[129] the fermi-momentum and Pauli blocking of nucleons are important. Fermi momentum is the momentum of the nucleons moving in the nucleus and is of the order of 200 MeV per nucleon for iron. Pauli blocking is effect that nucleons cannot access already filled states because of the pauli exclusion principle. The nucleus is normally modeled with the fermi gas model which simply supposes the nucleus has states filled up to the fermi momentum. The explicit form of the cross section is somewhat complicated and is given in many places[129, 69]. Instead of reproducing these results here a qualitative explanation will be given based on these sources. Since the nucleon is not a point particle form factors must be used to describe the interactions. From Lorentz invariance you write down form

factors associated with the scalar, psuedoscalar,vector, psuedovector and tensor terms. However, only terms which conserve G-parity are kept which eliminates the scalar and tensor terms. If then CVC[112][2] is invoked it is possible to come up with relationships between the remaining form factors that for most part allow the form factors to written in terms of experimentally well measured quantities with one exception, the hadronic axial current. This has to be parameterized in terms of the axial vector mass M_A, the uncertainty in knowledge of M_A is an important uncertainty in cross-section. Figure 5.7 shows the energy spectrum of the quasi-elastic events.

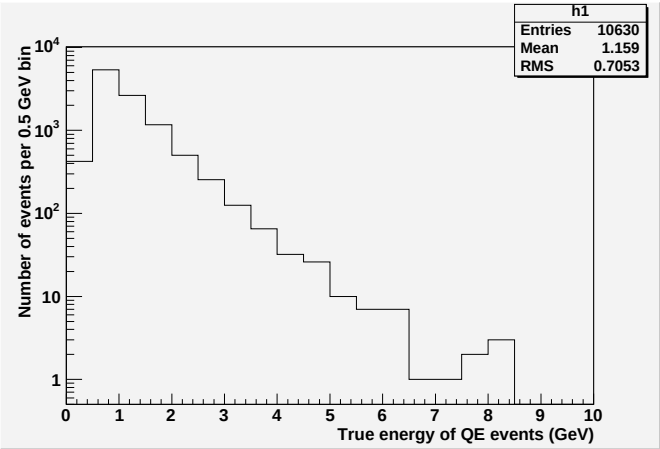

Figure 5.7: This shows the true neutrino energy of events after the filter for runs R179/180. All events show are events that under went an Quasi-elastic interaction. This shows the true neutrino energy of events after the filter for runs R179/180. All events show are events that under went an Quasi-elastic interaction. This is plotted between 0-10 GeV. Notice the average energy.

5.5.2 Resonance production

Resonance production happens when a neutrino interacts with nucleon and produces a short lived resonant particle like a Δ^+ that then decays into a π^+ and n for example.

[2]Conserved Vector Current

This was parameterized by Rein and Seghal[113] by using the baryon resonance model of Feynman, Kislinger and Ravndal[104] which uses a relativistic 3d harmonic oscillator to represent the 3 baryon state. For low energies this is dominated by the $\Delta(1232)$ although can include higher resonances as the energy is increased[129]. The energy spectrum of resonance production is shown in the figure below in figure 5.8.

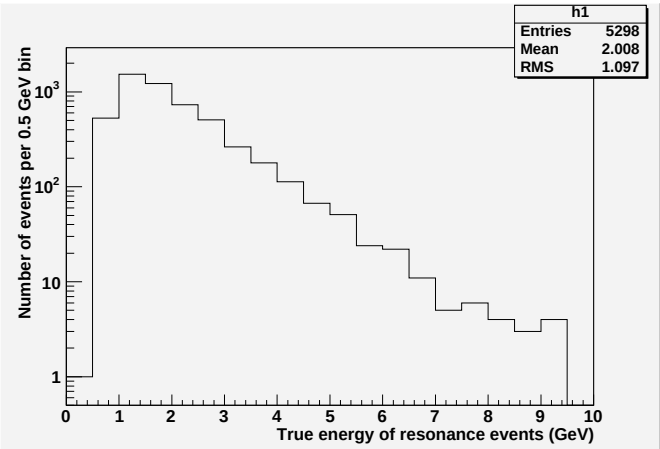

Figure 5.8: This shows the true neutrino energy of events after the filter for runs R179/180. All events show are events that under went resonance production. This shows the true neutrino energy of events after the filter for runs R179/180. All events show are events that under went resonance production. This is plotted between 0-10 GeV. Notice the average energy.

5.5.3 Deep Inelastic Scattering (DIS)

Deep inelastic neutrino-nucleon scattering can be thought of as the scattering of a neutrino off an a parton (quark for example). This suggests that the interaction is probing smaller scales and higher energies than either quasi-elastic or resonance production. This is indeed the case, as energies go up (for the most part above 10 GeV which matters for atmospheric neutrinos) DIS reproduces the measured neutrino cross section well. The details of the deep inelastic cross section will not be given here as they long

and are available elsewhere[129, 69]. Deep inelastic scattering like quasi-elastic scattering be discussed in terms of form factors. However, the most important point for this thesis is the following: neutrino-quark and anti-neutrino-quark have a different y dependence. Y is defined to be the fraction of the total energy lost by the lepton (or the fraction taken by the hadrons). Thus y is always between 0 and 1. Neutrino-quark scattering has no y-dependence while anti-neutrino-quark scattering is proportional to $(1-y)^2$. However, this gets complicated, for example simply counting the quark content of the nucleons does not work as the 'virtual sea' quarks also contribute. In any case at the energies, there are not that many DIS events anyway. Figure 5.9 shows the energy spectrum of the DIS events.

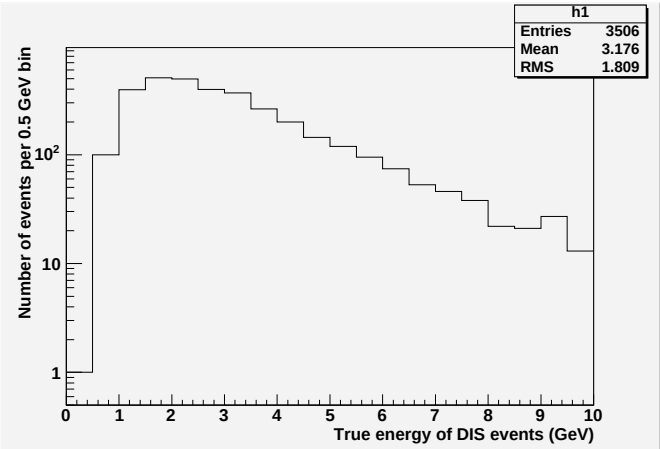

Figure 5.9: This shows the true neutrino energy of events after the filter for runs R179/180. All events show are events that under went an deep inelastic scattering (DIS). This shows the true neutrino energy of events after the filter for runs R179/180. All events show are events that under went an deep inelastic scattering (DIS). This is plotted between 0-10 GeV. Notice the average energy.

5.5.4 Neutrino versus Anti-Neutrino

The cross section between ν_μ-nucleon and $\bar{\nu}_\mu$-nucleon are different.The experimental situation is further complicated because the detector response and pattern recognition

depend on the fraction of energy in the shower which depends on the y-distribution as well. This means that the observed number of ν_μ and $\bar{\nu_\mu}$ cannot be directly related to the cross section as the detector effects must be taken into account. However, from a theoretical point of view it found that the biggest uncertainty in this is how to treat the resonance to DIS transition. By comparing the result of an resonance production model[113, 114] and a QCD-based method[115] a 12% difference can be found. This is the largest single systematic uncertainty but other uncertainties[116] such as Pauli Blocking, DIS shadowing and changing the axial vector mass contribute as well. The total uncertainty in the ratio of cross section between ν_μ and $\bar{\nu}_\mu$ is estimated to be 13.5%. It should be mentioned that this is dependent on fraction of quasi-elastic, resonance production and DIS in the sample which are of course energy dependent as is neutrino oscillations. Thus some care must be had making the estimate. However, given the small statistics in this thesis this is not a major concern.

Chapter 6

Data and Analysis

6.1 Introduction

The study of $\nu_\mu, \bar{\nu_\mu}$ neutrinos undergoing CC interactions producing a $\mu^\pm$ is the goal of this analysis. Atmospheric neutrino physics in the MINOS FD is dominated by the large background of downgoing $\mu^\pm$ produced in cosmic ray showers. To a good approximation all events in the far detector that trigger (or reconstruct) are background from muons from cosmic ray showers. If there is a single element that drives the event selection it is the elimination of down going muons from cosmic rays.

6.1.1 Strategy of analysis

As stated above the elimination of the cosmic ray muon background drives the analysis. This requirement might be the prime mover of the analysis but it is not the only one. It is also important to select events with high quality $\mu^\pm$ tracks so that the charge of the muon can be properly reconstructed. Poor quality tracks are not of interest as they cannot be used for charge ID. Thus the strategy of the analysis is to reduce the background until the sample consists of mostly $\mu^\pm$ produced by neutrinos which have some useful charge ID information. The main advantage of this approach is

that although many background events in the form of cosmic ray $\mu^{\pm}$ can enter the fiducial volume, almost all of them are at edges of the acceptance or contain poorly reconstructed tracks, while the signal is general reconstructs well and is not at the edge of the acceptance.

6.1.2 Overview of chapter

This chapter is important to the thesis and as a consequence is long. A brief outline is given here to orient the reader. Section 6.2 discusses the data and Monte Carlo samples that are used for the analysis, in particular which samples were chosen and why. Section 6.3 describes the first stage of data reduction which is an event filter that has the purpose of eliminating all data and MC events that are either poorly reconstructed or near the edge of the detector. Section 6.4 looks at the criteria that are used to select atmospheric neutrinos and why these cuts are applied. Section 6.5 deals with a detailed look at events that can give rise to an atmospheric neutrino background. Section 6.6 deals with several possible sources of systematic error introduced from the understanding (or lack thereof) related to the atmospheric neutrino sample. Section 6.7 concentrates on the stopping muons and how they are used as a control sample for the atmospheric neutrinos. This is important as charge ID and other reconstructed quantities can be cross checked against the MC expectation. Section 6.8 involves both the relative (MC-Data) normalization as well as the absolute normalization (data-livetime) using a variety of techniques. Section 6.9 concerns using stopping muons to calculate the vetoshield efficiency and false rejection rate.

6.1.3 Comparison with other work

This analysis is not the only analysis that has looked at atmospheric neutrinos in the MINOS far detector. Several dissertations[1][135] have been written on this topic. However, this analysis is somewhat different than the previously mentioned work through

the application of reconstruction algorithms: different demuxing, tracking, shower finding and track fitting algorithms are applied. It should be stated that the goal of each analysis was not exactly the same, for example, the amount of effort to keep poorly reconstructed events[1] is not the same in each analysis. In any case, the majority of cuts are not the same (although they are for the most part similar). The vetoshield was also handled in a different manner between the different analyses. The results of the comparison will be discussed in chapter 9.

6.2 Data and Monte Carlo

6.2.1 Data Set

The selection of the data set is an important first task in the analysis. It is essential to select data taken when the detector was working in a proper and understood manner. This process has several steps. First, the timeframe of the dataset and the most basic features (what type of trigger for example) of the dataset are determined. The next step is reduction of the dataset to a managable size by applying loose cuts refered to as filtering. The next step of the analysis is to apply cuts to the filtered sample to select candidate neutrino events. The final step is to eliminate any events that occurs when the detector is not in a physics taking state (Detector quality control).

Timeframe of Data Set

Since, the purpose of this analysis is to look for muons which can be charge identified, the state of the magnetic field is important. Both SM1 and SM2 did not have operational magnetic fields until the summer of 2003. It was decided that since the state of SM2 was in constant flux during it's construction the data after the completion of

[1] These events are irrelevant for charge ID, but might be important for a normalization in an attempt to extract oscillation parameters.

SM1 and before SM2 completion would not be used. The data set starts on August 7, 2003 with far detector Run 18302. The end date on the data set is slightly more arbitrary. However, the start of preliminary beam running in February 2005 has been chosen. The data set ends on the January 31, 2005 with Run 29085 (which ended early on the morning of February 1).

Criterion for Data Selection

There are several important criterion that any run must pass to be included in the data set. First, the detector must be in a data taking mode and not in some diagnostic mode. During the data set the run type which represented data taking mode evolved. The requirement for inclusion in the data set is RunType 2, 769 or 17153. The second requirement is that the trigger source is appropriate. For almost the entire data set this was the 4/5 plane trigger. Towards the end of the data set a second trigger known as the E4 trigger was added in anticipation of the beam running. This is not a problem and not a source of bias as effectively everything that passes 4/5 plane trigger also passes the E4 trigger. The trigger requirement for this data set is a 4/5 plane trigger or a E4 trigger.

Live Time

Many of the diagnostics tests done on the Far Detector are done using relatively short runs. These runs should not be included in the data set. However, an important quantitative question is: how much does this alter the total run time? The table below shows the effect of cutting shorter on total live time. If a time cut of 1 hour is used over 99 percent of the total possible live time is included. Given this eliminates many shorter diagnostic runs this is a reasonable trade off. The table 6.1 was generated by using the DBUSUBRUNSUMMARY database table. This table cannot be used to calculate the total livetime because some good runs are not included. The results are

still good enough for determining minimum time of a run for inclusion in the dataset[2].

Time Cut (s)	Type 2 (d)	Type 769 (d)	Type 17153 (d)	Total time (d)
60	192.90	188.86	54.92	436.68
300	192.75	188.84	54.90	436.49
1800	191.63	188.65	54.71	434.99
3600	190.60	187.99	54.30	432.89
5400	186.69	187.31	54.07	428.07

Table 6.1: This table shows the effect of changing the minimum amount of time a data run (type) must run to be included in the data sample. The time cut is the minimum time the run must last to be included and is measured in seconds. The different run types show the total amount of live time measured in days for the three types of runs as the time cut is varied. The total time is the sum of three run types for each given time cut. This suggests that a time cut of one hour retains more than 99% of the data taken during normal running.

6.2.2 Data filtering

Since almost all of the events are background it should be possible to eliminate almost all of the events by exploiting the unique signature of cosmic ray μ events. The cuts applied at this stage are designed to be sufficiently weak that almost all the signal events should survive. In this analysis this process is called data filtering as described in detail in section 6.3.

Detector Quality Control

The data quality control is designed to eliminate data taken when either the entire detector or a large fraction of the detector is in a unusual state. This unusual state could be caused by the magnetic field being off or a power outage during the run. This is done last, after the final selection of candidate events.

[2]The normalization is done in section 6.8 with data

6.2.3 Monte Carlo

The Monte Carlo (MC) simulation 'data' is handled in the most similar way possible when compared to the 'real' far detector data. The MC is the topic of appendix F and is discussed in greater detail their. The MC for the signal and (non-neutrino) backgrounds are generated as separate files. None of the MC files start the simulation at the initial airshower, rather all of assume some form for the initial distributions of particles. In the case of the cosmic muon sample, the events are distributed from a measured rock map. The neutrino events were generated with Neugen3[110] and could be generated with different hadronic interaction models and different flux models. However, most of the neutrinos (except noted) were generated using GCALOR[3]. Likewise there are more than 1 flux model that can be used. The Barr flux model is used except when otherwise stated.

6.3 Data Filtering

Since almost all the events in the MINOS Far Detector are background an efficient way to reduce them must be found. This is accomplished with a post reconstruction filter. The idea behind the filter is to eliminate events which are clearly not going to be considered fully contained candidates at a later stage of event selection. Thus the filter is designed to be loose in the sense that the neutrinos events that do fail this requirement are either so poorly reconstructed or near the detector edge that they would never be accepted. As will be shown later, the actual event selection cuts are more stringent. These cuts can be broken into four types of cuts, data selection cuts, demuxing cuts, fiducial cuts and event quality cuts.

[3]The hadronic models were tested at CalDet and there was some preference for GCALOR[88] over SLAC-GHESIA although it should be noted CalDet was designed to look at particles from a beam.

6.3.1 Data selection cut

Since the purpose of this analysis is to look for ν_μ and $\bar{\nu_\mu}$ it is important to look for single tracks. The data selection is all single track events that have passed the data quality control cuts. An additional requirement is that event cannot happen within 500 μs of a timeframe boundary. This cut is designed to prevent events getting 'split' into different time frames which could cause an event to look 'contained' if part of the event is in a separate snarl. A smaller time cut is almost certainly safe, however, given the current cut only loses 0.1% of events, this is not a concern.

6.3.2 Demuxing cut

The demuxing requirement is that the demultiplexer does not see evidence of a multi-muon event and that the fraction of stray planes in the U and V view is small. In particular the requirement is that the fraction of stray U planes to good U planes and the fraction of stray V planes to good V planes when added together in quadrature (squareroot of the sums squared) is less or equal to 0.20. The demultiplexing cut is probably the weakest cut in the filter.

6.3.3 Fiducial cut

The fiducial cuts are used to eliminate events that are near the physical edges of the detector. There is a requirement that the track does not start or end in the first or last 3 planes of a supermodule. This cuts out 12 of 484 active planes in the detector. There is also a requirement that the event does not start or end more than 3.8 meters from the detectors radial center. This is one of the most effective cuts. Finally, there is a requirement that the event does not start or end in the inner 0.35 meters. The first strips are about 25 cm from the center. This final cut is designed to reject events that enter the coil and scatter out.

6.3.4 Event Quality cut

The event quality control cut throws out events which either have clear pathological behavior or have so little information that the charge ID could never be determined. A track must be at least 6 tracklike planes long and must have at least half of the hits in the track be double ended. The track must reconstruct in both the U and V views. This means that the number of U and V planes in the track cannot differ by more than three. The track must start tracking and end tracking in a similar place in U and V: a track can 'skip' only one U plane or V plane at the track plane vertex or the track end. The fraction of tracklike planes to all planes in the track must be 75 percent or higher and the fraction of strips in the track divided by the number of tracklike planes must 2.5 or smaller . Finally, the track fitter must pass its internall consistency check.

6.3.5 Shower and shield requirement

Up to this point there is has been no requirement made on showers or the shield. It is required that there is no more than 1 shower in the event. Furthermore, for the one shower events it is required that the shower does not begin in the first or last three planes of a supermodule and the vertex of a shower is not less than 35 cm or more than 380 cm away from the radial center of the detector. The difference in the number of U and V views cannot differ by more than three for the shower. These cuts bias the shower vertex versus shower end. However, since the track is more important and these cuts are applied to both data and MC this is not as important as it might seem. The reason for this is an oddity in the way showers are reconstructed. However, it will later be shown this is not a problem.

6.3.6 Fiducial Mass post filter

After the filter is applied, the number of active planes is reduced from 484 to 472. The radial fiducial volume consists of all material such that $r \geq 0.35$m or $r \leq 3.8$m.

The detector mass can be approximated as the mass of the iron plus the mass of the scintillator. Using these assumptions a fiducial mass of 4950 tons is obtained. For comparsion using the measured mass [132] of all the steel (≈5200 tons) and another 260 tons for the scintillator gives an estimate that the total mass of the detector is 5460 tons. This means that the fiducial region has a fraction 0.90 of the total mass.

6.3.7 PreCoilHV Dataset

After the data filter is applied there is a dataset which includes data taken during both normal and abnormal times of running. The vast majority of this is time the detector is in a good condition. The main reason for the detector not to be in a good condition is either a coil problem or HV trip. Furthermore since the main background are muons entering the detector at odd angles (see the relevant sections of this chapter) all of this data is included in what is known as the PreCoilHV or simply post filter dataset. Even though this seems unusual it does allow one to show that many things are relatively independent of certain detector states. The rate of background during the unusual detector state are similar to when the detector is in a good state. However, the final event selection must be based on a subset of this sample, the candidate dataset.

6.3.8 Candidate Dataset

The candidate dataset is a subset of the PreCoilHV dataset. It includes only data from when the detector was found to be in a 'well operating' state. This means that no HV trips and the coil and veto shield had to be on.

6.4 Finding atmospheric neutrino ν_μ and $\bar{\nu}_\mu$

6.4.1 Selection Cuts applied to tracks

The selection cuts applied to the tracks from atmospheric neutrino events were based on the principle of eliminating events that were either not contained, poorly reconstructed or would not give a good charge sign. For each of the following cut an qualitative argument is given. It should be noted that the cuts are all chosen because the MC shows quantitatively that the cuts work. The effect of the cuts is shown over the next few pages on the MC signal and MC Background. For a full explanation and all the relevant plots see appendix G. To help guide the reader table 6.2 is presented before the indivual cuts. Table 6.2 shows the effects the cuts have on the signal MC.

Number of events	Cut Number	Events per kty	CC ν_μ	CC $\bar{\nu}_\mu$	Bkg. ν
19440	No cut	29.8 ± 0.4	12823	4381	2204
19077	1	29.2 ± 0.4	12606	4335	2136
18234	2	27.9 ± 0.4	12050	4083	2101
13749	3	21.1 ± 0.4	9389	3292	1068
11867	4	18.2 ± 0.3	8101	2777	989
9711	5	17.9 ± 0.4	6672	2216	823
9524	6	17.5 ± 0.4	6541	2165	818
7153	7	13.1 ± 0.3	5053	1715	385
5901	8	10.8 ± 0.3	4188	1530	183
5514	9	10.1 ± 0.3	3904	1431	179

Table 6.2: This table shows the effects of different tracking cuts on the atmospheric neutrino sample with zero and one showers. The errors shown are only statistical (95% CL). The total number of events is based on a 653 kty exposure for all the cuts up to cut 4, after cut 4 the exposure is 544 kty. The files used for this R179 and R180.

Track direction cut (1)

The track direction cut is based on looking at the directional vector at the track vertex and the track end point and requiring that the event not change direction by an unphysical amount. This was done to eliminate tracking errors. The precise requirement

is that the dot product of the directional vector at the vertex times the directional vertex at the end is 0.75 or larger. This cuts away a small fraction of the signal. Figure 6.1 shows the effect of cut 1.

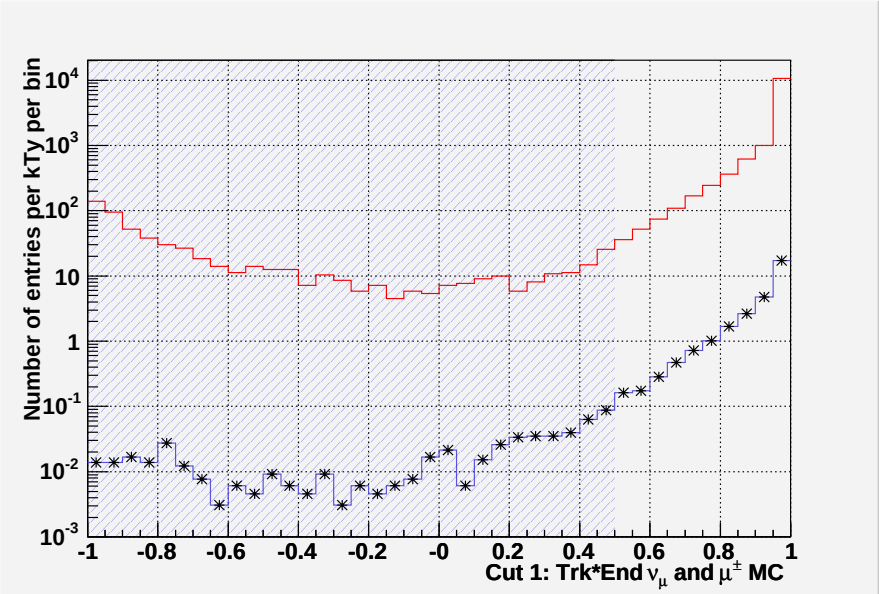

Figure 6.1: The track direction for MC cosmic background and MC ν is shown. The track direction for MC cosmic background and MC ν is shown. The cosmic MC background is shown with the red histogram and the ν MC is shown with the blue histogram with the marker. The area with the cross hash is cut from the sample. Both the Cosmic and ν are scaled to events per kTy. No statistical error bars are drawn. Both 0 and 1 shower data is shown together.

Z-direction cut (hard) (2)

This cut has a weak effect on the atmospheric neutrino sample but as will be shown a strong effect on the cosmic ray background. The physical motivation is that any track which reconstructs close to parallel to the plane will probably be of little usefull information. Since these events tend to go through the detector at a direction the detector was not optimized for this is not really a surprise. The cut that was applied required the absolute value of the directional cosine in the z direction to be 0.25 or

greater at the track vertex and track end. Figure 6.2 shows the effect of cut 2.

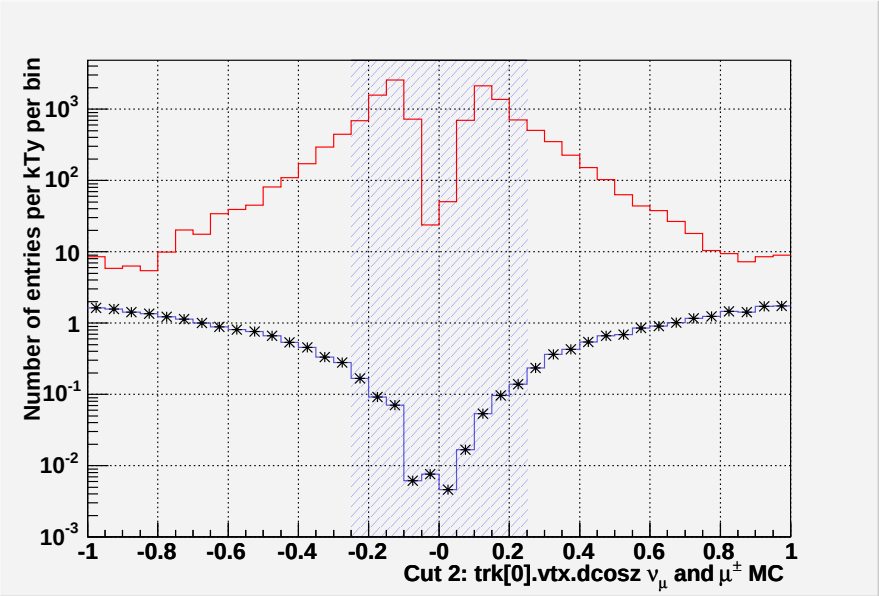

Figure 6.2: The cosmic MC background is shown with the red histogram and the ν MC is shown with the blue histogram with the marker. The area with the cross hash is cut from the sample. Both the Cosmic and ν are scaled to events per kTy. No statistical error bars are drawn. Both 0 and 1 shower data is shown together.

Digit fraction cut (3)

The number of digits per tracklike plane is unlike almost any other cut presented here in that it seems not to be efficient in that it eliminates a great deal of signal and does not remove a large fraction of the background. The cut takes a large amount of signal, effort was given to avoiding this but no fully acceptable solution was found. The cut is applied to accept events with on average 2 digit per tracklike plane or less. It should be noted that if the cut was loosened up the pulse height cut applied later would not be as efficient and the tracking on average would be worse. However, these background events must be removed. The one type of background this cut is good at removing is the non CC ν_μ,$\bar{\nu}_\mu$ neutrino background.

Z-direction cut (weak) (4)

This cut is the second of three cuts that involves the directional cosine in the z direction. The applied cut is: either the track vertex or the track end must have an absolute value of the directional cosine in z of 0.60 or greater. This is applied to require that at least one end of the track is going relatively perpendicular to the planes which tends to improve reconstruction.

Fiducial Volume cut (5)

The fiducial volume cut is actually seven cuts. These cuts are that the track vertex and track end must be 3.5 m or less radially from the center of the detector. The first and last plane of a track and the first and last plane of a shower must be more than 5 planes away from the end of a super module. Finally, the shower vertex must be 3.5 m or less radially from the center of the detector. This is the only cut applied to showers in the entire analysis (besides requiring 0 or 1 showers) and this is only a requirement the shower has some containment.

Zenith angle cut (6)

Muons from neutrinos that reconstruct below a zenith angle of 35 degrees or above a zenith angle of 145 do not in effect reconstruct at any substantial rate. This can be seen by the figure 6.3. This is in principle something that would be best to avoid as events with a small and large zenith angle have small and large path lengths, and this lower sensitivity to the oscillation paremeter space. Since the MC suggests that almost no signal are in these regions and a large background is in this region the cut must be made.

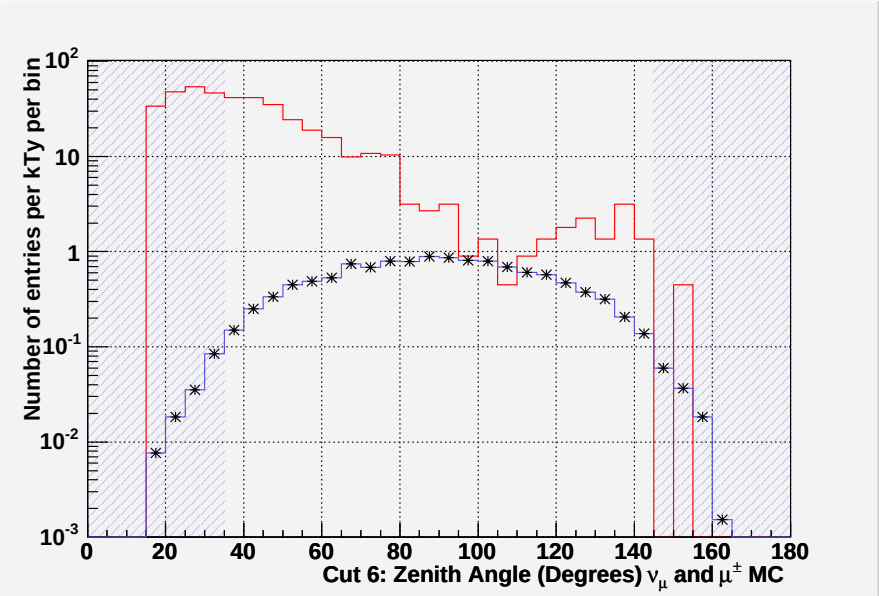

Figure 6.3: The track zenith angle for MC cosmic background and MC ν is shown. The cosmic MC background is shown with the red histogram and the ν MC is shown with the blue histogram with the marker. The area with the cross hash is cut from the sample. Both the Cosmic and ν are scaled to events per kTy. No statistical error bars are drawn. Both 0 and 1 shower data is shown together.

Pulse height fraction cut (7)

The pulse height cut is simply based on the premise that a CC $\nu_\mu, \bar{\nu}_\mu$ event should have most of the pulse height in the track. This does bias the selection against events with showers. However, given the purpose to identify the charge of the muon, eliminating a shower is not in itself a bad idea. The cut is applied at a fraction of 0.75.

8 tracklike plane cut (8)

Tracks must go a minimum of 8 tracklike planes. This has two ideas behind it. First, the more information about a track, the more likely the track will reconstruct well. Secondarily, the longer a track the more likely any curvature will be detectable. This means that some 6 and 7 tracklike plane long events will be eliminated, but they are

so short they cannot be used to get good charge ID, so this is an acceptable trade off.

Final Z-direction cut (9)

The final cut before the vetoshield is the third cut on the directional cosine in the Z-direction. The cut is the absolute value of the directional z cosine at the vertex plus the absolute value of the directional cosine in the z direction at the end must be greater than a set value. This value is 1.0 if the track vertex is 3.0 or less meter from the center and is 1.5 otherwise. This is the only cut that breaks the track vertex-track end symmetry. The reasoning behind is that if the track is deeply contained and passed the first 8 cuts there is no reason to cut hard on this. If it is more near edge the background is higher and the stronger cut is needed.

Final fiducial mass

The detector has a fiducial mass of 4.95 kT before any selection cuts are applied. The fiducial volume is reduced as 8 additional planes are removed from the fiducial volume and the maximum radial distance an event can start or end is reduced from 3.8 to 3.5 m. The result of this is a fiducial volume with a mass of 4.12 kT.

6.4.2 Results of cuts on atmospheric neutrinos

After all these 9 cuts are applied the following results are obtained. For all the neutrino results, the cases of zero and one shower will be examined seperately. Although in the end the zero and single shower samples are used together and the analysis of the two subsample is effectively identical[4], a separate examination is useful. This is done so the reader can observe the differences in how the cuts effect the signal and background in both subsets. The disadvantage of this is that it doubles the number of tables in

[4]The only differences come in the fiducial and shower quality requirements placed on the showers. The requirement on the tracks are identical.

chapter 6. See table 6.3 and 6.4 for the separate zero and one shower tables.

Number of events	Cut Number	Events per kty	CC ν_μ	CC $\bar{\nu}_\mu$	Bkg. ν
2381	No cut	3.6 ± 0.1	1782	545	54
2357	1	3.6 ± 0.1	1768	538	51
2297	2	3.5 ± 0.1	1728	519	50
2220	3	3.4 ± 0.1	1680	494	46
2071	4	3.2 ± 0.1	1575	450	46
1730	5	3.2 ± 0.1	1323	370	37
1714	6	3.2 ± 0.1	1313	364	37
1629	7	3.0 ± 0.1	1261	335	33
1322	8	2.4 ± 0.1	1020	285	17
1260	9	2.3 ± 0.1	973	270	17

Table 6.3: .
This table shows the effects of different tracking cuts on the atmospheric neutrino sample with no shower. The errors shown are only statistical (95% CL). The total number of events is based on a 653 kty exposure for all the cuts up to cut 4, after cut 4 the exposure is 544 kty. The files used for this R179 and R180.

An independent set of atmospheric neutrino MC which is identical in every way consists of runs R181 and R182. All the physics inputs and the fiducial exposures are identical. These files were not used to set the cuts as R179 and R180 were. Thus the use of this MC set is as a check against selection bias. See table 6.5 and 6.6.

Number of events	Cut Number	Events per kty	CC ν_μ	CC $\bar{\nu}_\mu$	Bkg. ν
17059	No cut	26.1 ± 0.4	11041	3868	2150
16720	1	25.6 ± 0.4	10838	3797	2085
15937	2	24.4 ± 0.4	10322	3564	2051
11529	3	17.7 ± 0.3	7709	2798	1022
9796	4	15.0 ± 0.3	6526	2327	943
7981	5	14.7 ± 0.3	5349	1846	786
7810	6	14.4 ± 0.3	5228	1801	781
5524	7	10.2 ± 0.3	3792	1380	352
4579	8	8.4 ± 0.2	3168	1245	166
4254	9	7.8 ± 0.2	2931	1161	162

Table 6.4: This table shows the effects of different tracking cuts on the atmospheric neutrino sample with one shower. The errors shown are only statistical (95% CL).The total number of events is based on a 653 kty exposure for all the cuts up to cut 4, after cut 4 the exposure is 544 kty. The files used for this R179 and R180.

Number of events	Cut Number	Events per kty	CC ν_μ	CC $\bar{\nu}_\mu$	Bkg. ν
1851	No cut	3.8 ± 0.2	1399	403	49
1829	1	3.7 ± 0.2	1382	401	46
1795	2	3.6 ± 0.2	1358	391	46
1724	3	3.5 ± 0.2	1311	370	43
1607	4	3.3 ± 0.2	1227	339	41
1315	5	3.2 ± 0.2	1002	276	37
1309	6	3.2 ± 0.2	999	273	37
1236	7	3.0 ± 0.2	952	254	30
983	8	2.4 ± 0.1	751	217	15
928	9	2.3 ± 0.1	711	203	14

Table 6.5: This table shows the effects of different tracking cuts on the oscillated ν_μ background with zero shower. The errors shown are only statistical (95% CL). The total number of events is based on a 492 kty exposure for all the cuts up to cut 4, after cut the exposure is 410 kty. The files used for this R181 and R182

Number of events	Cut Number	Events per kty	CC ν_μ	CC $\bar{\nu}_\mu$	Bkg. ν
12956	No cut	26.3 ± 0.5	8414	2958	1584
12703	1	25.8 ± 0.4	8256	2908	1539
12080	2	24.6 ± 0.4	7837	2721	1522
8745	3	17.8 ± 0.4	5877	2109	759
7391	4	15.0 ± 0.3	4928	1768	695
5931	5	14.5 ± 0.4	3959	1411	561
5817	6	14.2 ± 0.4	3876	1386	555
4196	7	10.2 ± 0.3	2815	1111	270
3441	8	8.4 ± 0.3	2338	997	106
3201	9	7.8 ± 0.3	2180	916	105

Table 6.6: This table shows the effects of different tracking cuts on the atmospheric neutrino sample with one shower. The errors shown are only statistical (95% CL).The total number of events is based on a 492 kty exposure for all the cuts up to cut 4, after cut 4 the exposure is 410 kty. The files used for this R181 and R182

6.4.3 Charge Identification

Since the main purpose of this thesis is test CPT, identifying the charge of $\mu^{\pm}$ from ν_μ,$\bar{\nu}_\mu$ is important. However, all events cannot have charge determined. In each of the following three tables the charge ID is broken down into high resolution, medium resolution and no resolution category. Each is then broken down by the number of events that pass and fail for $\nu_\mu, \bar{\nu}_\mu$ separately. This is done for no shower and one shower events separately as well. The fraction f is defined as the fraction of events with the right charge ID over the number of events with the right plus wrong charge ID. The correlated error σ_f is also calculated. The charge is determined by cutting on $\mid \frac{\sigma_{(q/p)}}{(q/p)} \mid$ which is the track fitters estimate of the uncertainity in $\frac{q}{p}$ divided by $\frac{q}{p}$. As this quantity becomes small the charge ID should become more accuarate. $\frac{q}{p}$ is the charge over the momentum and is one of the variable the track fitter returns from the Kalman filter.

$$f = \frac{r}{r+w} \tag{6.1}$$

$$\sigma_f = \frac{\sqrt{rw(r+w)}}{(r+w)^2} \tag{6.2}$$

High resolution charge ID

The high resolution sample is defined to have nearly perfect charge ID. This is obtained by requiring the event to have a charge ID of $\mid \frac{\sigma_{(q/p)}}{(q/p)} \mid <= 0.25$. This is a 4σ charge ID resolution according to the track fitter. See table 6.7.

Medium resolution charge ID

The high resolution sample is defined to have good charge ID. This is obtained by requiring the event to have a charge ID of $\mid \frac{\sigma_{(q/p)}}{(q/p)} \mid < 0.25$ and $\mid \frac{\sigma_{(q/p)}}{(q/p)} \mid \geq 2.0$. This is

ν_μ	R-ID	W-ID	Fraction	$\bar{\nu}_\mu$	R-ID	W-ID	Fraction
522	479	43	0.918 ± 0.012	172	163	9	0.948 ± 0.017
1784	1702	82	0.954 ± 0.005	801	772	29	0.964 ± 0.007

Table 6.7: This shows the charge identification ID for the high resolution sample for R179R180. The first line is no shower events and the second line is one shower events. All events have pass the normal cuts to be considered a fully contained candidate. In addition all of these events have a $\mid \frac{\sigma_{(q/p)}}{(q/p)} \mid <= 0.25$. R-ID means the event has the right (correct) charge ID and W-ID means the event has the wrong charge ID. The event is said to have correct charge ID if it reconstructs the correct signed μ for the given ν_μ or $\bar{\nu_\mu}$. The fraction shown has a 1 σ statistical uncertainty. Only CC events are considered.

a charge ID between 4 and 0.5 σ according to the track fitter. See table 6.8.

ν_μ	R-ID	W-ID	Fraction	$\bar{\nu}_\mu$	R-ID	W-ID	Fraction
355	233	122	0.656 ± 0.025	73	55	18	0.753 ± 0.050
937	671	266	0.716 ± 0.015	293	217	76	0.741 ± 0.026

Table 6.8: This shows the charge identification ID for the medium resolution sample for R179R180. The first line is no shower events and the second line is one shower events. All events have pass the normal cuts to be considered a fully contained candidate. In addition all of these events have a $\mid \frac{\sigma_{(q/p)}}{(q/p)} \mid < 0.25$ and $\mid \frac{\sigma_{(q/p)}}{(q/p)} \mid \geq 2.0$. R-ID means the event has the right (correct) charge ID and W-ID means the event has the wrong charge ID. The event is said to have correct charge ID if it reconstructs the correct signed μ for the given ν_μ or $\bar{\nu_\mu}$. The fraction shown has a 1 σ statistical uncertainty. Only CC events are considered.

No charge ID

The no charge ID sample has a charge ID which is consistent with a random charge Identification. This is obtained by requiring the event have an apparent charge sign with is less than 0.5σ. This suggest that the charge identification should be effectively random. This is what is observed. See table 6.9.

ν_μ	R-ID	W-ID	Fraction	$\bar{\nu}_\mu$	R-ID	W-ID	Fraction
96	53	43	0.552 ± 0.051	25	16	9	0.640 ± 0.096
210	106	104	0.505 ± 0.035	67	43	23	0.652 ± 0.059

Table 6.9: This shows the charge identification ID for the no charge ID sample for R179R180. The first line is no shower events and the second line is one shower events. All events have pass the normal cuts to be considered a fully contained candidate. In addition all of these events have a $\mid \frac{\sigma_{(q/p)}}{(q/p)} \mid \geq 2.0$. R-ID means the event has the right (correct) charge ID and W-ID means the event has the wrong charge ID. The event is said to have correct charge ID if it reconstructs the correct signed μ for the given ν_μ or $\bar{\nu_\mu}$. The fraction shown has a 1 σ statistical uncertainty. Only CC events are considered.

6.5 Backgrounds

The backgrounds to the ν_μ CC interactions are many. To first order they can be broken down into 'physics background' and 'non-physics background'. Physics background are background events caused by other neutrino interactions and cosmic μ. Even in the limit that the reconstruction is perfect, these events will still be a background[5]. The non-physics background are background events caused by a variety of effects such as event misreconstruction or inefficiency in the detector. These could in principle be reduced further.

6.5.1 Cosmic ray muons

Cosmic ray muons are basically the only source of events in the MINOS far detector. By the number of events alone this background must be greatly reduced. However, unlike other backgrounds the vetoshield is useful to reduce this background. The vetoshield which is not simulated in the MC is the last cut to be applied. This is important because the vetoshield efficiency can be determined separately. Thus the predicted number of events before and after the vetoshield cut can be applied to understand the analysis.

One significant issue is the normalization of the rate cosmic $\mu^\pm$ MC to the rate of data $\mu^\pm$. This normalization is not simple to calculate. The normalization will be estimated from the data. For the time being, the normalization will be based on a previous study [133] which observed 22.5 million muons in 468 live-days. This corresponds to a rate of 0.55 Hz. The observed number of muon (of any type) in the MC data set is 6.3 million. This corresponds to 131 days of livetime. Thus the exposure is 1.78 kty before cut 4 and 1.51 kty after cut 4. The issue of normalization will be returned to in detail later (section 6.8). The MC is based of MC run 651 to run 778. See table 6.10 and 6.11.

[5]The ν backgrounds are more irreducuble then the cosmic μ background.

Number of events	Cut Number	Events per kty
824	No cut	463 ± 32
784	1	440 ± 31
76	2	42.7 ± 9.6
59	3	33.1 ± 8.4
33	4	18.5 ± 6.3
8	5	$5.4^{+4.9}_{-3.4}$
7	6	$4.7^{+4.6}_{-2.9}$
1	7	$0.7^{+2.8}_{-0.7}$
0	8	≤ 2.09
0	9	≤ 2.09

Table 6.10: This table shows the effects of different tracking cuts on the $\mu^{\pm}$ background with zero shower. The errors shown are only statistical (95% CL). This shows the results before any vetoshield cut is applied.

Number of events	Cut Number	Events per kty
30294	No cut	17019 ± 192
28936	1	16256 ± 187
5609	2	3151 ± 82
3224	3	1811 ± 63
1618	4	909 ± 44
920	5	622 ± 40
515	6	348 ± 30
69	7	46.6 ± 11.0
62	8	41.9 ± 10.4
17	9	11.5 ± 5.5

Table 6.11: This table shows the effects of different tracking cuts on the cosmic $\mu^{\pm}$ background with one shower. The errors shown are only statistical (95% CL).This shows the results before any vetoshield cut is applied.

Cosmic MC truth to reco comparsion

An relevant question to ask about the cosmic ray MC is how well does it the reconstructed MC agree with the truth information. Since cosmic muons are the largest background to atmospheric neutrinos this of particular interest. The angular distributions of the cosmic muons explain a great deal about the nature of the cosmic muon background. The following three angular distributions are for zero and one showers events combined (although almost all events are single shower events). The three distribution are shown in figures 6.4,6.5 and 6.6 after the initial data filtering but before the tracking cuts.

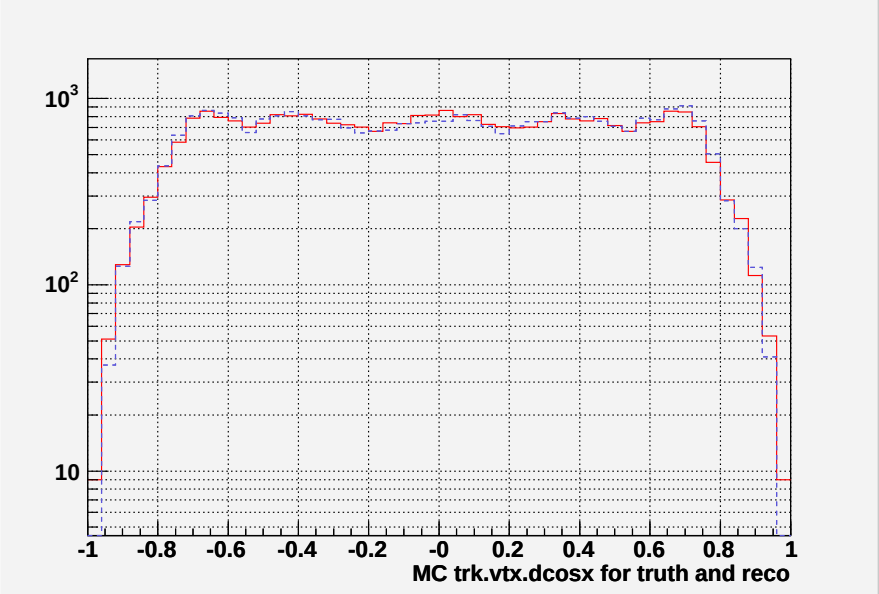

Figure 6.4: This shows the true directional cosine of the track in the x direction as the dashed line and the reconstructed directional cosine of the track at the vertex in the solid line. The agreement is nearly perfect.

These three plots explain many things about the cosmic muon background. The angular distributions in x and y seem for the most part to be as expected. Although the tail in the y direction looks troubling, it should be recalled that this before any

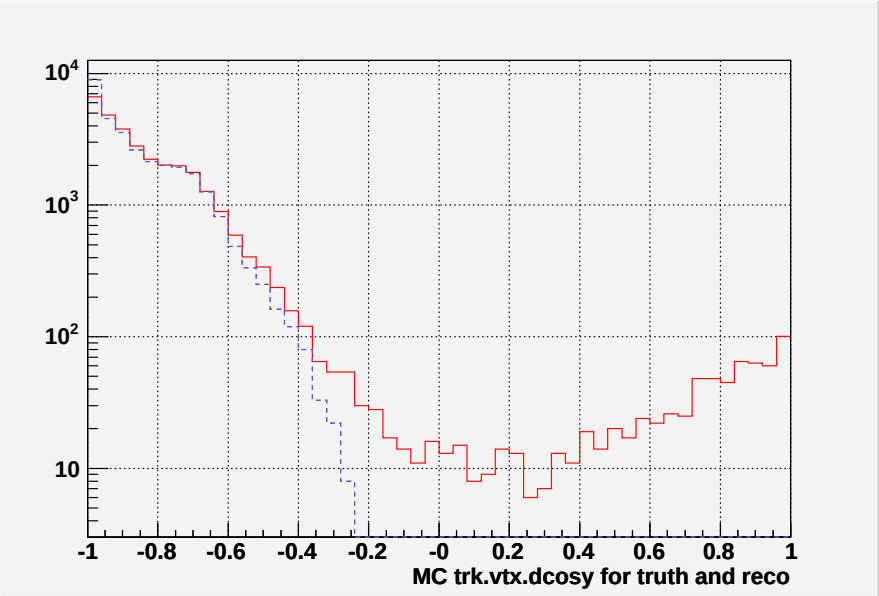

Figure 6.5: This shows the true directional cosine of the track in the y direction as the dashed line and the reconstructed directional cosine of the track at the vertex in the solid line. The agreement is good. The events in the tail appear to be coming up instead of down.

of the selection cuts for tracks are applied and these plot include events as short as 6 planes. The z directional cosine plot effectively explains why there a large cosmic background. The reason is that almost all the cosmics are entering parallel to the planes. However, they do not reconstruct well at these angles and are thus difficult to eliminate. These events should be compared to the stopping muon sample. All the muons in this sample are by definition a rare event as the vast majority of muons are already eliminated. It should not be surprising that a detector with a design like MINOS should have problems with these events as by entering at this steep angle the hits tend to be few and far between. This is why they appear to be contained. To verify the angular distributions in the simulation is correct these plots should be compared with the stopping muons. The stopping muons are rare because only a small range of energies will 'range out' in the detector, these cosmic muons are rare because of the

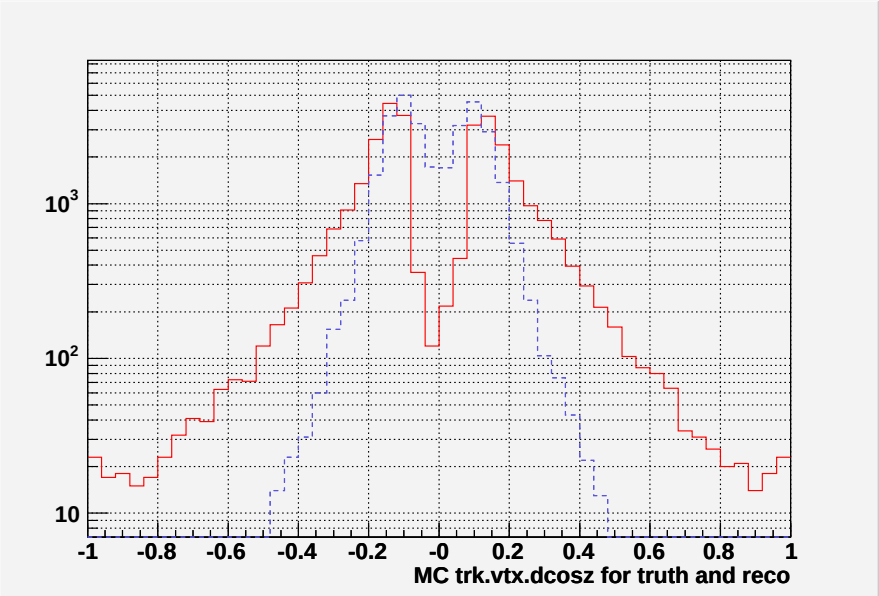

Figure 6.6: This shows the true directional cosine of the track in the z direction as the dashed line and the reconstructed directional cosine of the track at the vertex in the solid line. The agreement is poorer than x and y. However, this does show that almost all of these background events come from muons that are relatively parallel to the plane of the detector.

odd angle they enter the detector.

6.5.2 CC ν_e events

The ν_e backround is one of the irreducible backrounds in the MINOS FD. This is because there are a flux of ν_e,$\bar{\nu_e}$. Unlike the comsic ray background they must interact in the detector. However, it is expected that the background is small as e^- and e^+ will tend to shower and not form tracks. Since there is only about half as many ν_e as ν_μ to start with it seems reasonable to expect this to be a small background.

The following study is based on runs R181 and R182. These two runs were not used to set the cuts but were kept independent. These two MC runs were generated under the same simulation (flux model, hadronic interaction, ...) as runs R179 and R180 which were used to set the cuts. The fiducial exposure before cut 4 is 493 kty and the fiducial exposure after cut number 4 is 418 kty. See table 6.12 and 6.13.

Number of events	Cut Number	Events per kty
13	No cut	0.03 ± 0.01
12	1	0.02 ± 0.01
12	2	0.02 ± 0.01
9	3	0.02 ± 0.01
9	4	0.02 ± 0.01
9	5	$0.02^{+0.02}_{-0.01}$
9	6	$0.02^{+0.02}_{-0.01}$
9	7	$0.02^{+0.02}_{-0.01}$
3	8	0.01 ± 0.01
2	9	< 0.02

Table 6.12: This table shows the effects of different tracking cuts on the ν_e background with zero shower. The errors shown are only statistical (95% CL). The total number of events is based on a 492 kty exposure for all the cuts up to cut 4, after cut the exposure is 410 kty.

This is a small background as expected.

Number of events	Cut Number	Events per kty
1092	No cut	2.22 ± 0.13
1062	1	2.16 ± 0.13
1053	2	2.14 ± 0.13
500	3	1.02 ± 0.09
467	4	0.95 ± 0.09
378	5	0.92 ± 0.09
376	6	0.92 ± 0.09
180	7	0.44 ± 0.06
65	8	0.16 ± 0.04
64	9	0.16 ± 0.04

Table 6.13: This table shows the effects of different tracking cuts on the ν_e background with one shower. The errors shown are only statistical (95% CL).The total number of events is based on a 492 kty exposure for all the cuts up to cut 4, after cut 4 the exposure is 410 kty.

6.5.3 CC ν_τ events

The background from ν_μ that oscillate to ν_τ should be small. The $\tau^\pm$ cannot be observed directly given the particles short lifetime ($290.6 \pm 1.1 \times 10^{-15}$s[17]), thus it will decay before it has time to be tracked. There are at least three separate reasons for the expected suppression of ν_τ background. Although, the background is estimated with a MC simulation, a few simple arguments give a qualitative explanation of the small background. First, the $\tau^\pm$ lepton is much heavier ($m_\tau = 1777.03^{+0.30}_{-0.26}$ MeV [17]) than the $\mu^\pm$ or $e^\pm$. This leads to a production threshold to produce a $\tau^\pm$ in the CC interaction. For example, consider the following reaction:

$$\nu_\tau + p \rightarrow n + \tau^+ \tag{6.3}$$

Since the square of the 4-momentum is a relativistic invariant, evaluate the left hand side in the lab frame and the right hand term in the center of mass frame. This leads to:

$$m_{\nu_\tau}^2 + m_p^2 + 2E_{\nu_\tau} m_p = m_n^2 + m_\tau^2 + 2m_\tau m_n \tag{6.4}$$

Since in the lab frame the proton is at rest and in the center of frame at threshold the neutron and τ are at rest we can rewrite this and solve for E_{ν_τ}. To good approximation $m_n = m_p$ and $m_{\nu_\tau} = 0$. This leads to:

$$E_{\nu_\tau} \geq \frac{m_\tau^2}{2m_p} + m_\tau \tag{6.5}$$

Putting in $m_\tau = 1.777$ GeV and $M_p = 0.938$ GeV gives a requirement of $E_{\nu_\tau} \geq 3.4$ GeV. This can be reduced some if the Fermi motion of the target particle is taken into account.

The second reason for suppression involves the branching ratios for the τ. The tau decays to the lighter leptons through $\tau^- \rightarrow e^- + \bar{\nu_e} + \nu_\tau$ and $\tau^- \rightarrow \mu^- + \bar{\nu_\mu} + \nu_\tau$

each about 17 percent of the time and to hadronic channels the rest[17]. The electron and hadronic channel are similar to the NC and ν_e discussed in chapter which have a small acceptance. Thus only about $\approx \frac{1}{6}$ events have any realistic chance of being reconstructed.

The third reason for this suppression is that all of the ν_μ do not oscillate into ν_τ. The actual fraction is of course related to the oscillation parameters that experiment is trying to measure, so some care not to bias oneself. However, given the high energy that ν_τ must have in order to produce a charged τ in the first place, a first order guess would be that L/E should be oscillating rapidly and thus at most ≈ 0.5 of the ν_μ should have oscillated.

It is clear that these arguments suggest that few CC ν_τ should show up as a background to ν_μ. The quantitative estimate of this is now made with following study. This study is based on MC files R187,R188. The total exposure of these two runs is 256.6 kty. These two files have all the neutrinos changed to ν_τ. This is equivalent to a exposure of 231 kty fiducial. A total of 1102 events pass these requirements. However, this includes NC events. These NC events should be same independent of what type of neutrinos causes them. The number of CC ν_τ events is only 213, which gives an estimated flux of 0.92 ± 0.13 evts/kty (95% CL) after the filter is applied but before neutrino selection cuts are applied. The zero shower sample has only 8 CC events while the single shower sample has 205 events. See table 6.14 and 6.15.

The conclusion from this is that the oscillated ν_τ background is small as expected. In any realistic situation the number of ν_τ is actually smaller because as mentioned before every ν_μ does not oscillate into a ν_τ. Thus these number really should be taken as upper limits. These number are also an upper limit because the ν_e also oscillated to ν_τ instead of only the ν_μ. Given that there are about 2 ν_μ to each ν_e, this means that only about $\frac{2}{3}$ of these events are physical. Thus two estimates are given, a limit which is a worse case situation and more a reasonable estimate. For the no shower

Number of events	Cut Number	Events per kty
8	No cut	$0.03^{+0.04}_{-0.02}$
8	1	$0.03^{+0.04}_{-0.02}$
7	2	$0.03^{+0.03}_{-0.02}$
7	3	$0.03^{+0.03}_{-0.02}$
7	4	$0.03^{+0.03}_{-0.02}$
5	5	$0.03^{+0.03}_{-0.02}$
5	6	$0.03^{+0.03}_{-0.02}$
4	7	$0.02^{+0.03}_{-0.01}$
4	8	$0.02^{+0.03}_{-0.01}$
4	9	$0.02^{+0.03}_{-0.01}$

Table 6.14: This table shows the effects of different tracking cuts on the oscillated ν_τ background with zero shower. The errors shown are only statistical (95% CL). The total number of events is based on a 232 kty exposure for all the cuts up to cut 4, after cut the exposure is 193 kty.

events the background limit is ≤ 0.05 evts/kty (95% CL). For the single shower events the background limit is 0.17 ± 0.06 evts/kty (95% CL). If we make the assumption about the relative number of ν_e to ν_τ and assume that less than half of the ν_μ neutrino oscillate which is consistent as the sample is not going to be fully oscillated, a more reasonable is then ≤ 0.02 (95% CL) evts/kty for zero showers and 0.06 ± 0.02 evts/kty (95% CL) for one shower. In either case it is small compared to other backgrounds.

Number of events	Cut Number	Events per kty
205	No cut	0.88 ± 0.12
199	1	0.86 ± 0.12
191	2	0.82 ± 0.12
103	3	0.44 ± 0.09
92	4	0.40 ± 0.08
72	5	0.37 ± 0.09
71	6	0.37 ± 0.09
37	7	0.19 ± 0.06
35	8	0.18 ± 0.06
33	9	0.17 ± 0.06

Table 6.15: This table shows the effects of different tracking cuts on the ν_τ background with one shower. The errors shown are only statistical (95% CL).The total number of events is based on a 232 kty exposure for all the cuts up to cut 4, after cut 4 the exposure is 193 kty.

6.5.4 NC events

The NC background comes from all three flavors of neutrinos and is thus independent of the actual oscillation parameters, the NC events will produce a background. Like the previous two backrounds studied this is a irreducible background. More concerning is that $\pi^{\pm}$ will look like track in the far detector. In the case of a quasi-elastic scattering, the recoil proton can also look like a track. This latter situation is probably the most difficult if not impossible background to remove. See table 6.16 and 6.17.

Number of events	Cut Number	Events per kty
36	No cut	0.07 ± 0.02
34	1	0.07 ± 0.02
34	2	0.07 ± 0.02
34	3	0.07 ± 0.02
32	4	0.07 ± 0.02
28	5	0.07 ± 0.03
28	6	0.07 ± 0.03
21	7	0.05 ± 0.02
12	8	0.03 ± 0.02
12	9	0.03 ± 0.02

Table 6.16: This table shows the effects of different tracking cuts on the NC background for all neutrinos flavors with zero shower. The errors shown are only statistical (95% CL). The total number of events is based on a 492 kty exposure for all the cuts up to cut 4, after cut the exposure is 410 kty.

This is a small background as expected.

Number of events	Cut Number	Events per kty
492	No cut	1.00 ± 0.09
477	1	0.97 ± 0.09
469	2	0.95 ± 0.09
259	3	0.53 ± 0.06
228	4	0.46 ± 0.06
183	5	0.45 ± 0.06
179	6	0.44 ± 0.06
90	7	0.22 ± 0.05
41	8	0.10 ± 0.03
41	9	0.10 ± 0.03

Table 6.17: This table shows the effects of different tracking cuts on the NC background from all flavors of neutrinos with one shower. The errors shown are only statistical (95% CL).The total number of events is based on a 492 kty exposure for all the cuts up to cut 4, after cut 4 the exposure is 410 kty.

6.5.5 Neutron background

The neutrons from cosmic ray muons are a possible background for atmospheric neutrinos. These neutrons are produced when a muon interacts in the last few meters of rock around the detector a makes one or more neutrons. If the the muon that makes the neutron is observed in the detector the event can be easily vetoed.

However, sometimes the muon can miss the detector and the neutron hit the detector. This can cause a hadronic shower. Since this the purpose of this analysis is to look for muon tracks which can have there charge identified, conventional wisdom is that this should be a small background.

A nice and detailed study on the neutron background[131] was carried out. The results shown here are based on it. The neutron background was simulated by having cosmic ray muons interact in a rock 'box' around the detector. The muons were allowed to undergo all the relevant physical processes, these particles were tracked using GEANT4 with GHEISA for nuclear interactions. Events were sent to a more detailed detector simulation if there was at least 1 neutron with 100+ MeV. In total 330,000,000 muons were simulated which is a 4.7 live year exposure. Only 83803 of these events were passed to the detailed detector simulation of which only 39225 passed the trigger and reconstructed at least one track or one shower. See table 6.18 and 6.19.

After the cuts to remove the cosmic ray background this gets even smaller. The single event in the no shower shower sample is eliminated and fails multiple cuts (bad tracking, low pulse height fraction). The one shower sample also undergoes a large reduction in number of events. Only one event of the 44 remains. It has poorly reconstructed momentum and would clearly fail the charge ID requirements.

The conclusion of this is that the total background is ≤ 0.66 neutrons per year for no shower and $0.21^{+0.88}_{-0.21}$ single shower events per year (95% CL). The no shower case has a lower background which is MC statistics limited. All of this analysis has been done without application of the vetoshield. Because the vetoshield is not modeled in the

Number of events	Applied Cut	Events per year
83803	Tracked	17830 ± 125
39225	Reconstructed	8346 ± 83
25597	Single track	5446 ± 68
19895	1 track, 1 shower	4233 ± 59
1634	1 track, 0 shower	348 ± 17
44	Filtered 1 track, 1 shower	9.4 ± 2.8
1	Filtered 1 track, 0 shower	$0.21^{+0.88}_{-0.20}$

Table 6.18: This table shows the effects of different cuts on the neutron background. It should be pointed out that the filtered cuts are the starting point for event selection, not the end. The errors shown are only statistical (95% CL). The total number of events is based on a 4.7 live year exposure. The number of 'Tracked' events is the number of events that underwent full simulation. The number of 'Reconstructed' events is simply the number of events which passed the trigger and had at least one shower or one track. Even before the cuts to remove cosmic ray background, the neutron background is small.

detector MC, the effectiveness of the vetoshield in rejecting these events is not known. It is certainly possible that these high energy showers will trigger the vetoshield and thus reduce the background even more. However, given the smallness of this background, work on other backgrounds make more sense.

Number of events	Cut Number	Events per year
44	No cut	9.4 ± 2.8
42	1	8.9 ± 2.7
21	2	4.5 ± 1.9
14	3	3.0 ± 1.6
12	4	2.6 ± 1.5
1	5	$0.21^{+0.88}_{-0.20}$
1	6	$0.21^{+0.88}_{-0.20}$
1	7	$0.21^{+0.88}_{-0.20}$
1	8	$0.21^{+0.88}_{-0.20}$
1	9	$0.21^{+0.88}_{-0.20}$

Table 6.19: This table shows the effects of different tracking cuts on the neutron background with one shower. The errors shown are only statistical (95% CL). The total number of events is based on a 4.7 live year exposure.

6.5.6 Other backgrounds

There are other backgrounds that can be imagined but they seem unlikely. For example, up going muons could be a background, they are just like the down cosmic μ, however, since they are ν process, there expected rate is similar to the simulated ν rate. Even without the vetoshield this should be small.

6.5.7 Signal and background

The sum of signal and background is the observed quantity in the detector. The signal for this purpose is defined as $\mu^{\pm}$ produced in the CC interaction from ν_μ and $\bar{\nu_\mu}$ that have not undergone oscillations (no ν_τ). The background is everything else that mimics the signal. It is obvious that these statements are dependent on several assumptions that will be made now and will be readdressed in chapter 9. The first assumption is what backgrounds will be included in the calculation. The backgrounds that will be considered are the cosmic $\mu^{\pm}$, ν_e, NC interactions from all active neutrinos, neutrons and ν_τ interactions. Another assumption is will the signal and background be calculated before or after vetoshield and will the signal and background be calculated with or without oscillations. For purposes here the signal and background will be calculated with and without oscillation. The implications of the vetoshield for this will not be dealt with until chapter 9. The final assumption that will be made is of the exposure. An exposure of 5.0 kTy will be assumed. The exposure is actually important as the uncertainty in the counting statistics are almost alway larger the uncertainties from the MC acceptance[6]. See table 6.20.

[6]For example if a process was expected to have a rate of 7 ± 0.7 events per kTy for an exposure of 7.0 kTy the expected rate would be $49.0 \pm 7.0(stat.) \pm 4.9(syst.)$, where the the statistical uncertainty is just counting statstics on 49 expected events and the systematic uncertainty is the uncertainty on the expected number of events from the MC

Cut #	ν_μ	$\bar{\nu_\mu}$	Bkg. ν	Total ν	Cosmic-μ MC	Exp. Evts.
No Cut	98.2	33.8	16.9	148.9±25.4	70,000±7,000	70,150±7,000
1	96.5	33.2	16.4	146.1±25.0	66,900±6,700	67,050±6,700
2	92.3	31.3	16.1	139.7±24.1	12,790±1,290	12,930±1,290
3	71.9	25.2	8.2	105.4±18.8	7,390±750	7,500±750
4	62.0	21.3	7.6	90.9±16.6	3,715±380	3,810±380
5	61.3	20.4	7.6	89.3±16.4	2,088±220	2,177±221
6	60.1	19.9	7.5	87.5±16.1	1,175±128	1,263±129
7	46.4	15.8	3.5	65.7±12.8	157.5±24.6	223.2±27.7
8	38.5	14.1	1.7	54.3±11.0	139.5±22.6	193.8±25.1
9	35.9	13.2	1.5	50.7±10.4	38.3±10.0	89.0±14.4

Table 6.20: In this table the neutrinos are normalized to an unoscillated 5.0 kTy exposure. The neutrinos are from R179 and R180. This file assumes solar maximum and a Barr flux model. The errors shown are the quadrature sum of systematic and statistical errors. The neutrinos are assumed to have a 15% systematic uncertainty and the cosmic MC μ are assumed to have 10% systematic uncertainty. The background ν are non CC-ν_μ,$\bar{\nu_\mu}$ events that pass the selection. This does not include oscillated ν_τ. The cut number is the same as the cut selection shown in chapter 6. The MC shows zero and one shower events together and this is all before any vetoshield cut is applied. The normalization is explained later in chapter 6.8.

6.6 Systematic Errors-Neutrino MC

In the preceding sections the simulations have been carried out with a variety of assumptions about the physics models. An important question is how much does a change in these models change the physics results. Several possible variations in the neutrino MC are considered in this section to see what if any change happens in the selection of neutrinos. For references to systematics in the MINOS FD see [136] and for information on the MC, see Appendix F.

6.6.1 Particle tracking energies

In the previous MC files the particles were tracked until the particle energy went down to 100 KeV. A possible systematic error could be caused by this. To see what the effect of the this is, the tracking cuts were ran on a sample of MC that tracked particles down to 10 KeV. Everything thing else in the simulation was the same. These results are based on Run 184 and Run 185. The exposure is nearly exactly half of Run 179 and R180. See table 6.21 and 6.22.

Number of events	Cut Number	Events per kty	CC ν_μ	CC $\bar{\nu}_\mu$	Bkg. ν
1194	No cut	3.7 ± 0.2	934	238	22
1184	1	3.6 ± 0.2	926	236	22
1157	2	3.5 ± 0.2	903	232	22
1114	3	3.4 ± 0.2	876	216	22
1046	4	3.2 ± 0.2	822	202	22
837	5	3.1 ± 0.2	657	162	18
827	6	3.0 ± 0.2	650	159	18
784	7	2.9 ± 0.2	621	147	16
628	8	2.3 ± 0.2	489	131	8
596	9	2.2 ± 0.2	460	128	8

Table 6.21: This table shows the effects of different tracking cuts on the oscillated ν_μ background with zero shower. The errors shown are only statistical (95% CL). The total number of events is based on a 326 kty exposure for all the cuts up to cut 4, after cut the exposure is 272 kty. The files used for this R184 and R185

This suggests that the tracking cut of 100 KeV and tracking cut of 10 KeV are

Number of events	Cut Number	Events per kty	CC ν_μ	CC $\bar{\nu}_\mu$	Bkg. ν
8484	No cut	26.0 ± 0.6	5561	1900	1023
8312	1	25.5 ± 0.5	5460	1862	990
7922	2	24.3 ± 0.5	5206	1739	977
5791	3	17.8 ± 0.5	3917	1369	505
4986	4	15.3 ± 0.4	3326	1186	474
4045	5	14.9 ± 0.5	2703	942	400
3948	6	14.5 ± 0.5	2641	915	392
2805	7	10.3 ± 0.4	1934	707	164
2300	8	8.5 ± 0.3	1592	643	65
2117	9	7.8 ± 0.3	1467	586	64

Table 6.22: This table shows the effects of different tracking cuts on the atmospheric neutrino sample with one shower. The errors shown are only statistical (95% CL).The total number of events is based on a 326 kty exposure for all the cuts up to cut 4, after cut 4 the exposure is 272 kty. The files used for this R184 and R185

equally good as the selections select an equal number of events to within the statistical errors in each group.

6.6.2 Hadronic interaction model

In the previous MC files the particles were generated and propagated using the GCALOR. A possible systematic error could be caused by this model. The simplelest way to test this hypothesis is to use a different model. The so called SLAC-GHEISA model will be used for comparison. Everything thing else in the simulation was the same. These results are based on Run 183. The exposure is nearly exactly half of Run 179 and R180. See tables 6.23 and 6.24.

Number of events	Cut Number	Events per kty	CC ν_μ	CC $\bar{\nu}_\mu$	Bkg. ν
1346	No cut	4.1 ± 0.2	1023	289	34
1329	1	4.1 ± 0.2	1014	282	33
1310	2	4.0 ± 0.2	1002	275	33
1252	3	3.8 ± 0.2	957	265	30
1168	4	3.6 ± 0.2	893	246	29
960	5	3.5 ± 0.2	723	210	27
948	6	3.5 ± 0.2	713	208	27
891	7	3.3 ± 0.2	683	188	20
730	8	2.7 ± 0.2	552	167	11
687	9	2.5 ± 0.2	521	155	11

Table 6.23: This table shows the effects of different tracking cuts on the oscillated ν_μ background with zero shower. The errors shown are only statistical (95% CL). The total number of events is based on a 326 kty exposure for all the cuts up to cut 4, after cut the exposure is 272 kTy. The files used for this R184 and R185.

This suggests that the event selection is not sensitive to the hadronic interaction model.

Number of events	Cut Number	Events per kty	CC ν_μ	CC $\bar{\nu}_\mu$	Bkg. ν
8246	No cut	25.3 ± 0.5	5420	1836	990
8080	1	24.8 ± 0.5	5333	1796	951
7703	2	23.6 ± 0.5	5086	1688	929
5605	3	17.2 ± 0.5	3816	1297	492
4754	4	14.6 ± 0.4	3211	1085	458
3826	5	14.1 ± 0.4	2590	866	370
3738	6	13.7 ± 0.4	2526	848	364
2645	7	9.7 ± 0.4	1834	652	159
2185	8	8.0 ± 0.3	1534	582	69
2020	9	7.4 ± 0.3	1407	545	68

Table 6.24: This table shows the effects of different tracking cuts on the atmospheric neutrino sample with one shower. The errors shown are only statistical (95% CL).The total number of events is based on a 326 kty exposure for all the cuts up to cut 4, after cut 4 the exposure is 272 kty. The files used for this R184 and R185

6.6.3 Atmospheric neutrino flux model

In the previous MC files the neutrino flux model was the Barr0403i solar max model. A possible systematic error could be caused by this model. The simplelest way to test this hypothesis is to use a different model. The Battistoni solar max model is used for this comparison. These results are based on Run 186. See tables 6.25 and 6.26.

Number of events	Cut Number	Events per kty	CC ν_μ	CC $\bar{\nu}_\mu$	Bkg. ν
807	No cut	3.5 ± 0.2	624	164	19
800	1	3.4 ± 0.2	620	161	19
786	2	3.4 ± 0.2	610	157	19
762	3	3.3 ± 0.2	592	152	18
724	4	3.1 ± 0.2	563	143	18
575	5	3.0 ± 0.2	444	116	15
571	6	2.9 ± 0.2	441	115	15
540	7	2.8 ± 0.2	424	104	12
440	8	2.3 ± 0.2	338	96	6
423	9	2.2 ± 0.2	326	91	6

Table 6.25: This table shows the effects of a different flux model on the unoscillated ν_μ events with zero shower. The errors shown are only statistical (95% CL). The total number of events is based on a 233 kty exposure for all the cuts up to cut 4, after cut the exposure is 194 kTy. The files used for this R186.

Number of events	Cut Number	Events per kty	CC ν_μ	CC $\bar{\nu}_\mu$	Bkg. ν
5600	No cut	24.0 ± 0.6	3740	1180	680
5479	1	23.5 ± 0.6	3662	1157	660
5268	2	22.6 ± 0.6	3507	1106	655
3886	3	16.7 ± 0.5	2646	875	365
3359	4	14.4 ± 0.5	2257	761	341
2711	5	14.0 ± 0.5	1809	615	287
2666	6	13.7 ± 0.5	1776	604	286
1926	7	9.9 ± 0.4	1305	480	141
1559	8	8.0 ± 0.4	1075	428	56
1444	9	7.4 ± 0.4	991	399	54

Table 6.26: This table shows the effects of a different flux model on unoscillated ν_μ events with one shower. The errors shown are only statistical (95% CL).The total number of events is based on a 233 kty exposure for all the cuts up to cut 4, after cut 4 the exposure is 194 kty. The files used for this R186

The conclusion from this study is that none of these obvious candidate systematics change the event selection. This is not to say there are no systematics. This study suggests that the event selection is not strongly dependent on the neutrino model used. The systematic uncertainity and what value shall be assigned for the systematic uncertainity will be addressed in later sections of chapter 6 and in chapter 9. The value which will be quoted for the total uncertainity in ν rate is 15%.

6.7 Control Sample: Stopping Muons

Stopping muons provide an important control sample for the atmospheric neutrinos sample. This control studies allows a verification that the tracking software is performing in an expected manner. Although stopping muons and atmospheric are different event types, they are similar enough that this comparison is worthwhile.

6.7.1 Why Stopping Muons?

The stopping muons are defined to be muons that enter the detector from the outside and range out inside the detector. Almost all of them are produced in cosmic ray showers. A tiny fraction are neutrino induced rock muons. Given the fact that they are low energy, these muons are the subsample of cosmic muons most like the muons from atmospheric neutrinos.

However, they are many times more plentiful, this allows comparisons to done with higher statistics. This is not an ideal comparison as the comparison is really only valid between the track of the stopping muon and the track of the ν_μ induced muon. The comparison does not hold as well for the showers. Given that the analysis is much more dependent on track properties than on shower properties this is relatively small penalty to pay.

6.7.2 Selection of stopping muons

The selection criterion for stopping muons are similar when compared to atmospheric neutrino candidates. In fact the selection is identical except with the exception of the radial cuts. For a stopping muon the track must begin and end with radial coordinates of $r \geq 0.35$m and the track must either have a vertex at $r \geq 3.90$m and a track end at $r \leq 3.30$m or the case with vertex and end reversed. This is the post filter dataset. There is also the final dataset. The final stopping muons are the subset that pass all the

same cuts the candidate atmospheric neutrinos pass except the cut on the track vertex and track end in the radial direction is the same cut applied in the filter for stopping muons.

6.7.3 Comparison of stopping muons: Reconstruction to truth

If the stopping muons are to used as a control sample, it should be clear that these events are behaving in an understood way. To this goal the reconstructed muon can have the reconstructed quantities compared to the truth value for these quantities. This is done in figures 6.7, 6.8 and 6.9.

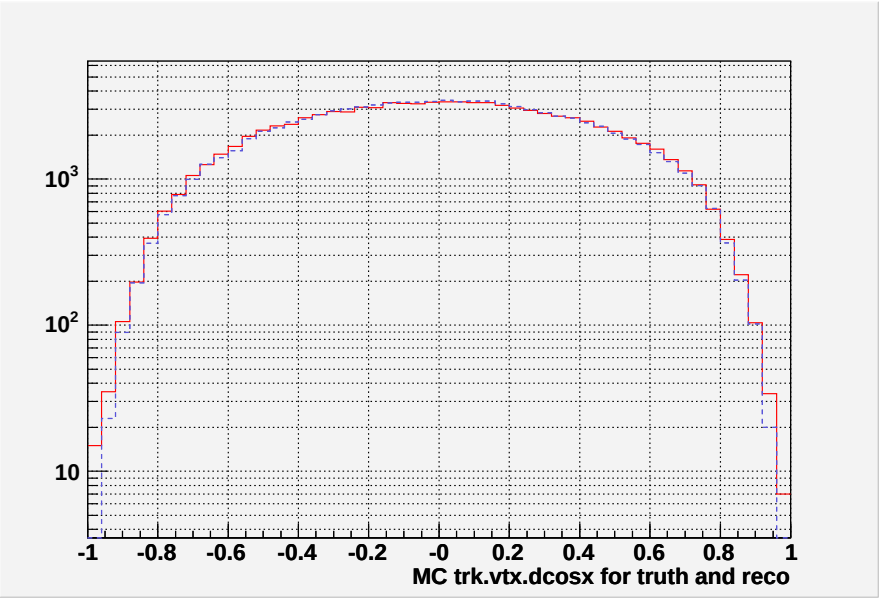

Figure 6.7: This shows the true directional cosine of the track in the x direction as the dashed line and the reconstructed directional cosine of the track at the vertex in the solid line. The agreement is nearly perfect.

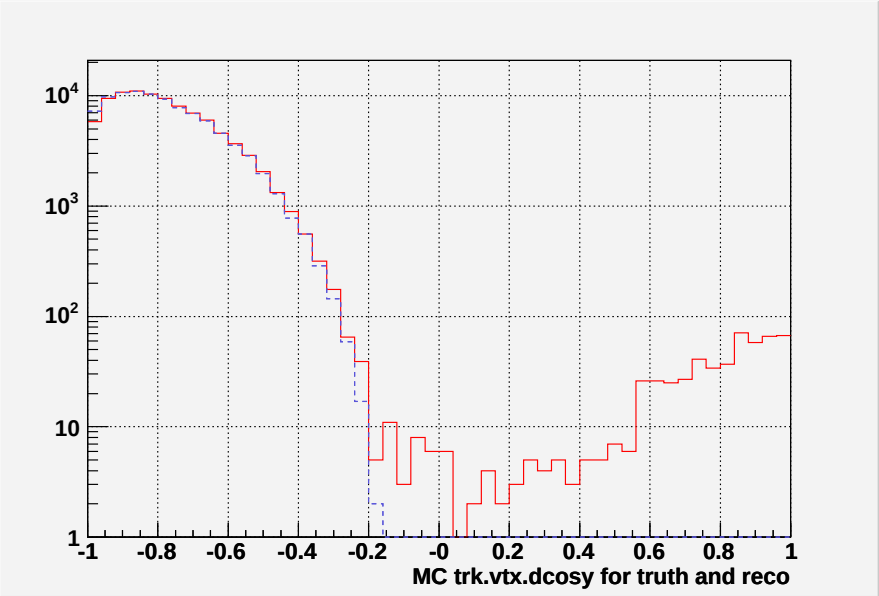

Figure 6.8: This shows the true directional cosine of the track in the y direction as the dashed line and the reconstructed directional cosine of the track at the vertex in the solid line. The agreement is good. The events in the tail appear to be coming up instead of down.

6.7.4 Comparison of stopping muons: Reconstructed MC to data

The topic of how well the reconstructed MC agrees to the data is discussed at great length in appendix D, so comment here will be brief. The comparsion is shown in figure 6.10, 6.11 and 6.12 for events after they pass the initial data filtering but before the (final) tracking cuts are applied. Zero and single shower events are combinded and plotted together. The data does not have any special data QA cuts applied, for details see appendix D. The agreement is extremely good and no major problems are observed.

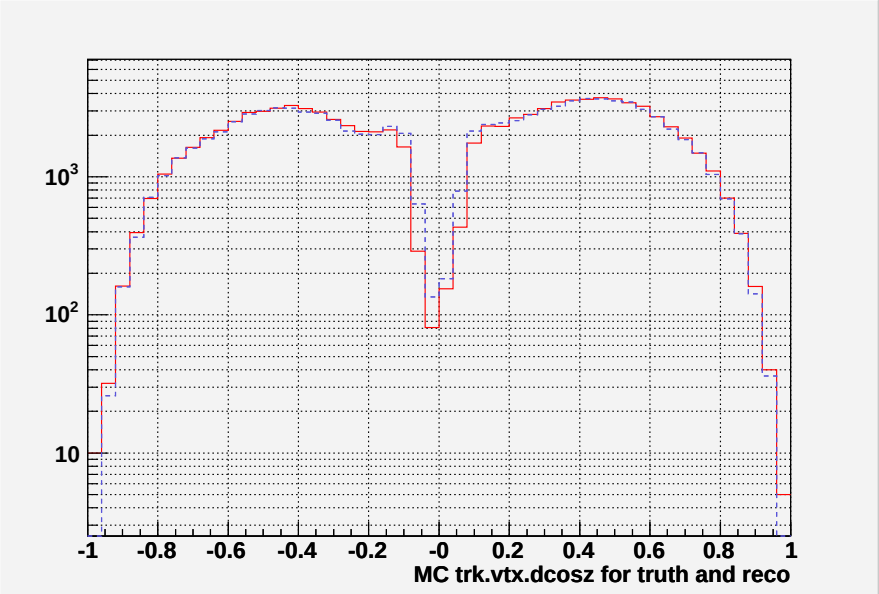

Figure 6.9: This shows the true directional cosine of the track in the z direction as the dashed line and the reconstructed directional cosine of the track at the vertex in the solid line. The agreement is nearly perfect. Compare this to the similar plot for the cosmic ray background events. The agreement is much better.

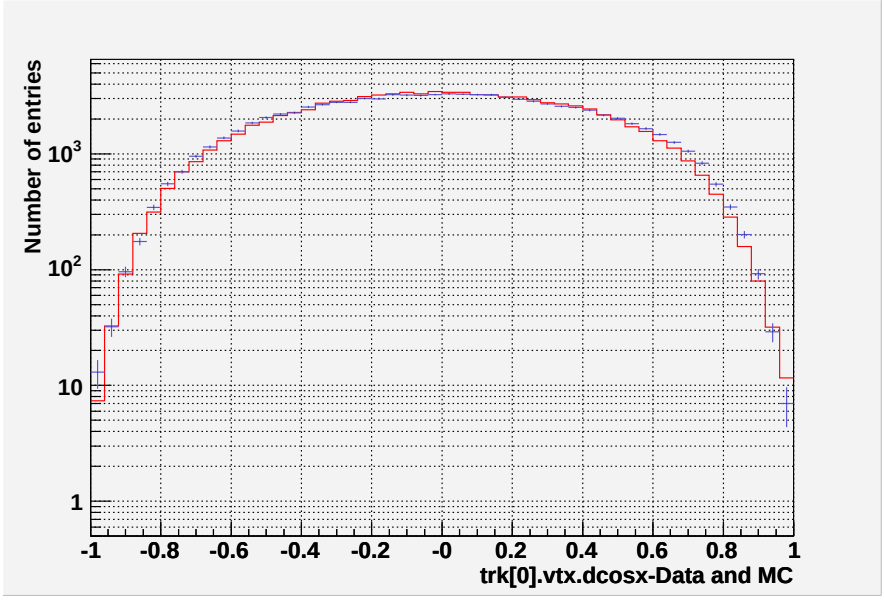

Figure 6.10: The directional cosine in the x direction at the track vertex for data and MC is shown. The agreement is nearly perfect. This shows data in red and MC in blue with error bars. The error bars are 1σ. The data is normalized by area down to the MC sample.

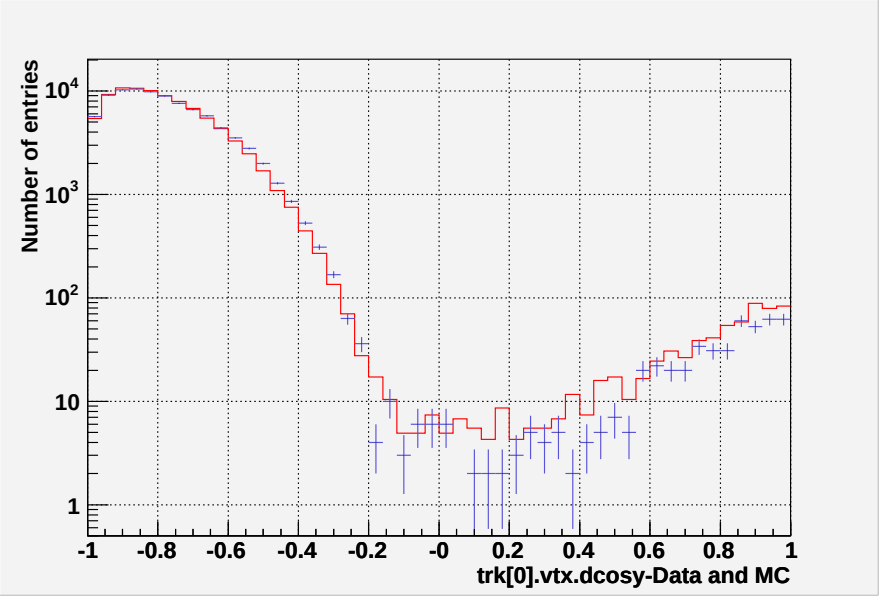

Figure 6.11: The directional cosine in the y direction at the track vertex for data and MC is shown. The agreement is good. The positive values of this are events that the software reconstruct going up. The MC has only down going events. This shows that the reconstruction error are being reproduced reasonably well in the MC. This shows data in red and MC in blue with error bars. The error bars are 1σ. The data is normalized by area down to the MC sample.

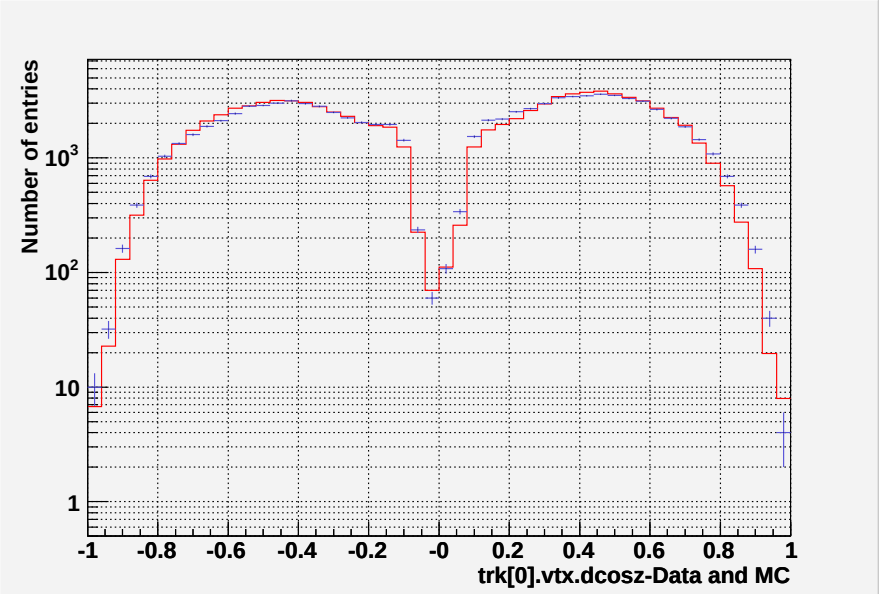

Figure 6.12: The directional cosine in the z direction at the track vertex for data and MC is shown. The agreement is pretty good. This shows data in red and MC in blue with error bars. The error bars are 1σ. The data is normalized by area down to the MC sample.

6.7.5 Comparison of charge ID

The use of stopping muons to check the charge ID is important as the stopping muons have a similar energy to the muons produced by ν_μ and $\bar{\nu}_\mu$. The comparison is not perfect as the fully contained sample cross the outer 0.5 m of the detector where the magnetic field is weaker than the inner region of the detector. However, this is still the most similar sample with any significant statistics. The question of charge ID comparison can be thought of two separate questions with regard to the stopping muons. The first question is does the stopping muon charge ID agree between data and MC. The second question is does charge ID from MC agree with the truth values.

With this all being said, the stopping muons should have nearly perfect charge ID as they tend to be longer on average and do not have hadronic interactions at an event vertex to confuse matters. This means that the charge ID should be 'as good as it gets' for any cosmic event. To study the reconstructed charge ID, the MC data to truth comparison is examined. This is done using two datasets, the post filter stopping dataset and final selection stopping dataset. This comparison will be done for all events in these samples and for a subset of events with a minor charge ID requirement made $\frac{|\sigma_{(q/p)}|}{|(q/p)|} \leq 2.0$. The MC is the standard cosmic MC sample (r651-r778). The fraction is defined in the same manner it was defined previously. Tables 6.27, 6.28, 6.29 and 6.30 contain information about the charge ID on different samples of stopping muons. Table 6.31 lists the charge ID efficency. Table 6.32 has the charge ratio. Table 6.33 and 6.34 look at charge ID variation with momentum.

Post filter dataset charge ID-all events

The post filter dataset shows good charge ID. This suggests that even before the selection cuts are applied the events the have enough curvature on average such that the charge ID can be measured.

μ^+	R-ID	W-ID	Fraction	μ^-	R-ID	W-ID	Fraction
6830	6610	220	0.968 ± 0.002	5814	5592	212	0.962 ± 0.002
43214	40629	2585	0.940 ± 0.001	34721	32734	1987	0.943 ± 0.001

Table 6.27: This shows the charge identification for stopping muons that pass the post filter requirements of stopping muons. The first line is no shower events and the second line is one shower events. R-ID means the event has the right (correct) charge ID and W-ID means the event has the wrong charge ID. The data is the standard r651-r778 MC. The charge ID is done by comparing reconstructed charge sign to the truth charge sign. The fraction shown has a 1 σ statistical uncertainty. No special charge cuts are made. This shows that charge ID for $\mu^{\pm}$ is consistant and the zero shower case has slightly better charge ID.

Post filter charge ID-selected

The high resolution sample is defined to have nearly perfect charge ID. This is obtained by requiring the event to pass the charge ID cut for stopping muons.

μ^+	R-ID	W-ID	Fraction	μ^-	R-ID	W-ID	Fraction
6754	6563	191	0.972 ± 0.002	5735	5558	177	0.969 ± 0.002
42113	40002	2111	0.950 ± 0.001	33936	32263	1673	0.950 ± 0.001

Table 6.28: This shows the charge identification for stopping muons that pass the post filter requirements of stopping muons with a charge ID requirement. The first line is no shower events and the second line is one shower events. R-ID means the event has the right (correct) charge ID and W-ID means the event has the wrong charge ID. The data is the standard r651-r778 MC. The charge ID is done by comparing reconstructed charge sign to the truth charge sign. The fraction shown has a 1 σ statistical uncertainty. The charge ID requirement is the weakest possible requirement used for the analysis $\frac{|\sigma_{(q/p)}|}{|(q/p)|} \leq 2.0$. This shows that charge ID for $\mu^{\pm}$ is consistant and the zero shower case has slightly better charge ID.

These results for the post filter requirement suggests that the charge ID has no evidence of reconstruction bias and that the events without showers do slightly better on average. It should be pointed out that the tracks in the neutrino analysis are not charge ID at this stage but after the candidates undergo the final analysis. Thus to compare the charge ID on (almost) the identical cuts, the smaller (but better reconstructed) final cuts must be used.

Final dataset charge ID-all events

The post filter dataset already shows good charge ID without further requirements.

μ^+	R-ID	W-ID	Fraction	μ^-	R-ID	W-ID	Fraction
990	987	3	0.997 ± 0.002	766	760	6	0.992 ± 0.003
2616	2589	27	0.990 ± 0.002	1867	1851	16	0.991 ± 0.002

Table 6.29: This shows the charge identification for stopping muons that pass the final requirements of stopping muons. The first line is no shower events and the second line is one shower events. R-ID means the event has the right (correct) charge ID and W-ID means the event has the wrong charge ID. The data is the standard r651-r778 MC. The charge ID is done by comparing reconstructed charge sign to the truth charge sign. The fraction shown has a 1 σ statistical uncertainty. No special charge cuts are made. This shows that charge ID for $\mu^{\pm}$ is consistant and the zero shower case has slightly better charge ID.

Final charge ID-selected

The high resolution sample is defined to have nearly perfect charge ID. This is obtained by requiring the event to pass the charge ID cut for stopping muons.

μ^+	R-ID	W-ID	Fraction	μ^-	R-ID	W-ID	Fraction
988	987	1	0.999 ± 0.001	764	758	6	0.992 ± 0.003
2609	2587	22	0.992 ± 0.002	1863	1849	14	0.993 ± 0.002

Table 6.30: This shows the charge identification for stopping muons that pass the final requirements of stopping muons with a charge ID requirement. The first line is no shower events and the second line is one shower events. R-ID means the event has the right (correct) charge ID and W-ID means the event has the wrong charge ID. The data is the standard r651-r778 MC. The charge ID is done by comparing reconstructed charge sign to the truth charge sign. The fraction shown has a 1 σ statistical uncertainty. The charge ID requirement is the weakest possible requirement used for the analysis $\frac{|\sigma_{(q/p)}|}{|(q/p)|} \leq 2.0$. This shows that charge ID for $\mu^{\pm}$ is consistant

The charge ID efficiency shows the efficiency of the final selection versus the post-filter selection. The fundamental question this addresses is do μ^+ and μ^- have the same chance of being accepted into the dataset. Since, the final dataset is already known to reconstruct all events that make into the set with high accuracy the question must

be both charge sign of events make it into the set with equal probability. The answer is no. The μ^+ get accepted at a slightly higher (but statistically significant) rate than μ^-. This was done by comparing the truth charge sign for events in the post filter and final set. This was done for both for events that passed and failed the charge ID cut (although as already shown nearly events pass the charge ID cut, so these two samples are highly correlated). The zero shower events show a bias but it is not statistically significant. The single shower events show a bias at well over 3σ. The bias appears to be on the order of 10 %. It is unclear of what physical mechanism should cause this.

Charge ID efficiency

Number of showers	Charge ID	μ^+ Eff.	μ^- Eff.
0	No	0.145 ± 0.004	0.132 ± 0.004
1	No	0.061 ± 0.001	0.054 ± 0.001
0	Yes	0.146 ± 0.004	0.133 ± 0.004
1	Yes	0.062 ± 0.001	0.055 ± 0.001

Table 6.31: This show the selection efficiency for a $\mu^\pm$ in the post filter being selected in the final selection. The efficiency is defined as $\eta = \frac{S}{S+U}$ where S is selected events and U is unselected events. Since, the final selection is designed to select tracklike events the results are not that surprising. The events with and without charge ID are obviously correlated in that the latter is nearly the entire subset of the former. The difference is charge ID for positive and negative charged events is not expected.

The selection bias with the stopping muons causes a bias in the charge ratio. This is simply because the μ^+ have a higher chance of being accepted so the charge ratio is high. The charge ratio is high by an amount consistent with the selection efficiency. It should be noted the charge ratio and the efficiency are calculated using the same data so they should be consistent.

Charge Ratio

The charge ratio is shown in table 6.32. The charge ratio does appear to change with the cuts but since the ratio is put into the MC by hand the meaning of this for the MC

is unclear.

Sample	# of showers	Charge ID	True Charge $\frac{\mu^+}{\mu^-}$	Observ. Charge $\frac{\mu^+}{\mu^-}$
Post Filter	0	No	1.18	1.17
Post Filter	1	No	1.25	1.21
Post Filter	0	Yes	1.18	1.14
Post Filter	1	Yes	1.24	1.21
Final	0	No	1.29	1.30
Final	1	No	1.40	1.39
Final	0	Yes	1.29	1.31
Final	1	Yes	1.40	1.39

Table 6.32: The MC has an inputed charge ratio of 1.25. These results several things. First the observed and true charge ratio for single shower events in higher than it is for no shower events. Secondarily, this suggests that the final cuts seem to raise the measured and true charge ratio. Thirdly, the measured and true charge ratio agree well. The events with and without the charge ID requirement are clearly correlated. The change in the charge ratio with the final cut is explained by the different charge ID efficiencies.

Charge ID:Variation with momentum

The charge ID is in general a function of momentum. If the momentum is too low the event will cross few planes and have a poor reconstruction. If the muon has too high of a momentum it will not curve in the field. To study this with the stopping muons, muons will be binned in there truth momentum. Only the final selection with charge ID applied will be considered as this is the set of data which is closest to the fully contained sample.

Charge Ratio:Data to MC

After the detailed study of charge ID using the MC truth and MC reconstructed data it must now be compared to the data. The value of this comparison is somewhat limited as the physical charge ratio could be different than the simulated charge ratio which is

True Momentum	μ^+	Right ID	Wrong ID	μ^-	Right ID	Wrong ID
0-1 GeV	21	21	21	12	11	1
1-2 GeV	251	250	1	194	192	2
2-3 GeV	232	232	0	172	171	1
3-4 GeV	140	140	0	95	94	1
4-5 GeV	123	123	0	109	109	0
5-6 GeV	127	127	0	105	105	0
6-7 GeV	62	62	0	50	50	0
7+ GeV	32	32	0	27	26	1

Table 6.33: This shows the change in charge ID efficiency as a function of the true momentum for events without showers. The momentum is the true momentum and charges are the truth charge for the muon.

True Momentum	μ^+	Right ID	Wrong ID	μ^-	Right ID	Wrong ID
0-1 GeV	54	51	3	23	21	2
1-2 GeV	642	630	12	396	389	7
2-3 GeV	650	647	3	397	394	3
3-4 GeV	373	372	1	247	247	0
4-5 GeV	291	290	1	257	256	1
5-6 GeV	334	333	1	322	322	0
6-7 GeV	173	172	1	157	156	1
7+ GeV	92	92	0	64	64	0

Table 6.34: This shows the change in charge ID efficiency as a function of the true momentum for events with a single shower. The momentum is the true momentum and charges are the truth charge for the muon.

put in by hand and is not a 'physical result' of the simulation[7]. The measured charge ratio for the MC is[8]: 1.367 ± 0.035 and 1.374 ± 0.028 for the data for the 'final' subset. This topic is complex, see Beall[134] for more details.

6.7.6 Forward versus reverse field

All the MC has been processed with a forward field. The data has a mixture of forward and reverse field. For the first part of the data sample the magnetic field was in the

[7]On the other hand if the simulated charge ratio was the result a full airshower simulation this conclusion could be different

[8]No systematics are assumed here, only statistical error

forward direction[9] until the summer of 2004 when it was reversed. The field is reversed for run 25768 and after. To see the result of the reversal of the magnetic field on the data the stopping muon set was broken into data that was ran with the forward field and data that was ran with the reverse field. The greatest fear is that the charge ID will depend on the field direction which of course it should not. There is no evidence of this seen in the data. This can be observed by looking at figures 6.13 and 6.14. The forward and reverse field data show that the charge ID is same for the forward and reverse field. There are 82,504 stopping muons with forward field and 65,074 stopping muons with reverse field.

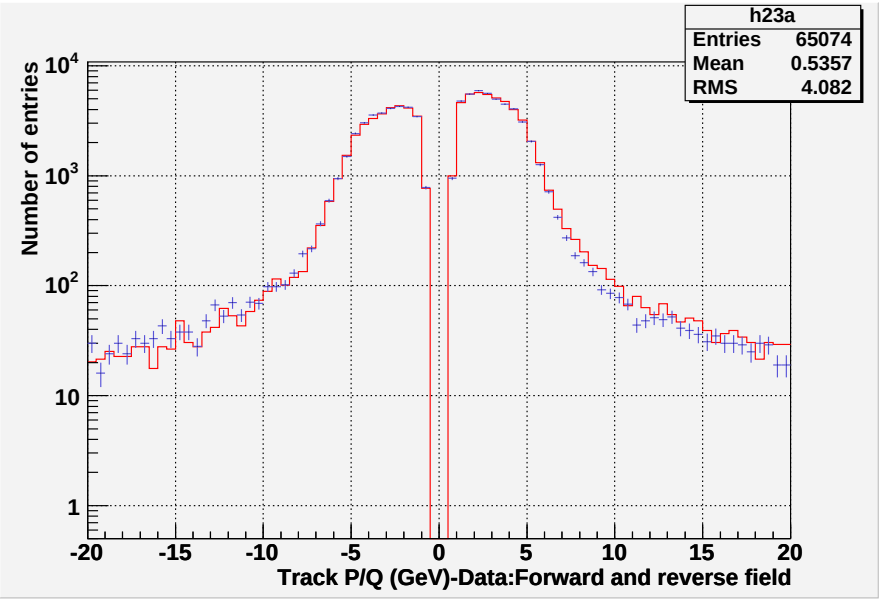

Figure 6.13: The fit track momentum (inverse of $\frac{q}{p}$) is shown for data with forward and reversed magnetic fields. There is excellent agreement. This is before any cuts to improve the charge reconstruction ID. This shows reverse data in red and forward data in blue with error bars. The error bars are 1σ. The reverse is normalized by area up to the MC sample.

[9]The forward field is defined to be the direction that will bend negatively charged particles inwards when coming from FNAL

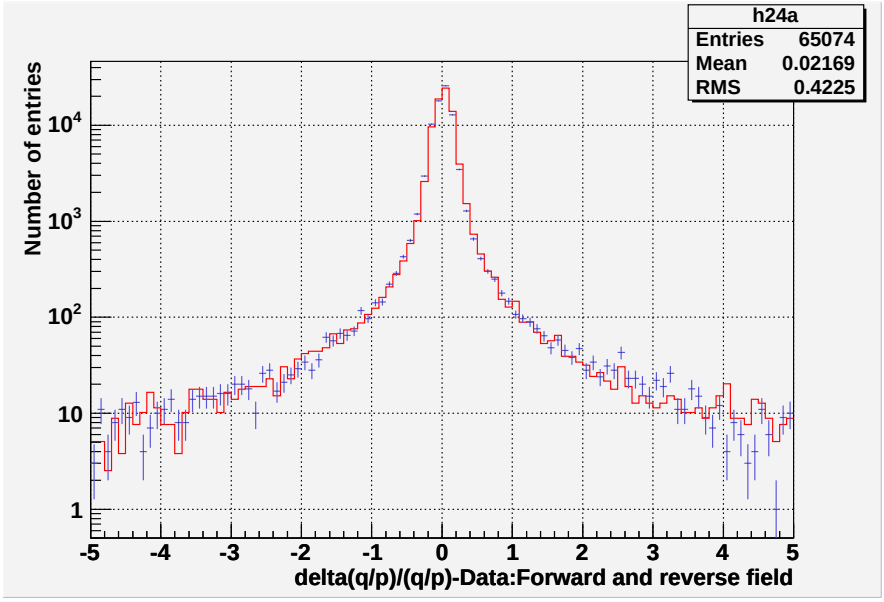

Figure 6.14: This shows the uncertainty in fit track momentum for data and MC. This is pretty good agreement. This shows reverse data in red and forward data in blue with error bars. The error bars are 1σ. The reverse data is normalized by area up to the forward data sample.

6.8 Normalization

The normalization of data to the Monte Carlo is not a simple exercise. This is in part caused by the fact that there is not just one normalization but several normalizations that must be carried out. The most important normalizations are the absolute normalization of the atmospheric neutrino flux and the normalization of the cosmic ray rate MC to data. The first of these is difficult for multiple reasons explained below, the latter seems like it should be simple, however, this is incorrect.

6.8.1 Absolute atmospheric neutrino flux normalization

This normalization unlike the other normalization discussed in this thesis must be done almost exclusively on MC. A good cross check of the atmospheric neutrino normalization could in principle be based on a comparison of atmospheric ν_e neutrinos (which do not oscillate) to the ν_μ. This is not really possible for MINOS as the atmospheric ν_e can not be extracted[10]. The total uncertainity of the neutrino rate will given a 15% uncertainity. As discussed in chapter 5 there is an disagreement as to what uncertainity is reasonable. This value is not an extreme value as it is near the middle of the estimates.

6.8.2 Cosmic ray flux data to MC normalization

Since there are so many muons this normalization seems that it should be straight forward. The importance of the normalization is in estimating the cosmic ray background correctly. Since, the shield is significant (especially for the one shower sample), a good estimate of this is needed. It should be pointed out that this is really two normalizations. The first normalization is simply the relative cosmic ray flux in the data versus the MC. After this is done another normalization must be done between cosmic ray

[10]This is to say the events cannot be extracted using the current analysis. Although, challenging given the topology of the events and the thick steel of the detector, it is possible that the ν_e signature could be detected by other analysis designed from the outset to look for them. However, even in this situation the question of whether this result is competitive with the uncertainties from MC is less clear.

data and detector livetime. As is shown in this section, a understood normalization can be determined and this give confidence in the both the cut selection and the eventual ability to estimate the cosmic μ background.

Long muon normalization

The long muon normalization is based on the idea of trying to find a set of long muons which can be used to robustly estimate the data to MC normalization. This was done by looking at well reconstructed single track muons. In particular all the single tracks were required to have 90 percent of the tracks planes be tracklike. The three length that were examined were (a) 31-50, (b)51-70 and (c) 71-120 tracklike planes long events. These were examined in both data and MC. The MC sample used r651-r778 which is the same cosmic ray MC used for the rest of the analysis. Three ratios are defined $r_1 = \frac{a}{b}$,$r_2 = \frac{a}{c}$,$r_3 = \frac{b}{c}$. With a total number of MC events (a+b+c) over 2.2 million the results have a tiny statistical errors. The data sample this ran over was the same sample as the one used for the analysis (PreCoilHV set). Because the large amount of data, the data was sampled on every eight snarls. The three ratios are obviously correlated with each other but in the end the most robust and consistent ratio will be used. The results are in table 6.35.

Data Type	r_1	r_2	r_3	Sum of events
MC	1.2575 ± 0.0021	1.1431 ± 0.0018	0.9090 ± 0.0015	2,247,702
Data	1.2267 ± 0.0036	1.1144 ± 0.0034	0.9085 ± 0.0029	627,754

Table 6.35: This shows the comparison for the three different ratios between data and MC. The data is only sampled at $\frac{1}{8}$ to keep the sample size reasonable. Only r_3 is consistent. r_3 is also robust that it does not change with time.

The robustness can bee seen by breaking the far detector up into a set of smaller time frames. These times are all on the order of a couple of month's long. The results are shown in table 6.36.

Thus events between 51-120 tracklike planes long are used for the normalization.

ratio	0308-0309	0310-0401	0402-0405	0406-0409	0410-0501
r_1	1.216 ± 0.014	1.235 ± 0.008	1.232 ± 0.008	1.224 ± 0.008	1.220 ± 0.008
r_2	1.099 ± 0.012	1.131 ± 0.007	1.110 ± 0.007	1.109 ± 0.007	1.114 ± 0.007
r_3	0.904 ± 0.010	0.916 ± 0.006	0.901 ± 0.006	0.906 ± 0.006	0.913 ± 0.006

Table 6.36: This shows the time variation of the normalization ratios in the data. The ratio are listed in the left most column and the date of the time frame is listed as year-month. None of the three tests show variation over time.

This is done by summing the number of events between 51 and 120 tracklike planes, correction for the fact only $\frac{1}{8}$ of the data is included in the normalization. The results if this is that there is 2.25 times more data than MC. This should be compared to the stopping muon normalization. The 31-50 tracklike plane sample is not particular good agreement. However, it can be used as an estimate of the uncertainty. Using these 31-50 plane events gives an estimate of 2.20 which is only about 2 percent from the estimated value using the long muons.

Stopping Muon normalization

The stopping muon sample provides an unique possibility to understand the normalization. These events are by definition similar to the signal in all possible ways with exception of the radial position cuts. This means that these events have similar energies and come from similar angular acceptances. The one fundamental (although small) wrinkle is that this sample includes partially contained neutrino events as the cuts are symmetric around the track vertex and track end. This could be eliminated by using timing cuts, although given that the size of this is on the same order of magnitude as the fully contained events this is negligible. The complication of using stopping muons is that the MC simulations have to be nearly perfectly correct. The reason for this is that if differences exists in the energy spectrum it will show as difference in the stopper much more than the through going muons. Another way to think about is that the rock maps have to be nearly perfect in order this agree perfectly with the data.

The simplest normalization that can be done is a simple count of the number MC stopping muons versus the number data stoppers. This is easy to do as the dataset for the stopper (PreCoilHV dataset) is the same data that was used for the long muon normalization. The only complication is that only $\frac{5}{7}$ of the stopper data is used. The number of stopper with 1 or less shower is 90569 in the MC. The number in the data 147,577. This leads to an estimate of a total of 206,608 events. This leads to an estimated normalization of 2.28, this is close to the estimate of the relative normalization using the long muons.

The stopping muons selection was identical between data and MC except only $\frac{5}{7}$ of the data was sampled. This was done by requiring the snarl number divided by 7 to have a remainder of 2 or more. This means that the number of data stopper must be multiplies by 1.4 to estimate the true number. To study the possible effects of the selections of zero shower versus one shower and to study the effects of the analysis cuts a study with stopping muons was carried out. The results are shown in table 6.37.

Sample	# of Shower	Number of MC Stop.	Number of data Stop.	N
Post filter	0	12634	23179	2.57
Post filter	1	77935	124398	2.23
Post filter	0 and 1	90569	147577	2.28
Final	0	1756	2767	2.21
Final	1	4483	7017	2.19
Final	0 and 1	6239	9784	2.20

Table 6.37: This shows different estimates for the normalization factor N. The post filter here means after the initial data filter with the exception of the radial cuts. The final sample is all the same cuts that are applied to the signal candidates except the radial cuts. As the results show the normalization is relatively independent of the number of showers. It is also almost independent of the analysis cuts.

The results of that the relative normalization of data to MC can be made using different sets of events and these results are reasonably robust to the details of the event reconstruction.

Cosmic ray flux to livetime

The cosmic ray flux can be normalized to livetime using either the long muon normalization or the stopping muon normalization. To do the long normalization, the same muons used to the MC-data normalization are used. The difference is in order to get a large enough statistical data set to have small statistical error no sampling will be used. The idea behind this is simple: count the number of events in a given time bin and then use this to estimate the rate of events and then by knowing the total count of events the total livetime can be found. However, it is more complicated in practice. A sample period in January 2005 is chosen where all long runs between 28949 and 29019 that run a full 8 hours are used. The total livetime of this dataset is 8.668 days and there was no high voltage trips and the magnetic field was in the reverse position the entire time. There was a total of 28,911 B type muons and a total of 31,542 C type muons for a total of B and C type muons of 60,453. The total data set has (with 1/8 sampling) 396,325 muons of type (B+C), correcting for the sampling, this leads to a projected 3,170,600 muons. The estimated livetime from this method is then 454.6 ± 1.8 livedays[11]. For comparison the stopping muons were compared for the same time. A total of 2705 stopping muons were observed during this time compared to 147,577 events in the total dataset. This corresponds to a livetime of 472.9 ± 9.1 days and is consistent with the value from the long muons.

6.8.3 Rebel-Mufson normalization

It would be useful to have another normalization available for a cross check. A study of comsics muons at the far detector done by B.Rebel and S.Mufson[133] potentially provides an independent cross check. However, the comparison can not be carried out as

[11] This is based on an statistical uncertainty in the number events in the un-sampled set (58,324) but not the uncertainty from the sampled set (396,325). No systematic uncertainty is assumed. Each of the 26 runs that are used to calculate to run time have run times known to within a second

directly as it might appear. The selection criteria are sufficiently different that a direct comparison is really not possible. Thus there is no easy way to verify the normalization.

6.8.4 Final normalization

The main purpose of the final normalization is two fold. First, in order to present a reproducible physics result some statement on the absolute normalization should be presented. Second the absolute normalization is needed to properly predict the number of neutrinos from the MC. For the cosmic μ background this is less important as the the relative normalization provides enough information to look at the background rejection. The estimated detector livetime from the data (before any additional data quality cuts) is: $454.5 \pm 1.8(stat.)$ livedays, where the statistical error is just from counting statistics. This can be used by the neutrino MC to give an exposure in kiloton years. An additional issue is that the detector was not in a fully operational state the entire time the data was being taken. This is because the coil and HV were in different states.

Normalization before quality control

The normalization before the quality control cuts is simply based on the exposure of 454.5 ± 1.8 livedays. This corresponds to a fiducial exposure of 5.1 kTy, given the fiducial mass of 4.12 kT after the selection cuts are applied.

Normalization after quality control

The times the detector was runnings but had either a HV trip or a coil turned off must be removed from the dataset. This was done by using the same data the main analysis used. If a candidate event is found to be in such a time frame it is removed. However, this is only applied to the final events after all the cuts. The advantage of this is that it requires only a few events to be examined, the disadvantage of this is that the true

detector livetime must still be estimated. This is done using the same database tables[12] of the main analysis to define a good and bad running time. The high voltage trip time frames are defined over the entire detector. This means either the entire detector is usable or it is not. The entire time that the detector had a bad HV flag is only 1.03 days. In a similar way the coil current was defined to have good and bad time frames, however, unlike the HV this was defined on a SM basis. Thus for example, SM1 could be in good data taking state and SM2 could be in a unusable state. For SM1 this is 20.95 days and for SM2 this is 17.36 days.

Before any cuts the estimated exposure is 5.1 kTy, under the assumption that the detector was running during all the time when it was in a unusable data taking state, the most the fiducial exposure can be reduced to is only 4.9 kTy[13]. The total number of time the HV went off or the coil(s) were in not at there proper current measures is well over 100, but a large fraction of the total times comes from just a few episodes. These events can be looked at to further improve the livetime estimate. The largest single time the coil was off was a little over 5 days in the summer of 2004. Both supermodules were off for the same time of 5.2 days (to within 15 min. over 5 days). From looking at the rate of events during this time frame it is decided to estimate a total livetime of 5.0 kTy[14].

6.9 Vetoshield

The vetoshield selection is the last step in the event selection. This is made more difficult because currently there is no MC simulation of the vetoshield. However, there

[12]Provided to me by Andy Blake

[13]This is calculated taking into account the different mass of SM1 and SM2. Furthermore, if for example SM2 has the coil turned off but SM1 coil is in a good running state an event in SM1 would be allowed.

[14]The event rate over the 5 days was somewhat lower than it is during normal running. This is why the 5.0 kTy value is used

are two samples of events that have information relevant to the vetoshield. The stopping muons are an excellent control sample, and the candidate data is used to estimate the true background as the cosmic $\mu^{\pm}$ MC should not be believed to this level of precision[15] and the MC does not include the vetoshield anyway.

6.9.1 What is required from the vetoshield?

The vetoshield must have two properties: high efficiency and a low false event rejection. By high efficiency it is meant that the event must tag vetoshield activity consistant with a muon or other particle (like a spallation neutron or γ from a cosmic $\mu^{\pm}$ that might or might not interact in the detector) as often as possible. By low false rejection it is meant that some vetoshield activity must acceptable as a random hit during a real neutrino interaction should not be tagged as an event. These two must be balanced. The vetoshield has timing information and events can be broken into an early,in-time and late category. This is important as it allows vetoshield cuts which have both high efficiency and low false rejection and give a quantitative estimate of the efficiency and false rejection rate.

6.9.2 Vetoshield cuts:Control sample-Stopping Muon

The vetoshield cuts are based on two basic principles: the cosmics μ background and backgrounds associated with the cosmic μ should be spatially and temporally correlated with the track vertex and a μ should deposit more energy per strip than random noise. The way this is implemented is by looking at the in-time category and require both the average pulse height per digit be below a certain value and require no activity around a spatial window near the track vertex. The exact values of these are determined with the use of a control sample-the stopping muons. Before this can be done the different

[15] In the future with a better and more fully realistic model of the detector and shield, this should be more simple.

state of the detector during the period of collection must be addressed. For run 22,600 and after a 30μs pre-trigger window was read out. The in-time time window goes from 50ns before the track vertex time to 150 ns after the track vertex time. Thus the pre-trigger window is 150 times longer than the in-time window. As it will be shown, it is valuable to consider the situation when there is 0,1 and 2+ digits in a give time window as separate cases. The reasons for this is that the no activity situation is clearly the best that you can do and hopefully this is what the majority of the signal events show. However, in order to have a small false rejection rate the possibility of non zero vetoshield activity must be considered, this as it will be shown suggests that 1 digit events should be considered differently from event with more than 1 digit. Since the vetoshield does not have anywhere near 4π solid angle coverage[16], but rather coverage to reject the dominant background of downward going muons, there will a small but non-zero fraction of events that should not activate the shield as they never trace back to the shield. A final comment about the data used for the following analysis, the vast majority of the data is from when the detector was in normal operations, no attempt was made to remove data from when the detector was in a odd configuration as these would not effect the vetoshield and most of what is done depends weakly on the tracking. First, the distribution of digit for stopping muons will be given for in-time hits, early hits before the 30μs pre-trigger window was implemented and early hits after the 30μs pre-trigger window was implemented.

6.9.3 Number of digits and the vetoshield

The vetoshield activity can be parameterized by the number of digits in the vetoshield. This is a powerfull tool when looking at in-time veto shield hits. This is presented by first examining the case with no digits, then the case with 1 digit and finally the case

[16]For the fully contained analysis the acceptance is actually less than 2π solid angle as the events must stop in the detector (unlike a through going muon which can hit the vetoshield before or after it exists the detector). The regions without coverage have basically no background.

with 2+ digits. It should be noted that this is not the order which they determined it is simply the order which they given. In order to make the following discussion more clear, the final result of this will be given here as a guide to the rest of the chapter. Any event with a in-time hit within 1 meter of the projected track will be vetoed as will any events which average more than 180 in-time adc counts per digits for events with 2+ digits. The single hit have no pulse height requirement as it gives rise to high false rejection rate. Table 6.38 shows the results of this study.

Run time	Digits	Events	Frac. of events	# 'hit' events	Frac.:'hit' events
Pre	0	838	0.0204 ± 0.0007	633	0.7554 ± 0.0149
Pre	1	1877	0.0456 ± 0.0010	1719	0.9158 ± 0.0064
Pre	2+	38489	0.9341 ± 0.0012	37623	0.9775 ± 0.0008
Post	0	2377	0.0223 ± 0.0005	1643	0.6912 ± 0.0095
Post	1	5148	0.0484 ± 0.0007	4826	0.9375 ± 0.0034
Post	2+	98848	0.9293 ± 0.0008	96570	0.9770 ± 0.0004
All	0	3215	0.0218 ± 0.0004	2276	0.7079 ± 0.0080
All	1	7025	0.0476 ± 0.0006	6545	0.9317 ± 0.0030
All	2+	137337	0.9306 ± 0.0007	134193	0.9771 ± 0.0004

Table 6.38: This shows the number of in-time vetoshield digits for before (Pre) the pre-trigger window change (run 22600), after (Post) the change and the total (All).There are a total of 41,204 events for events before the pre-trigger window and 106,373 events that are after the pre-trigger window. The pre trigger window should effect the in-time conditions. The efficiency is defined as $\eta = \frac{S}{S+U}$ where S is selected events and U is unselected events. The efficiency for the all selection of events is obviously correlated with the pre and post selection. The fourth column is the fraction of hits that have 0,1 or 2+ digits. The code can estimate if a given event should hit the vetoshield. The number of hit events are simply the number of events that should intersect the shield. The fraction of hit events is the number of hit event divided by the total number of events of that type. The conclusion of this is that events with a high number of digits have the best chance of pointing back to the vetoshield and the efficiency will be dominated by the 2+ digit event category because $93.06 \pm 0.07\%$ of events have 2+ in-time digits.

0 digit sample

The case when the in-time shield is not hit is clearly the most favorable situation for a candidate neutrino event. The only possible test that you might need to do is to verify

the shield was actually operating at the time of the event. Provided the shield was operating, this would strengthen the case for a neutrino. However, since the control sample of stopping muons is being investigated, the fraction of events without vetoshield hits is an important way to calculate the shield inefficiency.

1 digit sample

The 1 digit background is the most difficult sample to understand, because it possible and even likely that some neutrinos will have a single hit in the vetoshield. Part of the challenge is to properly model this sample because as it will soon be shown this sample is responsible for the majority of false dead time. Some detailed results will be given below. See figure 6.15, 6.16 and 6.17.

The two distributions for early hits can be approximated as poisson distributions. If you take the mean value of the number of digits from early hits and then MC a Poisson distribution with these values inputed, the resulting simulated distribution will have a mean value consistent with the observed distribution but a more narrow distribution than the observed distribution. However, this is enough to show that for the in-time hits only the single hit case must be examined for causing false rejection. This can be seen by taking the poisson distribution mean μ_{early} and on the assumption that random noise is the same in all time categories simulate the expected number of events in the in-time window by $\mu_{early} = \frac{t_{in-time}}{t_{early}} \cdot \mu_{in-time}$. For the data after run 22600 the $\frac{t_{in-time}}{t_{early}} = \frac{1}{150}$. This might be estimated using the high-statistics data after run 22600, but because the in-time vetoshield timing did not change at run 22600, the estimated background is valid for all runs. Taking the $\mu_{early} = 14.42$, the mean of the distribution for the in-time events is $\mu_{in-time} = 0.096$. From this distribution of events with 0,1,2 and 3+ digits in-time that cause false rejection can be estimated. It should be noted that since the observed distribution has a wider tail than the MC, a possible problem this causes is that the events in the high side tail 'fluctuate up' to give a higher false

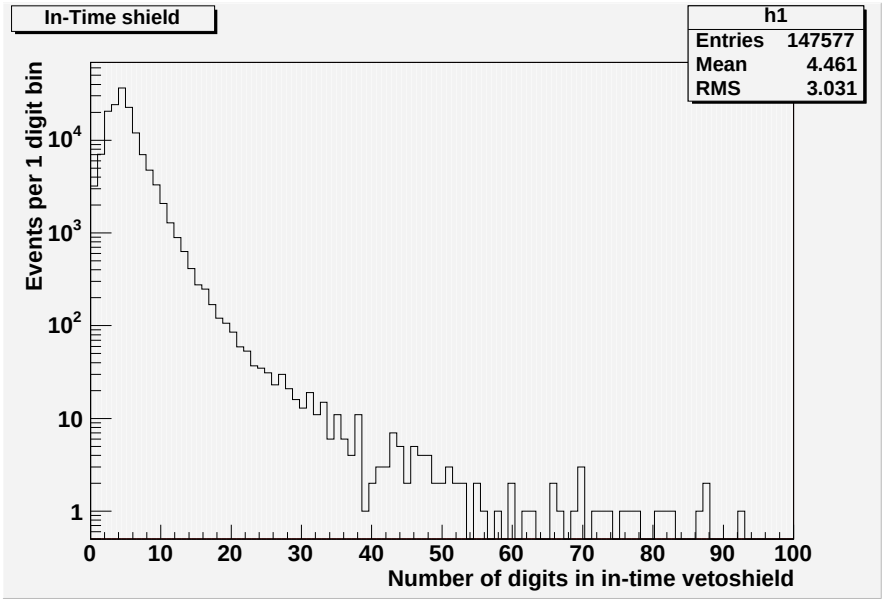

Figure 6.15: This shows the number of in-time digits in the vetoshield from stopping muon sample for all events. Since the pre-trigger change at run 22,600 should not have any effect on events in-time (it was checked) the in-time events can be plotted together. This shows that the mean number of digits of an vetoshield event is about 4 digits, since the vetoshield is doubled layered and each hit strip should produce two digits this seems consistent. The tail (a couple events go beyond 100 digits) shows that sometimes the detector gets hit with a shower of particles.

rejection than this argument suggests. However, it is easy to simulate higher values of $\mu_{in-time}$ and compare them with the corresponding values in μ_{early} until the tails in the MC are larger than the data. This is done in table 6.39.

Even though it is clear only single digit hits are significant, the number of single digit hits could be a problem for estimating the false rejection rate as it is the range of 10-15% from the simulation. However, it is expected that the average energy of these hits is lower than the those associated with a muon which has only a single hit. Since this can only be estimated from data this has to be done carefully. Ideally, this would be done using single hits in the early vetoshield. The statistics are almost non-existant in the post run 22600 sample, while they are relatively ample in the pre 22,600 sample.

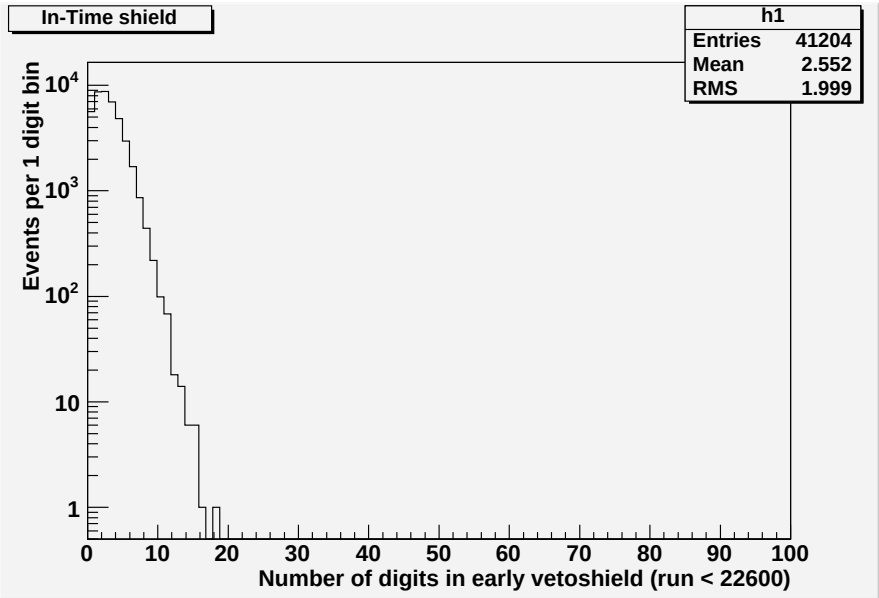

Figure 6.16: This shows the number of early digits in the vetoshield from stopping muon sample for all events before run 22600. This is almost all random noise.

As will shown in the next section, the requirement to eliminate the majority of muons with 2+ hits is an average of 180 or more adc counts/digit in-time in the vetoshield. In addition the cut requiring no hit within 1 meter of the projected track will be applied. A significant difference is that the spatial distribution is single digit in-time are correlated with the projected track location while the early hits are not. To do this all runs were used and all events with 1 in-time hit in the vetoshield were examined. The tables 6.40 and 6.41 shows the efficiency of these cuts.

2+ digit sample

The 2+ digit sample is different from the 1 digit sample in that false rejection is not a concern. This allows for both a spatial cut and a pulse height cut to be applied. It is tempting to use the projection of the track to ask if an event is suppose to hit the shield and have different cuts for the case where the track was suppose to hit the vetoshield

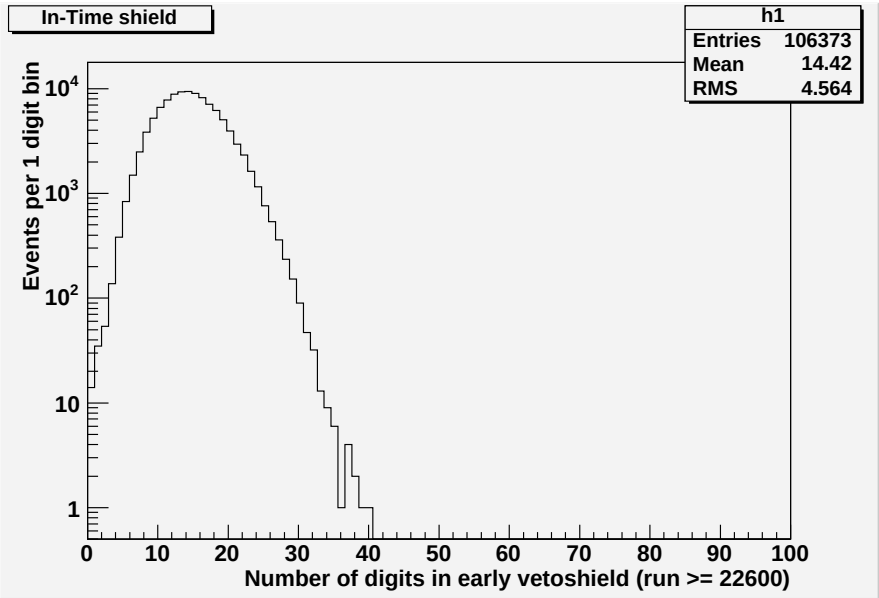

Figure 6.17: This shows the number of early digits in the vetoshield from stopping muon sample for all events after run 22600. This is almost all random noise. The reason the central value is larger is that the time window is longer than for events before run 22600.

compared to when the track is suppose to miss the shield. This is not done because it raises the possibility of hard understand (especially without a detector and vetoshield MC) systematics in the vetoshield acceptance and it increases the dependence of the results on tracking. Instead only two relatively simple and straight forward cuts are applied, a pulse height cut and a cut on the nearest digit to the projected track. Table 6.42 and 6.43 show the efficency of these cuts.

The net result of these two cuts is that for 2+ in-time digits the muon rejection rate is good. By requiring an event to pass the both the spatial cut and the pulse height cut the total efficiency can be determined. Only 117 events out of 137,337 have both 180 adc counts per digit or less and no hits within 1 meter of the projected track. The rejection efficiency for these events is $99.91 \pm 0.01\%$. There are 134,193 events that are projected to hit the shield and 134,104 are tagged for an efficiency of $99.93 \pm 0.01\%$

μ_{early}	Equivalent $\mu_{in-time}$	0 digit events	1 digit events	2+ digit events
14.4	0.096	96,577	9343	453
15.0	0.100	96,381	9468	494
18.0	0.120	94,233	11,444	696
21.0	0.140	92,585	12,869	919
24.0	0.160	90,477	14,634	1260

Table 6.39: This is the simulation of random noise that is in the in-time window for the vetoshield. Every MC experiment has 106,373 events, the same number of events that are in the post run 22600 data set for stopping muons. This is equivalent to simple poisson statistics. The left most column shows the expected mean number of digits for early hits in the pre-trigger window era (run 22600+), the next column shows what would be expected number of digits in the in-time window. The next three columns, show the number of events with 0,1 and 2+ digits in them in the in-time window. The point is the following: if there is no digits in the in-time window there can be no false rejection, but only single digit noise must be evaluated as even in the final extreme case ($\mu_{in-time}$=0.16) with about 66% more noise than is observed, only about a 1% of events would be expected to have more 1 digit of noise in-time with vetoshield.

and there 3144 events which are projected to miss the shield and tagging efficiency of these events is $99.11 \pm 0.17\%$, although as mentioned before given the dependence on additional dependence on tracking this is not used and it clearly does not change the result in any significant way.

Efficiency

The total efficiency η can be defined as the following where N is the number of events of a certain type:

$$\eta = \eta_{0digit} \cdot \frac{N_{0digit}}{N_{tot}} + \eta_{1digit} \cdot \frac{N_1 digit}{N_{tot}} + \eta_{2+digit} \cdot \frac{N_{2+digit}}{N_{tot}} \tag{6.6}$$

The result of this calculation is that the total efficiency is 97.4±0.1% for the stopping muon sample, since nothing can be done to improve the rejection of events that fail to produce a digit, 2.2% of this inefficiency cannot be improved (by cuts) no matter what is done. This means in principle no more than 0.4% of the remaining inefficiency could be improved. This would either increase the dead time or require an improved model

Spatial cut (m)	Early events	η:early events	In-time events	η:in-time events
0.10	23	0.003 ± 0.001	2381	0.339 ± 0.006
0.20	49	0.006 ± 0.001	4146	0.590 ± 0.006
0.50	125	0.014 ± 0.001	6045	0.860 ± 0.004
1.00	250	0.029 ± 0.002	6566	0.935 ± 0.003
2.00	487	0.056 ± 0.002	6660	0.948 ± 0.003

Table 6.40: This shows the vetoshield efficiency(η) for single digit hits events for all runs. There are a total of 8682 single digit events for the early events and 7025 single digit events that are in-time. The efficiency is defined as $\eta = \frac{S}{S+U}$ where S is selected events and U is unselected events. The efficiency for a single digit during the pre-trigger window is important because it shows that there is a $2.9 \pm 0.2\%$ chance of a random hit being within 1 meter of the projected track. When combined with the adc distribution this will lead to an estimate of the false rejection rate. The rejection of cosmic μ is $93.47 \pm 0.29\%$.

ADC cut (count)	Early events	η:early events	In-time Events	η:in-time events
100	23	0.003 ± 0.001	6	< 0.001
120	106	0.012 ± 0.001	26	0.004 ± 0.001
140	987	0.114 ± 0.003	166	0.024 ± 0.002
160	2453	0.283 ± 0.005	422	0.060 ± 0.003
180	3751	0.432 ± 0.005	751	0.107 ± 0.004

Table 6.41: This shows the vetoshield efficiency(η) for single digit hits events for all runs. There are a total of 8682 single digit events for the early events and 7025 single digit events that are in-time. The efficiency is defined as $\eta = \frac{S}{S+U}$ where S is selected events and U is unselected events. The efficiency for a single digit during the pre-trigger window is important because it shows that there is a $43.2 \pm 0.5\%$ chance of a random hit having 180 or less adc counts. This is clearly too high of a rate of false rejection.

of the shield.

False rejection rate

The false rejection rate must be modeled on the stopping muon sample. The false rejection rate is defined to be the expected chance of falsely rejection an atmospheric neutrino event because of noise in the shield. It is assumed that random noise is the only possible cause of this false rejection ans that any other vetoshield hits in-time with the shield are caused by background particles. Furthermore it is assumed that

Spatial cut (m)	Number of events	Efficiency of cut
0.05	46598	0.3393 ± 0.0013
0.10	78232	0.5696 ± 0.0013
0.20	109795	0.7995 ± 0.0011
0.30	128545	0.9360 ± 0.0007
0.50	133784	0.9741 ± 0.0004
1.00	135618	0.9875 ± 0.0003
2.00	136392	0.9931 ± 0.0002

Table 6.42: This shows the vetoshield efficiency(η) for 2+ digit hit events for all runs. There are a total of 137337 2+ digit events that are in-time. The efficiency is defined as $\eta = \frac{S}{S+U}$ where S is selected events and U is unselected events. The rejection rate for the 1 meter cut is $98.75 \pm 0.03\%$. For the total efficiency the pulse height cut must also be included.

PH cut (ADC/digit)	Number of events	Efficiency of cut
100	136819	0.9963 ± 0.0002
120	135843	0.9891 ± 0.0003
140	134108	0.9765 ± 0.0004
160	131253	0.9557 ± 0.0006
180	127301	0.9269 ± 0.0007
200	122084	0.8889 ± 0.0008

Table 6.43: This shows the vetoshield efficiency(η) for 2+ digit hits events for all runs. There are a total of 137337 events that are in-time. The efficiency is defined as $\eta = \frac{S}{S+U}$ where S is selected events and U is unselected events. The cut requiring 180 or adc/digit eliminates $92.69 \pm 0.07\%$ of events. For the total efficiency the spatial cut must be included.

the noise in the pre-trigger window is all caused by random noise and that any noise in the in-time window is the same type of signal. It is clear that the false rejection rate is small and because of this a worst case scenario will be calculated. The model will assume random noise with a mean distribution of hits that is 66% higher than the time window corrected results based on pre-trigger hit distribution suggests as likely.For this model it is predicted that $85.0 \pm 0.1\%$ of the events have 0 random hits, $13.7 \pm 0.1\%$ have 1 hit and $1.2 \pm 0.1\%$ have 2 digits (3+ digits are less than 0.1%). However, the fraction of hits that pass the 1 meter spatial cut is known to be $2.9 \pm 0.2\%$ from looking at single hits in the pre-trigger window for single digit events. The fraction of events

from the pre-trigger window with 2 digits that have a single hit within 1 meter of the projected track is $5.3 \pm 0.2\%$. Thus before any cut on adc is made the projected false rejection rate can be calculated by using the observed efficiencies. This gives a false rejection rate of $0.5 \pm 0.1\%$. This is already small compared to other inefficiencies and is truly a worse case situation. However, because the adc distribution is peaked at lower pulse height than the single digits this leads to an excessive increase in false dead time. This is why the single hit have no pulse height requirement. There are 8769 events with 2 digits in the pre-trigger for all events[17] and only 110 of them have less than 180 adc per digit. This is such a small fraction that the estimated false rejection is still only $0.5 \pm 0.1\%$. On the other hand if the (lower pulse height) spectrum for single hit digits is used instead of the spectrum of the double hit digits, the false rejection rate doubles to 1%. Given the number of worst case assumptions used for that estimate it appears safe to state the false rejection rate at $\leq 1\%$ and under dire (but more realistic) scenarios as $0.5 \pm 0.1\%$

Stopping muons-Final dataset

All of this has been done on the full set of stopping muons. However, there is a smaller sub-sample which have a more stringent set of cuts, the final dataset. Since the muons in this sample are up to the radial fiducial cut identical to the final neutrino candidates, these events are useful as they have a angular distribution more similar to the final candidate neutrino events. The entire process of setting the cuts is not going to be redone, but the results will be highlighted. The fraction of events with 0,1 and 2+ digits are $1.92 \pm 0.14\%$,$3.19 \pm 0.18\%$ and $94.89 \pm 0.22\%$ the no digit rate is consistent with the rate in the larger subsample while the 1 and 2+ rates are not. The fraction of events with 2+ digits is higher which will increase the efficiency and decrease the dead

[17] Although there still many more events in pre run 22600 (8715) than the post run 22600 (54), the means are nearly identical and the rms are similar.

time. The cut efficiency on single digit events is $91.99 \pm 1.54\%$ and the cut efficiency on 2+ digit events is $99.98 \pm 0.02\%$. This leads to a total efficiency of $97.8 \pm 0.3\%$ which is slightly better although not statistically significantly better than the full muon sample. The false rejection rate cannot change as the model does not change.

6.9.4 Stopping Muon vetoshield conclusion

The stopping muon sample has shown that a vetoshield efficiency of $97.4 \pm 0.1\%$ and a false rejection rate of $0.5 \pm 0.1\%$ are possible with the modest requirement that the nearest hit in the shield is more than 1 m away from the projected track location and that for events with 2 or more digits in the shield the total pulse height in the shield is 180 adc counts per digit or less. In chapter 9, this topic will have to be briefly revisited as the angular distributions of the events entering the sample are somewhat different and this could weakly change the results. The process is the same and the answer is not significantly different.

Chapter 7

Statistical Tests and CPT violation

7.1 Introduction

The simple selection of neutrino events does not make a physics result. The physics results must ask a question. The question here is do the neutrinos behave in a way which is consistent with the CPT theorem? This is a quantitative question which must have a quantitative result. The physics results presented in this thesis have a low enough number of events that the poisson nature of a small event sample cannot be ignored, it is important that the results of this poisson nature are understood.

7.2 How to search for CPT violation?

Since this is a low statistic experiment, a proper statistical technique must be used. These statistic tests can be broken up into two types. The first type of statistical test is a model dependent test. The second type of statistical test is a model independent test.

7.2.1 Model dependent tests

In a model dependent test, the first thing that is needed is a particular model of CPT violation in the neutrino sector. However, since CPT violation has never been observed, it is not clear which model should be tested. The method employed should have the ability to validate or reject the CPT violating model. This leads to a possible problem as a test designed to reject a particular model of CPT violation might not be sensitive to a different CPT violating theory.

7.2.2 Model independent tests

In a model independent test the fundamental question is simply whether the observed neutrino oscillation behavior is consistent with the prediction of the CPT Theorem ($P_{\nu_\mu \to \nu_\mu} = P_{\bar{\nu_\mu} \to \bar{\nu_\mu}}$). This does not depend on any given theory of CPT violation. If CPT violation was observed, the model independent tests could not be used to tell what are the fundamental causes the CPT violation (Lorentz violation,...).

7.3 Testing Barger's Model

Barger's model can in principle be tested by looking at a difference in the $\frac{L}{E}$ distributions for ν_μ and $\bar{\nu}_\mu$. However, as will become evident in chapter 9 the statistics for this do not exist currently. Indeed the statistics are so poor that a seperate $\frac{L}{E}$ for ν_μ and $\bar{\nu}_\mu$ would just not have enough statistics to have any meaningfull results. However, it should be stated that the technique of measuring the $\frac{L}{E}$ for neutrino and anti-neutrino is arguably the best way[1] to test the Barger model.

[1]The best way here means the method with the most physically motivated method. Since the measurement of the $\frac{L}{E}$ spectrum allows for the extraction of the oscillation parameters, this is clearly well motivated.

7.4 Asymmetry test

The asymmetry test is one of the simplest tests that can be applied to search for CPT violation. This test does not use the information from the spectrum only the total count of events.

7.4.1 Definition of Asymmetry test

The asymmetry test is simply defined as:

$$\sum_{i,j} A(E_i, L_j) = \sum_{i,j} \frac{N_-(E_i L_j) - N_+(E_i L_j)}{N_-(E_i L_j) + N_+(E_i L_j)} \tag{7.1}$$

This expression has i bins in neutrino energy E and j bins in path length L. N_- is the number of muons in a given bin produced by a neutrino interaction. N_+ is the number of anti-muons in a given bin produced by a anti-neutrino interaction. Given the relatively low statistics of this experiment, the number of bins will be relatively small. This test is similar to the ρ test which is considered in chapter 8. The key difference between the two tests is that the ρ is designed to be centered at zero.

7.4.2 1 bin test

In the case of the 1 bin test, the expression for the asymmetry takes a simple form:

$$A(N_-, N_+) = \frac{N_+ - N_-}{N_+ + N_1} \tag{7.2}$$

The uncertainity in the asymmetry also takes a simple form:

$$\sigma_A(, N_-, N_+) = \frac{2N_- N_+}{(N_- + N_+)^2} \sqrt{\frac{1}{N_-} + \frac{1}{N_+}} \tag{7.3}$$

In figure 7.1 the asymmetry test for an ensemble of 100,000 experiments is shown with $N_- = 20, N_+ = 10$ in case of no oscillations (CPT conservation). In figures

7.2 and 7.3 the same CPT conserving physics is shown for $N_- = 20, N_+ = 10$ and $N_- = 20, N_+ = 10$ which is 2× and 5× the statistics. Cleary as the total number of events are increased, the statistical power of the test is increased. Figure 7.4, 7.5 and 7.6 show the same models as 7.1, 7.2 and 7.3 is used with an CPT conserving oscillation modeled as ν_μ and $\bar{\nu}_\mu$ oscillate with the same parameters[2]. For 7.4,7.5 and 7.6 it is assumed 30% of the unoscillated neutrino are oscillated[3].

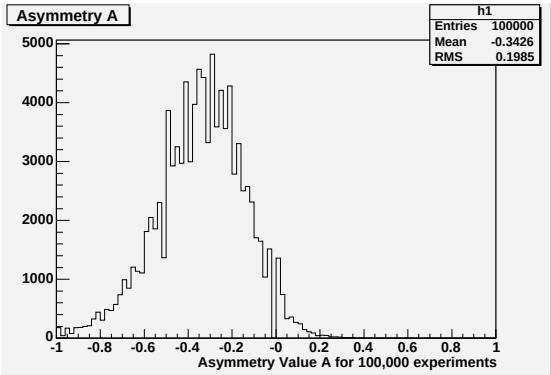

Figure 7.1: This shows the results of an ensemble of 100,000 experiments with the asymmetry test. This shows the unoscillated (CPT conserving) asymmetry test with $N_- = 20, N_+ = 10$. There are no systematics assumed and perfect charge ID. The spikes are caused by the poisson variations and go away once systematics are added. This has a total of 30 ν events.

[2]This is CPT conserving

[3]It is also assumed the same fraction of ν and $\bar{\nu}$ oscillate for a given set of oscaillation parameters. This is actually not true. The difference is small but no correction for it is made here. In chapter 9 the correction is made

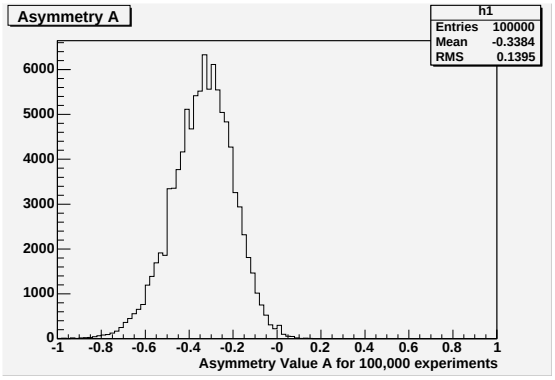

Figure 7.2: This shows the results of an ensemble of 100,000 experiments with the asymmetry test. This shows the unoscillated (CPT conserving) asymmetry test with $N_- = 40, N_+ = 20$. There are no systematics assumed and perfect charge ID. The spikes are caused by the poisson variations and go away once systematics are added. This has a total of 60 ν events.

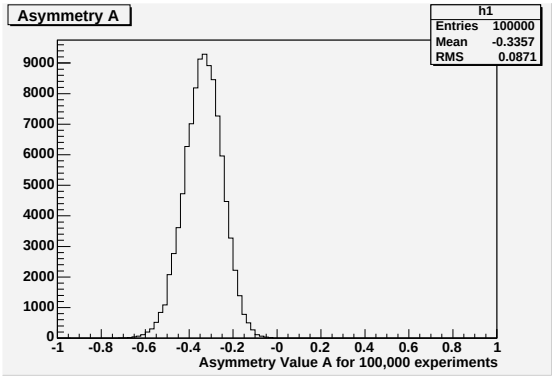

Figure 7.3: This shows the results of an ensemble of 100,000 experiments with the asymmetry test. This shows the unoscillated (CPT conserving) asymmetry test with $N_- = 100, N_+ = 50$. There are no systematics assumed and perfect charge ID. The spikes are caused by the poisson variations and go away once systematics are added. This has a total of 150 ν events.

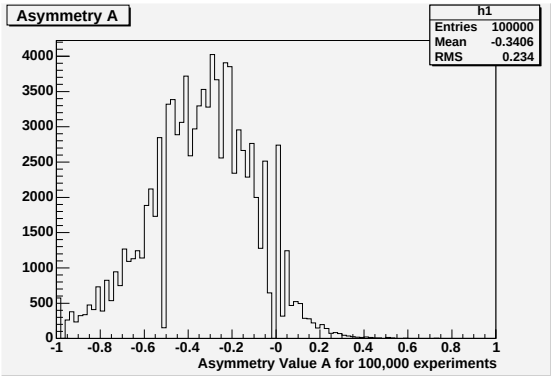

Figure 7.4: This shows the results of an ensemble of 100,000 experiments with the asymmetry test. This shows the oscillated (CPT conserving) asymmetry test with $N_- = 14, N_+ = 7$. There are no systematics assumed and perfect charge ID. The spikes are caused by the poisson variations and go away once systematics are added. This has a total of 21 nu events.

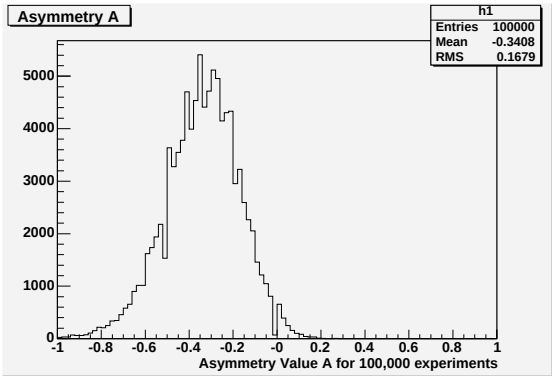

Figure 7.5: This shows the results of an ensemble of 100,000 experiments with the asymmetry test. This shows the oscillated (CPT conserving) asymmetry test with $N_- = 28, N_+ = 14$. There are no systematics assumed and perfect charge ID. The spikes are caused by the poisson variations and go away once systematics are added. This has a total of 42 ν events.

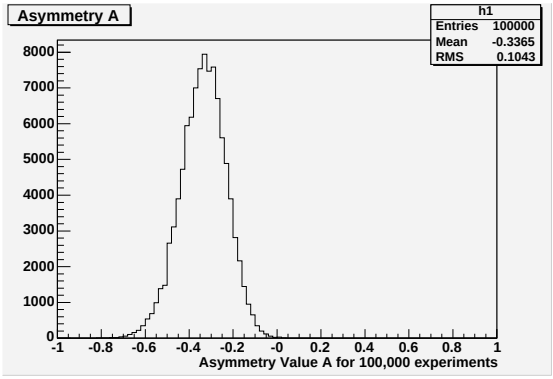

Figure 7.6: This shows the results of an ensemble of 100,000 experiments with the asymmetry test. This shows the oscillated (CPT conserving) asymmetry test with $N_- = 70, N_+ = 35$. There are no systematics assumed and perfect charge ID. The spikes are caused by the poisson variations and go away once systematics are added. This has a total of 105 nu events.

All of the examples so far have been CPT conserving. Although many possible CPT violating models could be used, the simplest and most drastic variety of CPT violating model will be examined in figure 7.7, 7.8 and 7.9. This model consists of ν ocsillating with 30% of the unoscillated sample oscillating and no oscillation for $\bar{\nu}$.

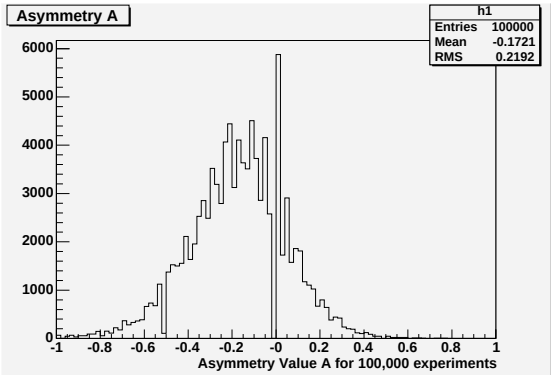

Figure 7.7: This shows the results of an ensemble of 100,000 experiments with the asymmetry test. This shows the oscillated (CPT violating) asymmetry test with $N_- = 14, N_+ = 10$. There are no systematics assumed and perfect charge ID. The spikes are caused by the poisson variations and go away once systematics are added. This has a total of 21 ν events.

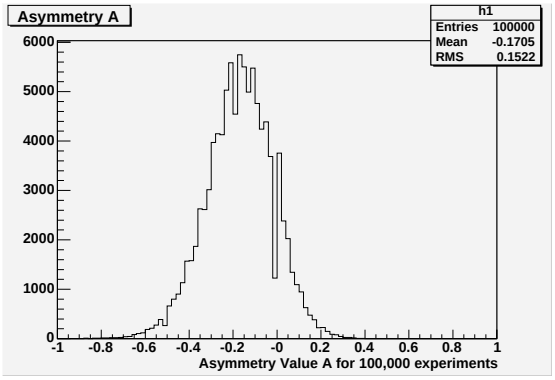

Figure 7.8: This shows the results of an ensemble of 100,000 experiments with the asymmetry test. This shows the oscillated (CPT violating) asymmetry test with $N_- = 28, N_+ = 20$. There are no systematics assumed and perfect charge ID. The spikes are caused by the poisson variations and go away once systematics are added. This has a total of 42 nu events.

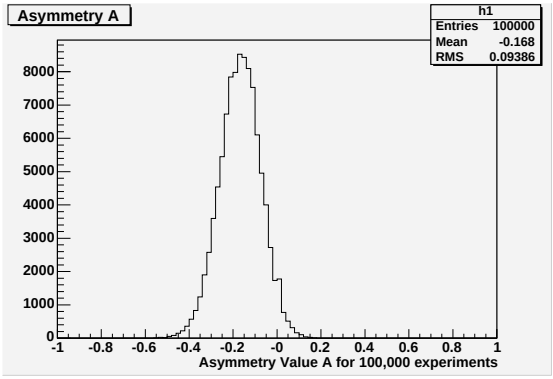

Figure 7.9: This shows the results of an ensemble of 100,000 experiments with the asymmetry test. This shows the oscillated (CPT violating) asymmetry test with $N_- = 70, N_+ = 50$. There are no systematics assumed and perfect charge ID. The spikes are caused by the poisson variations and go away once systematics are added. This has a total of 105 ν events.

The consclusion that is reached is with the $\approx$ 30 events expected in sample even large CPT violating models cannot be excluded. With 2$\times$ and 5$\times$ the statistics the asymmetery tests statistical power to look for CPT violation increases although given the ideal nature of the toy MC presented here it is unclear even with 5$\times$ the statistics a serious CPT test can be carried out with the asymmetry test. Part of the reason for this is that oscillation cannot on average remove more than 50% of events. If an unusually large difference in expected versus observed asymmetry was observed it could in principle suggest a problem with the cross section, neutrino flux or physics[4], however, it could not be caused by differences in normal oscillations.

7.5 Ratio test

The ratio test like the asymmetry test is a simple test to look for CPT violation. The idea of the ratio test is to try and cancel out systematics in the neutrino flux and cross-section. The penalty that is paid with this is that the statistics get put in the four bins. This means that the lowest bin can be a problem in the small statistics limit.

7.5.1 Definition of Ratio test

The ratio test can be defined by the following set of equations:

$$r_- = \frac{\mu_{up}}{\mu_{down}} \tag{7.4}$$

$$r_+ = \frac{\mu_{up}}{\mu_{down}} \tag{7.5}$$

$$R_{CPT} = \frac{r_+}{r_-} \tag{7.6}$$

[4]You could at least imagine some process (I never said well motivated process) that could cause this. For example,$\bar{\nu}_\mu$ decays and ν_μ do not decay. It is probably safe to say this is really unlikely

It is important to make sure the denominators of these three equations never go to zero. This explains the form of the three equations. Since the up going neutrinos are expected to have oscillated and the downward going neutrinos have not, r_-,r_+ have this form. Similarly, because there are more neutrino than anti-neutrino interactions expected, R_{CPT} has it form. Part of the justification of the up-down ratio test is that some of the systematic uncertainties cancel. This must be weighed against the loss of statistics by taking the neutrino events and breaking it up into four bins. Since, the upgoing $\bar{\nu}_\mu$, should be the smallest fraction of the events, statistical flucations must be considered carefully. To study the power (and limits) of the ratio test, a simulation was ran. In this simulation it is assumed that there are no systematic errors and the charge and direction (up vs. down) determination are perfect. This means that this simulation is the limit of what can be done. The first simulation shows the ratio test in absence of oscillation in figure 7.10. In this simulation $r_- = r_+$ (CPT conservation) and the total number of neutrino events is 30 (un-oscillated). The ratio of $\frac{\nu_\mu}{\bar{\nu}_\mu}$=2.0. This means that there 5 up and 5 down going $\bar{\nu}_\mu$,events and 10 up and 10 down going ν_μ events. No systematic error and perfect charge and up versus down discrimination is assumed. Figure 7.10 shows the results of an ensemble of 100,000 experiments with the previously mentioned parameters. R_{CPT} is plotted between 0 and 10 over 400 bins.The variation is caused by poisson flucations alone. $R_{CPT} = 1$ is the value that would be expected from CPT conservation. The results of figure 7.10 have such a large range that even in this best possible[5] situation the statistical variations make this test almost worthless. This is unfortunate as the number presented in figure 7.10 are similar to the final number in this thesis. This means that without anymore work the ratio test should not be used for this thesis, but it is still possible with higher statistics the test will be powerful at testing CPT. So in figure 7.11 and 7.12 shows the same plot as 7.10

[5]This is true since the effect of oscillation will be to remove events from the up going events making the bad statistical situation worse.

with 5 and 10 times the statistics. These cases of five and tens times the exposure will be used as the test cases for the ratio test. In figure 7.13 and 7.14 shows the effects of a CPT conserving oscillation in which none of the down going events oscillated but only half of the upgoing neutrino remain for the 5 and 10 times exposure. Finally, in figures 7.15 and 7.16 the results of a test in which neutrinos oscillate and anti-neutrinos do not oscillate is considered for the 5 and 10 times exposure cases.

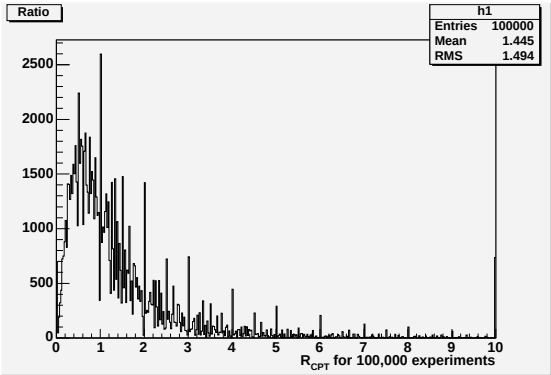

Figure 7.10: This shows the results of an ensemble of 100,000 experiments with the ratio test. This shows the unoscillated (CPT conserving) ratio test with $\frac{\nu_\mu}{\overline{\nu}_\mu}$=2.0. There are no systematics assumed and perfect charge ID. The spikes are caused by the poisson variations and go away once systematics are added. This has a total of 30 ν events. Clearly at this level of statistics, the test is not useful.

The results with the larger exposure are impressive enough (much smaller tails) that the comparison of these should be made against CPT conserving and CPT violation oscillations.

Certainly with an expsoure 10× greater than the current exposure the ratio test does have the potential to observe CPT violation. However, this is for the maximal possible violation that is possible and even in this case a bit of luck is required. This suggests that for the near term the ratio test will not be a valuable method to search for CPT violation.

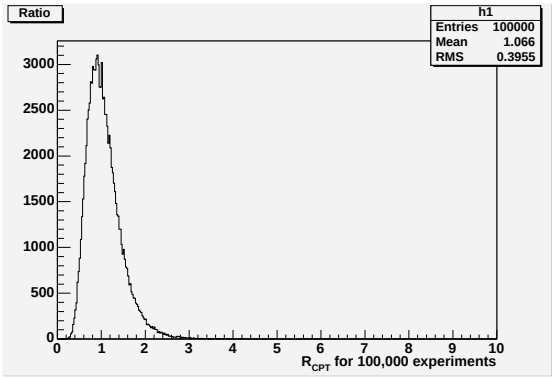

Figure 7.11: This shows the results of an ensemble of 100,000 experiments with the ratio test. This shows the unoscillated (CPT conserving) ratio test with $\frac{\nu_\mu}{\bar{\nu}_\mu}$=2.0. There are no systematics assumed and perfect charge ID. This has a total of 150 ν events.

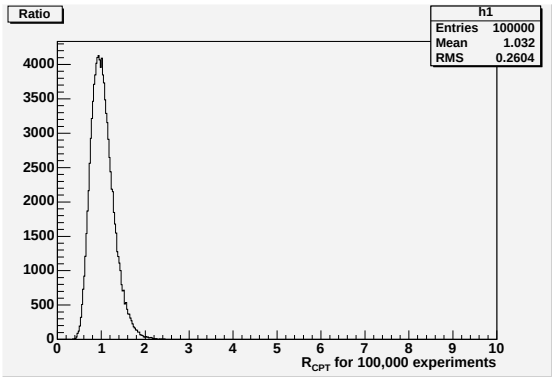

Figure 7.12: This shows the results of an ensemble of 100,000 experiments with the ratio test. This shows the unoscillated (CPT conserving) ratio test with $\frac{\nu_\mu}{\bar{\nu}_\mu}$=2.0. There are no systematics assumed and perfect charge ID. This has a total of 300 ν events.

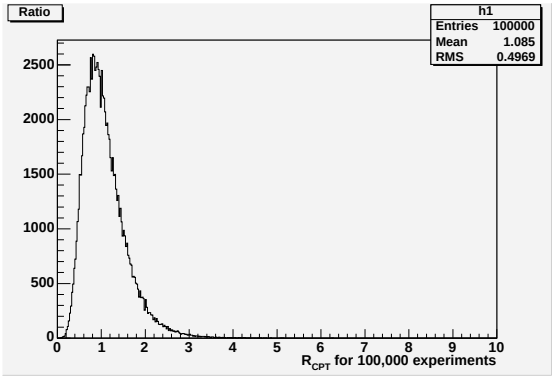

Figure 7.13: This shows the results of an ensemble of 100,000 experiments with the ratio test. This shows the oscillated (CPT conserving) ratio test with $\frac{\nu_\mu}{\bar{\nu}_\mu}$=2.0. The oscillation is taken to be no downward ν oscillate and the up going ν are fully oscillated with the same parameters for ν and $\bar{\nu}$. There are no systematics assumed and perfect charge ID. This has a total of 150 ν events.

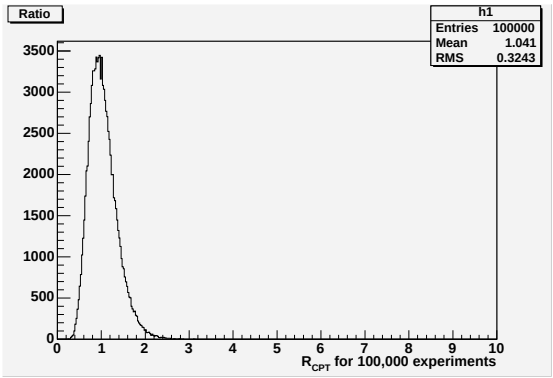

Figure 7.14: This shows the results of an ensemble of 100,000 experiments with the ratio test. This shows the oscillated (CPT conserving) ratio test with $\frac{\nu_\mu}{\bar{\nu}_\mu}$=2.0. The oscillation is taken to be no downward ν oscillate and the up going ν are fully oscillated with the same parameters for ν and $\bar{\nu}$. There are no systematics assumed and perfect charge ID. This has a total of 300 ν events.

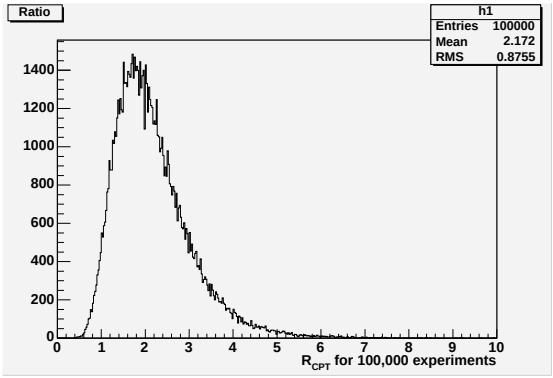

Figure 7.15: This shows the results of an ensemble of 100,000 experiments with the ratio test. This shows the oscillated (CPT violating) ratio test with $\frac{\nu_\mu}{\overline{\nu}_\mu}$=2.0. The oscillation is taken to be no downward ν oscillate and the up going ν are fully oscillated with the requirement that only ν_μ oscillate. There are no systematics assumed and perfect charge ID. This has a total of 150 ν events.

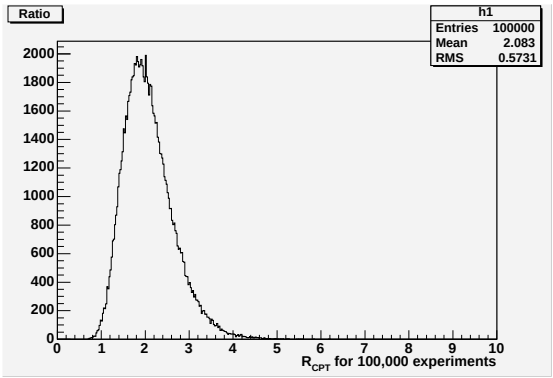

Figure 7.16: This shows the results of an ensemble of 100,000 experiments with the ratio test. This shows the oscillated (CPT violating) ratio test with $\frac{\nu_\mu}{\overline{\nu}_\mu}$=2.0. The oscillation is taken to be no downward ν oscillate and the up going ν are fully oscillated with the requirement that only ν_μ oscillate. There are no systematics assumed and perfect charge ID. This has a total of 300 ν events.

Chapter 8

The ρ test

8.1 Introduction

The central topic of this thesis is CPT conservation. In order to come to a quantitative answer on this topic more than one technique can be used. A statistical test (or tests) can be used to determine if CPT is conserved or not conserved.

8.2 The ρ test

The ρ test is an asymmetry test designed to test CPT conservation in atmospheric neutrinos. The ρ test is defined to be:

$$\sum_{i,j} A(E_i, L_j) = \sum_{i,j} \frac{N_-(E_i L_j) - \rho(E_i L_j) N_+(E_i L_j)}{N_-(E_i L_j) + \rho(E_i L_j) N_+(E_i L_j)} \tag{8.1}$$

This expression has i bins in neutrino energy E and j bins in path length L. N_- is the number of muons in a given bin produced by a neutrino interaction. N_+ is the number of anti-muons in a given bin produced by a anti-neutrino interaction. ρ is the ratio of expected neutrino to anti-neutrino interactions reconstructed in the far detector assuming CPT conservation in a given bin. ρ must be calculated from Monte Carlo

studies. Given the relatively low statistics of this experiment, the number of bins will be relatively small[1].

8.2.1 ρ test for 1 bin

The simplest implementation of the ρ test is the case of i=j=1. This is just one bin. In this situation the uncertainty is easy to write down. The expression for the asymmetry is:

$$A = \frac{N_- - \rho N_+}{N_- + \rho N_+} \tag{8.2}$$

The uncertainty is simply given to be:

$$\sigma_A(\rho, \frac{\sigma_\rho}{\rho}, N_-, N_+) = \frac{2\rho N_- N_+}{(N_- + \rho N_+)^2}\sqrt{\frac{1}{N_-} + \frac{1}{N_+} + (\frac{\sigma_\rho}{\rho})^2} \tag{8.3}$$

This expression is based on only statistical errors ($\sqrt{N}$) for N_-, N_+. Even though this expression is simple it shows the importances of understanding the systematic error.

8.3 Advantages and disadvantages of the ρ test

The advantage of the ρ test is that the mean value of the ρ test should be centered around zero[2]. This makes the interpertation of the results somewhat easier to understand when compared with the normal asymmetry test. The second advantage is that it gives an easy to understand way of accessing the systematic error. The disadvantage of this is that it introduces another parameter ρ, which must be modeled and understood.

---

[1] Obviously, a large number of bins will result in some bins with few events. The smaller number of events means the poisson flucations will dominate. An alternative way to go about this would be a bin free test. This test has possible advantage but is more complex and is not done

[2] As will be seen the fact that poisson statistics are important for small statistics changes this a little bit.

8.4 Calculating ρ from Monte Carlo

Maybe the most significant possible problem with the ρ test is that it is dependent on properly calculating the $\rho(E_i, L_j)$ values from MC. If this is calculated incorrectly it is possible to create a false asymmetry in the data. This means special care must be taken to prevent this from happening.

In general $\rho(E_i, L_j)$ is a product of separate ρ terms.

$$\rho(E_i, L_j) = \rho_1(E_i, L_j)\rho_2(E_i, L_j)\rho_3(E_i, L_j)\ldots \tag{8.4}$$

Each of these ρ's must be understood. The different ρ's come from both physics and detector effects. Since the purpose of the ρ test is to compensate for any factor that would induce a fake asymmetry, every know asymmetry must be identified. From the physics point of view, differences in flux (ν_μ and $\bar{\nu_\mu}$ production differences) and cross section differences must be considered. There are also detector/acceptance effects, which although might have different causes will be considered one systematic uncertainty. In the MC simulation it is not the individual values that matter, rather the product. However, breaking the terms up is useful to estimate the systematic uncertainty separately and calculating the total systematic uncertainty.

8.4.1 ρ_{Flux}

ρ_{Flux} is only going to modeled as a function of energy E and not L. Intially, it is tempting to think that ρ_{Flux} cannot be a function of L (or zenith angle) but this is actually not true. The reason is that the earth's magnetic field breaks the symmetry with regard to zenith angle. This could change ρ_{Flux} as in principle it alters the energy distribution of particles interacting in the atmosphere. However, for the low energies events that are observed in MINOS the flux ratio is only a bit above 1 with a systematic error (see chapter 5) of a few percent. The exact value of the flux ratio and the uncertainty in the

flux ratio depend on the details of the calculation. There is some energy dependence in the flux ratio and breaking the flux ratio into energy bins is justified although it will not make much of a difference.

8.4.2 $\rho_{Cross-Section}$

$\rho_{Cross-section}$ is only modeled as a function of energy as the place around the earth the neutrino is produced cannot change the nucleon-neutrino cross section. The cross section ratio is somewhat above 2 for the energies at the far detector[3]. The uncertainty in the neutrino cross-section ratio also depends on the events be selected. For example, at higher energies when DIS dominates the cross-section, the ratio is well known. However at the energies of majority of the MINOS FD events the situation is more complex (see chapter 5). Certainly here it is possible that breaking up ρ by energy can make sense provided there are enough event to justify the binning.

8.4.3 $\rho_{Detector}$

$\rho_{Detector}$ does actually in general vary with both L and E. However, the most important systematics to understand are one which treat the ν_μ and $\bar{\nu}_\mu$ differently. For example a difference in charge ID efficiency will be important to understand.

8.5 How does the ρ test tell CPT conservation from CPT Violation?

The ρ test must be able to tell the difference between CPT violation and conservation. The test must both discriminate against false signals and show real signals.

[3]This depends on many things. Such as the stage of reconstruction and the energy of the particular events in question

8.5.1 Statistical power of ρ test 1 bin

A first look of the statistical power of the ρ test is shown here with the simple 1 bin test. To make this study an ensemble of experiments is studied. An example of this is shown is figure 8.1. In this example an ensemble of 100,000 experiments were examined. For purposes of the example each experiment has ρ= 2.0, σ_ρ= 0.20 and an expectation N_-=20,N_+=10. There are 100 equal size bins in A. The variation is caused by systematic error and fluctuation in the counting statistics. The counting statistic in N_-,N_+ are modeled here by poisson statistics and the systematic error is modeled by smearing the ρ value by σ_ρ. Since the input of this model is CPT conservation, CPT conservation should be what is observed. For the most part this is true. The estimate of uncertainty from equation 8.3 is σ_ρ=0.20, this is close to the estimate from the rms of the distribution (0.214) and from the a from the guassian fit (0.207). It is important that on average this test gives an asymmetry of zero. The mean is -0.0001 and the fit to the guassian has a mean of 0.0037 ± 0.0007[4]. The asymmetry on the tails can be explained because of poisson statistics. The $N_+ = 10$ will fluctuate down to zero, but it cannot fluctuate below 0. However, the same will not happen (as often) with $N_- = 20$, thus the tails are not symmetric. It is important to note that with the poisson statistics the number $N_\pm$ is the number of expected events, not the number of observed events. This is important because the number of expected events depends on the oscillation parameters $(\Delta^2_m, sin^2(2\theta))$.

Sensitivity and robustness with no CPT violation

The model $\rho = 2.0$,$\sigma_\rho = 0.20$,$N_- = 20$,$N_+ = 10$ shown in Figure 8.1 will be used as the standard statistical model. In order to look at the robustness of the model, variation from this standard model will be made. In Figures 8-2 and 8-3 show the same ρ and

[4]The guassian fit here fails to have a mean consistent with zero. This is simply because the statstics are small as will be shown later with larger statistics this becomes a smaller problem

σ_ρ with $N_- = 40$,$N_+ = 20$ and $N_- = 60$,$N_+ = 30$. In figures 8.4,8.5 and 8.6 the effect of changing the systematic error by keeping everything else the same and using systematics of $\sigma_\rho = 0.10$,$\sigma_\rho = 0.30$ and $\sigma_\rho = 0.40$ is shown. In figures 8.7,8.8 and 8.9 the total number of expected events and the 10% in ρ are kept constant as the value of ρ is allowed to go to 1.0,1.5 and 2.5. These models are without CPT violation. Indeed these models are without oscillations. However, since the CPT theorem says the oscillations treat neutrinos and anti-neutrinos the same[5], these numbers could be thought of as the expectations from an oscillated sample with higher statistics. Table 8.1 shows the net result of these nine different tests.

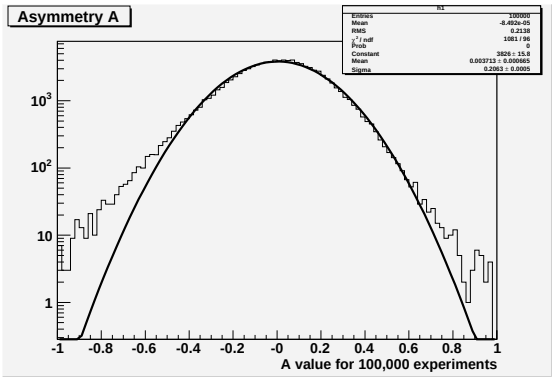

Figure 8.1: This shows the results of an ensemble of 100,000 experiments with the 1-bin test. In each experiment $\rho = 2.0$,$\sigma_\rho = 0.20$,$N_- = 20$,$N_+ = 10$. The variation is caused by the gaussian variation of ρ and the poisson variation in N_-,N_+. The distribution is fit to a guassian. Note the log scale.

All of these results are without any CPT violation. CPT violation will be added by changing the probability of oscillations between ν_μ and $\bar{\nu_\mu}$. Figure 8.10 shows the identical parameters as shown in 8.1 but with a CPT conserving equal oscillations between ν_μ and $\bar{\nu_\mu}$. Figure 8.11 shows the same (70% oscillation probability) for ν_μ but

[5]This makes the assumptions that ν_μ and $\bar{\nu}_\mu$ come from the same directions which they do and they have an identical energy spectrum which is not true. Although, the energy spectrum are similar they are not the same. For purposes of these plot this will be ignored, although for the final physics results the difference will be included.

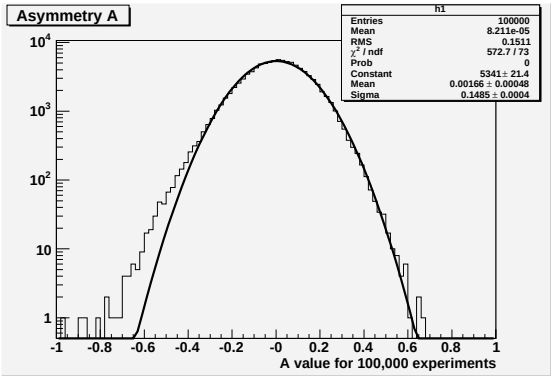

Figure 8.2: This shows the results of an ensemble of 100,000 experiments with the 1-bin test. In each experiment $\rho = 2.0$,$\sigma_\rho = 0.20$,$N_- = 40$,$N_+ = 20$. The variation is caused by the gaussian variation of ρ and the poisson variation in N_-,N_+. The distribution is fit to a guassian. Note the log scale.

no oscillation for $\bar{\nu}_\mu$. Figure 8-12 shows the nominal oscillation parameters for ν_μ and full oscillation for $\bar{\nu}_\mu$. Since these two cases are the extreme cases it is pretty clear that with these statistics even large CPT violation cannot be ruled out. Unfortunately, this thesis has statistics similar to the statistics in this toy MC. This says that large CPT violation cannot be ruled out at the present time[6]. However, what if there are 5 times the data? Figures 8-13,8-14 and 8-15 are identical to 8-10,8-11 and 8-12 except with 5 times the statistics.

[6]The systematics uncertainty, number of events and fraction of oscillated events are all close to the real values discussed in chapter 9

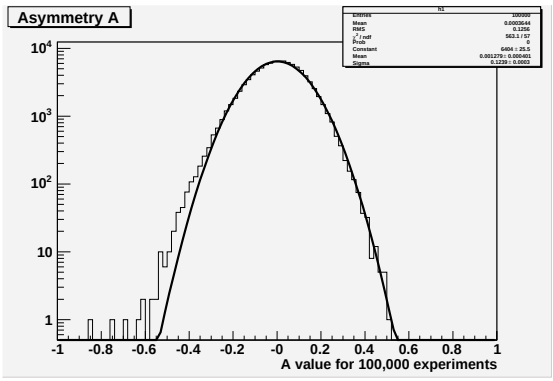

Figure 8.3: This shows the results of an ensemble of 100,000 experiments with the 1-bin test. In each experiment $\rho = 2.0$,$\sigma_\rho = 0.20$,$N_- = 60$,$N_+ = 30$. The variation is caused by the gaussian variation of ρ and the poisson variation in N_-,N_+. The distribution is fit to a guassian. Note the log scale.

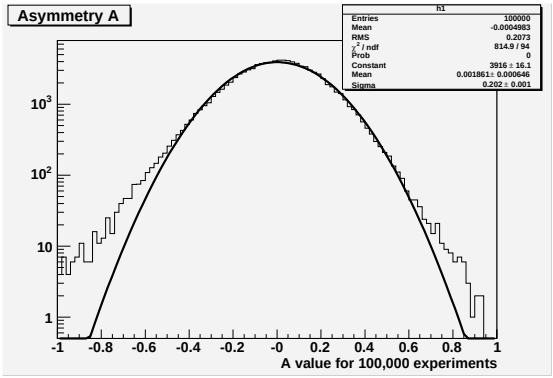

Figure 8.4: This shows the results of an ensemble of 100,000 experiments with the 1-bin test. In each experiment $\rho = 2.0$,$\sigma_\rho = 0.10$,$N_- = 20$,$N_+ = 10$. The variation is caused by the gaussian variation of ρ and the poisson variation in N_-,N_+. The distribution is fit to a guassian. Note the log scale.

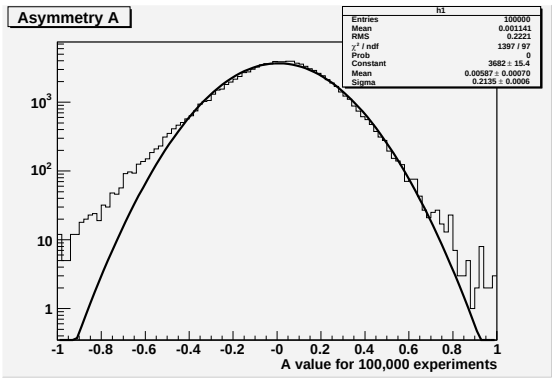

Figure 8.5: This shows the results of an ensemble of 100,000 experiments with the 1-bin test. In each experiment $\rho = 2.0$,$\sigma_\rho = 0.30$,$N_- = 20$,$N_+ = 10$. The variation is caused by the gaussian variation of ρ and the poisson variation in N_-,N_+. The distribution is fit to a guassian. Note the log scale.

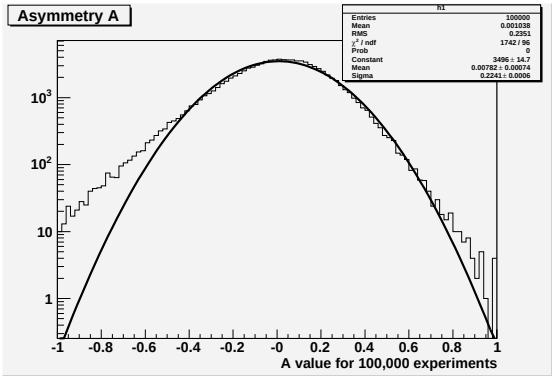

Figure 8.6: This shows the results of an ensemble of 100,000 experiments with the 1-bin test. In each experiment $\rho = 2.0$,$\sigma_\rho = 0.40$,$N_- = 20$,$N_+ = 10$. The variation is caused by the gaussian variation of ρ and the poisson variation in N_-,N_+. The distribution is fit to a guassian. Note the log scale.

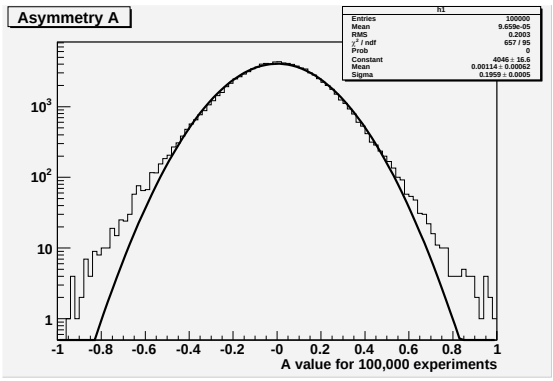

Figure 8.7: This shows the results of an ensemble of 100,000 experiments with the 1-bin test. In each experiment $\rho = 1.0$,$\sigma_\rho = 0.10$,$N_- = 15$,$N_+ = 15$. The variation is caused by the gaussian variation of ρ and the poisson variation in N_-,N_+. The distribution is fit to a guassian. Note the log scale.

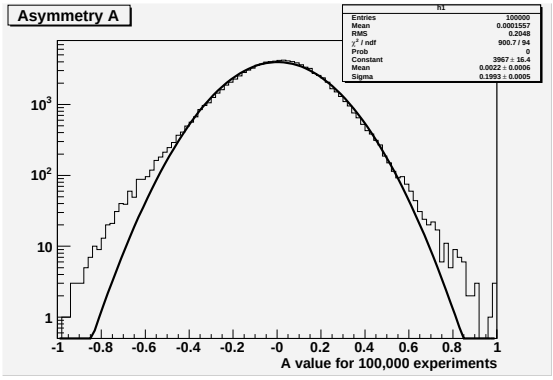

Figure 8.8: This shows the results of an ensemble of 100,000 experiments with the 1-bin test. In each experiment $\rho = 1.5$,$\sigma_\rho = 0.15$,$N_- = 18$,$N_+ = 12$. The variation is caused by the gaussian variation of ρ and the poisson variation in N_-,N_+. The distribution is fit to a guassian. Note the log scale.

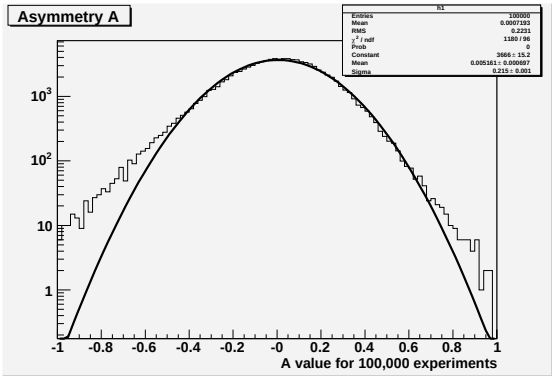

Figure 8.9: This shows the results of an ensemble of 100,000 experiments with the 1-bin test. In each experiment $\rho = 2.5$,$\sigma_\rho = 0.25$,$N_- = 21.43$,$N_+ = 8.57$. The variation is caused by the gaussian variation of ρ and the poisson variation in N_-,N_+. The distribution is fit to a guassian. Note the log scale.

N_-	N_+	ρ	σ_ρ	$\bar{A}_{gaus}$	σ_A	RMS_A	$\sigma_{A-form.}$
20	10	2.0	0.20	0.004	0.206	0.214	0.200
40	20	2.0	0.20	0.002	0.149	0.151	0.146
60	30	2.0	0.20	0.001	0.124	0.126	0.122
20	10	2.0	0.10	0.002	0.202	0.207	0.195
20	10	2.0	0.30	0.006	0.214	0.222	0.208
20	10	2.0	0.40	0.008	0.224	0.235	0.218
15	15	1.0	0.10	0.001	0.196	0.200	0.189
18	12	1.5	0.15	0.002	0.199	0.205	0.193
21.43	8.57	2.5	0.25	0.005	0.215	0.223	0.208

Table 8.1: For this table only 3 significant place were used and the uncertainties in the guassian fits is not shown. The $\bar{A}_{gaus}$ is the mean value from the gaussian fits to the distribution and σ_A is the guassian width from the fit.σ_{A-form} is predicted width from the simple propagation of errors given in formula 8-3. In all cases the simple predicted value for the mean should be zero as it is designed to always give. There is a small bias in the mean. This bias is caused by the fact that poisson statistics cannot fluctuate below zero and because there are more N_- than N_+, the N_- are more gaussian. The bias goes away as the counting statistics get large and the bias goes away as ρ goes to 1. The predicted uncertainty from formula 8.3 is always the lowest estimate (Since it was derived assuming guassian statistics this is not a surprise), the RMS value is the largest and guassian fit is the middle. As with the mean as $\rho \rightarrow 1$ and counting statistics become large the uncertainty in A agree with the simple estimate. However, the three estimates uncertainty agree to better 10% for all cases.

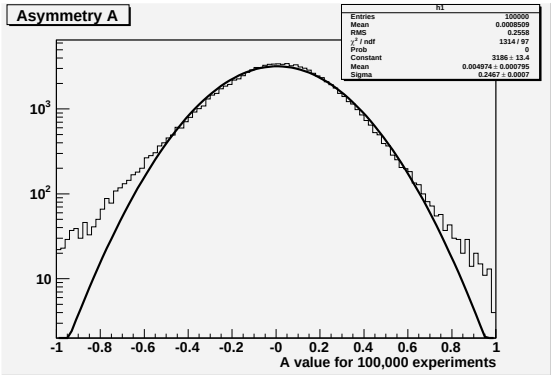

Figure 8.10: This shows the results of an ensemble of 100,000 experiments with the 1-bin test. In each experiment $\rho = 2.0$,$\sigma_\rho = 0.20$,$N_- = 14$,$N_+ = 7$. The variation is caused by the gaussian variation of ρ and the poisson variation in N_-,N_+. The distribution is fit to a guassian. Note the log scale.

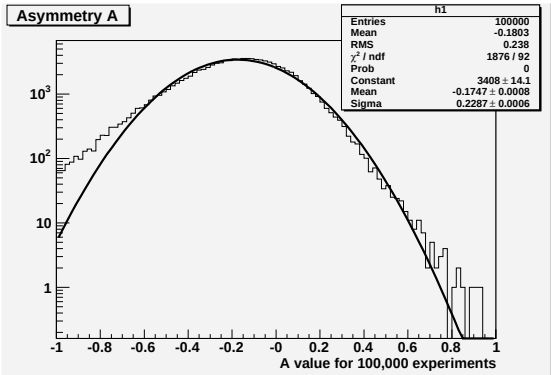

Figure 8.11: This shows the results of an ensemble of 100,000 experiments with the 1-bin test. In each experiment $\rho = 2.0$,$\sigma_\rho = 0.20$,$N_- = 14$,$N_+ = 10$. The variation is caused by the gaussian variation of ρ and the poisson variation in N_-,N_+. The distribution is fit to a guassian. Note the log scale.

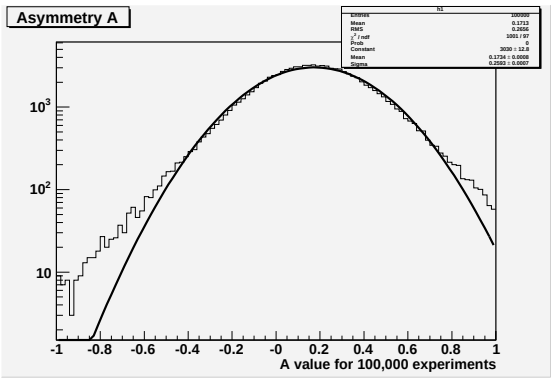

Figure 8.12: This shows the results of an ensemble of 100,000 experiments with the 1-bin test. In each experiment $\rho = 2.0$,$\sigma_\rho = 0.20$,$N_- = 14$,$N_+ = 5$. The variation is caused by the gaussian variation of ρ and the poisson variation in N_-,N_+. The distribution is fit to a guassian. Note the log scale.

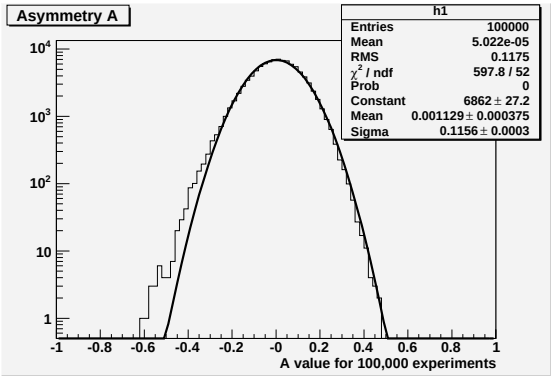

Figure 8.13: This shows the results of an ensemble of 100,000 experiments with the 1-bin test. In each experiment $\rho = 2.0$,$\sigma_\rho = 0.20$,$N_- = 70$,$N_+ = 35$. The variation is caused by the gaussian variation of ρ and the poisson variation in N_-,N_+. The distribution is fit to a guassian. Note the log scale.

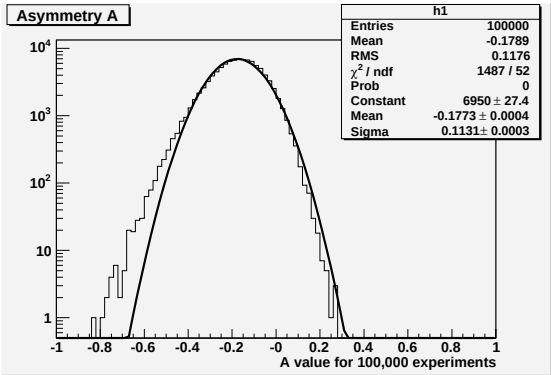

Figure 8.14: This shows the results of an ensemble of 100,000 experiments with the 1-bin test. In each experiment $\rho = 2.0$,$\sigma_\rho = 0.20$,$N_- = 70$,$N_+ = 50$. The variation is caused by the gaussian variation of ρ and the poisson variation in N_-,N_+. The distribution is fit to a guassian. Note the log scale.

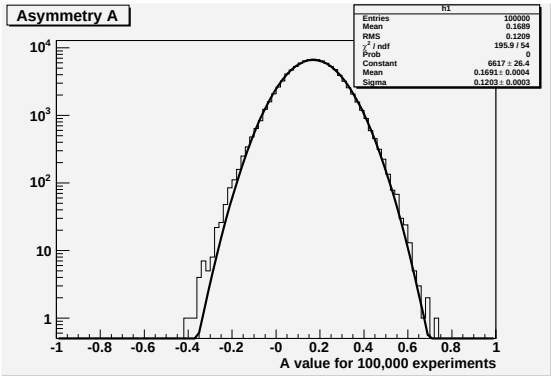

Figure 8.15: This shows the results of an ensemble of 100,000 experiments with the 1-bin test. In each experiment $\rho = 2.0$,$\sigma_\rho = 0.20$,$N_- = 70$,$N_+ = 25$. The variation is caused by the gaussian variation of ρ and the poisson variation in N_-,N_+. The distribution is fit to a guassian. Note the log scale.

Chapter 9

Final results and Conclusions

9.1 Neutrino event selection:MC

9.1.1 Selected neutrino properties

The properties of the selected neutrino events are important to understand in order that a physics measurement can be made. These properties include the energy distribution, Y distribution and the event direction. These properties must be taken from the neutrino MC. There is no easy way to verify the values with data.

Y-distribution

An important question is what y distribution does the selected neutrinos reside in. This can be answered by simply looking at the selected neutrinos y distribution. It is clear after looking at the y-distribution that the cuts select neutrinos with a low y values. The y distribution is shown in figure 9.1:

Neutrino direction

The observed direction of the track is not the same as the true direction of the neutrino. This happens in part because the reconstruction software cannot reconstruct

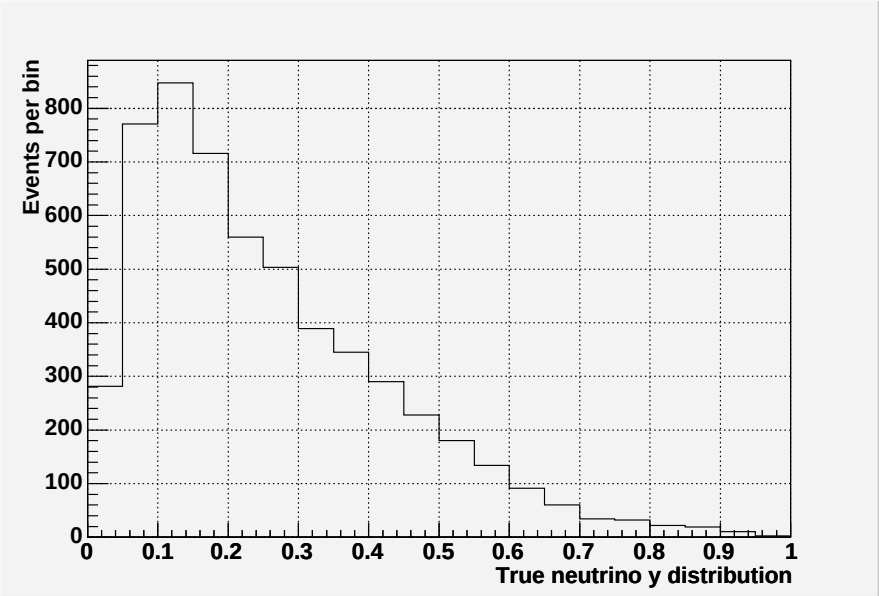

Figure 9.1: This shows the selected MC events y-distribution.

the track with perfect precision, although because of kinematics and fermi-motion the distributions are smeared out anyway. This is shown in figure 9.2.

Energy distribution

The energy of the selected events is a standard plot that one would like to understand as it is important for oscillations. Figure 9.3 shows the energy distribution.

9.2 Final event selection

The nine cuts discussed in chapter 6 are applied to the dataset. The results of this work are the final event selections and are presented in table 9.1. It should be expected that the cuts treat the data and MC in a similar way. Although, the final estimate of the background will be based on sidebands in the data, not the cosmic μ MC. The reasons for this are discussed later in this chapter.

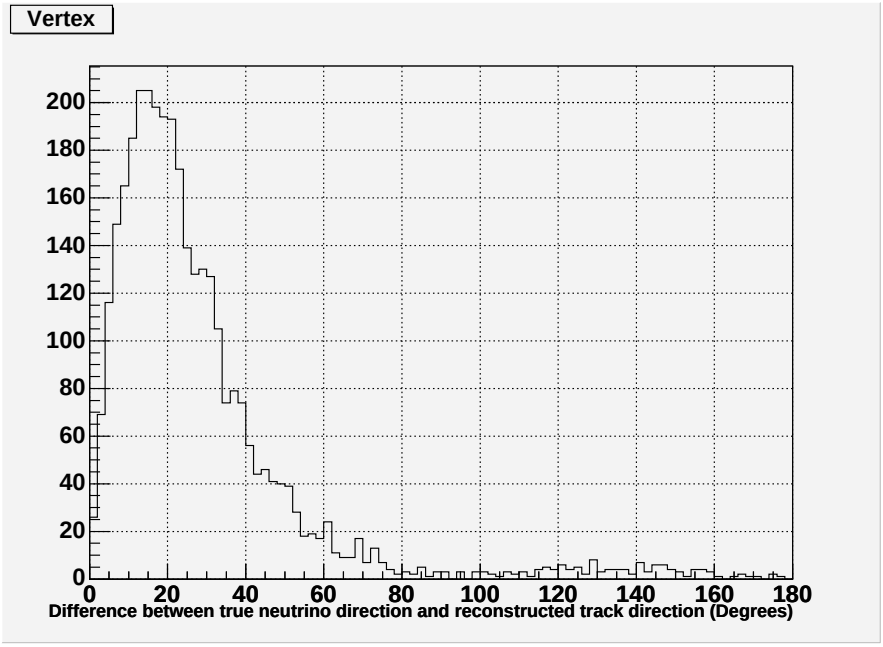

Figure 9.2: This shows the difference between the reconstructed track and true neutrino direction of the selected MC events. This causes the smearing in L which limits the power of atmospheric neutrino experiments to measure oscillation parameters.

The overall result from table 9.1 is positive. The cuts do seem to act in the same way on data and MC. The results given so far are for no oscillations. If the oscillations parameters[1] are $\Delta m^2 = 2.4 \times 10^{-3} eV^2$,$sin^2(2\theta) = 1.0$ then the predicted number of neutrinos events are 33.5±7.7[2]. The result of this reduction in rate is to make the agreement between expected events and data worse then it was before. However, this is based on an estimate of the cosmic μ MC alone. This is not done (in the end) as

[1]This value is chosen because it is what the Cambridge group choose to use for it's analysis. However, the results are not that sensitive provided the true oscillations parameters are not extremely different.

[2]This number is not just dependent on the oscillation parameters chosen, it also depends on the production height model that is used. The production model used is a delta function at 25 km. If for example a delta function at 50 km is used the expected number of events is 31.6±7.3 events for the same oscillation parameters,$\Delta m^2 = 2.4 \times 10^{-3} eV^2$,$sin^2(2\theta) = 1.0$. The real way to do this is to use the Ruddick model as given in chapter 5. However, the oscillation parameter fit is not the main purpose of this thesis so the 25 km delta function will be used.

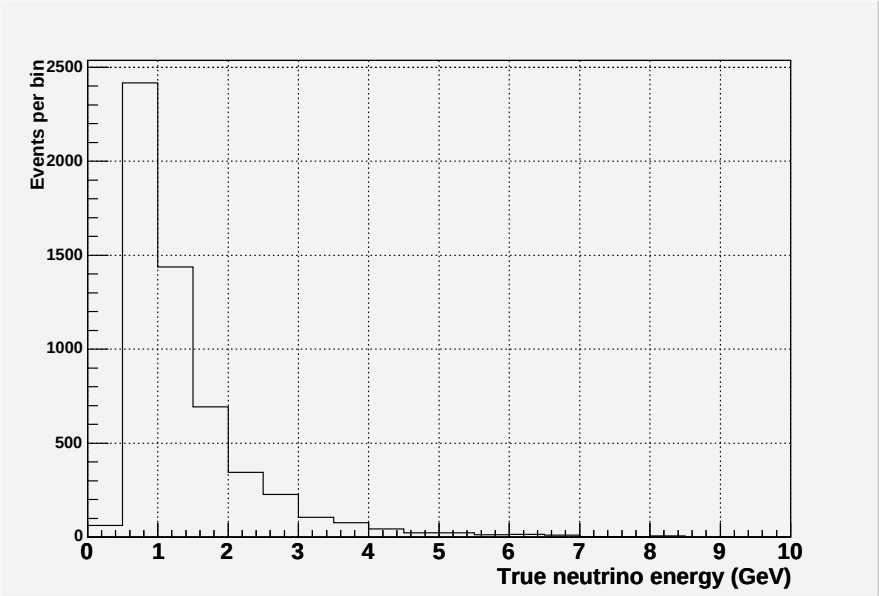

Figure 9.3: This shows the true energy distribution of the events in GeV.

a better way to estimate the background is with a sideband (see section 9.5) in the data. From the sideband, it is possible to estimate that 79 ± 15 events are the cosmic μ background. This should be compared with the 38±10 from the MC alone. As will be shown, the data based estimate agrees well with the number of vetoed events while the MC based estimate does not.

9.3 Background estimation

Before the vetoshield there are a variety of backgrounds that survive all the cuts. However, the total number of background is small after the vetoshield. Table 9.2 shows the background from both ν and the background from neutrons and cosmic μ.

Thus the total number of expected events in the far detector is 53.1±10.4 events (1σ). If the systematic and statical errors are broken down the result is an expectation of 50.7±7.6(syst.)±7.1(stat.) ν events and (to one significant figure) 2.4±0.2(syst.)±0.3(stat.)

Cut #	ν_μ	$\bar{\nu_\mu}$	Bkg. ν	Total ν	Cosmic-μ MC	Exp. Evts.	Data
None	98.2	33.8	16.9	148.9±25.4	70,000±7,000	70,150±7,000	73,488
1	96.5	33.2	16.4	146.1±25.0	66,900±6,700	67,050±6,700	69,970
2	92.3	31.3	16.1	139.7±24.1	12,790±1,290	12,930±1,290	14,737
3	71.9	25.2	8.2	105.4±18.8	7,390±750	7,500±750	8,491
4	62.0	21.3	7.6	90.9±16.6	3,715±380	3,810±380	4,589
5	61.3	20.4	7.6	89.3±16.4	2,088±220	2,177±221	2,415
6	60.1	19.9	7.5	87.5±16.1	1,175±128	1,263±129	1,284
7	46.4	15.8	3.5	65.7±12.8	157.5±24.6	223.2±27.7	292
8	38.5	14.1	1.7	54.3±11.0	139.5±22.6	193.8±25.1	253
9	35.9	13.2	1.5	50.7±10.4	38.3±10.0	89.0±14.4	112

Table 9.1: In this table the neutrinos are normalized to an unoscillated 5.0 kTy exposure. The neutrinos are from R179 and R180. This file assumes solar maximum and a Barr flux model. The errors shown are the quadrature sum of systematic and statistical errors. The neutrinos are assumed to have a 15% systematic uncertainty and the cosmic MC μ are assumed to have 10% systematic uncertainty. The background ν are non CC-ν_μ,$\bar{\nu_\mu}$ events that pass the selection. This does not include oscillated ν_τ. The cut number is the same as the cut selection shown in chapter 6. The data and MC show the zero and one shower events together and this is all before any vetoshield cut is applied. The none cut is just the post filter result. After the vetoshield a total of 41 events are observed.

cosmic μ events. The cosmic μ background is calculated by using vetoshield efficency[3] and the estimate of background from data.

9.4 Final Vetoshield results

In chapter 6 a detailed look at the stopping muon sample was used to determine that the vetoshield efficiency was $97.4 \pm 0.1\%$ and had a false rejection rate of $0.5 \pm 0.1\%$. This is not the absolute end of the story because the stopping muons and the candidate events have different angular distributions and this could lead to differences in vetoshield performance. To test this the candidate dataset will have the relevant qualities compared with the stopping muon sample to see if there is any differences. This will be done with the total candidate dataset before the final selections cuts are applied

[3] As caculated in section 9.4

Background	Number of events
Neutron	≤ 4.5 (95% C.L)
Cosmic-MC μ	1.15 ± 0.60 (95% C.L)
Cosmic-Data μ	2.4 ± 0.8 (95% C.L)
ν_e	0.80 ± 0.31 (95% C.L)
NC	0.65 ± 0.26 (95% C.L)
ν_τ	0.41 ± 0.20 (95% C.L)
Total	4.3 ± 0.9 (95% C.L)
Total ν	1.86 ± 0.45 (95% C.L)

Table 9.2: This shows the final estimates of the backgrounds to CC ν_μ signal. All entries show zero and single showers and also show ν and $\bar{\nu}$. All are normalized to a 5.0 kTy exposure. The estimates of the cosmic μ background based on MC and the sideband are shown after the vetoshield efficiency is applied. The neutron result is the only estimate given before the vetoshield. Given that these neutrons enter the detector in spallation events that shower the area with other neutrons and photons it likely most of these events will be tagged and no neutrons will enter the dataset. The ν_τ rate is based on full oscillation, in this sense it is really an upper limit. If realistic oscillation parameters are put in the ν_τ rate changes by only 20%. The total ν background rate cannot be improved with an improved vetoshield, it is irreducible with regard to the cuts used. The total estimate of 4.3 ± 0.9 background events is based on the data estimate for cosmic μ.

to get good statistics. The vetoshield cuts determined from the stopping muons are to accept any event that has no in-time vetoshield hit within 1 m of the projected track and 180 adc counts per digit or less for all events with 2+ in-time digits.

9.4.1 Digit distribution

The digit distribution is important as this is the first way the vetoshield data is categorized. The zero, one[4] and two or more digits sample each give different contributions to the vetoshield efficiency and false rejection rate. Given the differences in the angular distributions and event quality (stopping μ are reconstructed well on average) it might

[4]If the zero digit case contains neutrinos it must be increased in the candidate set. In particular, the candidate set has 1732 events with zero in-time digit hits. From the stopping set it can estimated that $1600 \pm 40 \pm 30$ events should have zero digits in the candidate set. Although already consistent with the estimate number events, if some of the candidate events are from neutrinos, the agreement becomes better still.

even be surprising if these were exactly the same, although they should be close. The digit distribution is shown in table 9.3.

Number of Digits	Stopping Sample fraction	Candidate sample fraction
0	0.0218 ± 0.0004	0.0236 ± 0.0006
1	0.0476 ± 0.0006	0.0644 ± 0.0009
2+	0.9306 ± 0.0007	0.9121 ± 0.0010

Table 9.3: The stopper dataset is same set that was used in section 6.9. The candidate dataset contains 73,488 events. The conclusion of this is that the vetoshield efficiency is lower for the candidate events than it is for the stopping muons. This is small but significant difference. The zero digit result is only slightly higher than expected and is not really significant. The fraction of 1 and 2+ digits is different and this will change the efficiency.

The conclusion that is reached from the candidate sample vetoshield distribution is that the vetoshield efficiency is going to be lower than the stopping muon sample because the relative fraction of 1 digit to 2+ digit event is higher in the candidate events than in the stopping muons and the 1 digit events have a lower rejection rate. The cause of this is not known, although given the better tracking that can be expected from the stopping muons this is not a hugh surprise.

9.4.2 1 digit

The 1 digit sample is important as it is the second leading source of inefficiency behind the 0 digit sample. The single digit sample is shown in table 9.4.

9.4.3 2+ digit

The 2+ digit dataset should have near perfect rejection if the stopper sample can be used as a guide. This is the case although the rejection is not as good as it was for the stopping muon sample. The stopping muons 1 meter spatial cut rejects $98.75 \pm 0.03\%$ of events while the same cut in the candidate sample gives $95.81 \pm 0.08\%$ rejection (see table 9.5). In a similar fashion, the pulse height cut rejects $92.69 \pm 0.07\%$ in the stopping

Spatial cut (m)	Stopping sample fraction	Candidate sample fraction
0.10	0.339 ± 0.006	0.283 ± 0.007
0.20	0.590 ± 0.006	0.528 ± 0.007
0.50	0.860 ± 0.004	0.840 ± 0.005
1.00	0.935 ± 0.003	0.918 ± 0.004
2.00	0.948 ± 0.003	0.944 ± 0.003

Table 9.4: This shows the vetoshield efficiency(η) for single digit hits events for all runs. There are a total of 7025 single digit events for the stopping muon sample and 4731 events for the candidate sample. The efficiency is defined as $\eta = \frac{S}{S+U}$ where S is selected events and U is unselected events. The rejection of cosmic μ is $93.47 \pm 0.29\%$ for the stopping muon sample and $91.82 \pm 0.40\%$ for the candidate sample.

muons and only $91.73 \pm 0.11\%$ in the candidate sample (see table 9.6). The net rejection of the 2+ digit events is $99.91 \pm 0.01\%$ in the stopping muons and $99.68 \pm 0.02\%$ in the candidate events.

Spatial cut (m)	Efficiency on stopper	Efficiency on candidate sample
0.05	0.3393 ± 0.0013	0.2808 ± 0.0017
0.10	0.5696 ± 0.0013	0.4890 ± 0.0019
0.20	0.7995 ± 0.0011	0.7096 ± 0.0018
0.30	0.9360 ± 0.0007	0.8360 ± 0.0014
0.50	0.9741 ± 0.0004	0.9121 ± 0.0011
1.00	0.9875 ± 0.0003	0.9581 ± 0.0008
2.00	0.9931 ± 0.0002	0.9757 ± 0.0006

Table 9.5: This shows the vetoshield efficiency(η) for 2+ digit hit events for all runs. There are a total of 137337 2+ digit events that are in-time for the stopper sample and 67025 for the candidate sample. The efficiency is defined as $\eta = \frac{S}{S+U}$ where S is selected events and U is unselected events. The rejection rate for the 1 meter cut is $98.75 \pm 0.03\%$ for the stopper sample and $95.81 \pm 0.08\%$, for the candidate events. For the total efficiency the pulse height cut must also be included.

9.4.4 Efficiency and false rejection rate

Because the inefficiency is dominated by the events that trigger without any in-time vetoshield activity (0 digit) sample, the fact that the 1 and 2+ digit sample have a slightly lower efficiency does not change the total efficiency that much. The total efficiency is defined the same way it was defined for the stopping muon set:

PH cut (ADC/digit)	Number of stopper sample	Efficiency on candidate sample
100	0.9963 ± 0.0002	0.9954 ± 0.0003
120	0.9891 ± 0.0003	0.9874 ± 0.0004
140	0.9765 ± 0.0004	0.9724 ± 0.0006
160	0.9557 ± 0.0006	0.9498 ± 0.0008
180	0.9269 ± 0.0007	0.9173 ± 0.0011
200	0.8889 ± 0.0008	0.8745 ± 0.0013

Table 9.6: This shows the vetoshield efficiency(η) for 2+ digit hits events for all runs. There are a total of 137337 2+digit events that are in-time for the stopper sample and 67025 for the candidate sample. The efficiency is defined as $\eta = \frac{S}{S+U}$ where S is selected events and U is unselected events. The cut requiring 180 or adc/digit eliminates $92.69 \pm 0.07\%$ for the stopper sample and $91.73 \pm 0.11\%$ for the candidate sample. For the total efficiency the spatial cut must be included.

$$\eta = \eta_{0digit} \cdot \frac{N_{0digit}}{N_{tot}} + \eta_{1digit} \cdot \frac{N_1 digit}{N_{tot}} + \eta_{2+digit} \cdot \frac{N_{2+digit}}{N_{tot}} \tag{9.1}$$

For the stopping muons this give an total efficiency of $97.4 \pm 0.1\%$, for the candidate sample this gives an efficiency of $96.8 \pm 0.2\%$ for the candidate events. The false rejection is somewhat model dependent (see Chapter 6.9 for details), but was found to safely be less than $0.5 \pm 0.1\%$ from the stopping muons. This really should be independent of the event identified in the detector, the only two ways that the false rejection could change was if the random noise in the shield was different in the stopping and candidate samples or if the 1 or 2 (3 or more random digits are rare) digit hits have a spatial correlation in the candidate data that was not apparent in the stopping data. Both of these were looked at and there is no evidence of either. Thus the false rejection can be used from the stopping muon sample without any correction.

9.5 Results-Selected events

The selected events are the neutrino candidates. This can be looked at both before and after the vetoshield. By looking at these events it is possible to see if the events look like the expected signal or background.

9.5.1 Before the vetoshield

Before the vetoshield there are 112 events. This should be compared with an expectation (without oscillation) of 89.0 ± 14.4 events. This is consistent with the expectation although the situation is really more complex for two reasons. First, it is expected there are neutrino oscillations that lower the expected number of neutrinos and the μ background is based on a cosmic μ MC not data.

9.5.2 Independent estimate of background

Since the background of cosmic muons is dominated by events entering the detector from strange directions and are odd events in general, a valid question might be does the estimated μ background really agree with data in a quantitative manner? The answer to this is no. The background seems to underestimate the true background by as much as a factor of 2. Thus with this level of disagreement a independent way to estimate the background is useful. This will be done by looking at a sideband to the selected candidate events. An ideal sideband would have many events for large statistics but be as similar to the data as possible. This was accomplished by relaxing cut number 7[5] and keeping all the other cuts (all 8 of them) the same. In particular all events with a ph fraction less than 0.75[6] were used with all other cuts being the same. This gives 507 events of which 492 have a shower. When the identical cuts are applied to the cosmic μ MC the result is 225 events of which 221 have a single shower. The ratio[7] of these is 2.25 ± 0.18 is consistent with the normalization. This suggests that the number of cosmic μ events is consistent between data and MC in the sideband. The

[5]Cut 7 is the fraction of pulse height in the track versus total pulse height in the event

[6]This is exclusive. None of these events are in the signal region.

[7]The astute reader might wonder if this comparison is really correct as the data should contain some signal events (neutrinos) and all of events in the cosmic ray set will not be vetoed. It is not but if the corrections are carried out the answer does not change and an additional possible uncertainty has been added. So the 'almost' correct solution is given.

difficulty comes in extrapolating this to the signal region.

To accomplish this extrapolation the following will be done. The number of data events in the sideband region will be compared with the number of data events that pass all the cuts through cut 6 and have the sideband pulse height fraction (< 0.75). Then the same thing will be done for the cosmic μ MC sample. A total of 992 data events in the sideband (972 with a shower) pass all cuts up to six being used with the sideband ph fraction. This means that in the data the fraction of events in the sideband that remain after cuts 8 and cut 9 is 0.51 ± 0.03. When the cosmic μ MC has all the applied cuts up to cut 6 with the requirement for the sideband ph fraction a total of 452 events pass. The fraction of events that remain after cut 8 and cut 9 in the sideband region of the cosmic μ MC is 0.50 ± 0.04. On the other hand, the cosmic μ MC predicts 70 events that pass all the cuts up to and including the ph fraction cut (7) and only 17 that pass all 9 cuts which is a fraction of 0.28 ± 0.07. There are many more events in the sideband than in the signal region for the cosmic μ MC. Since the fraction of events that get cut in the sideband region when cut 8 and cut 9 are applied agree between the data and MC it will be used to estimate the background in the signal region. The estimate will be based on assuming that the signal region has a fraction of 0.50 ± 0.04 event survive cut 8 and cut 9 not 0.28 ± 0.07. This is done because there are many more events (MC cosmic μ) in the sideband region than in the signal region so the statistics are better. This also reduces the dependence of the tracking in the background sample. Remember the background events that enter the sample after the first 6 cuts are not average muons, they are extraordinary muons with just the correct properties to make it this far into the detector without being tagged as background. The observed signal is not such an extraordinary event and is not unlike many other signal events[8]. With the use of the passing fraction of 0.50 ± 0.04, the estimate for the

[8]The probability of a cosmic μ to pass the first 6 cuts of the analysis is $\approx 10^{-5}$ while the probability of an signal event making it pass the first 6 cuts is ≈ 0.1. The exact numbers depend somewhat on the precise comparison, but the point is evident. The signal events (ν_μ) are not that unusual for

of cosmic μ background is increased from 38 ± 10 to 79 ± 15. An valuable cross check would be to use other sidebands in different quantities. This is not as easy as it might appear. Other sidebands were examined and either had lower statistics or had events that were not that similar to the signal. The implication of this sideband study is that the cosmic μ MC background is underestimated by factor of about two[9]. Considering that the odds of a muon enetering this sample are on the order of 10^{-6} or less this is not unacceptable. Given the current understanding of the MC, the data sideband must be used to estimate the background.

9.5.3 After the vetoshield

After the vetoshield requirement on hits, 43 events are observed in the data. It is expected that all of these events should have 0 (mostly) or 1 (a few) or 2 (unlikely) hits. It is observed that 40 events have 0 digits, 1 event has 1 digit and 2 events have 3 digits. This is a bit of a surprise, 3 digits events are not expected and not consistent[10]. Does this mean the vetoshield model is flawed? Not necessarily, the first point that should be made is that if you ignore the two events the result of 41 events with no hits and 1 event with 1 hit is perfectly consistent with the prediction of the noise model. The second point is that the two events which have 3 digits are at the edge of acceptance. Both have poor charge resolution and so neither event would enter the sample to test CPT in any case.

ν events that form a short track, the cosmic μ events are unusual. The implication is that details of the reconstruction matter more for background than for signal. The signal have 'normal' angular acceptances, tracking and other quantities and the background at this late stage of reconstruction do not.

[9]The amount of this underestimation is difficult to judge with the limited statistics in the cosmic μ MC sample.

[10]If the most (unrealistically) worst case scenario false rejection model from section 6.9 is used it can be estimated that the probability of two events with 3 digits of random noise is $\leq 10^{-6}$, under more realistic model it is even more unlikely.

Modified vetoshield cut

A possible way to deal with the extra events is to modify the vetoshield cuts[11] .The effect of changing the vetoshield cut to require that no event has more than 2 in-time hits is easy to calculate. The first point is that the false rejection does not change as three in-time hits are rare to start with. However, the efficiency is improved, although the improvement is small. The reason for this is that the 2+ digits samples had almost perfect rejection to start with and there is nearly no room for improvement. In the stopping muon sample there was 117 events that were not vetoed, this is reduced to only 44 events after requiring no more than 2 hits. The candidate sample goes from 213 let through down to 70 events un-vetoed. However, because the in-efficiency is almost completely dominated by the 0 and 1 digit in-efficiencies the effect of this is small. The new total efficiency for candidates are 0.970 ± 0.002 and for the stopping muons it is 0.975 ± 0.001.

9.5.4 Properties of selected events

After the vetoshield is applied the event selection is complete. An important question to ask is do the reconstructed candidate event have characteristics consistent with neutrinos. If the answer to this is no, then the validity of the analysis can be questioned.

[11]This is clearly not a 'blind analysis' way of dealing with the events but it is not in particular that biased either. This is because the main purpose of the analysis is to investigate CPT and these events do not enter that data set as they are poorly reconstructed. A second point is this cut was seriously considered before the vetoshield cuts were set with the stopping muons and only rejected out of a desire to keep the cuts as simple as possible. Thirdly, the cut is clearly justified by looking at the false rejection model and the pre-trigger window data. It is clear three in-time hits occur randomly in the short in-time window less than one in a thousands events. The final point is it does not really change the final physics distributions for the non-charge ID events. It is certainly true the distribution looks slightly better with the two events removed, given the size of statical uncertainties, systematic uncertainties, differences between the real and MC detector, the lack of a vetoshield MC and uncertainty in the actual physics, there is no reason to really believe this difference is significant. On the other hand given how close the events are to the edge of acceptance of the detector and the excessive vetoshield activity, it is completely reasonable to think they are most likely background. The point of this is that accepting the two events does not improve the physics results in a quantitatively measurable manner but vetoing them is not quantitatively unjustifiable either.

The properties that can be checked in the candidate sample fall into different categories. The first category of tests is to see if the distribution of the events in the detector is consistent with expectation. The second category of tests is to see if the reconstruction is consistent with neutrinos. The third category of tests is to see if the physics results are consistent with the expectations of neutrino oscillation. For all the following results the modified veto shield cut is applied. In all of the figure the red solid line is the pre-vetoshield candidates, the blue dashed line is an unoscillated 5.0 kTy atmospheric neutrino exposure and the black points with error bars are the final candidate events.

Detector distributions

The following six distributions are shown, the track vertex in y (9.4) and z (9.5), the directional cosine at the track vertex in x (9.6) and z (9.7) and the radial position of the track vertex (9.8) and track end (9.10). All six show good agreement to the ν MC.

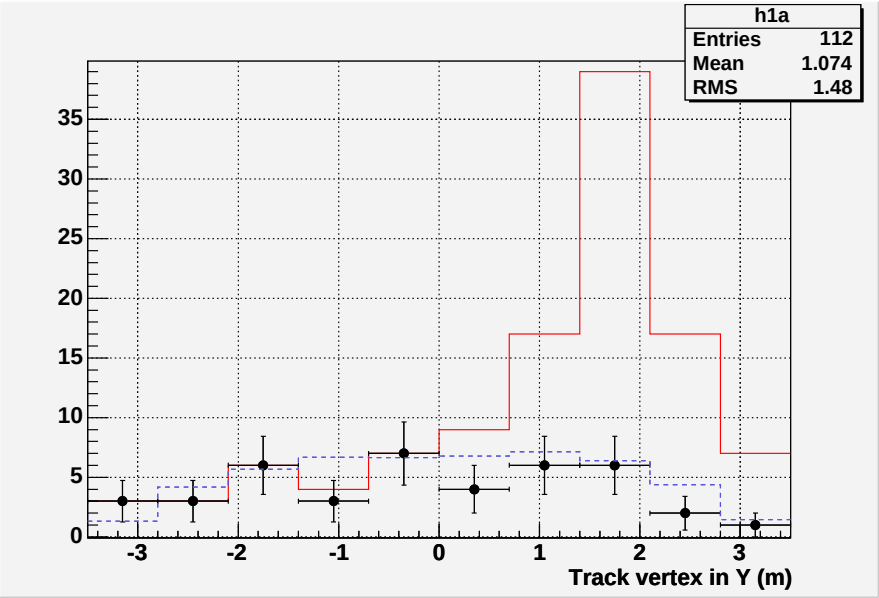

Figure 9.4: This shows the track vertex in Y. The red solid line is the pre-vetoshield candidates. The blue dashed line is an unoscillated 5.0 kTy atmospheric neutrino sample. The black points with error bars are the final candidate events.

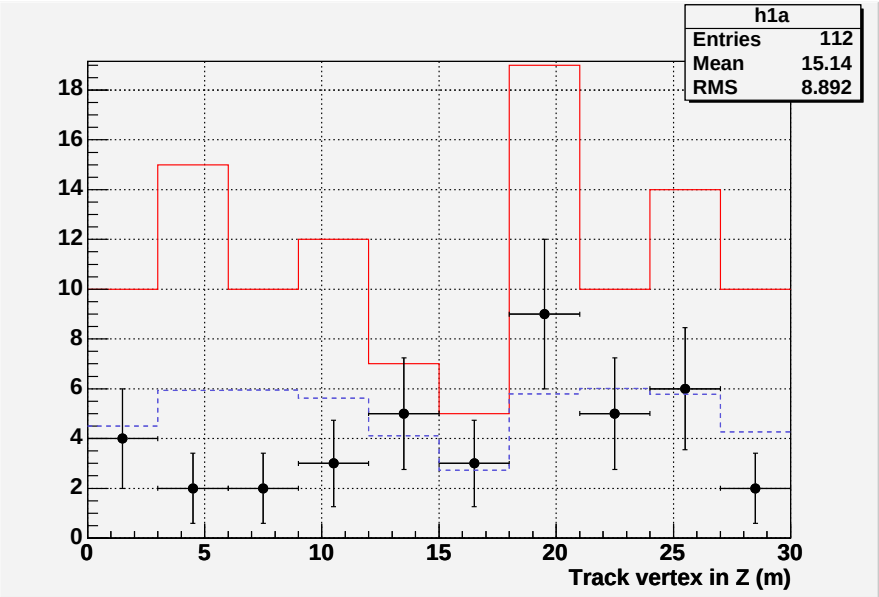

Figure 9.5: This shows the track vertex in Z. The red solid line is the pre-vetoshield candidates. The blue dashed line is an unoscillated 5.0 kTy atmospheric neutrino sample. The black points with error bars are the final candidate events.

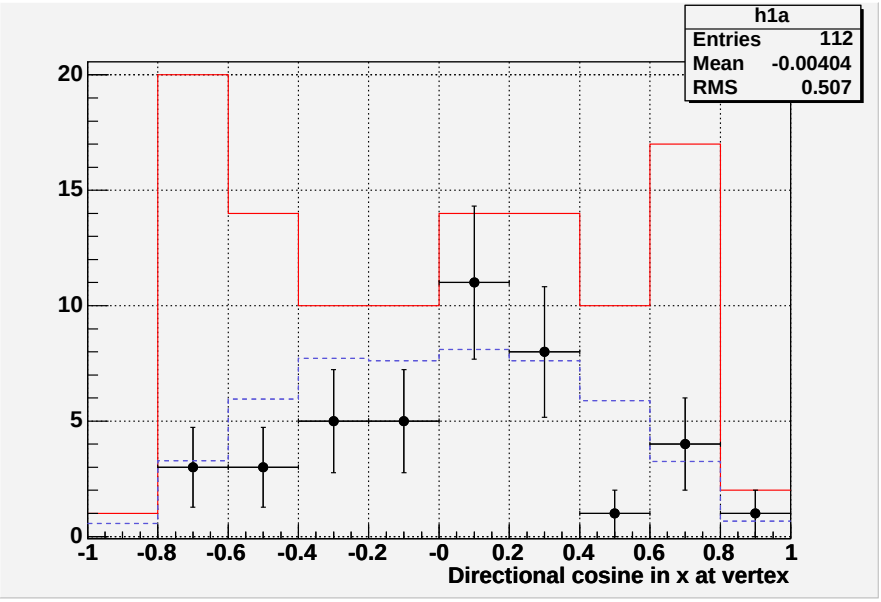

Figure 9.6: This shows the directional cosine with respect to x at the track vertex. The red solid line is the pre-vetoshield candidates. The blue dashed line is an unoscillated 5.0 kTy atmospheric neutrino sample. The black points with error bars are the final candidate events.

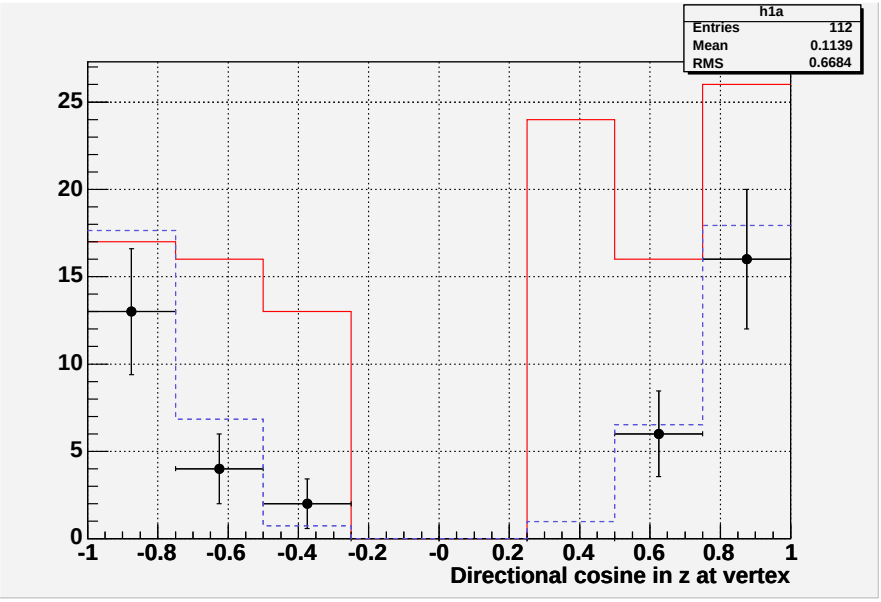

Figure 9.7: This shows the directional cosine with respect to z at the track vertex. The red solid line is the pre-vetoshield candidates. The blue dashed line is an unoscillated 5.0 kTy atmospheric neutrino sample. The black points with error bars are the final candidate events.

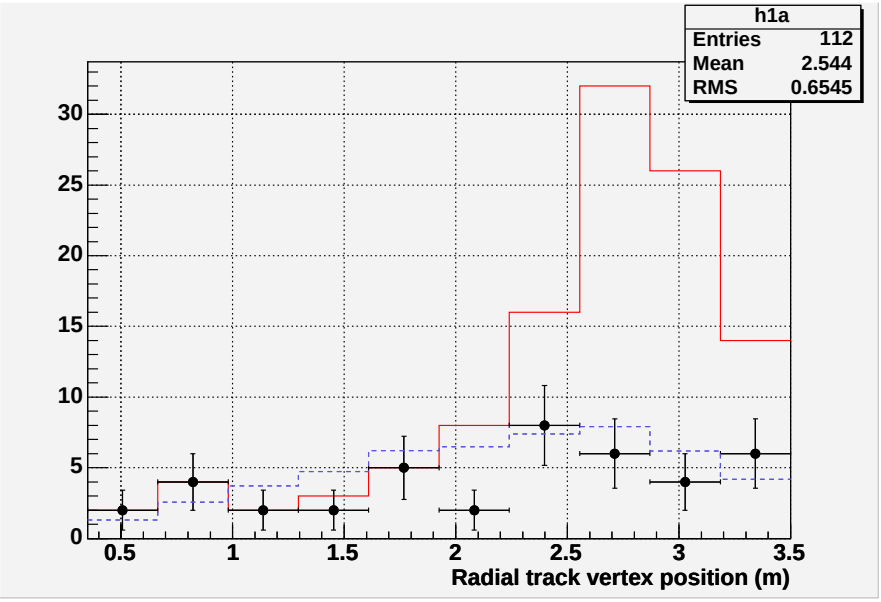

Figure 9.8: This shows the radial position (m) of the track vertex. The red solid line is the pre-vetoshield candidates. The blue dashed line is an unoscillated 5.0 kTy atmospheric neutrino sample. The black points with error bars are the final candidate events.

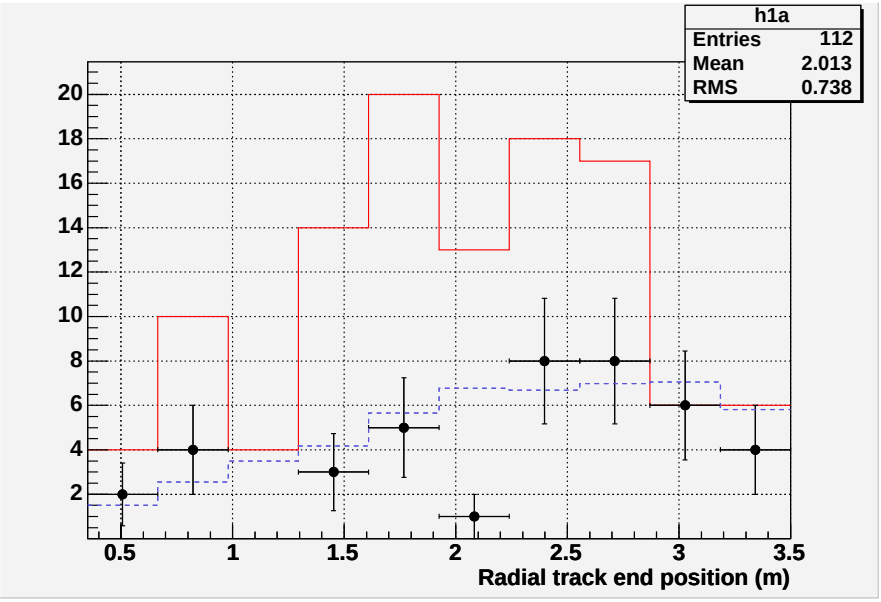

Figure 9.9: This shows the radial position (m) of the track end point. The red solid line is the pre-vetoshield candidates. The blue dashed line is an unoscillated 5.0 kTy atmospheric neutrino sample. The black points with error bars are the final candidate events.

Reconstruction distributions

The reconstruction quantities that will be look at are the number of tracklike planes (9.11), the fitted tracks χ^2 per dof (9.12), the number of showers in the event (9.13), the number of planes in a shower (9.14), the fraction of total ph in the track (9.15) and $\frac{1}{\beta}$ (9.16) distribution which is sensitive to the event timing. These show that events being reconstructed as candidates are actually being reconstructed as the ν MC would predict.

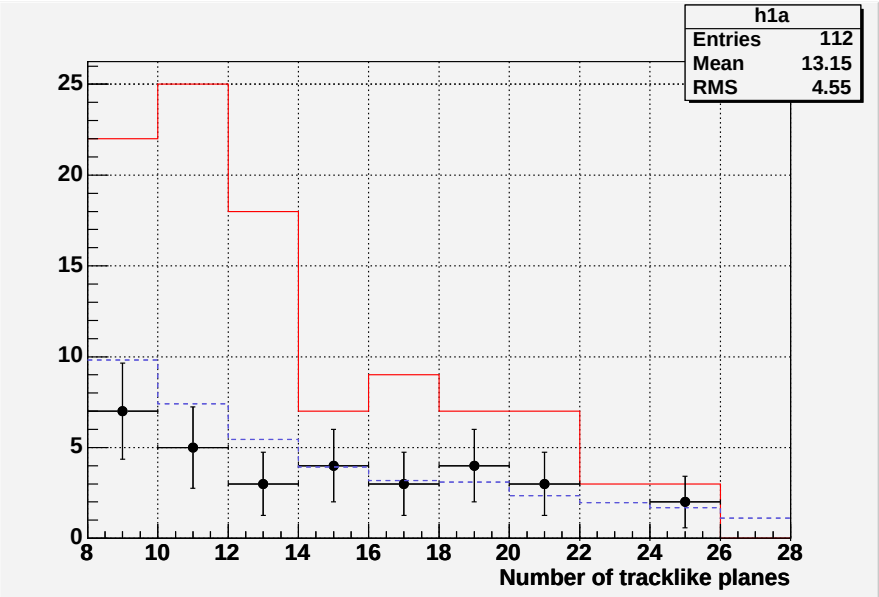

Figure 9.10: This shows the number of tracklike planes in an event. The red solid line is the pre-vetoshield candidates. The blue dashed line is an unoscillated 5.0 kTy atmospheric neutrino sample. The black points with error bars are the final candidate events.

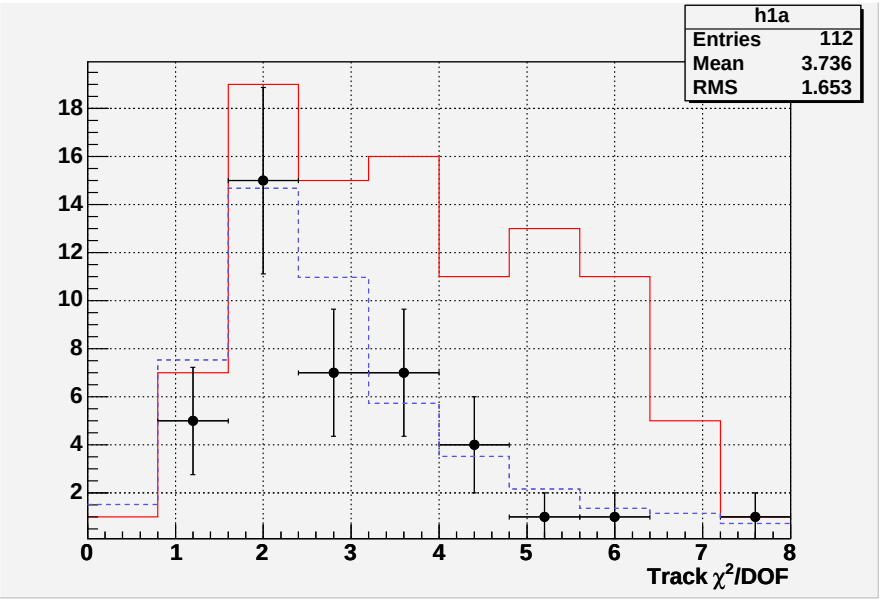

Figure 9.11: This shows the χ^2 per degree of freedom for the tracks. The red solid line is the pre-vetoshield candidates. The blue dashed line is an unoscillated 5.0 kTy atmospheric neutrino sample. The black points with error bars are the final candidate events.

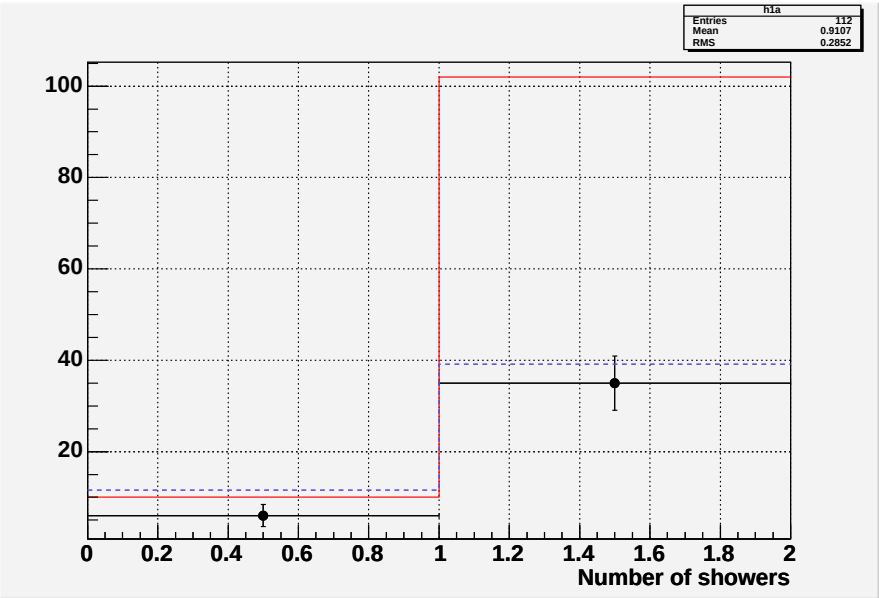

Figure 9.12: This shows the number of showers in the event. The red solid line is the pre-vetoshield candidates. The blue dashed line is an unoscillated 5.0 kTy atmospheric neutrino sample. The black points with error bars are the final candidate events.

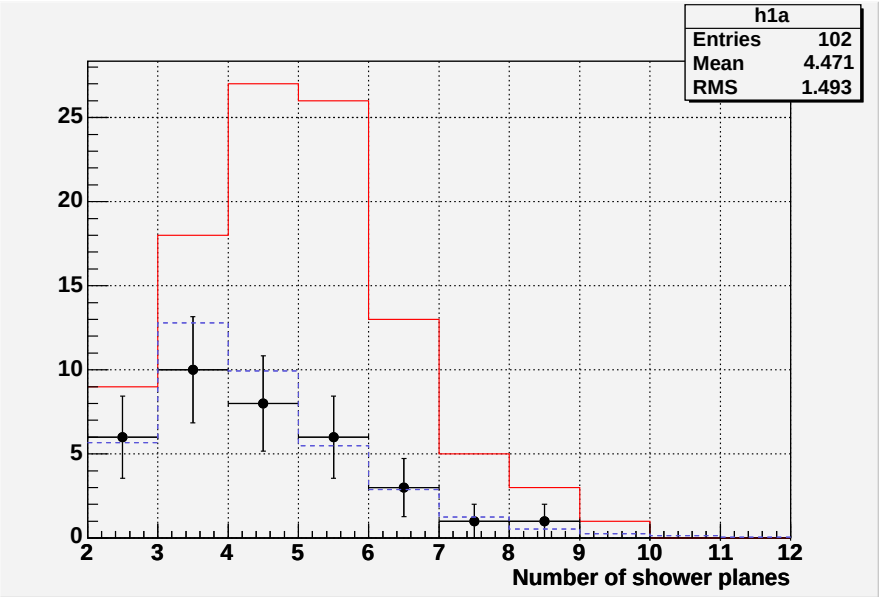

Figure 9.13: This shows the number of planes in a shower. The red solid line is the pre-vetoshield candidates. The blue dashed line is an unoscillated 5.0 kTy atmospheric neutrino sample. The black points with error bars are the final candidate events.

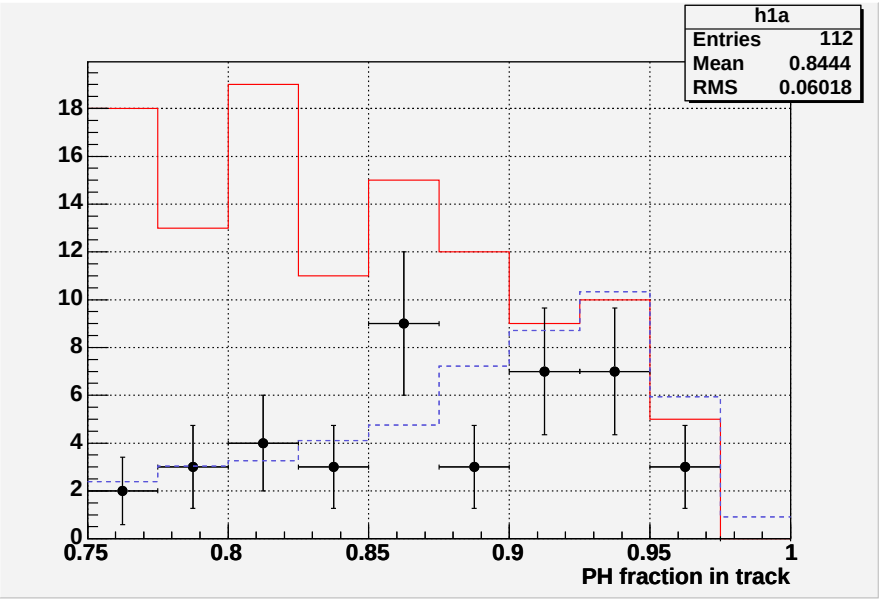

Figure 9.14: This shows the ph fraction in the track versus the total ph in the event. The red solid line is the pre-vetoshield candidates. The blue dashed line is an unoscillated 5.0 kTy atmospheric neutrino sample. The black points with error bars are the final candidate events.

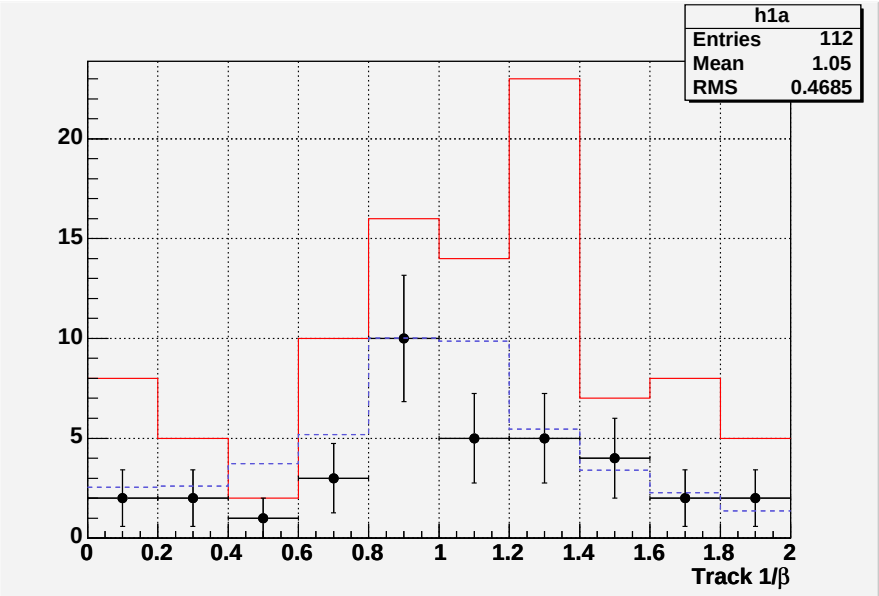

Figure 9.15: This shows the $\frac{1}{\beta}$ distribution which is 1 over the absolute value of the particles apparent speed. This is sensitive to the timing. The red solid line is the pre-vetoshield candidates. The blue dashed line is an unoscillated 5.0 kTy atmospheric neutrino sample. The black points with error bars are the final candidate events.

Physics distributions

The physics distribution look for the effects of neutrino oscillation. These include the zenith angle distribution (9.17), the track momentum (9.18) by range, the neutrino energy (9.19) and L/E distribution (9.20).

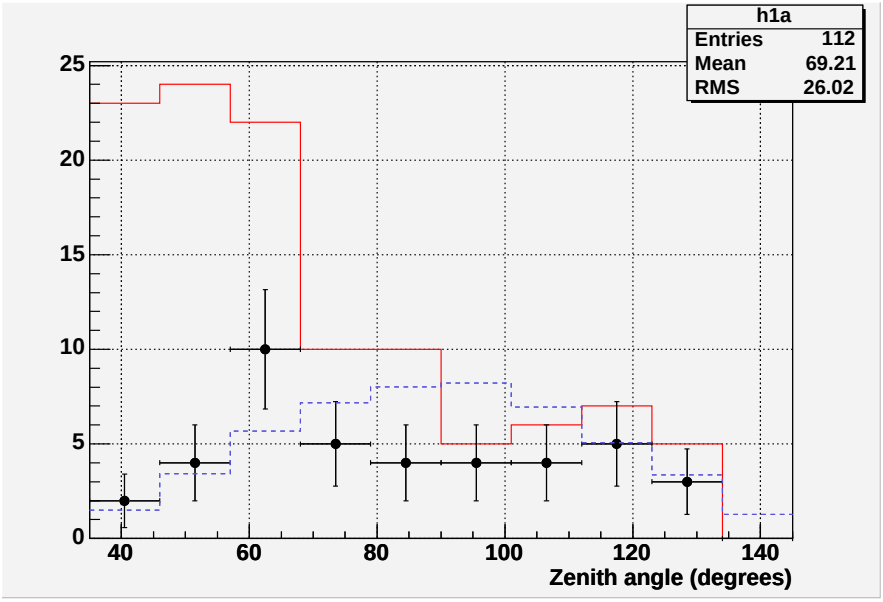

Figure 9.16: This shows the zenith angle of the track. The red solid line is the pre-vetoshield candidates. The blue dashed line is an unoscillated 5.0 kTy atmospheric neutrino sample. The black points with error bars are the final candidate events.

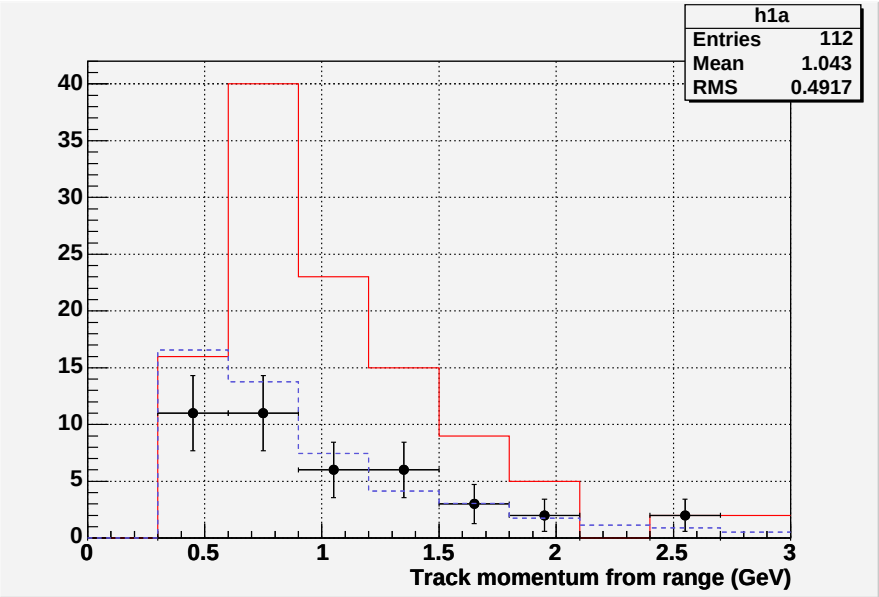

Figure 9.17: This shows the track momentum by range (GeV). The red solid line is the pre-vetoshield candidates. The blue dashed line is an unoscillated 5.0 kTy atmospheric neutrino sample. The black points with error bars are the final candidate events.

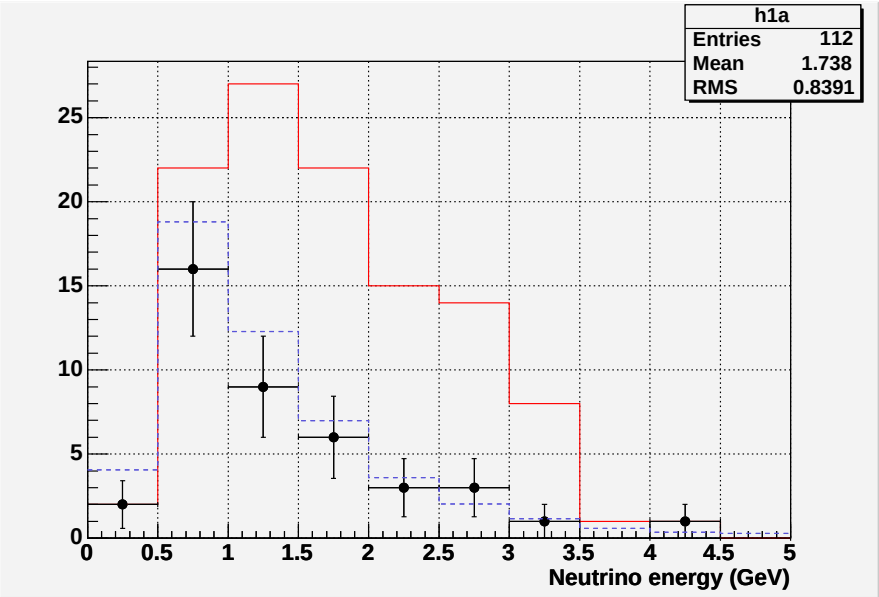

Figure 9.18: This shows the reconstructed neutrino energy (GeV). The low energy events are surpressed.The red solid line is the pre-vetoshield candidates. The blue dashed line is an unoscillated 5.0 kTy atmospheric neutrino sample. The black points with error bars are the final candidate events.

9.5.5 Charge ID of selected events

There are 28 events with a definite charge identification in the high resolution charge ID set. These events consist of 18 ν_μ and 10 $\bar{\nu}_\mu$. The momentum of these events is shown in figure 9.20. The results show no significant evidence of a difference for either charge sign. In addition to the 28 events with high resolution charge ID there are 7 events with medium charge ID and 6 events with no charge ID. In the absence of non-neutrino background the expectations without oscillation are 30.6±7.2 events with high-resolution charge ID, 16.1±4.7 medium resolution charge ID events and $4.0^{+4.6}_{-2.5}$ events with no charge ID.

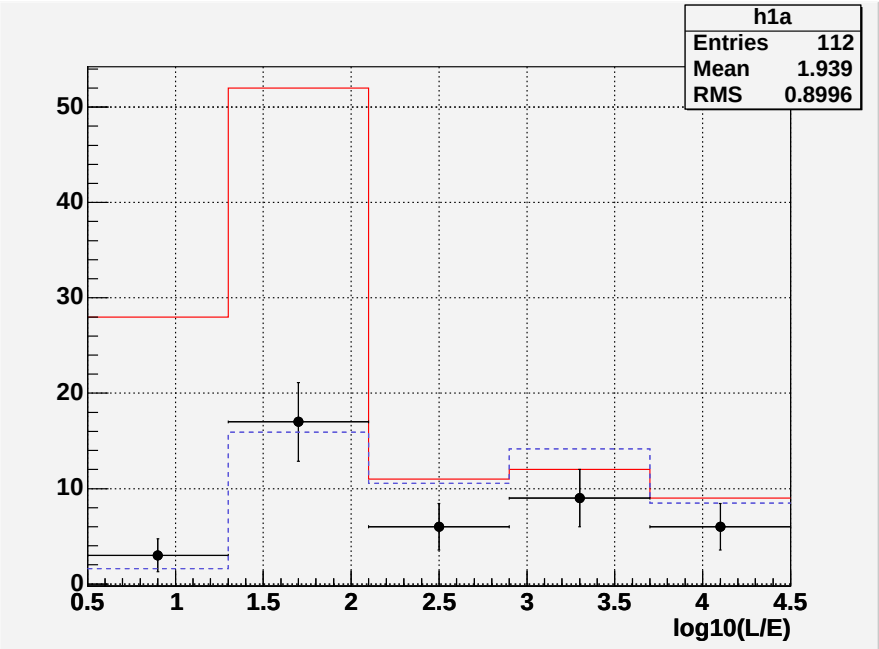

Figure 9.19: This shows the log10(L/E) distribution. Note the suppression at high L/E. The red solid line is the pre-vetoshield candidates. The blue dashed line is an unoscillated 5.0 kTy atmospheric neutrino sample. The black points with error bars are the final candidate events.

9.6 Comparison with previous analysis

The main (also known as the 'Cambridge analysis') analysis[136] and the the physics that went into the main analysis is documented in several sources[136][1][135]. The work of this thesis is an (almost) independent analysis of this work. The two data sets are similar but not identical and both analysis use the same MC, there is not perfect and complete overlap of the data. The comparison shows that using the two analysis that a similar but not identical set of neutrino candidates event can be found. These two analysis give physics results that are consistent with each other. Furthermore, the reconstructed events that are identified in both data sets reconstruct with similar values for important physical quantities. The conclusion of this is that the two sets are

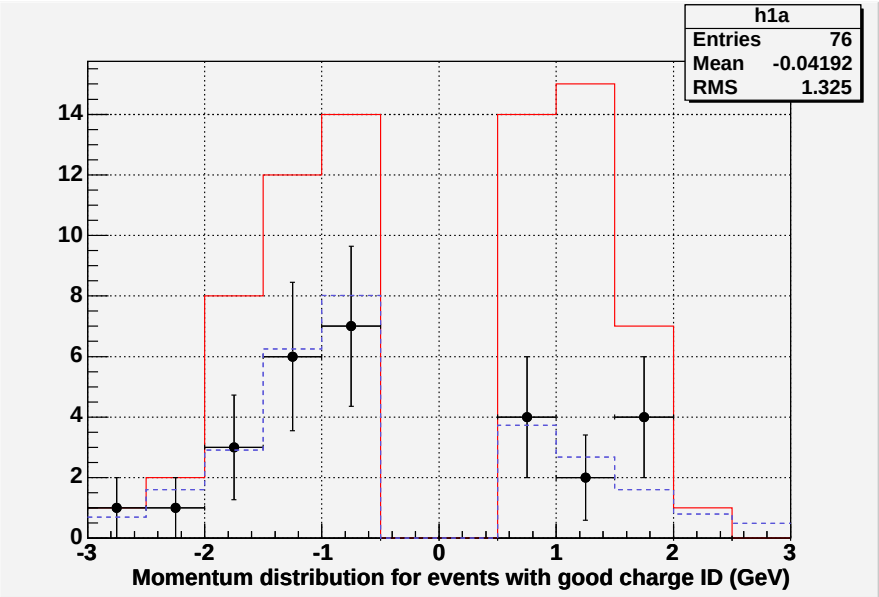

Figure 9.20: This shows the track momentum by curvature for the events with good ($4\sigma+$) charge ID. The red solid line is the pre-vetoshield candidates. The blue dashed line is an unoscillated 5.0 kTy atmospheric neutrino sample. The black points with error bars are the final candidate events.

consistent with each other to within the statistics.

9.6.1 MC Comparison

Since the analysis techniques are different and the software is different, an interesting cross check is to see what fraction of the MC signal and MC background agree on an event by event basis (in other words which MC events are selected by both analysis). An expectation is that the MC background should not overlap that much as the ways for eliminating the background differ. However, the signal should have not a large but not complete overlap.

MC-Background

The background should be different as the ways the cuts eliminate background are different. The main analysis has 53 background events in the cosmic μ MC for which the same files thar were processed for this analysis. As a reminder there were 17 cosmic μ MC background events in this analysis. Only 1 events appears in both datasets. This is strong evidence that the two analysis are being limited by different backgrounds with different causes. This is also evidence that the two selection are in basically independent.

MC-Signal

A comparison of signal was made using R179. This was done by comparing the number of signal events that reconstructed up to a certain snarl number. The number of snarls was chosen such that there were 250 event that passed the main analysis cuts for fully contained neutrinos. In the same sample there were 124 events that passed the analysis presented in this thesis. For the events that passed the analysis presented here, 105 events passed the main analysis. Thus most of the events reconstructed in this analysis are expected to be reconstructed in the main analysis[12]. Although the counting statistics increase the uncertainty, the conclusion of this is that it would be expected that something like $42 \pm 5\%$ of events that pass the main analysis also pass the analysis presented here.

9.6.2 Selected events

There are 24 events selected by both analysis. This compares to only 4 events which are tagged by the vetoshield in both analysis. In the main analysis 69 events are identified as signal and 130 events are vetoed by the vetoshield. A simple estimate suggests that

[12]This is in the absence of oscillation

from the (statics limited) MC study that $2.2^{+10.1}_{-2.1}(95\%C.L)$ events should be vetoed in both studies[13]. A relevant question is why are there 24 events in common and not more? There are several answers to this valid question. First, this is not unexpected, as the MC predicts this should happen. Indeed with 69 events in the main analysis it is predicted that 29 ± 6 events should be in both.[14] The conclusion of this is that the fractions of events being identified in both analysis as signal is consistent with MC predictions for signal and the fraction being identified in both sets as background is consistent with MC predictions for background.

9.6.3 Charge ID

In the main analysis, the observed number of events with definite charge sign was 34 ν_μ and 18 $\bar{\nu_\mu}$. In this analysis 18 ν_μ and 10 $\bar{\nu_\mu}$ events are observed. The charge ID requirement on these events were determined independently by each analysis to give good charge ID within the context of the given analysis. The charge ID for the main analysis is stated to be 2 sigma while the charge ID for this analysis is 4 sigma[15]. These results are consistent with each other. There are 12 events which are selected in both sets with a good charge ID, all 12 are reconstructed with the same charge ID in both samples.

---

[13]No systematics and an identical exposure are being assumed but with such poor statistics in does not matter that much.

[14]This number is calculated assuming that the oscillations does not change the expectation from the unoscillation comparison. The uncertainty includes both the uncertainty in the fraction and the uncertainty from counting statistics.

[15]It should be noted that these two values cannot be easily compared and the uncertainty in charge ID is assigned from the track fitter based on some formula. The actual charge ID mis-identification rate must be found from comparing the true charge to the reconstructed charge for neutrino events.

9.6.4 Physics results

There are several physics results from the analysis[136]. One such analysis is the ratio of ν_μ to $\bar{\nu}_\mu$. The result from the main analysis[136] is $0.53^{+0.21}_{-0.15}$ ± 0.03. The central value of this result for this analysis is 0.56. Even before any statistical or systematic errors are assigned it is clear that this answer is consistent with this physics result from the main analysis.

9.6.5 Event by event comparison

As mentioned before 24 events are in both datasets. However, simply knowing that the result is expected does not still explain why it is this way. The reasons that an events is one analysis and not in another analysis is varied. Another significant question is do the events look similar in both analysis and do these events have the same reconstructed physical quantities from which physics can be extracted.

Non-common events

The reason that an event is not in the common set of events is not dominated by any particular cause. Some events fail a cut a large amount other fail a cut by the smallest possible amount and some events would fail multiple cuts. There are 45 events that the main analysis found that were not found in this analysis. By looking at each event, a reason for it failure was found (this list is in the order the analysis is done). Three events failed because the data was not included in the analysis. Fifteen events failed the event filter, nine events had too many digits per tracklike plane, one event failed cut 4 (directional cosine in z direction), two events were not in the fiducial volume, three events failed the zenith angle cut, ten events failed the pulse height fraction cut and two events failed the final cut (directional cosine in z). It should be stated that many but not all of the events that failed the digit cut also fail the pulse height cut. The most surprising result of this is that so many results fail the event filter as the filter was

designed to have loose acceptance for neutrinos. The reason for these events failures is even more varied than it is for event that fail later in the analysis chain. These reasons include failed tracking, non-fiducial volume (initial volume), muon goes between the two super-modules (main analysis allows this), too big of a difference in U and V plane number and failed demuxing. There is no single failure that seems to dominate this set.

Comparison of reconstruction properties

For the most part the reconstruction properties of the events agree well between the different reconstructions. An example of this is shown in the table 9.7.

Run	Snarl	Planes	VtxX	VtxY	VtxZ	ν E	Q
18581	63807	14,14	-0.57,-0.59	-1.86,-1.82	2.63,2.71	1.40,0.86	-,?
18866	62010	32,33	-1.58,-1.92,	-0.48,-0.47	26.61,26.79	2.77,2.17	+,?
20131	33435	15,16	-1.97,-1.82	2.06,2.30	19.65,19.77	1.0,1.15	-,-
22509	24855	18,17	0.83,0.83	-0.10,-0.14	10.30,10.31	0.86,0.98	-,?
24088	8719	17,17	2.03,2.02	0.99,0.97	21.02,21.02	0.94,0.98	-,-
26000	60501	11,11	2.71,2.72	0.93,0.94	7.92,7.94	0.62,0.61	+,?
27721	13243	20,21	-0.05,-0.07	-0.44,-0.41	19.65,19.65	1.20,1.38	+,+
27781	54144	10,10	-2.84,-2.84	-1.15,-1.16	13.22,13.23	0.56,0.67	?,?
22919	7988	36,36	0.70,0.63	0.58,0.60	5.30,5.38	1.84,2.08	+,+
25831	21795	8,8	-2.68,-2.70	1.87,1.87	24.53,24.53	0.43,0.47	?,?
27184	116702	19,19	-0.42,-0.43	1.27,1.28	20.72,20.72	0.76,0.91	-,-

Table 9.7: In each case the first event is from this analysis and the second event is from the Cambridge analysis. Planes is the number of planes in the event. The ν E is neutrino energy in GeV. The vertex positions are in meters and the charge comparison (Q) is for event that have high charge ID resolution in this analysis and given an good charge ID in the Cambridge analysis.

9.7 Results-Statistical test

The two statistical tests that will be examined are the asymmetry and ρ test. For both tests (and indeed any test) it is important to understand what the expected result is. To be specific it is expected that in 5.0 kTy that there should be 30.6 ± 7.2

events in the high charge ID subset in the absence of oscillation. The 30.6 events consist of 21.2 CC-ν_μ, 8.9 CC-$\bar{\nu}_\mu$ and 0.5 events of NC/ν_e background. The expectation with $\Delta m^2 = 2.4 \times 10^{-3} eV^2$,$sin^2(2\theta) = 1.0$ is 14.4 CC-ν_μ, 6.2 CC-$\bar{\nu}_\mu$ and 0.5[16] event of background[17]. The background from the cosmic μ is somewhat more difficult to estimate as the cosmic MC is statistics limited. An estimate from the vetoed background gives 0.8 of an event of background for both ν_μ and $\bar{\nu_\mu}$ independent of oscillation. The charge ID efficiency (chapter 6) is 95%[18] The results from the experiment are 18 events consistent with ν_μ and 10 events consistent with $\bar{\nu}_\mu$.

9.7.1 ρ test results

For the ρ test this means that if the comparison is done against an unoscillated ν spectrum ρ will be 2.24 and for comparison against a oscillated[19] ($\Delta m^2 = 2.4 \times 10^{-3} eV^2$,$sin^2(2\theta) = 1.0$) ρ=2.14. These number are calculated based on the expected values of N_+ and N_- by simply calculating $N_+ = N_{+\nu} + N_{+bkg}$ and $N_- = N_{-\nu} + N_{-bkg}$. The systematic uncertainty is taken to be 15% of ρ[20]. The expected value of A data for the hypothesis of no oscillation is -0.109 and is -0.086 for the hypothesis of normal CPT conserving oscillations from the data. This is clearly consistent with the expected value from the simulation of 100,000 experiments shown in figure 9.21 and 9.22. In figure 9-23, the data is tested against the hypothesis of large CPT violation. In figure 9.23 the

[16]These events are consistent with being evenly divided by charge although the statistics are limited.

[17]The precise value of the background is somewhat statistics limited in the MC. The ν_e will not oscillate and the NC background should not change even with oscillation. The ν_τ background should not be larger than about 0.1 events and some fraction of this will have good charge ID. In any case this is a small effect.

[18]The charge ID is consistent with 95% for all the events except the zero shower ν_μ which might be as small as 91%. Certainly when averaging over all the events the 95% number is acceptable.

[19]The measured values of A is weakly dependent on the oscillation parameters. This is a consequence of the fact that the selected ν_μ and $\bar{\nu}_\mu$ do not have identical energy spectrums. In any case it should be remembered that ρ test is made to have an expected value for A of 0.

[20]It does not matter much if this is 20% or 10%.

ν_μ do not oscillate but the $\bar{\nu}_\mu$ oscillate at $\Delta m^2 = 2.4 \times 10^{-3} eV^2$,$sin^2(2\theta) = 1.0$. The ρ test predicts an asymmetry value of $0.00 \pm 0.08(syst.) \pm 0.24(stat.)$ for oscillation parameters of $\Delta m^2 = 2.4 \times 10^{-3} eV^2$,$sin^2(2\theta) = 1.0$ compared to the observed asymmetry value of $-0.09 \pm 0.08(syst.) \pm 0.31(stat.)$.

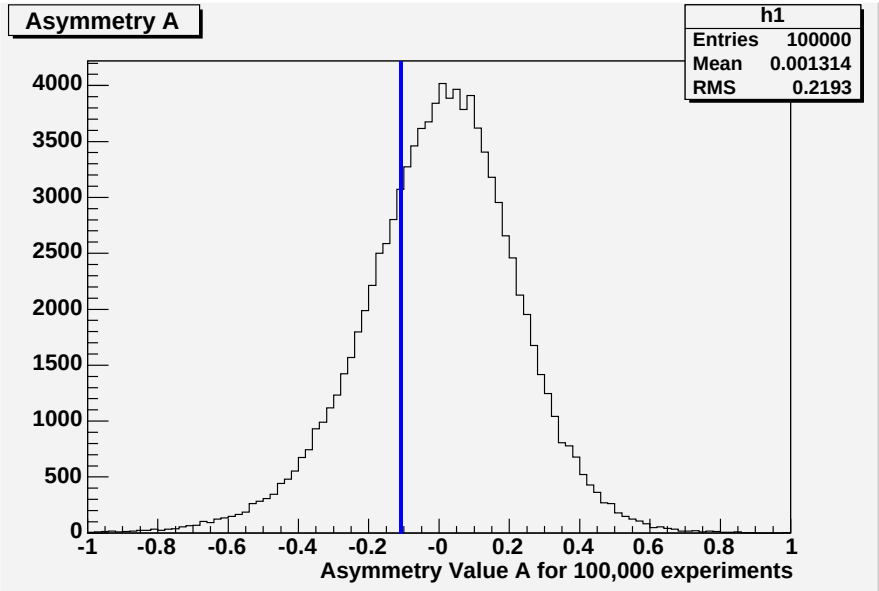

Figure 9.21: This shows an ensemble of 100,000 experiments with the ρ test. The line is the measured value of A based on an assumption of no neutrino oscillation. There is a 15% systematic uncertainty assumed. This suggests that the measured results are completely consistent with CPT conservation, although even large CPT violation could not be ruled out the existing statistics.

9.7.2 Asymmetry test results

In figures 9-24,9-25,9-26,9-27,9-28 and 9-29 the result for the asymmetry test are shown for a comparison against no oscillation, oscillation with parameters of $\Delta m^2 = 2.4 \times 10^{-3} eV^2$,$sin^2(2\theta) = 1.0$ and a CPT violating oscillation with $\Delta m^2 = 2.4 \times 10^{-3} eV^2$,$sin^2(2\theta) = 1.0$ for $\bar{\nu}_\mu$ and no oscillation for ν_μ for two different approaches to modeling the background. The observed events are 18 ν_μ and 10 $\bar{\nu}_\mu$. When generating an asymmetry

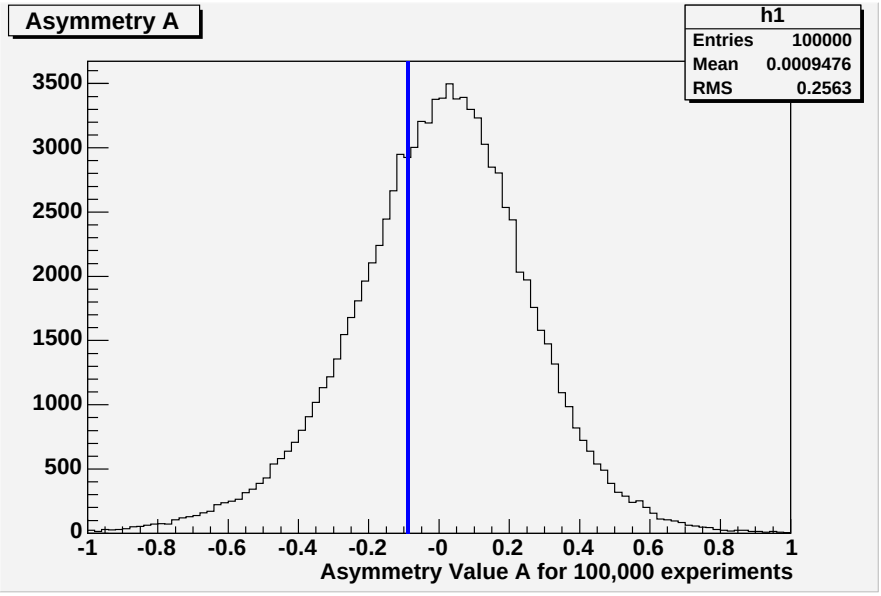

Figure 9.22: This shows an ensemble of 100,000 experiments with the ρ test. The line is the measured value of A based on an assumption of neutrino oscillation parameters of $\Delta m^2 = 2.4 \times 10^{-3} eV^2$,$sin^2(2\theta) = 1.0$. There is a 15% systematic uncertainty assumed. This suggests that the measured results are completely consistent with CPT conservation, although even large CPT violation could not be ruled out the existing statistics.

plot two different things can be done. The estimated background can be put in the model of the asymmetry distribution or the background can be substracted off the data and the signal only MC can be used to generate the expected distribution. Both methods are shown. Figures 9-24, 9-25 and 9-26 are modeled for the background being added to the model, while figures 9-27, 9-28 and 9-29 are for the background subtraction from signal. For the first three plots the data point is -0.286, for the other three plots the data point is at -0.296. In any case the results are not significantly different from the ρ test, the data is completely consistent with CPT conservation but cannot rule out large CPT violation with the current statstics. For the asymmetry test the asymmetry value is expected to be $-0.40 \pm 0.23(stat.only)$ for oscillation parameters of $\Delta m^2 = 2.4 \times 10^{-3} eV^2$,$sin^2(2\theta) = 1.0$ and an observed value of $-0.29 \pm 0.18(stat.)$

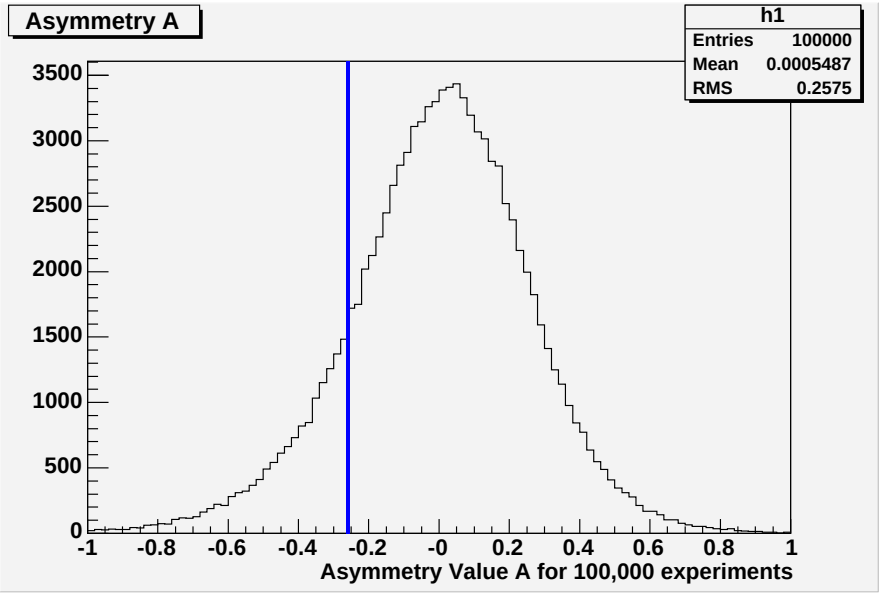

Figure 9.23: This shows an ensemble of 100,000 experiments with the ρ test. The line is the measured value of A based on an assumption of neutrino oscillation parameters of $\Delta m^2 = 2.4 \times 10^{-3} eV^2$,$sin^2(2\theta) = 1.0$ for $\bar{\nu}_\mu$ and no oscillation for ν_μ. There is a 15% systematic uncertainty assumed. This shows that the current data cannot rule out large CPT violation.

is seen.

9.8 Conclusion

The MINOS far detector has been used to find atmospheric neutrinos. Further, MINOS is the first deep underground atmospheric experiment to be able to separate ν and $\bar{\nu}$. In the end 41 candidate ν_μ and $\bar{\nu}_\mu$ events are observed with an expectation of 53.1±7.6(system.)±7.2(stat.) unoscillated events or 31.6±4.7(system.)±5.6(stat.) events with $\Delta m^2 = 2.4 \times 10^{-3} eV^2$,$sin^2(2\theta) = 1.0$ as oscillation parameters. A total of 28 events are charge ID with high confidence and these events consist of 18 ν_μ and 10 $\bar{\nu}_\mu$. This should be compared with an expectation of 14.4 ν_μ and 6.2 $\bar{\nu}_\mu$ for oscillation parameters of $\Delta m^2 = 2.4 \times 10^{-3} eV^2$,$sin^2(2\theta) = 1.0$. The ρ test

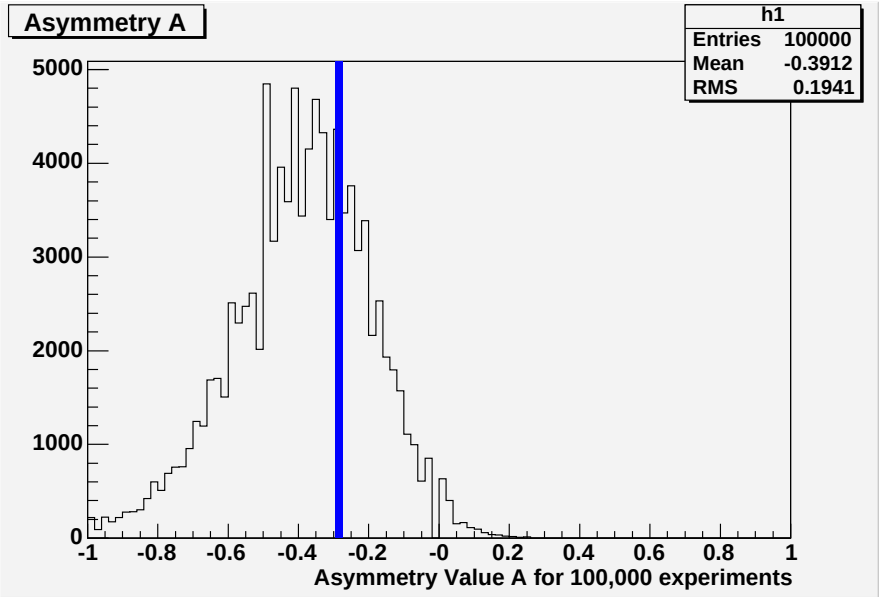

Figure 9.24: This shows an ensemble of 100,000 experiments with the asymmetry test. The line is the measured value of A based on an assumption of no neutrino oscillation. There is a 15% systematic uncertainty assumed. This suggests that the measured results are completely consistent with CPT conservation, although even large CPT violation could not be ruled out the existing statistics.

predicts an asymmetry value of $0.00 \pm 0.08(syst.) \pm 0.24(stat.)$ for oscillation parameters of $\Delta m^2 = 2.4 \times 10^{-3} eV^2$,$sin^2(2\theta) = 1.0$ compared to the observed asymmetry value of $-0.09 \pm 0.08(syst.) \pm 0.31(stat.)$. For the asymmetry test the asymmetry value is expected to be $-0.40 \pm 0.23(stat.)$ for oscillation parameters of $\Delta m^2 = 2.4 \times 10^{-3} eV^2$,$sin^2(2\theta) = 1.0$ and an observed value of $-0.29 \pm 0.18(stat.)$, (no systematic error is estimated, see chapters 7 and 8). No statistically significant evidence of CPT violation in the neutrino sector is observed.

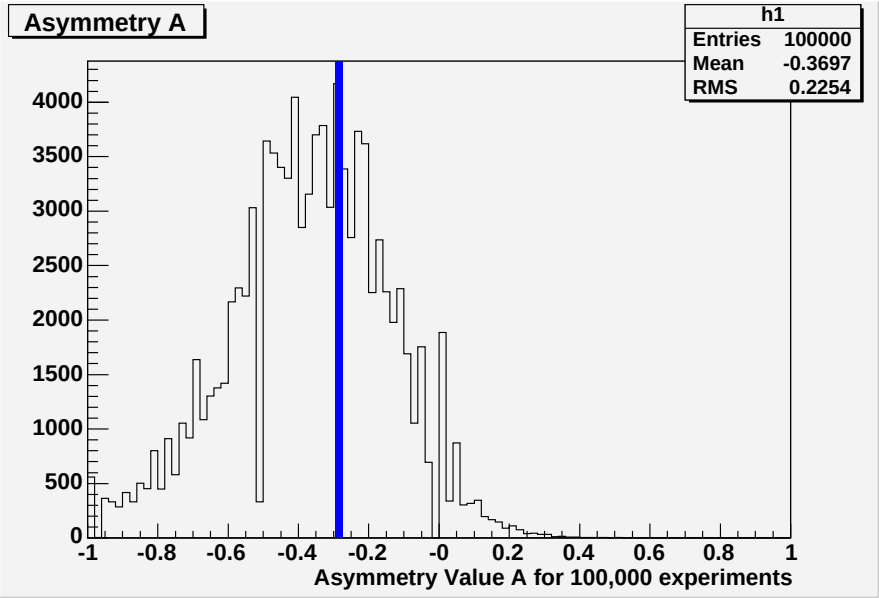

Figure 9.25: This shows an ensemble of 100,000 experiments with the asymmetry test.The line is the measured value of A based on an assumption of neutrino oscillation parameters of $\Delta m^2 = 2.4 \times 10^{-3} eV^2$,$sin^2(2\theta) = 1.0$. There is a 15% systematic uncertainty assumed. This suggests that the measured results are completely consistent with CPT conservation, although even large CPT violation could not be ruled out the existing statistics.

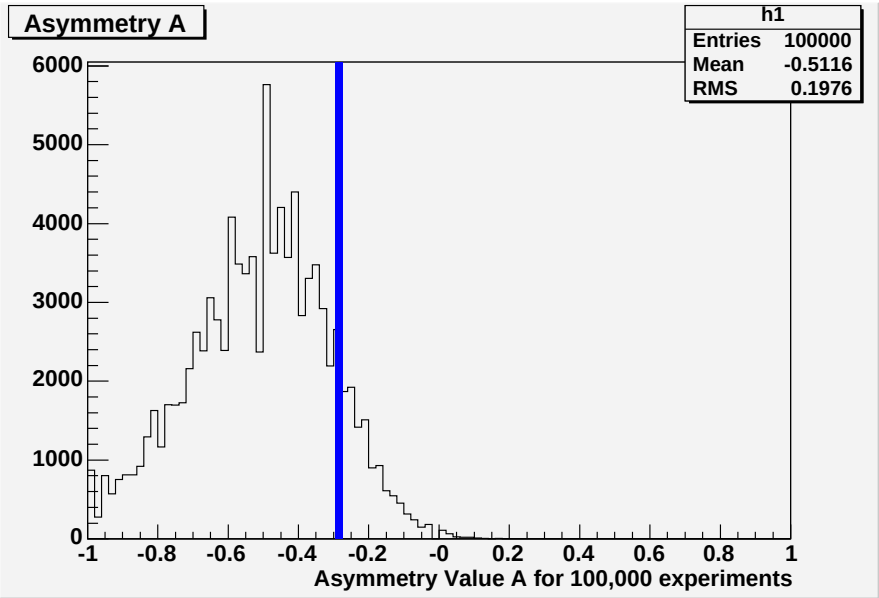

Figure 9.26: This shows an ensemble of 100,000 experiments with the asymmetry test. The line is the measured value of A based on an assumption of neutrino oscillation parameters of $\Delta m^2 = 2.4 \times 10^{-3} eV^2$,$sin^2(2\theta) = 1.0$ for $\bar{\nu}_\mu$ and no oscillation for ν_μ. There is a 15% systematic uncertainty assumed. This shows that the current data cannot rule out large CPT violation.

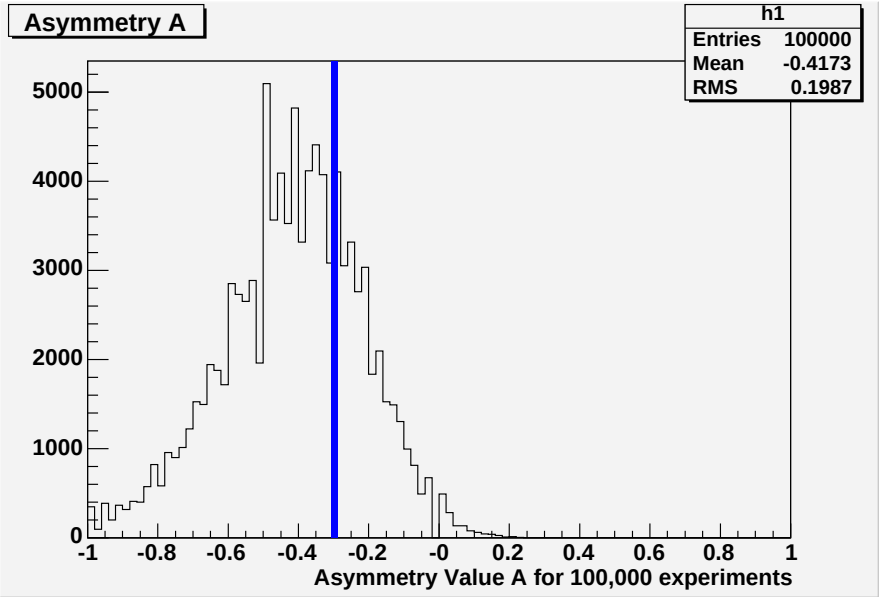

Figure 9.27: This shows an ensemble of 100,000 experiments with the asymmetry test. The line is the measured value of A based on an assumption of no neutrino oscillation. There is a 15% systematic uncertainty assumed. This suggests that the measured results are completely consistent with CPT conservation, although even large CPT violation could not be ruled out the existing statistics.

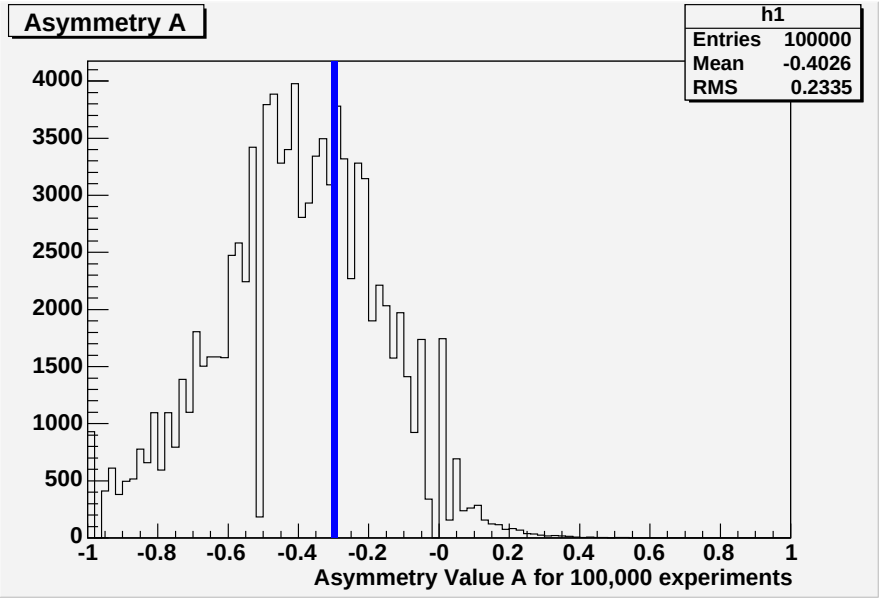

Figure 9.28: This shows an ensemble of 100,000 experiments with the asymmetry test. The line is the measured value of A based on an assumption of neutrino oscillation parameters of $\Delta m^2 = 2.4 \times 10^{-3} eV^2$,$sin^2(2\theta) = 1.0$. There is a 15% systematic uncertainty assumed. This suggests that the measured results are completely consistent with CPT conservation, although even large CPT violation could not be ruled out the existing statistics.

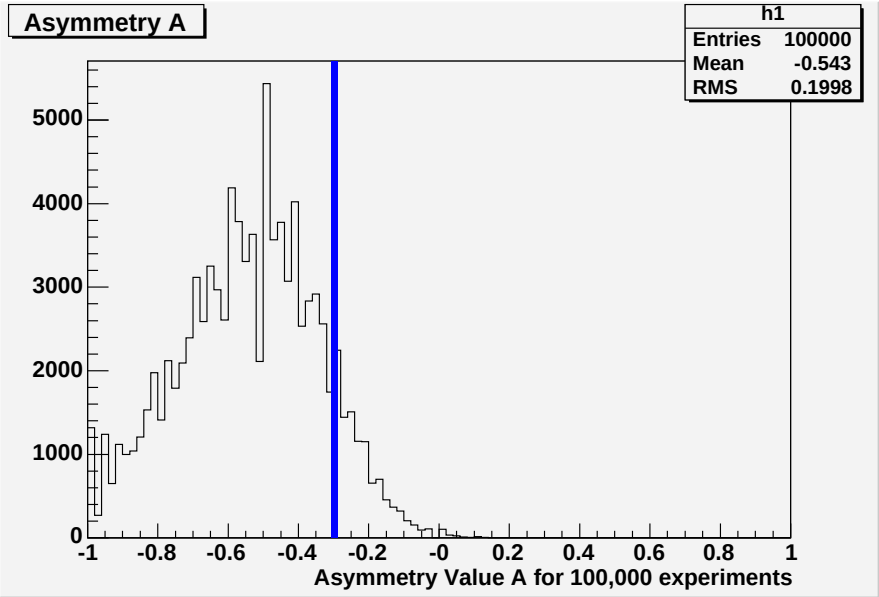

Figure 9.29: This shows an ensemble of 100,000 experiments with the asymmetry test. The line is the measured value of A based on an assumption of neutrino oscillation parameters of $\Delta m^2 = 2.4 \times 10^{-3} eV^2$,$sin^2(2\theta) = 1.0$ for $\bar{\nu}_\mu$ and no oscillation for ν_μ. There is a 15% systematic uncertainty assumed. This shows that the current data cannot rule out large CPT violation.

Appendix A

Fundemental particles

A.1 Fundemantal Standard Model particles

The properties of all SM particles are too many and detailed to write down here. However, in Table A.1 and A.2 a brief overview of some properties of the leptons, quarks and force carrying bosons are presented. For more detail refer to the Review of Particle Physics [17].

Particle	Mass (MeV)	Electric Charge	Spin	Generation	Type
e	0.511	-1	1/2	First	Lepton
ν_e	$< 3 \times 10^{-6}$	0	1/2	First	Lepton
μ	105	-1	1/2	Second	Lepton
ν_μ	< 0.19	0	1/2	Second	Lepton
τ	1777	-1	1/2	Third	Lepton
ν_τ	< 18	0	1/2	Third	Lepton
u	1-5	2/3	1/2	First	Quark
d	3-9	-1/3	1/2	First	Quark
s	75-170	-1/3	1/2	Second	Quark
c	1150-1350	2/3	1/2	Second	Quark
b	4000-4400	-1/3	1/2	Third	Quark
t	$174,000 \pm 5,100$	2/3	1/2	Third	Quark

Table A.1: The table above shows some of the important properties of the three generations of leptons and quarks. The neutrino mass limits are given without any assumptions of neutrino oscillations.[17]

Particle	Mass (MeV)	Electric Charge	Spin	Force	Number
γ	0	0	1	Electromagnetic	1
$W^{\pm}$	80,000	± 1	1	Weak	2
Z^0	91,000	0	1	Weak	1
g	0	0	1	Strong	8

Table A.2: This lists the SM force carrying bosons and some important properties. The number refers to how many of this type of particle exists (there are 8 distinct gluons for example)[17]

Appendix B

The Minos Collaboration

The MINOS Collaboration

Main Injector Neutrino Oscillation Search

November 2005

P. Adamson[8,15], C. Andreopoulos[21], K.E. Arms[16], R. Armstrong[11], D.J. Auty[24], S. Avvakumov[23], D.S. Ayres[1], B. Baller[8], B. Barish[5], P.D. Barnes Jr.[14], G. Barr[18], W.L. Barrett[30], E. Beall[1,16], B.R. Becker[16], A. Belias[21], R. H. Bernstein[8], D. Bhattacharya[19], M. Bishai[4], A. Blake[6], B. Bock[17], G.J. Bock[8], J. Boehm[9], D.J. Boehnlein[8], D. Bogert[8], P.M. Border[16], C. Bower[11], E. Buckley-Geer[8], C. Bungau[24], J.D. Chapman[6], D. Cherdack[27], S.K. Chernichenko[20], S. Childress[8], B.C. Choudhary[8], J.H. Cobb[18], A.J. Culling[6], J.K. de Jong[10], M. Dierckxsens[4], M.V. Diwan[4], M. Dorman[15,21], D. Drakoulakos[2], T. Durkin[21], A.R. Erwin[32], C.O. Escobar[28], J. Evans[18], E. Falk Harris[24], G.J. Feldman[9], T.H. Fields[1], R. Ford[8], M.V. Frohne[3], H.R. Gallagher[27], G.A. Giurgiu[1], A. Godley[22], J. Gogos[16], M.C. Goodman[1], P. Gouffon[29], E. Grashorn[17], N. Grossman[8], K. Grzelak[18], A. Habig[17], D. Harris[8], P.G. Harris[24], J. Hartnell[21], E.P. Hartouni[14], R. Hatcher[8], K. Heller[16], C. Howcroft[5], J. Hylen[8], D. Indurthy[26], G.M. Irwin[23], M. Ishitsuka[11], D. Jaffe[4], C. James[8], L. Jenner[15], D. Jensen[8], T. Kafka[27], H.J. Kang[23], S.M.S. Kasahara[16], M.S. Kim[19], G. Koizumi[8], S. Kopp[26], M. Kordosky[15], D.J. Koskinen[15], S.K. Kotelnikov[13], A. Kreymer[8], S. Kumaratunga[16], K. Lang[26], J. Ling[22], P.J. Litchfield[16], R.P. Litchfield[18], P. Lucas[8], V. Makeev[8], W.A. Mann[27], A. Marchionni[8], A.D. Marino[8], M.L. Marshak[16], J.S. Marshall[6], A. McGowan[1,16], J.R. Meier[16], G.I. Merzon[13], M.D. Messier[11], D.G. Michael[5†], W.H. Miller[16], S.R. Mishra[22], C. Moore[8], J. Morfin[8], L. Mualem[16], S. Mufson[11], S. Murgia[23], J. Musser[11], D. Naples[19], J.K. Nelson[31], H. Newman[5], T.C. Nicholls[21], J.P. Ochoa-Ricoux[5], W.P. Oliver[27], V.A. Onuchin[20], T. Osiecki[26], R. Ospanov[26], J. Paley[11], V. Paolone[19], A. Para[8], T. Patzak[7], Z. Pavlovich[26], G.F. Pearce[21], C.W. Peck[5], E.A. Peterson[16], D.A. Petyt[16], H. Ping[32], R. Piteira[7], R. Pittam[18], R.K Plunkett[8], D. Rahman[16], R.A. Rameika[8], T.M. Raufer[18], B. Rebel[8], J. Reichenbacher[1], D.E. Reyna[1], C. Rosenfeld[22], H.A. Rubin[10], K. Ruddick[16], V.A. Ryabov[13], R. Saakyan[15], M.C. Sanchez[9], N. Saoulidou[8], J. Schneps[27], P. Schreiner[3], V.K. Semenov[20], P. Shanahan[8], W. Smart[8], V. Smirnitsky[12], C. Smith[15], A. Sousa[27], B. Speakman[16], P. Stamoulis[2], P.A. Symes[24], N. Tagg[18], R.L. Talaga[1], E. Tetteh-Lartey[25], J. Thomas[15], M.A. Thomson[6], G. Tinti[18], I. Trostin[12], V.A. Tsarev[13], G. Tzanakos[2], J. Urheim[11], P. Vahle[15], C. Velissaris[32], V. Verebrysov[12], B. Viren[4], C.P. Ward[6], D.R. Ward[6], M. Watabe[25], A. Weber[18,21], R.C. Webb[25], A. Wehmann[8], N. West[18], C. White[10], S.G. Wojcicki[23†], D.M. Wright[14], Q.K. Wu[22], T. Yang[23], F.X. Yumiceva[31], H. Zheng[5], M. Zois[2], and R. Zwaska[26].

† **Co-Spokespersons**

Argonne[1] - Athens[2] - Benedictine[3] - Brookhaven[4] - Caltech[5] - Cambridge[6] - Collège de France[7] - Fermilab[8] - Harvard[9] - IIT[10] - Indiana[11] - ITEP-Moscow[12] - Lebedev[13] - Livermore[14] - UCL-London[15] - Minnesota[16] - Minnesota-Duluth[17] - Oxford[18] - Pittsburgh[19] - Protvino[20] - Rutherford[21] - South Carolina[22] - Stanford[23] - Sussex[24] - Texas A&M[25] - Texas-Austin[26] - Tufts[27] - UNICAMP-Brazil[28] - USP-Brazil[29] - Western Washington[30] - William & Mary[31] - Wisconsin[32]

Appendix C

Post Filter Data-MC Comparison

C.0.1 Introduction

After the data filter is applied, the final selection for atmospheric neutrinos begin. A fundamental question must be asked: do the data and MC background agree? It is important that the data and MC have at a minimum a qualitative agreement. The reason is that the cuts applied to MC must behave in a similar way to the cuts on the data if the results are to be believed. Certainly, they are not expected to agree perfectly. The MC does not perfectly reproduce the detector and the data has not had a final data quality assurance at this stage of reconstruction.

C.0.2 Post Filter-Data(PreCoilHV)

The post filter dataset is all data runs of the proper run type that lasted more than 1 hour. This includes some runs when the detector had an HV trip or magnetic coils issues (mostly coil). These events are on the order of 5-10 percent of the run time. This set is referred to as the PreCoilHV set. Although, this data must be taken out for the final analysis, it does not have to be cut from this stage of analysis as the backgrounds for fully contained events appear to be somewhat insensitive to the detector state. This

data set is cut down for the final analysis. This was processed with minossoft release R1.14.1 using magnetic field map 202.

C.0.3 Post Filter-MC

The MC data are only cosmic ray muons. Since, this background dominates by number at this stage of analysis, this is true to a good approximation. The MC is a simulation of cosmic ray muons and nothing else. This dataset consists of cosmic muon runs r651-r778 (not every run in this range). This was processed using minossoft release R1.14.1 and magnetic field map 201.

C.0.4 Known differences in MC and data

The MINOS detector MC is still undergoing refinements and improvements. It should not be that shocking that some of these quantities do not agree perfectly and many agree better than a naive observer might expect. There are several potentially significant differences known:

Magnetic field

There is actually two different magnetic field issues that could be a problem. The first is that MC and data use different magnetic field maps. This is not as bad of a situation as might be expected. The differences between the two maps is small in absolute size and mainly involves magnetic field at the 'ears' which is both small and out of the fiducial volume at this stage of reconstruction ($r \leq 3.8$m). The second issue is that MC is generated and reconstructed using a magnetic field in the forward direction. The data at this stage is in forward,reverse and (a bit) in no field. The part with no field will be removed from the final dataset before the final part of the analysis. Chapter 4 and 6 have information on both issues raised here.

Detector

The detector geometry is idealized in the MC. The rotations and mis-alignment of strips, module and scintillator planes are not reproduced in the MC. The z-direction spacing is a constant in the MC. This is not realistic. Although, these physical effects do happen in the far detector, they are small.

C.0.5 Post Filter-Cuts

As a quick review the cuts that are applied to data and MC are as similar as possible. Because of the details on what time the MC events are given when generated, the data has a fraction of 0.001 events thrown out compared to MC (this can be thought of as a different normalization). With this exception the cuts are the same, in particular the cuts are:

General

The run must be one hour or more long, be a physics run and contain one and only one track. The event must have either one or no showers associated with the event. The demuxer must not flag the event as a possible multi-muon and the fraction of stray planes to valid planes found by the demuxer for the U and V views when added in quadrature must be smaller than 0.20.

Tracks

The tracks must be 6 or more tracklike planes long and have a fraction of tracklike planes to planes of 0.75 or greater. The track cannot begin or end in the first or last three planes of a SM. The track must begin and end with radial coordinates of $r \geq 0.35$ m and $r \leq 3.8$ m. The track must have an average of at least 1.5 digits per strip and cannot have more than 2.5 digits per tracklike plane. The track cannot not have an absolute difference between the number of U and V view planes greater than three and

must start and end tracking in both views at the same time (can only miss one plane). Finally, the tracking must pass the internal consistency check.

Shower

The shower cannot begin in the first or last three planes of a SM. The shower vertex must greater than 0.35 m from the coil and less than 3.8 m from the center, the absolute difference between the number of U and V view planes must be 3 or less.

C.0.6 Results

The following pages have 24 plots. These show the comparison of data to MC for the results after the initial filter is applied. In each plot, the red histogram without error bars are data and the blue points with error bars is MC. These plots are normalized by area. The data are normalized down to the MC sample size by area. When these plots show a figure related to tracks it is for tracks with both zero showers and single showers. The plots with shower related quantities are obviously only for events with a single shower. The plots are all on a log scale. The MC is background only and the data is background + (a tiny) signal. The total number of data and MC events broken down by the number of showers is given in table C.1. The number of events in table C.1 is consistent with the number of events based on a normalization of long muons.

Number of Shower (s)	MC events	Data events	Expected MC events
0	824	2,565	1,854±65(stat)±186(syst)
1	30294	70,923	68,160±390(stat)±6820(syst)
Total	31118	73,488	70,020±400(stat)±7000(syst)

Table C.1: This shows the number of events for the data and MC after the filter is applied. The final column shows the number of events expected from an independent normalization. The systematic error is taken to be 10 percent. The zero shower case seems to underestimate the background. Although slightly troubling, the total background in the zero shower channel is small to start with. However, two things should be remembered: the analysis is based on tracks and not showers and because the relative ratio of zero to one shower event is small, the zero shower case is sensitive to small shower efficiency differences.

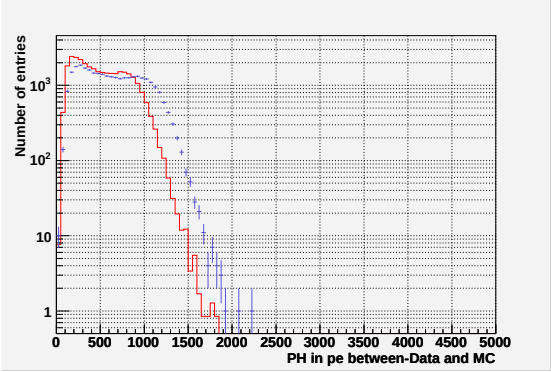

Figure C.1: The pulse height of the track measured in PE (photo-electron) is for the data and MC is shown. There is a clear difference. The MC has a higher light amount than the data. This however already known. This plot shows the largest single difference of any plot. This shows data in red and MC in blue with error bars. The error bars are 1σ. The data are normalized by area down to the MC sample.

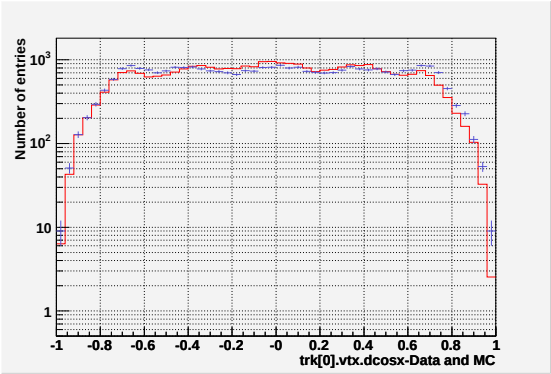

Figure C.2: The directional cosine in the x direction at the track vertex for data and MC is shown. The agreement is good. This shows data in red and MC in blue with error bars. The error bars are 1σ. The data are normalized by area down to the MC sample.

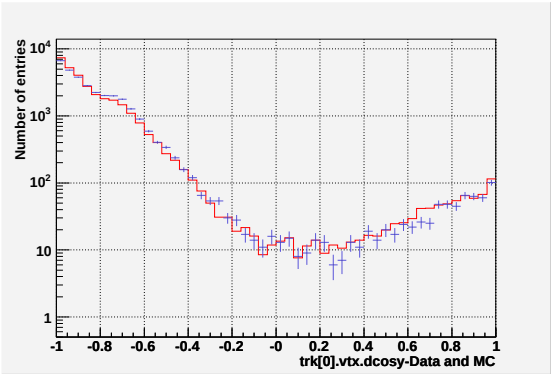

Figure C.3: The directional cosine in the y direction at the track vertex for data and MC is shown. The agreement is good. The positive values of this are events that the software reconstruct going up. The MC has only down going events. This shows that the reconstruction error are being reproduced reasonably well in the MC. This shows data in red and MC in blue with error bars. The error bars are 1σ. The data are normalized by area down to the MC sample.

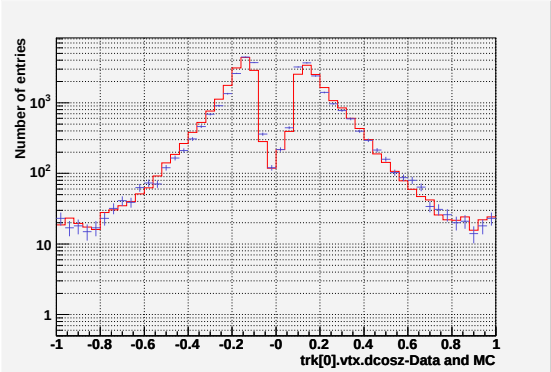

Figure C.4: The directional cosine in the z direction at the track vertex for data and MC is shown. The analysis to find the fully contained events use the distribution for multiple cuts. The only place the agreement is not really good is values around zero. The first cut in the next stage of reconstruction eliminates these event first. This shows data in red and MC in blue with error bars. The error bars are 1σ. The data are normalized by area down to the MC sample.

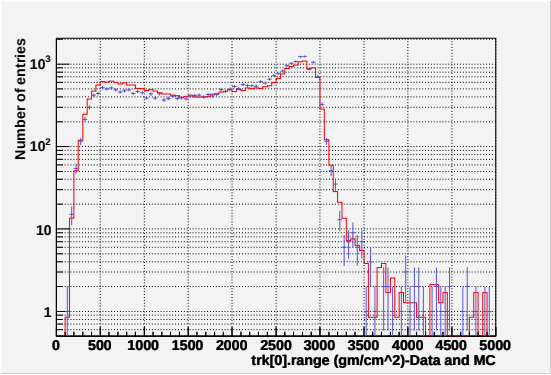

Figure C.5: The track range in $\frac{gm}{cm^2}$ is shown for data and MC. The difference at low range ($\frac{gm}{cm^2}$) is real. The effect is not caused by a normalization problem with low energy events as stopping muons see this effect too. The effect appears to go away with stricter cuts. This shows data in red and MC in blue with error bars. The error bars are 1σ. The data are normalized by area down to the MC sample.

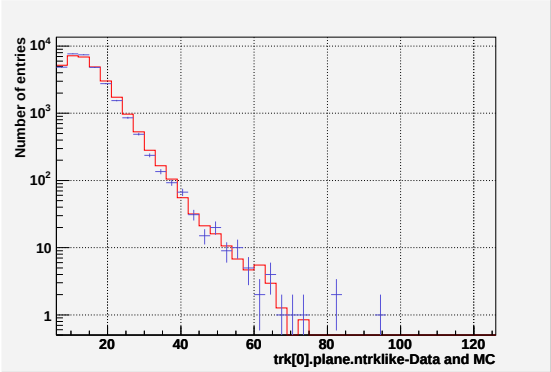

Figure C.6: The number of tracklike planes for the track is shown for the data and MC. The tracklike planes are one that do not evidence of excessive hits. The agreement is good. This shows data in red and MC in blue with error bars. The error bars are 1σ. The data are normalized by area down to the MC sample.

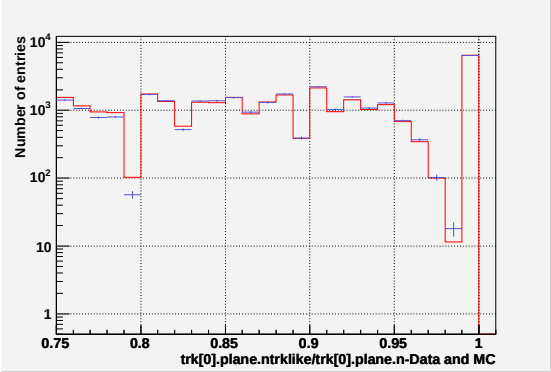

Figure C.7: The fraction of tracklike planes versus all planes in a track is shown for data and MC. This fraction suggests the data and MC track look nearly identical. The agreement is nearly perfect with many points on top of each other. This shows data in red and MC in blue with error bars. The error bars are 1σ. The data are normalized by area down to the MC sample.

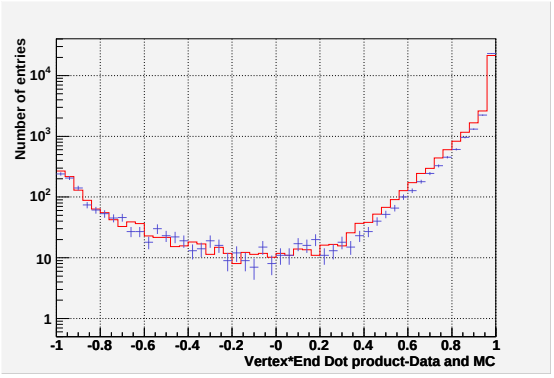

Figure C.8: The dot product of the vertex directional vector and end directional vector is shown for data and MC. The real neutrino events have almost no odds of 'bending backwards'. This means that events with values of this dot product smaller than about 0.5 have either a reconstruction error or unusual muon. The shapes agree reasonably well, the highest (most straight track) value is a bit higher in MC than data, and this appears to shift the normalization for the rest of the plot. This is not unexpected considering the differences in geometry. This shows data in red and MC in blue with error bars. The error bars are 1σ. The data are normalized by area down to the MC sample.

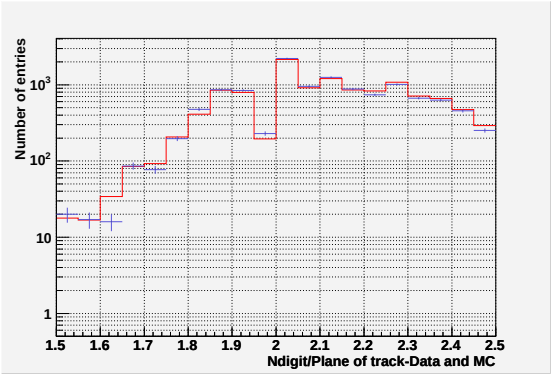

Figure C.9: This show the fraction of total digits to tracklike planes for data and MC. This is a measure of the average number of hits to tracklike planes. A similar plot for total planes could be made, but it should be remembered that all of these events have a high fraction of tracklike planes and the tracklike planes are more relevant to the analysis than the total number of planes. In any case the agreement is extremely good. This shows data in red and MC in blue with error bars. The error bars are 1σ. The data are normalized by area down to the MC sample.

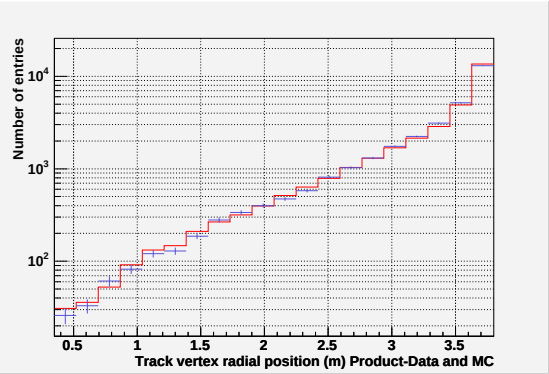

Figure C.10: This shows the track radial vertex position for data and MC. The radial vertex position is simply the radial distance from the center of the detector to the reconstructed track vertex. Since almost all the background interacts in the outer part of the detector and the fully contained ν_μ, $\bar{\nu}_\mu$ happen at all radial positions, this must agree well both near the edge and in the inner part of the detector. The agreement appears to be good over all radial ranges. It should be pointed out that since the data filter cuts are track vertex-end symmetric, the track end distribution is important, although probably not as important. This is one of the most significant distributions for this analysis. This shows data in red and MC in blue with error bars. The error bars are 1σ. The data are normalized by area down to the MC sample.

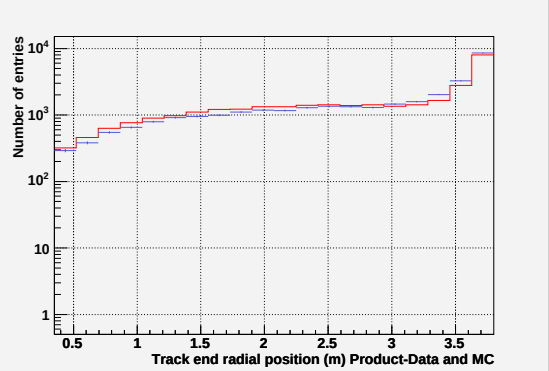

Figure C.11: This shows the track radial end position for data and MC. It is simply the position in radial space the track end is reconstructed. This is clearly something significant to get right. The distribution seem to agree well. This shows data in red and MC in blue with error bars. The error bars are 1σ. The data are normalized by area down to the MC sample.

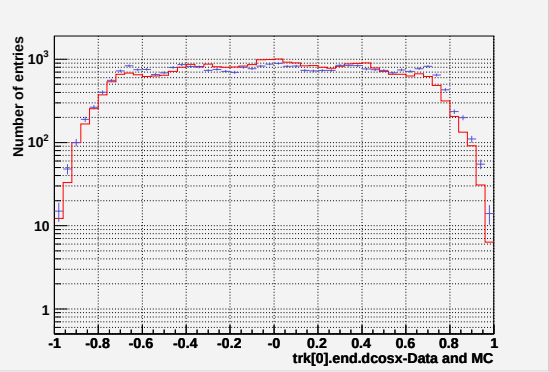

Figure C.12: The directional cosine in the x direction at the track end for data and MC is shown. The agreement is good. This shows data in red and MC in blue with error bars. The error bars are 1σ. The data are normalized by area down to the MC sample.

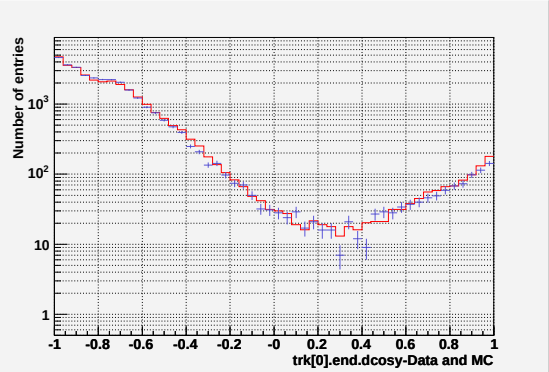

Figure C.13: The directional cosine in the y direction at the track end for data and MC is shown. The agreement is good.This shows data in red and MC in blue with error bars. The error bars are 1σ. The data are normalized by area down to the MC sample.

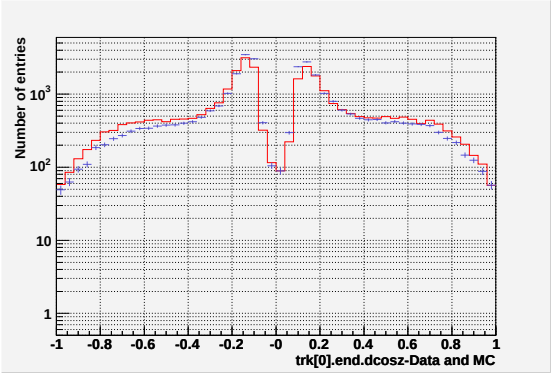

Figure C.14: The directional cosine in the z direction at the track end for data and MC is shown. This distribution is important for the analysis. The disagreement here (and the track vertex directional cosine z) at near 0 lead to this region to be cut out of the sample at the next stage of analysis, although overall the agreement is not bad. This shows data in red and MC in blue with error bars. The error bars are 1σ. The data are normalized by area down to the MC sample.

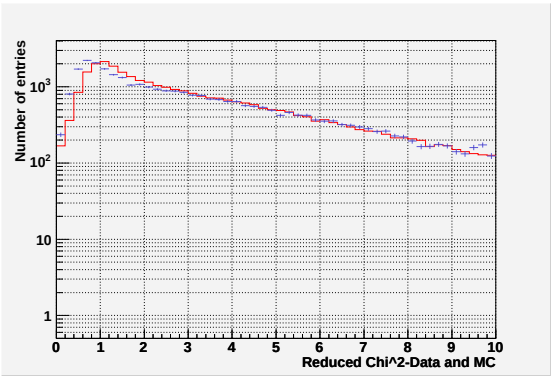

Figure C.15: The χ^2 per degree of freedom ($\frac{\chi^2}{ndof}$) is shown for data and MC. The agreement is much better than might be expected as the $\frac{\chi^2}{ndof}$ is really sensitive to differences in the geometry. Since, the geometry for MC is known to be overly simple, this is somewhat impressive. As expected with an ideal geometry the $\frac{\chi^2}{ndof}$ is better for MC. This shows data in red and MC in blue with error bars. The error bars are 1σ. The data are normalized by area down to the MC sample.

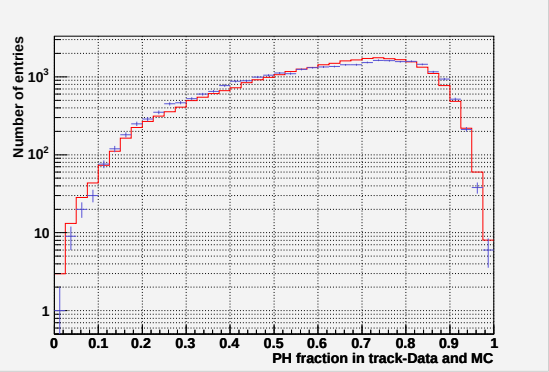

Figure C.16: The fraction of PH in a track versus the total event PH is shown for data and MC. The shapes quantitatively agree well at a high PH fraction. Given the 10%-15% difference in normalization this is much better, as would be expected for a ratio. This shows data in red and MC in blue with error bars. The error bars are 1σ. The data are normalized by area down to the MC sample.

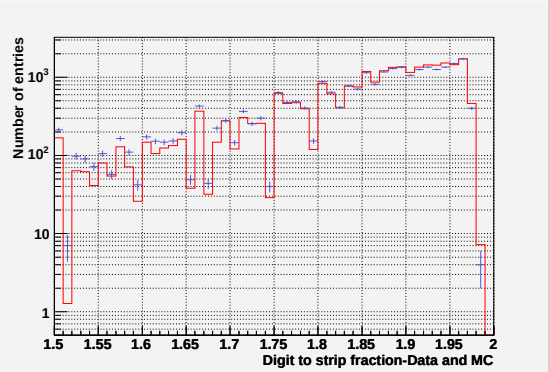

Figure C.17: The fraction of digits to all strips in the track is shown for data and MC. This is a measure of the average fraction of hits to strips for a track. A high number suggests that the track is made almost only of double ended strips. The agreement is good. This shows data in red and MC in blue with error bars. The error bars are 1σ. The data are normalized by area down to the MC sample.

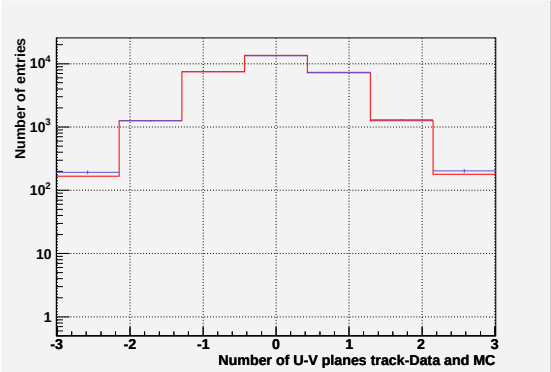

Figure C.18: The difference in U and V view planes in a track is shown. Since U and V view planes alternate, it is expected that the track should be tracked in both the U and V view. The data and MC agree. This shows data in red and MC in blue with error bars. The error bars are 1σ. The data are normalized by area down to the MC sample.

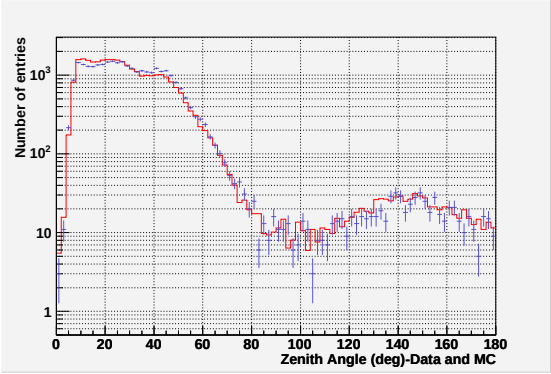

Figure C.19: The zenith angle in degrees is shown for data and MC. A zenith angle of 0 is up and zenith angle of 180 is down. The MC does not reproduce the zenith below 20 degrees particularly well, This is not a substantial problem as there is almost no neutrino signal which reconstructs from this region. This does reproduce the background of upgoing events well. This shows data in red and MC in blue with error bars. The error bars are 1σ. The data are normalized by area down to the MC sample.

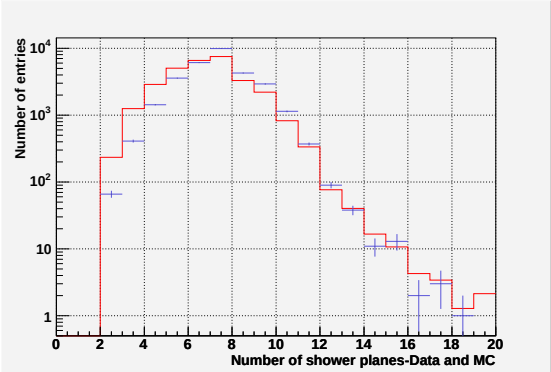

Figure C.20: The number of shower planes in the single shower events for data and MC is shown. Since almost no shower cuts were applied this is pretty good agreement. Although, the short showers on the left of the plot shows some disagreement, the two distributions peak at the same point. This shows data in red and MC in blue with error bars. The error bars are 1σ. The data are normalized by area down to the MC sample.

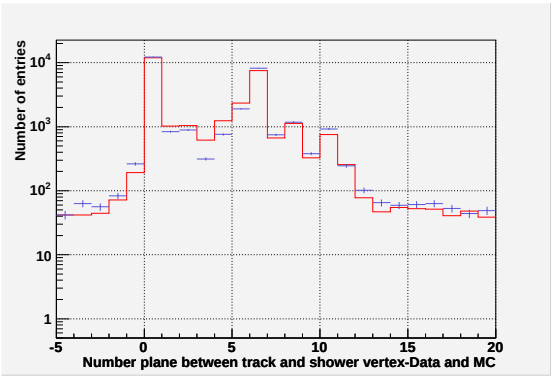

Figure C.21: The number of planes between the shower vertex and track vertex is shown for data and MC. The agreement is good. The odd shape is related to a bug in the shower code that makes all showers 'start' at the lowest possible z position (smallest plane number). This might be troubling but the data and MC treats the effect in the same way. This shows data in red and MC in blue with error bars. The error bars are 1σ. The data are normalized by area down to the MC sample.

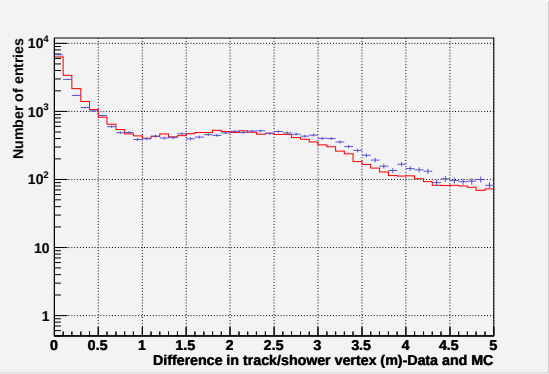

Figure C.22: The difference in position of the track vertex and shower plane in x-y space is shown for data and MC. Because the shower always reconstructs the shower vertex at the lowest possible z position, the evaluation of this distribution is somewhat complicated. The two main points are the data and MC agree (given the complicated nature of this distribution, you could imagine reasons it could disagree more) and it is peaked at zero (the shower is happening 'along' the track). This shows data in red and MC in blue with error bars. The error bars are 1σ. The data are normalized by area down to the MC sample.

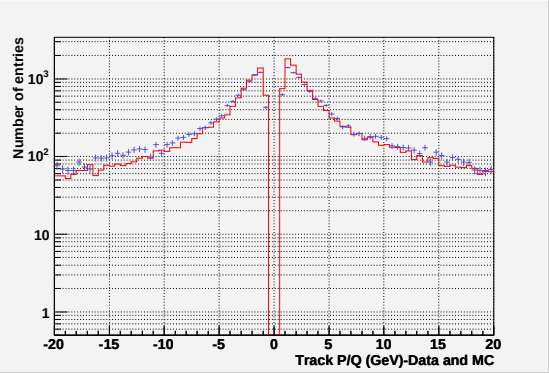

Figure C.23: The fit track momentum (inverse of $\frac{q}{p}$) is shown for data and MC. The data has more low momentum events but besides that there is good agreement. Since the sample has had no cuts to improve the charge and momentum ID and both the data and MC sample are dominated by either event misreconstruction or events entering at odd angles, this is impressive. This shows data in red and MC in blue with error bars. The error bars are 1σ. The data are normalized by area down to the MC sample.

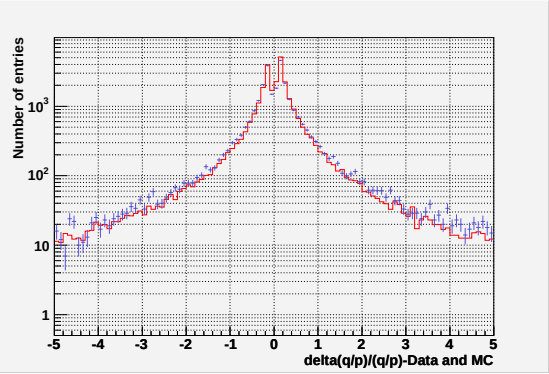

Figure C.24: This shows the uncertainty in fit track momentum for data and MC. This is pretty good and as good as you might expect at this stage of the analysis chain given the type of events in this sample (see previous plot). This shows data in red and MC in blue with error bars. The error bars are 1σ. The data are normalized by area down to the MC sample.

Appendix D

Post Filter Stopper Data-MC Comparison

D.0.7 Introduction-Why Stoppers?

An important idea in the analysis is to see if it is possible to verify the cut selection on an independent set of data. The stopping muon dataset is a mutually exclusive set of data with events of a similar energy distribution to the fully contained sample. There is also high statistics. This sample is used to verify charge ID and vetoshield performance. The events selected in this selection are identical in every way to the fully contained sample except that they have a different requirement on where they enter the detector in the radial coordinate. The selection is such that any partially contained neutrino events are included in the real data.

D.0.8 Post Filter-Data(PreCoilHV)

The post filter dataset is all data runs of the proper run type that lasted more than 1 hour. This includes some runs when the detector had an HV trip or magnetic coils issues (mostly the latter). These events are on the order of 5-10 percent of the run time.

This set is referred to as the PreCoilHV set. Although, this data must be taken out for the final analysis, it does not have to cut from this stage of analysis as the backgrounds for fully contained events appear to be somewhat insensitive to the detector state. This data set is cut down for the final analysis. This was processed with minossoft release R1.14.1 using magnetic field map 202.

D.0.9 Post Filter-MC

The MC data are only cosmic ray muons. The MC is a simulation of single cosmic ray muons and nothing else. This dataset consists of cosmic muon runs r651-r778 (not every run in this range). This was processed using minossoft release R1.14.1 and magnetic field map 201.

D.0.10 Known differences in MC and data

The MINOS detector MC is still undergoing refinements and improvements. It should not be that unexpected that some of these quantities do not agree perfectly and many agree better than a naive observer might expect. There are several potentially significant differences known:

Magnetic field

There is actually two different magnetic field issues that could be a problem. The first is that MC and data use different magnetic field maps. This is not as bad of a situation as might be expected. The differences between the two maps is small in absolute size and mainly involves magnetic field at the 'ears' which is both small and mostly out of the fiducial volume at this stage of reconstruction. The second issue is that MC is generated and reconstructed using a magnetic field in the forward direction. The data at this stage is in forward,reverse and (a bit) in no field. The part with no field will be removed from the final dataset before the final part of the analysis. Chapter 4 and 6

have information on both issues raised here.

Detector

The detector geometry is idealized in the MC. The rotations and mis-alignment of strips, module and scintillator planes are not reproduced in the MC. The z-direction spacing is a constant in the MC. This is not realistic. Although, these physical effects do happen in the far detector, they are small.

D.0.11 Post Filter Stoppers-Cuts

As a quick review the cuts that are applied to data and MC are as similar as possible. Because of the details on what time the MC events are given when generated, the data has a fraction of 0.001 events thrown out compared to MC (this can be thought of as a different normalization). With this exception the cuts are the same, in particular the cuts are:

General

The run must be one hour or more long, be a physics run and contain one and only one track. The event must have either one or no showers associated with the event. The demuxer must not flag the event as a possible multi-muon and the fraction of stray planes to valid planes found by the demuxer for the U and V views when added in quadrature must be smaller than 0.20.

Tracks

The tracks must be 6 or more tracklike planes long and have a fraction of tracklike planes to planes of 0.75 or greater. The track cannot begin or end in the first or last three planes of a SM. The track must begin and end with radial coordinates of $r \geq 0.35$m and the track must either have a vertex at $r \geq 3.90$m and a track end at

$r \leq 3.30$m or the case with vertex and end reversed. The track must have an average of at least 1.5 digits per strip and cannot have more than 2.5 digits per tracklike plane. The track cannot not have an absolute difference between the number of U and V view planes greater than three and must start and end tracking in both views at the same time (can only miss one plane). Finally, the tracking must pass the internal consistency check.

Shower

The shower cannot begin in the first or last three planes of a SM. The shower vertex must greater than 0.35 m from the coil and absolute difference between the number of U and V view planes must be 3 or less.

D.0.12 Results

The following pages have 24 plots. These show the comparison of data to MC for the results after the initial filter is applied. In each plot, the red histogram without error bars are data and the blue points with error bars is MC. These plots are normalized by area. The data is normalized down to the MC sample size by area. When these plots show a figure related to tracks it is for tracks with both zero showers and single showers. The plots with shower related quantities are obviously only for events with a single shower. The plots are all on a log scale. The MC is background only and the data is background + (a tiny) signal. The total number of data and MC events broken down by the number of showers is given in table D.1. The number of events in table D.1 is consistent with the number of events based on a normalization of long muons.

Number of Shower (s)	MC events	Data events	Expected MC events
0	12,634	23,179	20300±250(stat)±2030(syst)
1	77,935	124,398	125,250±450(stat)±12500(syst)
Total	90,569	147,577	145,560±480(stat)±14560(syst)

Table D.1: This shows the number of events for the data and MC after the filter for stopping muons is applied. The final column shows the number of events expected from an independent normalization. The systematic error is taken to be 10 percent. The data was sampled at a relative rate of $\frac{5}{7}$, thus the normalization must be corrected. The zero shower case seems to underestimate the number of events just like the candidate events. Although slightly troubling, the total events in the zero shower channel is small to start with. However, two things should be remembered: the analysis is based on tracks and not showers and because the relative ratio of zero to one shower event is small, the zero shower case is sensitive to small shower efficiency differences.

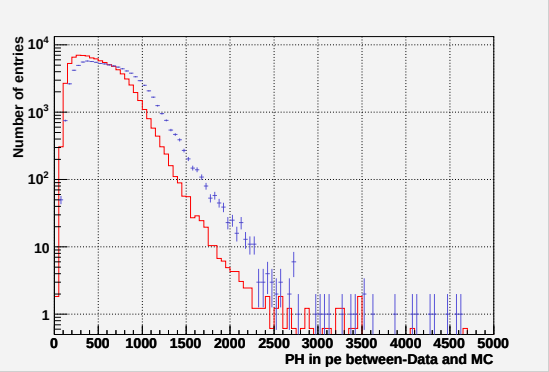

Figure D.1: The pulse height of the track measured in PE (photo-electrons) is for the data and MC is shown. There is a clear difference. The MC has a higher light amount than the data. This however already known. This plot shows the largest single difference of any plot. This shows data in red and MC in blue with error bars. The error bars are 1σ. The data are normalized by area down to the MC sample.

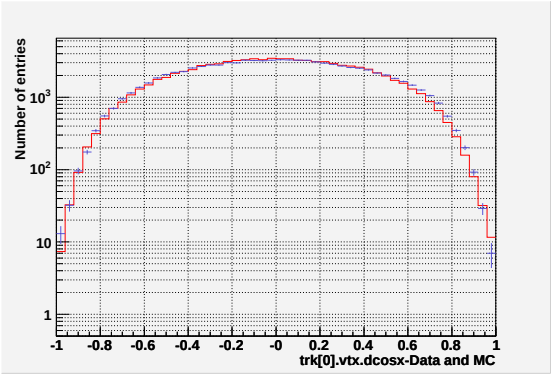

Figure D.2: The directional cosine in the x direction at the track vertex for data and MC is shown. The agreement is nearly perfect. This shows data in red and MC in blue with error bars. The error bars are 1σ. The data are normalized by area down to the MC sample.

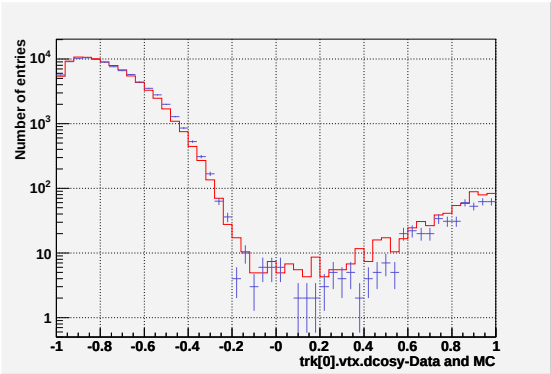

Figure D.3: The directional cosine in the y direction at the track vertex for data and MC is shown. The agreement is good. The positive values of this are events that the software reconstruct going up. The MC has only down going events. This shows that the reconstruction error are being reproduced reasonably well in the MC. This shows data in red and MC in blue with error bars. The error bars are 1σ. The data are normalized by area down to the MC sample.

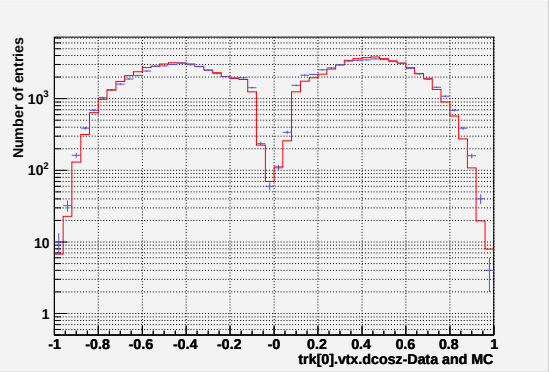

Figure D.4: The directional cosine in the z direction at the track vertex for data and MC is shown. The agreement is pretty good. This shows data in red and MC in blue with error bars. The error bars are 1σ. The data are normalized by area down to the MC sample.

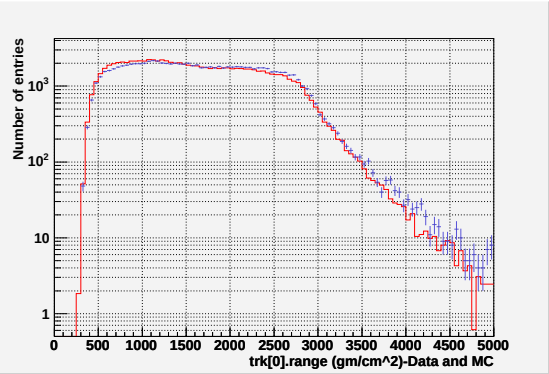

Figure D.5: The track range in $\frac{gm}{cm^2}$ is shown for data and MC. The difference at low range ($\frac{gm}{cm^2}$) is real. A similar effect is seen in candidate events. The effect appears to go away with stricter cuts. This shows data in red and MC in blue with error bars. The error bars are 1σ. The data are normalized by area down to the MC sample.

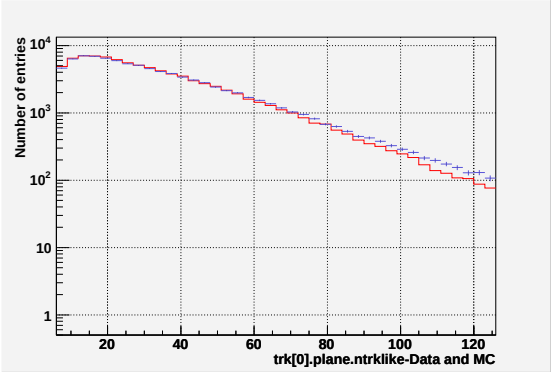

Figure D.6: The number of tracklike planes for the track is shown for the data and MC. The tracklike planes are one that do not evidence of excessive hits. The agreement is good except for planes which have reasonable agreement. This shows data in red and MC in blue with error bars. The error bars are 1σ. The data are normalized by area down to the MC sample.

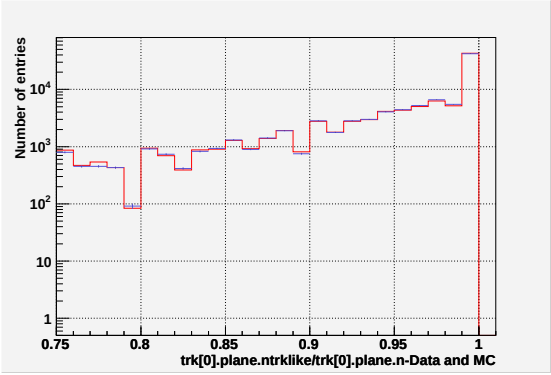

Figure D.7: The fraction of tracklike planes versus all planes in a track is shown for data and MC. This fraction suggests the data and MC track look nearly identical. The agreement is nearly perfect. This shows data in red and MC in blue with error bars. The error bars are 1σ. The data are normalized by area down to the MC sample.

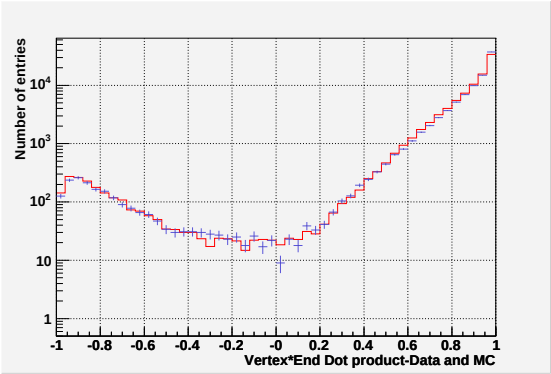

Figure D.8: The dot product of the vertex directional vector and end directional vector is shown for data and MC. The real neutrino events have almost no odds of 'bending backwards'. This means that events with values of this dot product smaller than about 0.5 have either a reconstruction error or unusual muon. The agreement is good. This shows data in red and MC in blue with error bars. The error bars are 1σ. The data are normalized by area down to the MC sample.

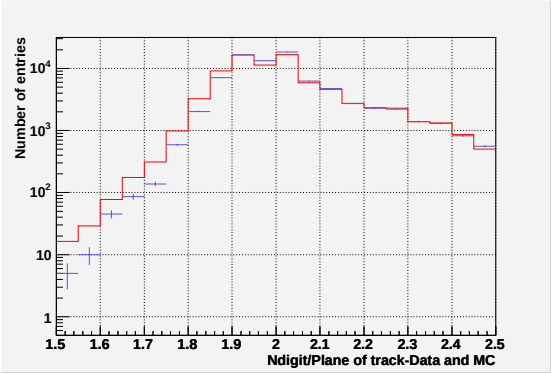

Figure D.9: This shows the fraction of total digits to tracklike planes for data and MC. This is a measure of the average number of hits to tracklike planes. The agreement is good. This shows data in red and MC in blue with error bars. The error bars are 1σ. The data are normalized by area down to the MC sample.

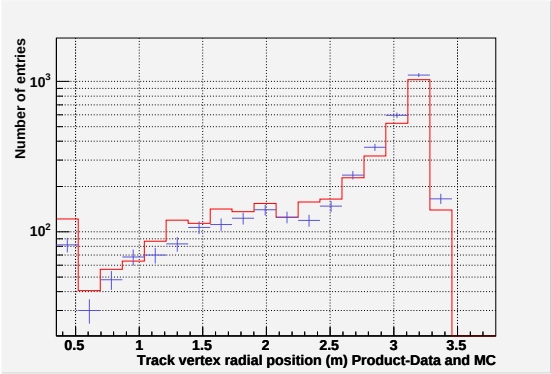

Figure D.10: This shows the track radial vertex position for data and MC. The radial vertex position is simply the radial distance from the center of the detector to the reconstructed track vertex. This plot is somewhat interesting. All the 'stoppers' should reconstruct a vertex at $r \geq 3.9$m, thus this is the radial vertex distribution of misreconstructed cosmic muons. Although, the data has a tiny fraction of partially contained event, it is mostly misreconstructed muons. The fact that these misreconstructions agree so well is remarkable, This shows data in red and MC in blue with error bars. The error bars are 1σ. The data are normalized by area down to the MC sample.

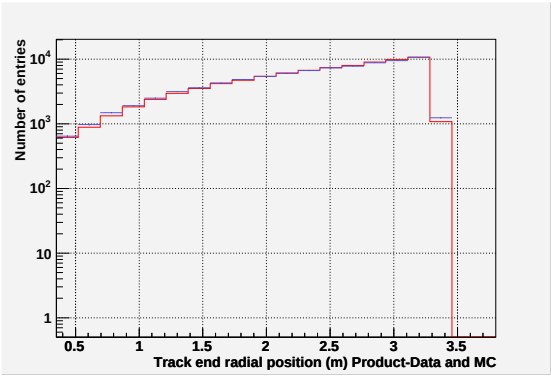

Figure D.11: This shows the track radial end position for data and MC. It is simply the position in radial space the track end is reconstructed. The track radial positions are sensitive in this sample to reconstruction errors and the track radial end is sensitive to the correctly reconstructed stopper. The agreement here is nearly perfect. This shows data in red and MC in blue with error bars. The error bars are 1σ. The data are normalized by area down to the MC sample.

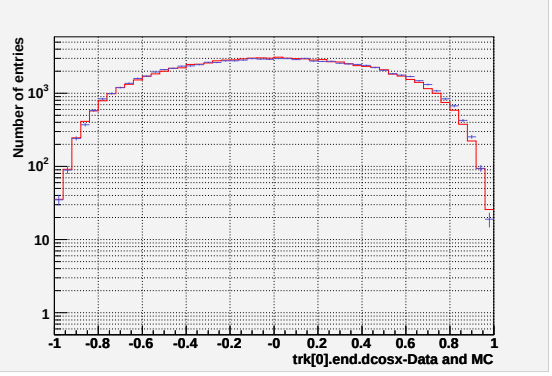

Figure D.12: The directional cosine in the x direction at the track end for data and MC is shown. The agreement is almost perfect. This shows data in red and MC in blue with error bars. The error bars are 1σ. The data are normalized by area down to the MC sample.

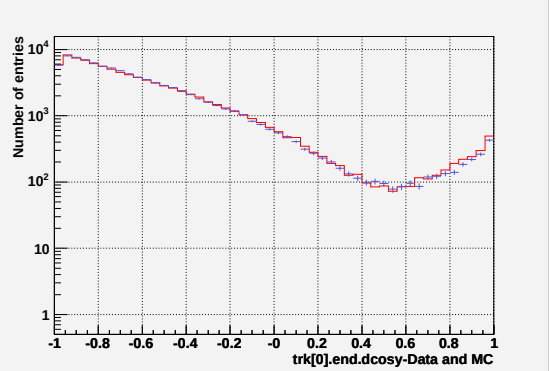

Figure D.13: The directional cosine in the y direction at the track end for data and MC is shown. The agreement is almost perfect.This shows data in red and MC in blue with error bars. The error bars are 1σ. The data are normalized by area down to the MC sample.

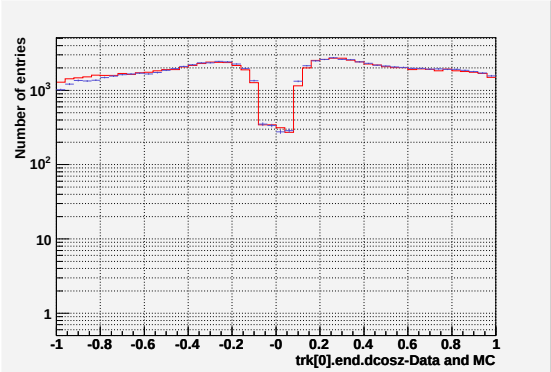

Figure D.14: The directional cosine in the z direction at the track end for data and MC is shown. The agreement is good. This shows data in red and MC in blue with error bars. The error bars are 1σ. The data are normalized by area down to the MC sample.

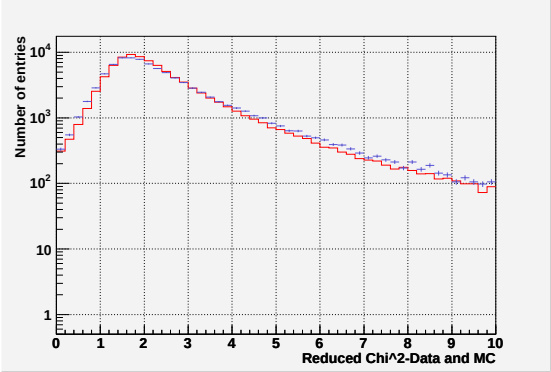

Figure D.15: The χ^2 per degree of freedom ($\frac{\chi^2}{ndof}$) is shown for data and MC. The agreement is much better than might be expected as the $\frac{\chi^2}{ndof}$ is really sensitive to differences in the geometry. Since, the geometry for MC is known to be overly simple, this is somewhat impressive. As expected with an ideal geometry the $\frac{\chi^2}{ndof}$ is better for MC. This shows data in red and MC in blue with error bars. The error bars are 1σ. The data are normalized by area down to the MC sample.

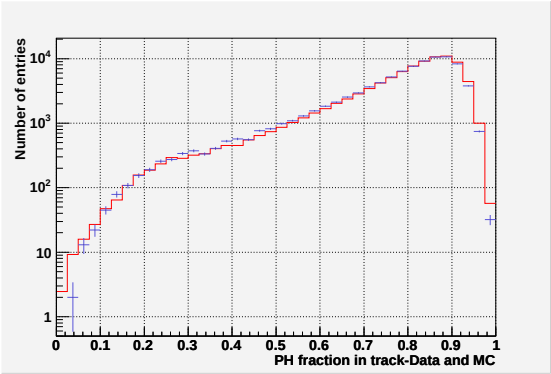

Figure D.16: The fraction of PH in a track versus the total event PH is shown for data and MC. The agreement is good. Given the 10%-15% difference in normalization this is much better, as would be expected for a ratio. This shows data in red and MC in blue with error bars. The error bars are 1σ. The data are normalized by area down to the MC sample.

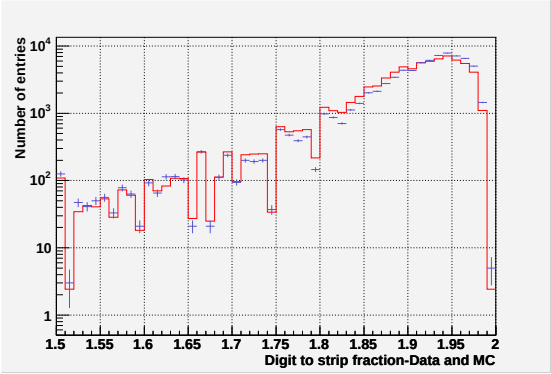

Figure D.17: The fraction of digits to all strips in the track is shown for data and MC. This is a measure of the average fraction of hits to strips for a track. A high number suggests that the track is made almost only of double ended strips. The agreement is good. This shows data in red and MC in blue with error bars. The error bars are 1σ. The data are normalized by area down to the MC sample.

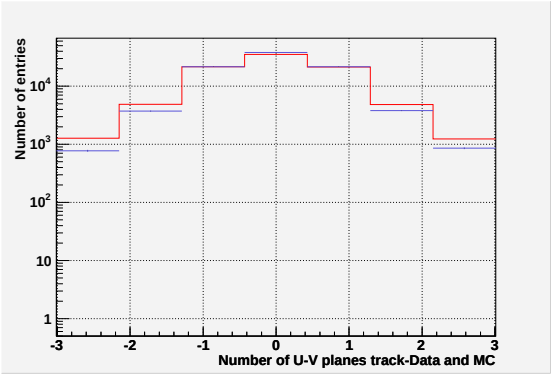

Figure D.18: The difference in U and V view planes in a track is shown. Since U and V view planes alternate, it is expected that the track should be tracked in both the U and V view. The data and MC agree. This shows data in red and MC in blue with error bars. The error bars are 1σ. The data are normalized by area down to the MC sample.

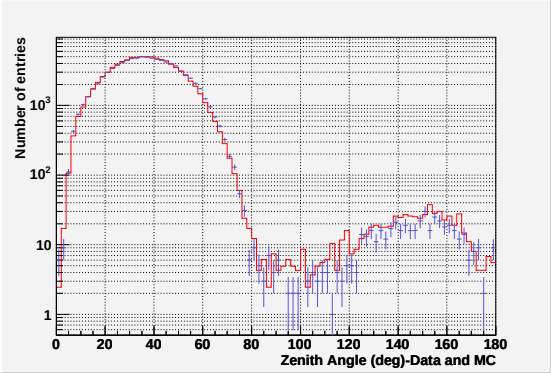

Figure D.19: The zenith angle in degrees is shown for data and MC. A zenith angle of 0 is up and zenith angle of 180 is down. The agreement is almost perfect and better than the similar distribution for candidate events. This shows data in red and MC in blue with error bars. The error bars are 1σ. The data are normalized by area down to the MC sample.

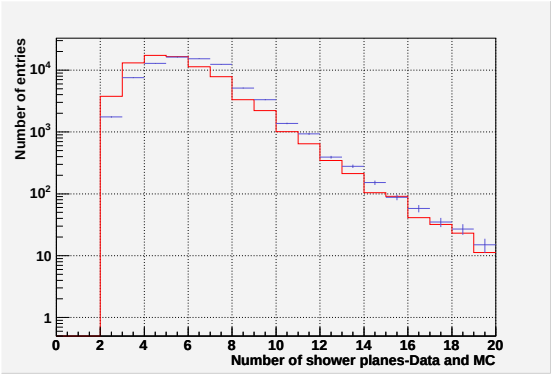

Figure D.20: The number of shower planes in the single shower events for data and MC is shown. Since almost no shower cuts were applied this is pretty good agreement. This shows data in red and MC in blue with error bars. The error bars are 1σ. The data are normalized by area down to the MC sample.

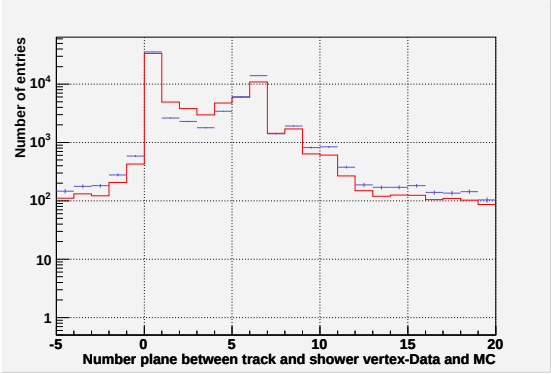

Figure D.21: The number of planes between the shower vertex and track vertex is shown for data and MC. The agreement is good. The odd shape is related to a bug in the shower code that makes all showers 'start' at the lowest possible z position (smallest plane number). This might be troubling but the data and MC treats the effect in the same way. This shows data in red and MC in blue with error bars. The error bars are 1σ. The data are normalized by area down to the MC sample.

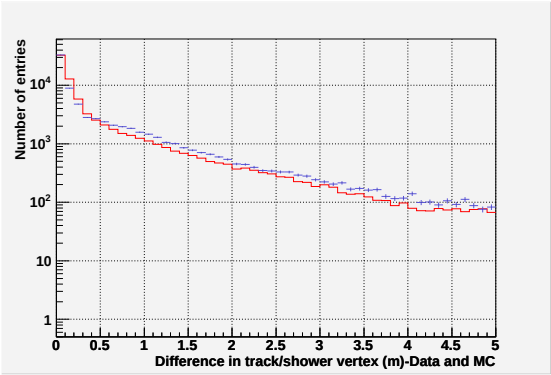

Figure D.22: The difference in position of the track vertex and shower plane in x-y space is shown for data and MC. Because the shower always reconstructs the shower vertex at the lowest possible z position, the evaluation of this distribution is somewhat complicated. The two main points are the data and MC agree (given the complicated nature of this distribution, you could imagine reasons it could disagree more) and it is peaked at zero (the shower is happening 'along' the track). This shows data in red and MC in blue with error bars. The error bars are 1σ. The data are normalized by area down to the MC sample.

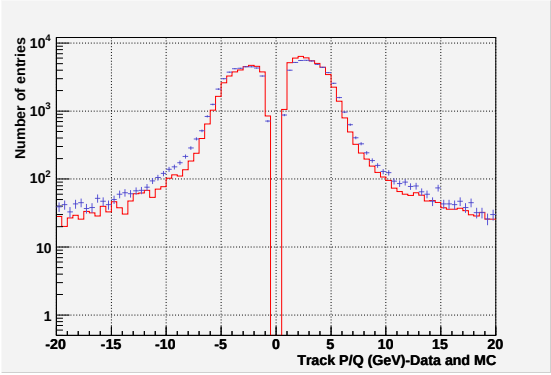

Figure D.23: The fit track momentum (inverse of $\frac{q}{p}$) is shown for data and MC. There is good agreement with the possible exception of the charge ratio. This is before any cuts to improve the charge reconstruction ID. This shows data in red and MC in blue with error bars. The error bars are 1σ. The data are normalized by area down to the MC sample.

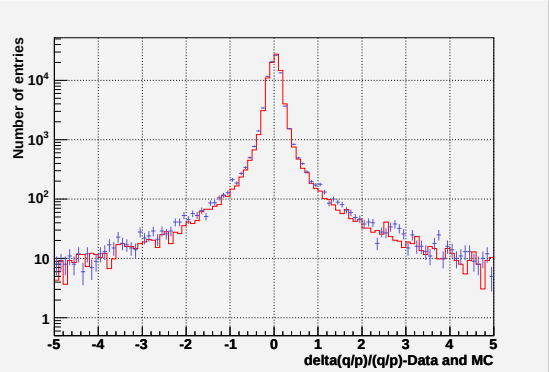

Figure D.24: This shows the uncertainty in fit track momentum for data and MC. This is pretty good agreement. This shows data in red and MC in blue with error bars. The error bars are 1σ. The data are normalized by area down to the MC sample.

Appendix E

Event Displays

E.1 Event Display overview

This appendix shows a variety of events and the event displays associated with with these events. This is meant to show a sampling of different event classes for both signal and in particular event backgrounds. There are two different types of event displays shown. There is an event display which shows the digits and the reconstructed and truth data in the case the event is a MC event. There is also an event display which shows the event as it looks in the detector. Each of these events displays exist for any given event. However, only one of the two could be shown. For a listing of the events see table E.1.

E.2 Event display list

Number	Run	Snarl	Event Type	Data type
1	179	334	ν_μ	MC
2	179	517	ν_μ	MC
5	179	3115	NC	MC
6	179	16	ν_e	MC
7	652	4361	Cosmic μ	MC
8	662	71395	Cosmic μ	MC
9	662	54961	Cosmic μ	MC
10	187	4162	ν_τ	MC
11	3043	301	n	MC
12	21323	4187	Cand.	DATA
13	22919	7988	Cand.	DATA
14	18581	63807	Cand.	DATA
15	27184	116702	Cand.	DATA

Table E.1: This is a listing of the events shown in the event displays. The first column is the number of the event in the listing. The second and third column are the run and snarl number of the event. The fourth column show the event type (ν_μ or ν_e for example). The final column shows if the event is MC or data. The MC events are shown first.

E.2.1 MC:CC-ν_μ

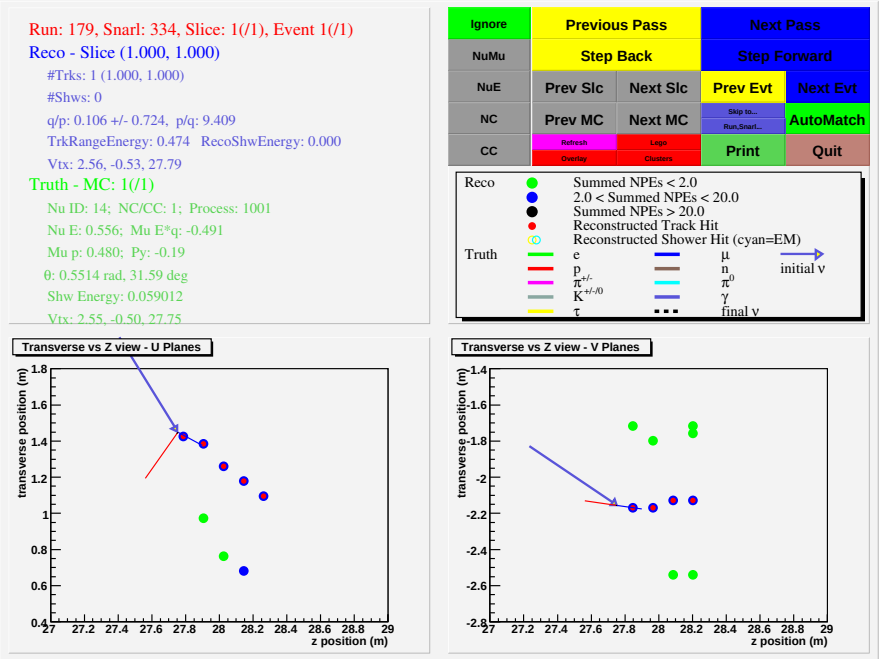

Figure E.1: Run 179, Snarl 334-ν_μ event

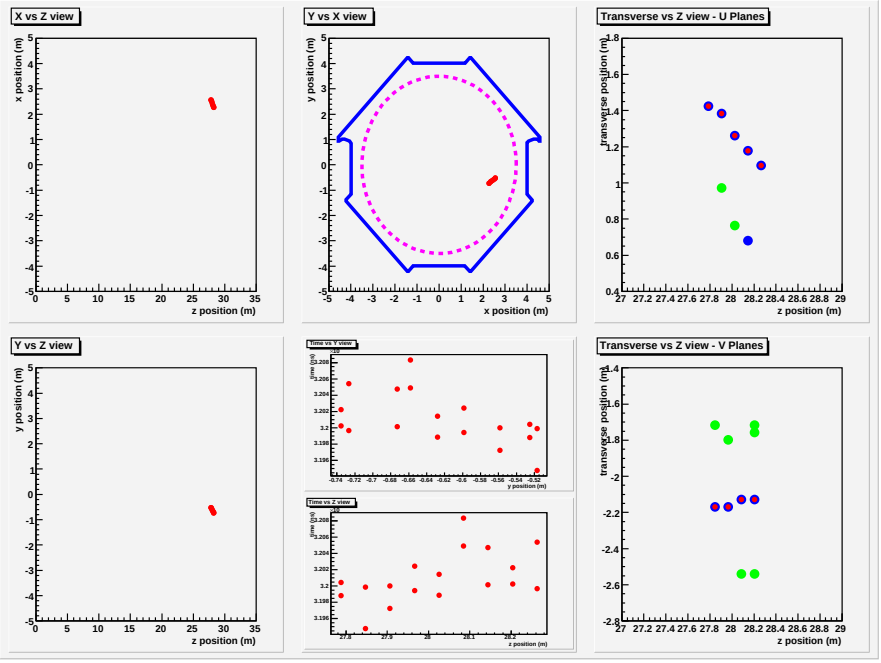

Figure E.2: Run 179, Snarl 334-ν_μ background event

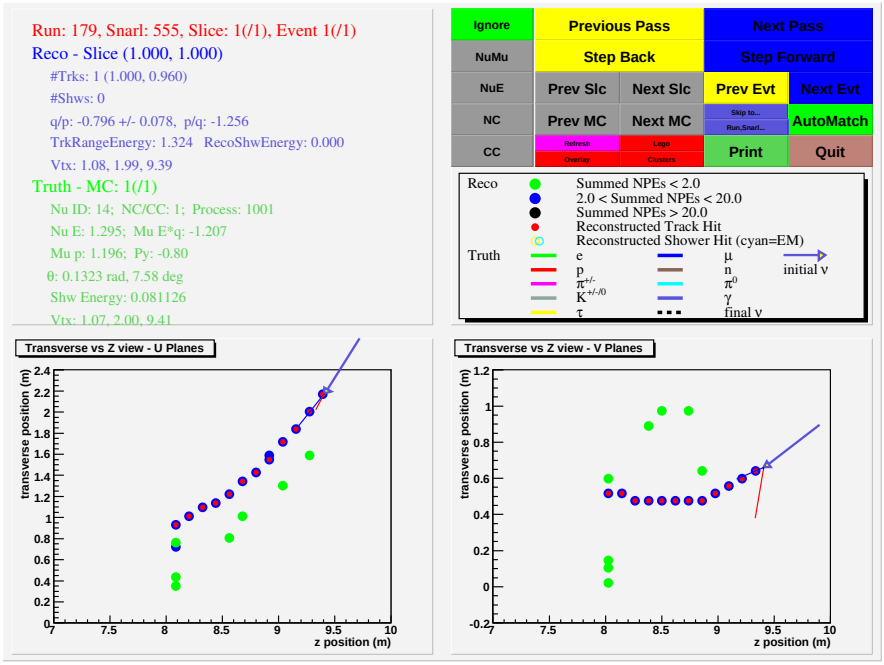

Figure E.3: Run 179, Snarl 555-ν_μ background event

E.2.2 MC:CC-ν_e

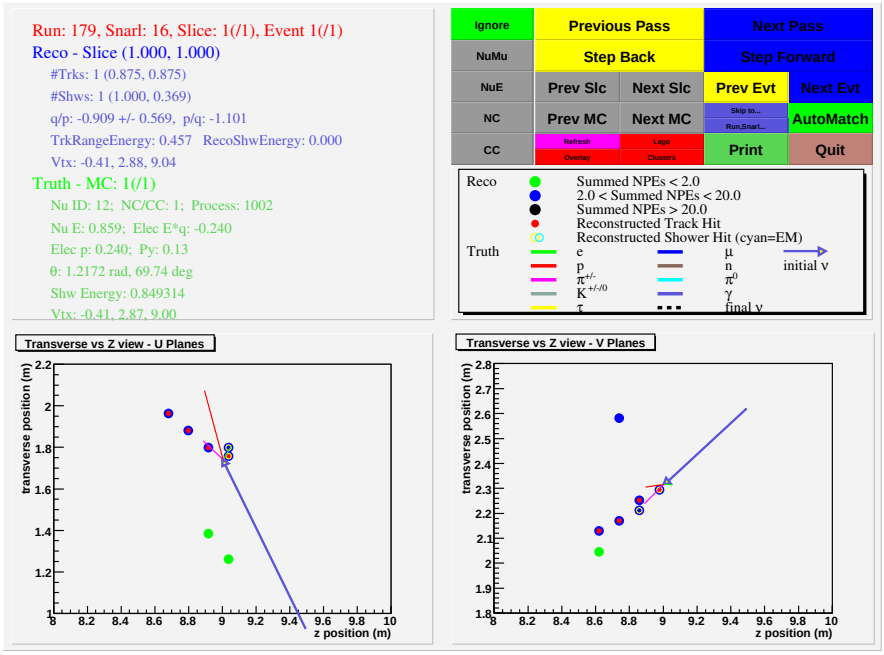

Figure E.4: Run 179, Snarl 16-ν_e background event

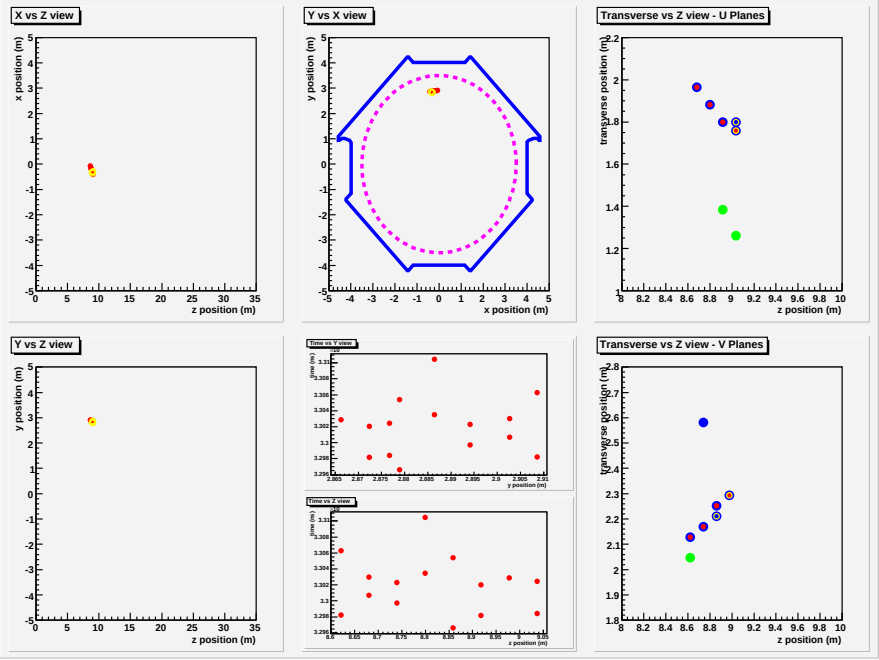

Figure E.5: Run 179, Snarl 16-ν_e background event

E.2.3 MC:NC

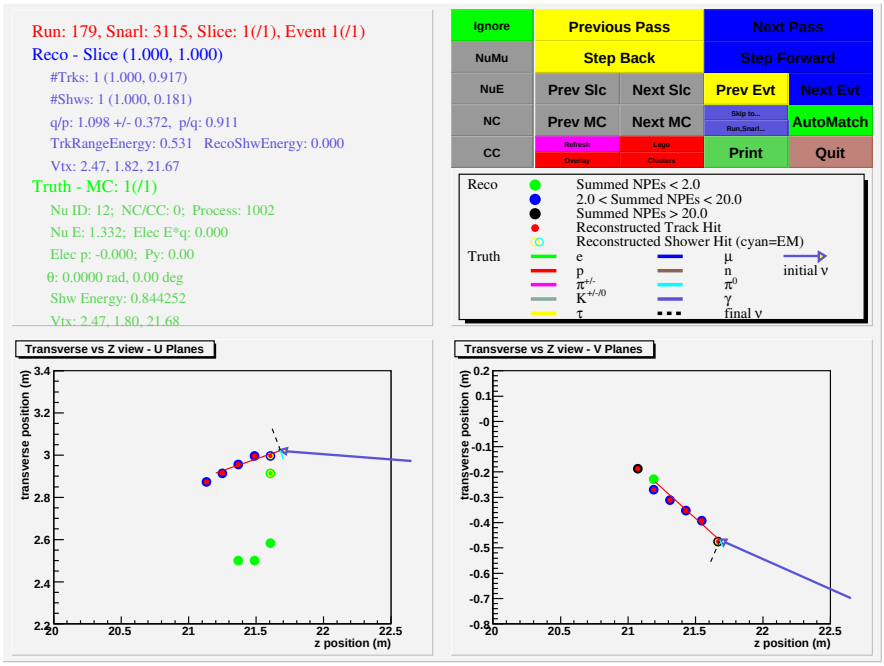

Figure E.6: Run 179, Snarl 3115-NC background event

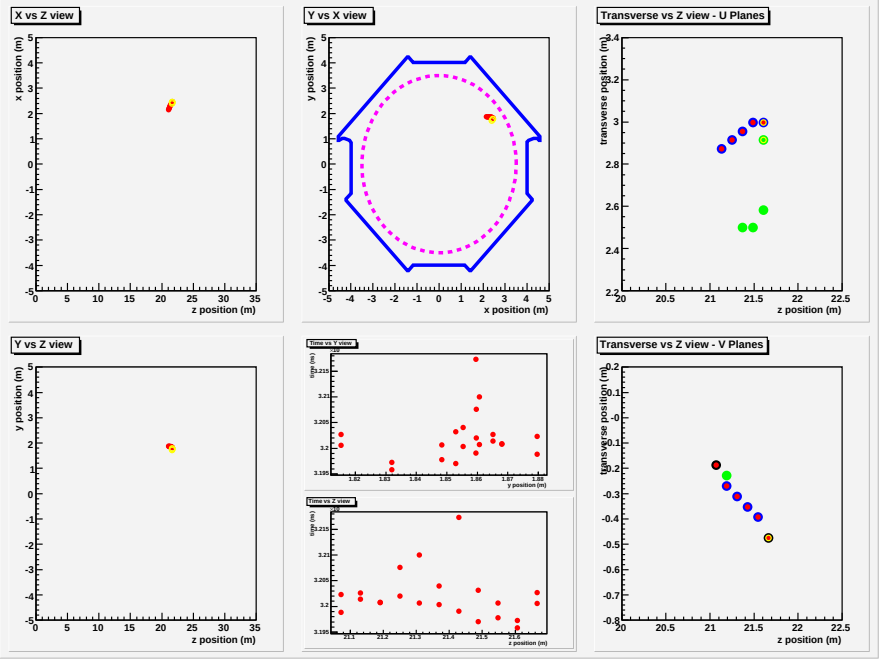

Figure E.7: Run 179, Snarl 3115-NC background event

E.2.4 MC:CC-ν_e

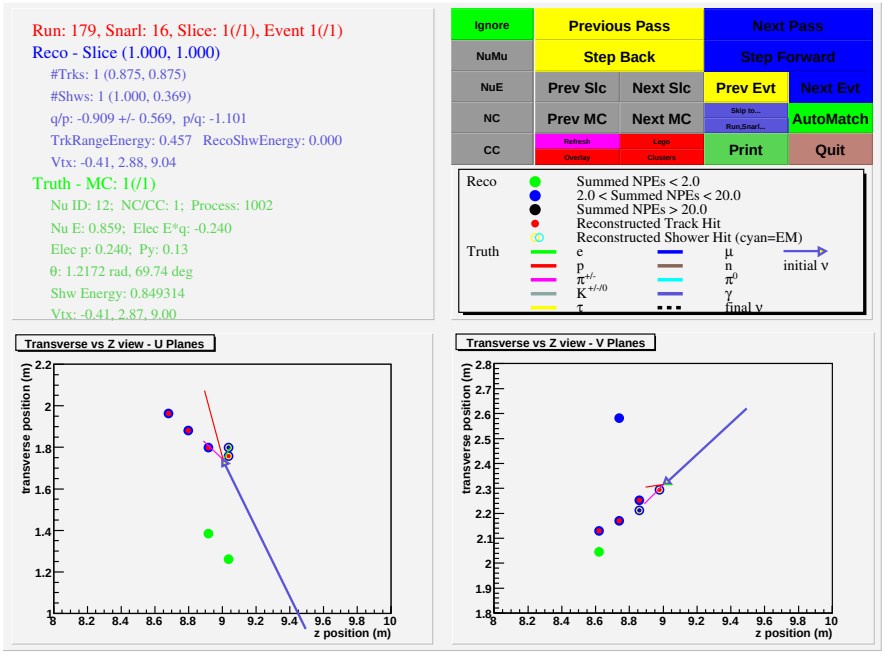

Figure E.8: Run 179, Snarl 16-ν_e background event

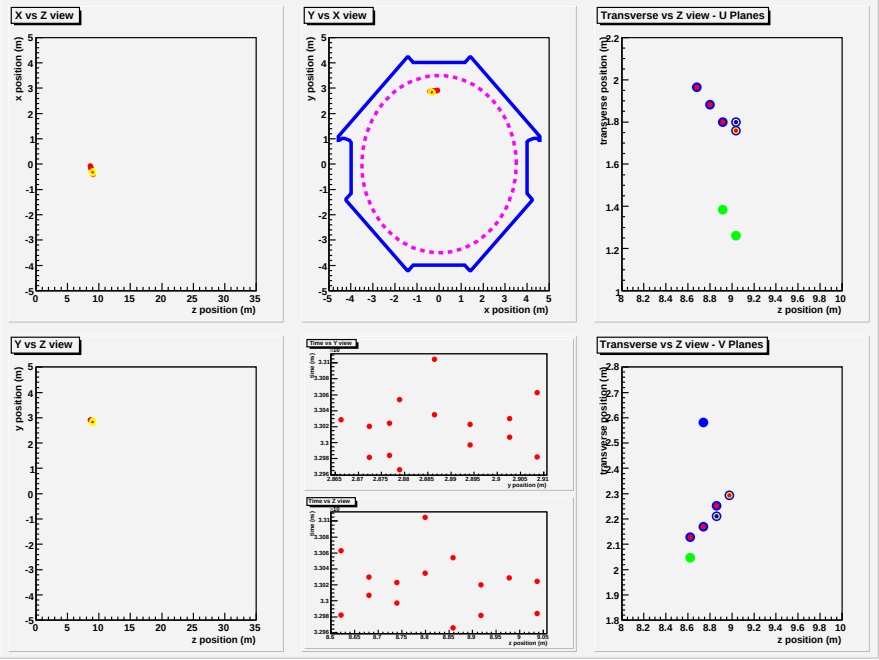

Figure E.9: Run 179, Snarl 16-ν_e background event

E.2.5 MC:Cosmic μ

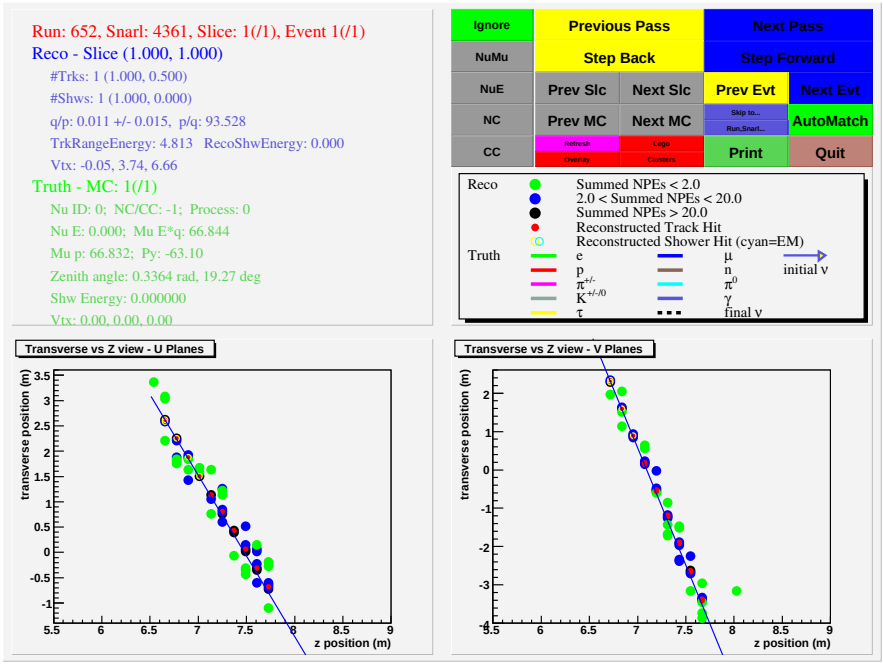

Figure E.10: Run 652, Snarl 4361- Cosmic μ background event-fails cut 2

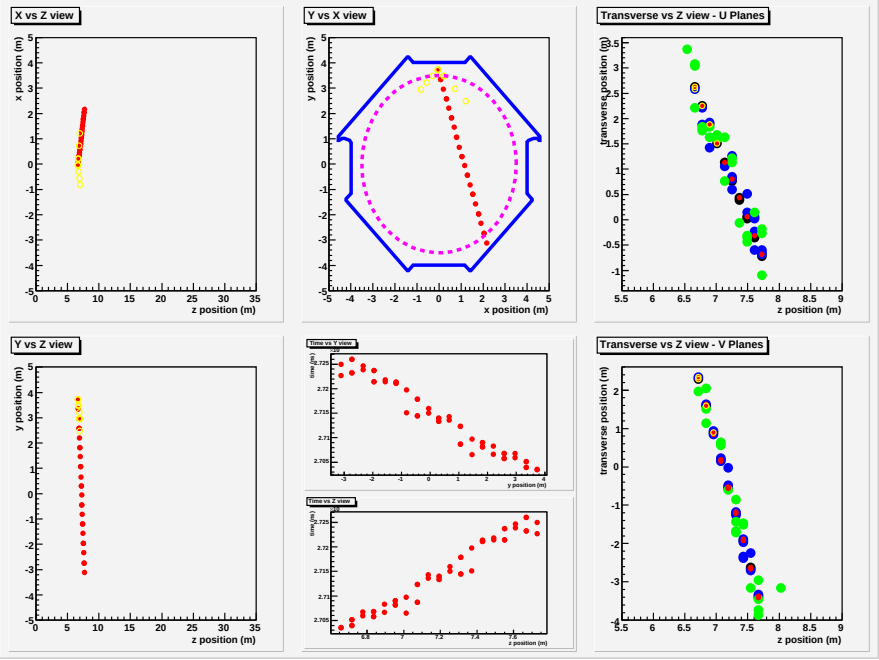

Figure E.11: Run 652, Snarl 4361- Cosmic μ background event-fails cut 2

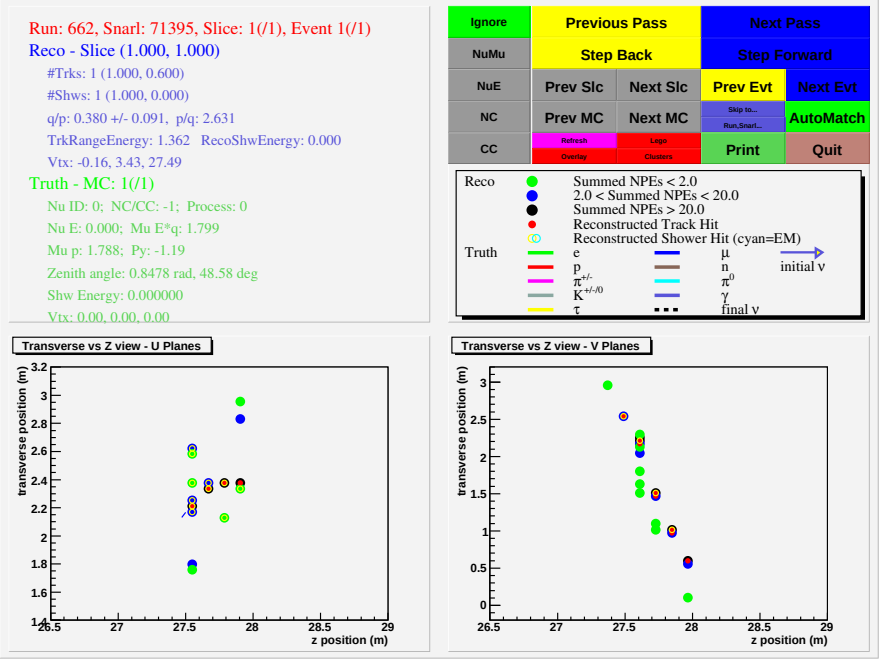

Figure E.12: Run 662, Snarl 71395-Cosmic μ background event-fails cut 7

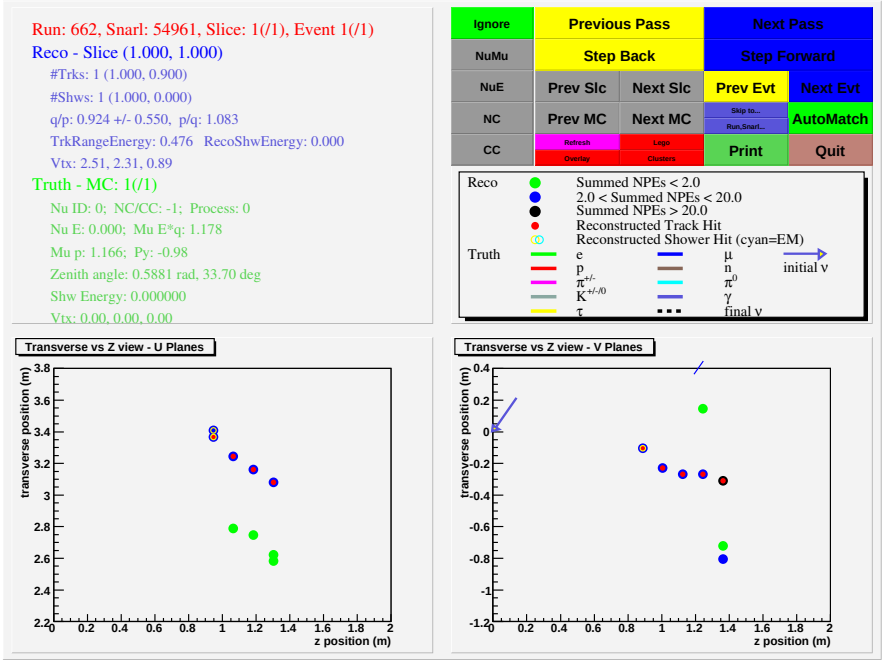

Figure E.13: Run 662, Snarl 54961-Cosmic μ background (passes all cuts)

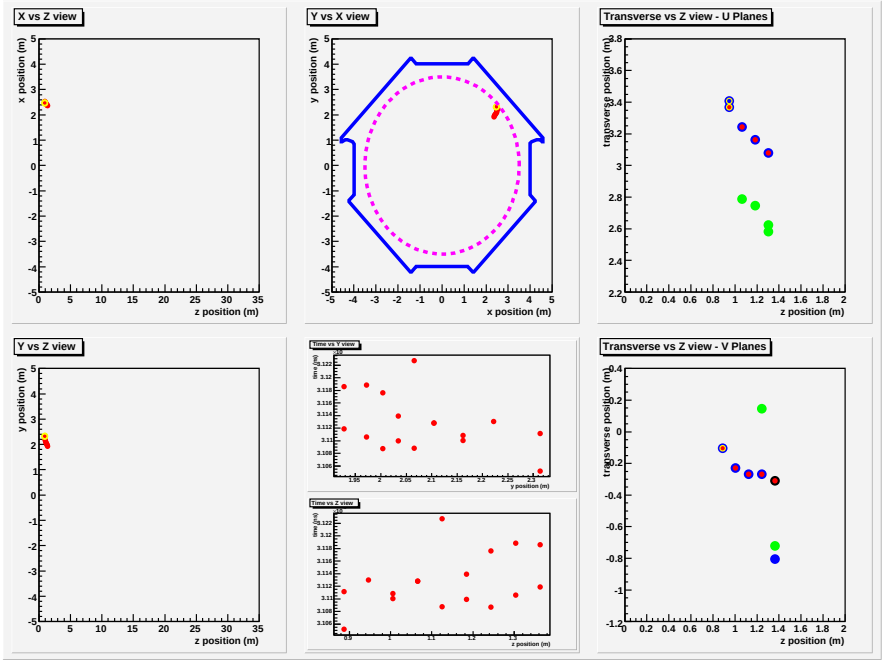

Figure E.14: Run 662, Snarl 54961-Cosmic μ background (passes all cuts)

E.2.6 MC:CC-ν_τ

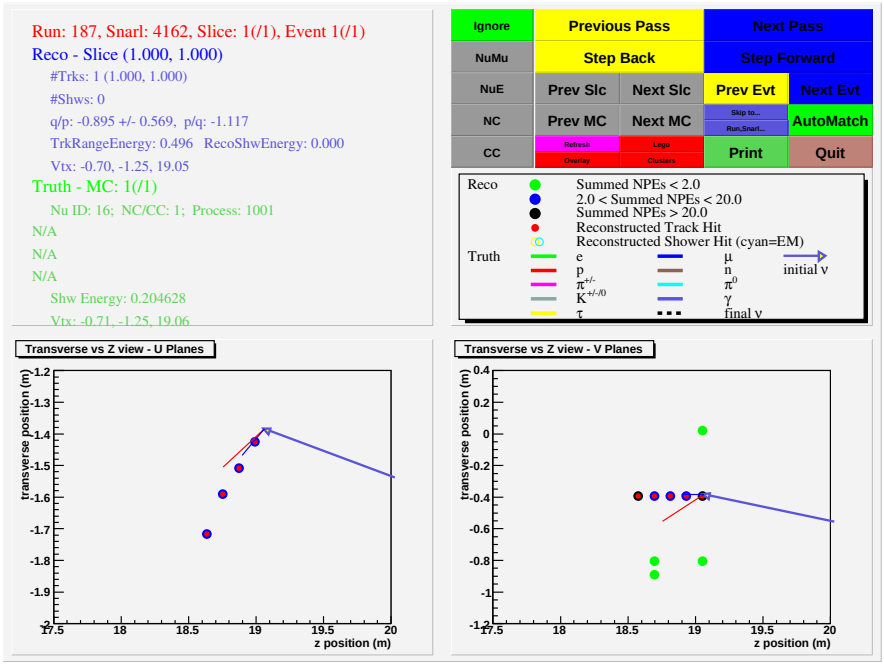

Figure E.15: Run 187, Snarl 4162-ν_τ background event

E.2.7 MC:Neutron

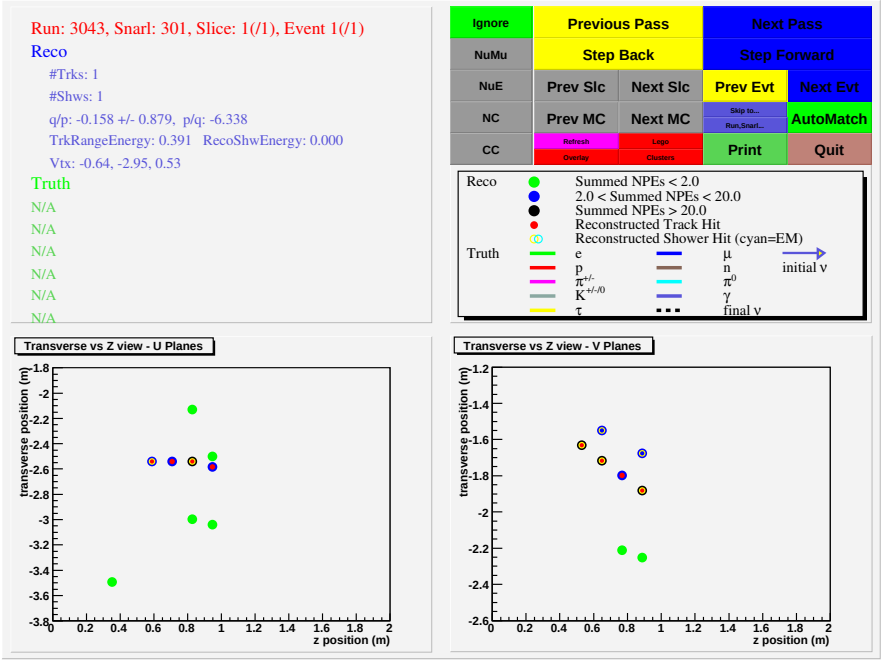

Figure E.16: Run 3043, Snarl 301-Only n background event

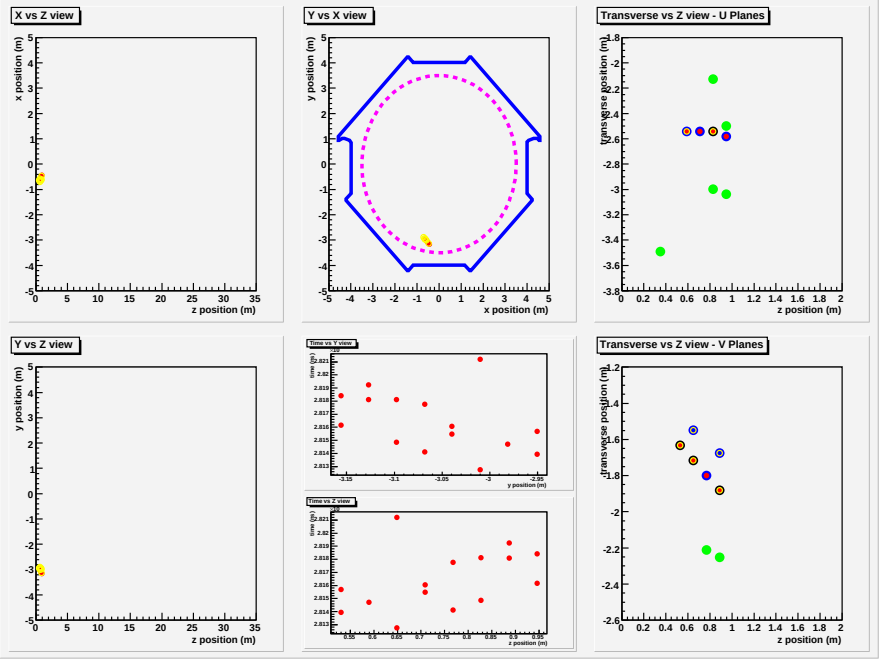

Figure E.17: Run 3043, Snarl 301-only n background event

E.2.8 Data

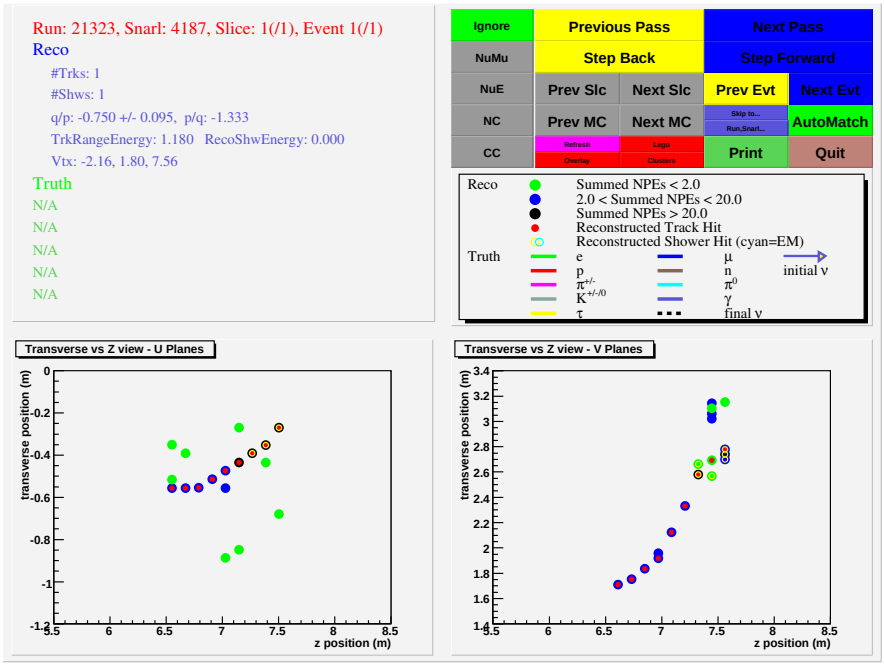

Figure E.18: Run 21,323 Snarl 4,187-Data

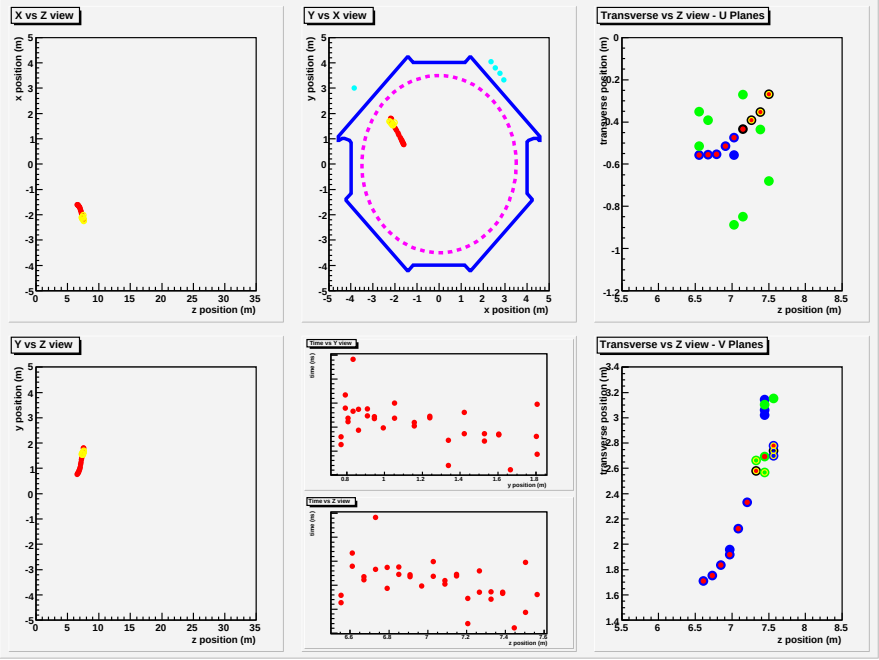

Figure E.19: Run 21,323 Snarl 4,187

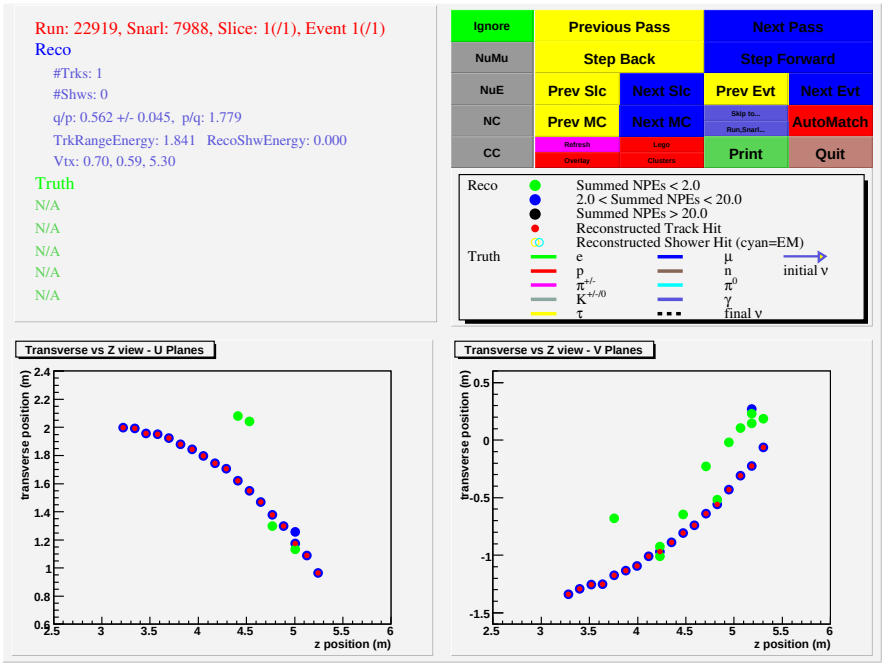

Figure E.20: Run 22,919 Snarl 7,988-Data

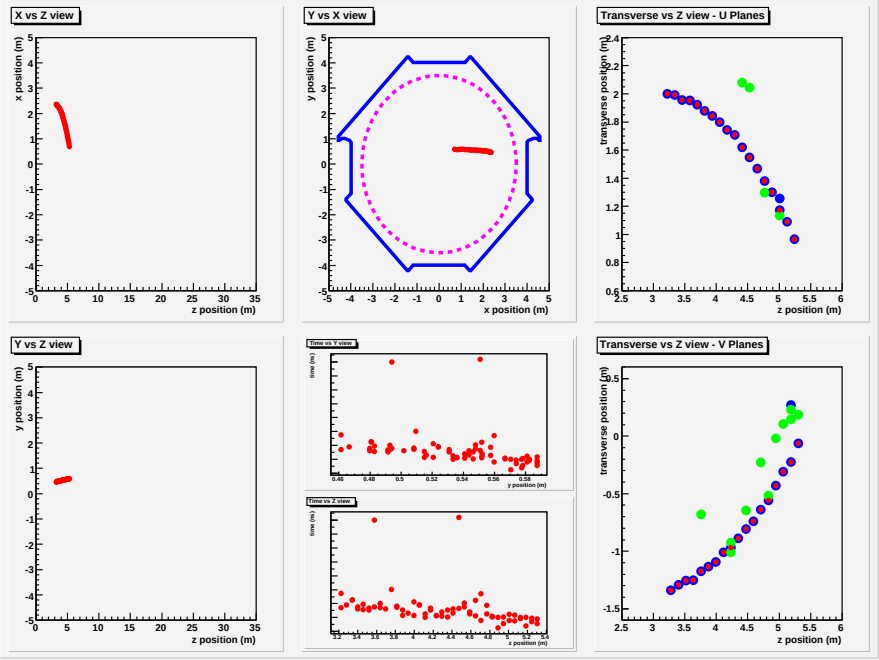

Figure E.21: Run 22,919 Snarl 7,988

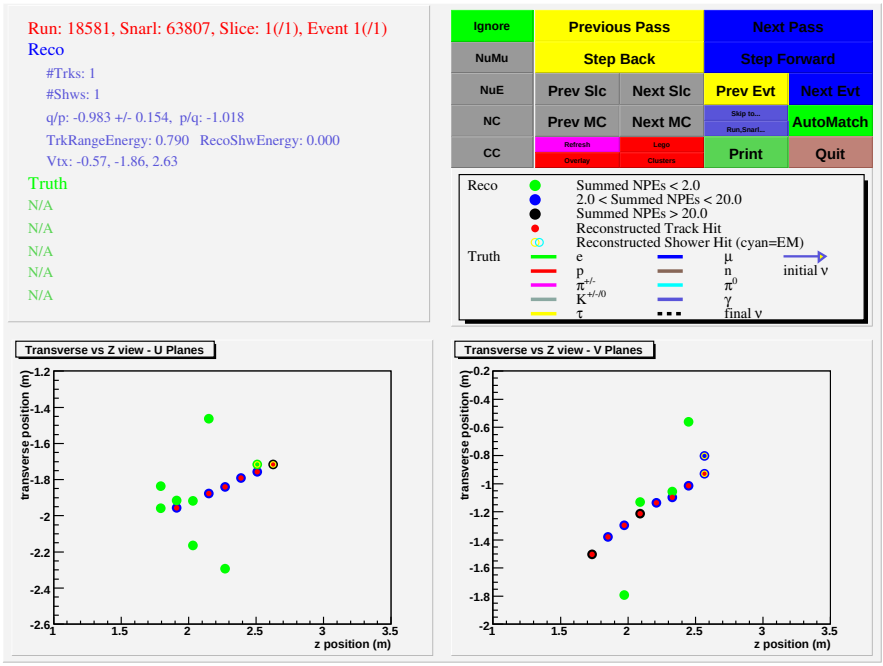

Figure E.22: Run 18,581 Snarl 63,807-Data

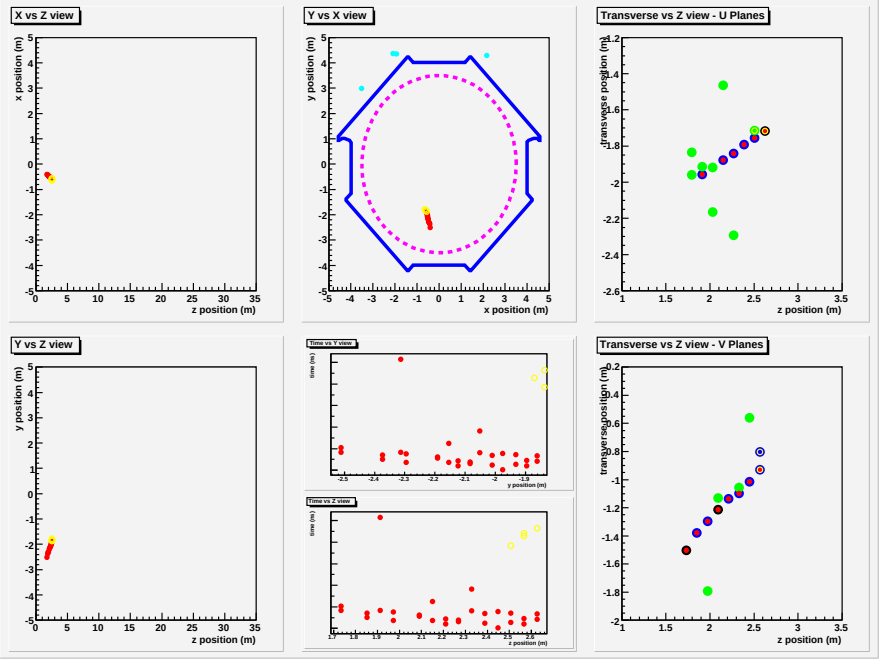

Figure E.23: Run 18,581 Snarl 63,807

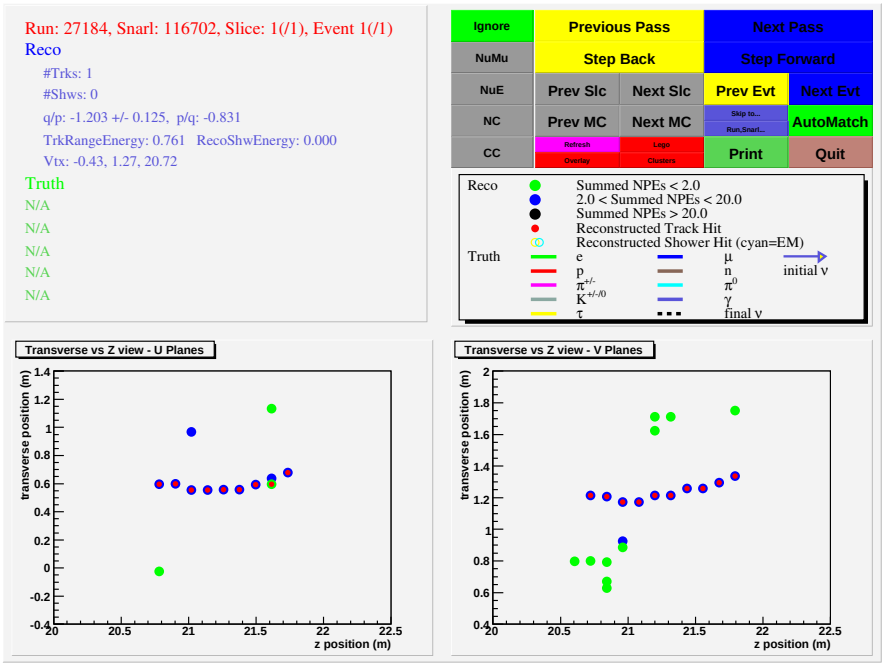

Figure E.24: Run 27,184 Snarl 116,702-Data

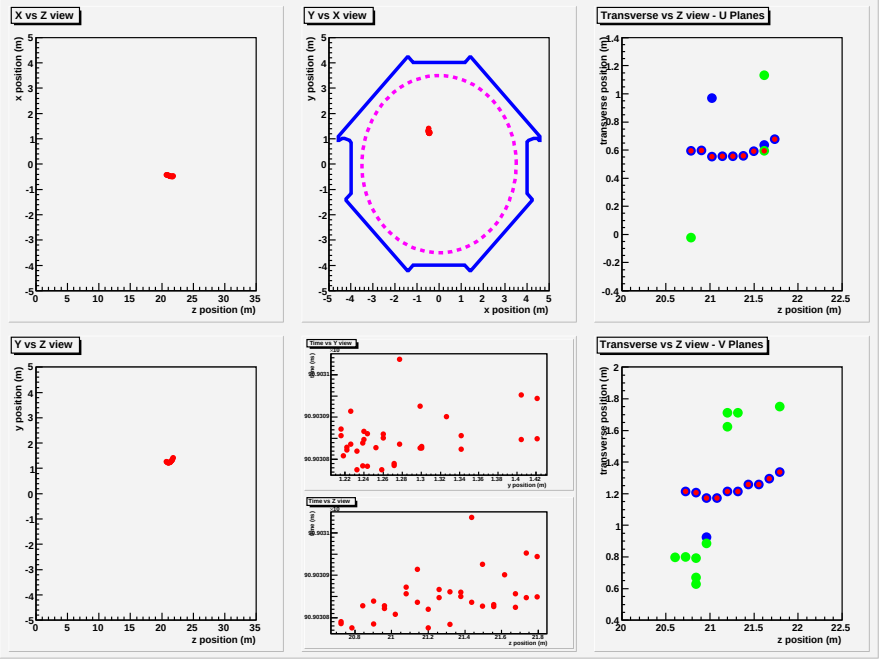

Figure E.25: Run 27,184 Snarl 116,702

Appendix F

Monte Carlo overview

F.1 Monte Carlo overview

MC is treated as similar to data as possible in the MINOS reconstruction. Some of the known differences are in the magnetic field map and the ideal geometery used by the MC. Although other appendices have detailed data-MC comparison, this appedix lists what was used for MC.

F.2 Monte Carlo used in analysis

This is a listing[1] of the MC runs used for the analysis.

F.2.1 ν MC

The ν MC information is shown in table F.1. This lists all the ν MC used in the analysis.

[1] This information was provided by P.Ward at Cambridge

Run	Exp. (kTy)	Flux	ν E (GeV)	Hadronic	Track. cuts (KeV)
179	360.5	Barr	0.2-50	GCALOR	100
180	360.5	Barr	0.2-50	GCALOR	100
181	183.0	Barr	0.2-50	GCALOR	100
182	360.5	Barr	0.2-50	GCALOR	100
183	360.5	Barr	0.2-50	SLAC-GHEISA	100
184	180.0	Barr	0.2-50	GCALOR	10
185	180.0	Barr	0.2-50	GCALOR	10
186	257.6	Battistoni	0.1-50	GCALOR	100
187	76.6	Barr	0.2-50	GCALOR	100
188	180.0	Barr	0.2-50	GCALOR	100

Table F.1: This shows the basic information for the ν MC used. All the runs were generated with Neugen3 and magnetic field map 201. All fluxes were assumed to be at solar max. A GEANT 3 simulation was used. Only runs 187 and 188 have ν_τ

F.2.2 Cosmic μ MC

Runs 651 to run 778 were the cosmic μ MC runs used for the analysis (not every run between 651-778 used). These files had a 100 KeV tracking cut and assumed a $\frac{\mu+}{\mu-}$ ratio of 1.25. The distribution is based on a rock map of Soudan.

F.2.3 Neutron MC

Runs 3033-3043 were generated with Geant4 to simulate neutronos in rock. Each file had a tracking cut off of 100 KeV. See chapter 6 for more details.

Appendix G

MC Cut selection comparisons

G.1 Cuts

This shows the effects of the cuts on the MC Cosmic μ background and on the MC atmospheric neutrino sample (R179R180). What is shown in this section is the effect of applying these cuts in the same order they are applied in the analysis. Thus Cut 2 is after Cut 1 has already been applied. All of the event rates are shown for events per kTy. No error bars are shown. The actual calculation of background do use the correct statistics, but the error bars made the plots 'too busy' and were more of a nuance, than an aid. Most of the cuts have a clear advantage of throwing out excessive background to the signal. The one cut which has the lowest relative effect is the digits to tracklike plane cut. It is true that the efficiency of this cut is low, but it is also needed. The later cuts would not look as good as they do without it.

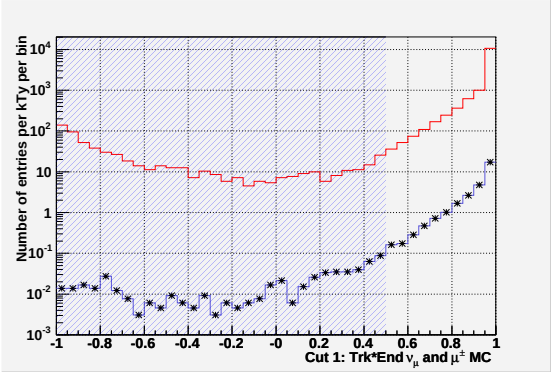

Figure G.1: The dot product of the track vertex times the track end vectors for MC cosmic background μ and MC ν is shown. The cosmic MC background is shown with the red histogram and the ν MC is shown with the blue histogram with the marker. The area with the cross hash is cut from the sample. Both the cosmic background μ and ν are scaled to events per kTy. No statistical error bars are drawn. Both 0 and 1 shower data is shown together.

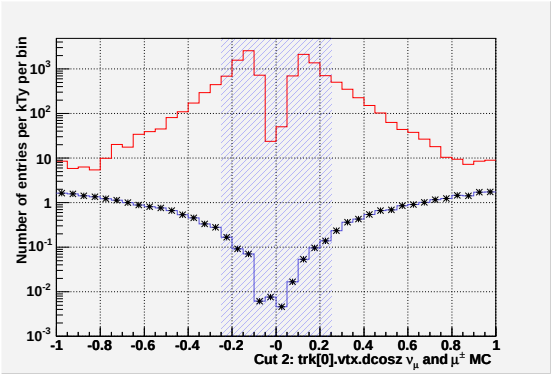

Figure G.2: The track vertex directional cosine in the z-direction for MC cosmic background μ and MC ν is shown. The cosmic MC background is shown with the red histogram and the ν MC is shown with the blue histogram with the marker. The area with the cross hash is cut from the sample. Both the cosmic background μ and ν are scaled to events per kTy. No statistical error bars are drawn. Both 0 and 1 shower data is shown together.

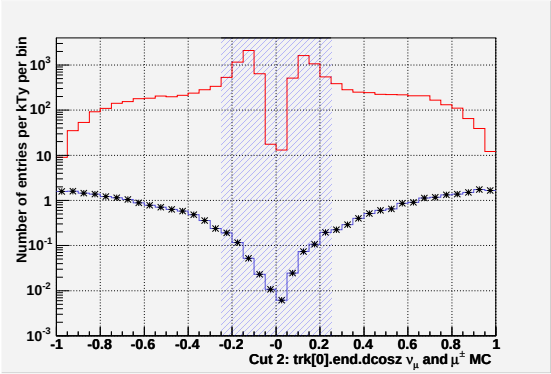

Figure G.3: The track end directional cosine in the z-direction for MC cosmic background μ and MC ν is shown. The cosmic MC background is shown with the red histogram and the ν MC is shown with the blue histogram with the marker. The area with the cross hash is cut from the sample. Both the cosmic background μ and ν are scaled to events per kTy. No statistical error bars are drawn. Both 0 and 1 shower data is shown together.

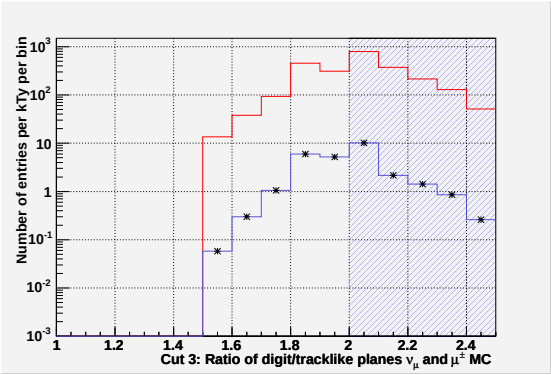

Figure G.4: The fraction of digit per tracklike plane for MC cosmic background μ and MC ν is shown. The cosmic MC background is shown with the red histogram and the ν MC is shown with the blue histogram with the marker. The area with the cross hash is cut from the sample. Both the cosmic background μ and ν are scaled to events per kTy. No statistical error bars are drawn. Both 0 and 1 shower data is shown together.

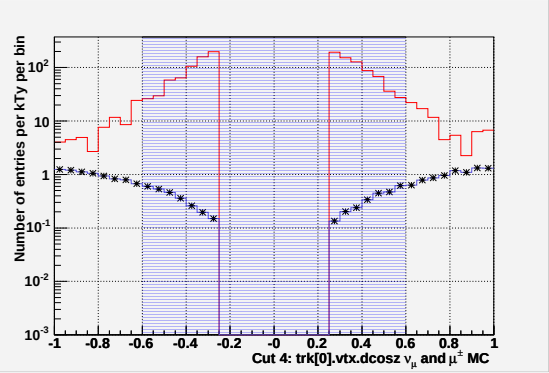

Figure G.5: The track vertex directional cosine in the z-direction for MC cosmic background μ and MC ν is shown. The cosmic MC background is shown with the red histogram and the ν MC is shown with the blue histogram with the marker. The area with the cross hash is cut from the sample. Both the cosmic background μ and ν are scaled to events per kTy. No statistical error bars are drawn. Both 0 and 1 shower data is shown together.

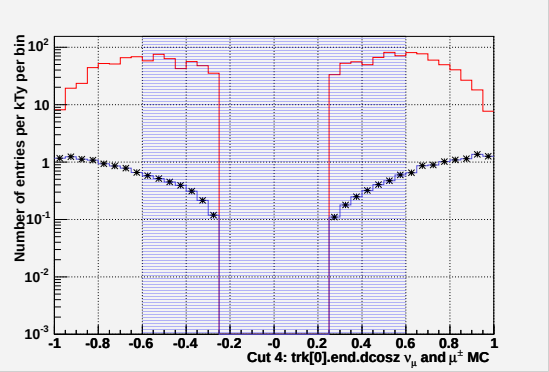

Figure G.6: The track end directional cosine in the z-direction for MC cosmic background μ and MC ν is shown. The cosmic MC background is shown with the red histogram and the ν MC is shown with the blue histogram with the marker. The area with the cross hash is cut from the sample. Both the cosmic background μ and ν are scaled to events per kTy. No statistical error bars are drawn. Both 0 and 1 shower data is shown together.

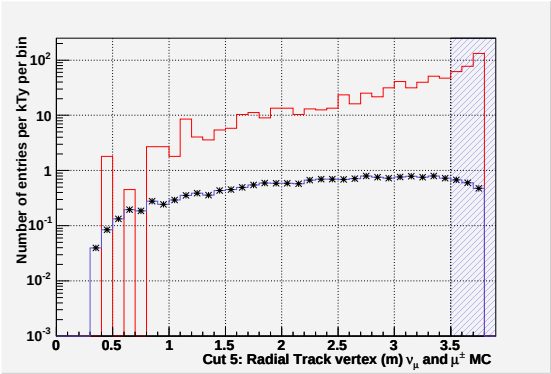

Figure G.7: The radial track vertex position in meters for MC cosmic background μ and MC ν is shown. The cosmic MC background is shown with the red histogram and the ν MC is shown with the blue histogram with the marker. The area with the cross hash is cut from the sample. Both the cosmic background μ and ν are scaled to events per kTy. No statistical error bars are drawn. Both 0 and 1 shower data is shown together.

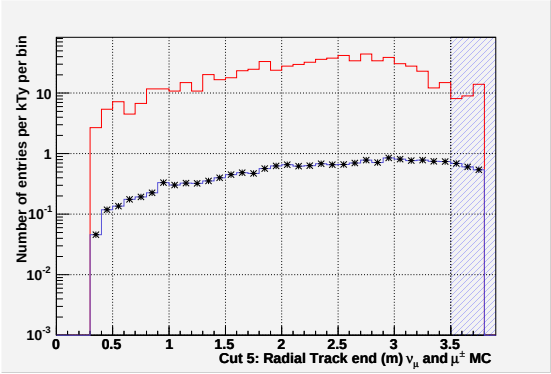

Figure G.8: The radial track end position in meters for MC cosmic background μ and MC ν is shown. The cosmic MC background is shown with the red histogram and the ν MC is shown with the blue histogram with the marker. The area with the cross hash is cut from the sample. Both the cosmic background μ and ν are scaled to events per kTy. No statistical error bars are drawn. Both 0 and 1 shower data is shown together.

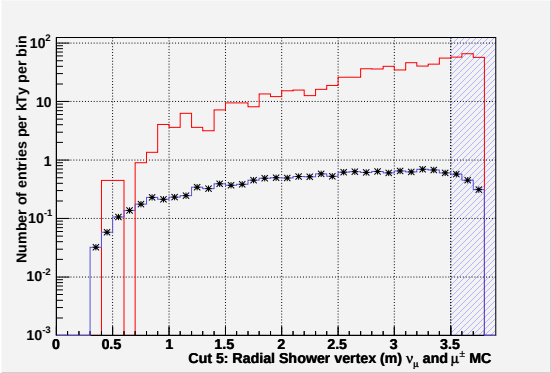

Figure G.9: The radial position of the shower vertex in meters for MC cosmic background μ and MC ν is shown. The cosmic MC background is shown with the red histogram and the ν MC is shown with the blue histogram with the marker. The area with the cross hash is cut from the sample. Both the cosmic background μ and ν are scaled to events per kTy. No statistical error bars are drawn. Only 1 shower data is shown.

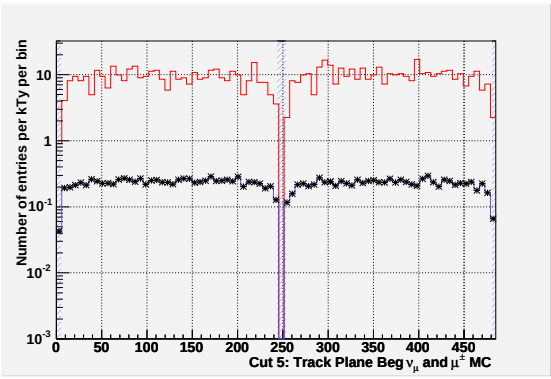

Figure G.10: The first plane in the track for MC cosmic background μ and MC ν is shown. The cosmic MC background is shown with the red histogram and the ν MC is shown with the blue histogram with the marker. The area with the cross hash is cut from the sample. Both the cosmic background μ and ν are scaled to events per kTy. No statistical error bars are drawn. Both 0 and 1 shower data is shown together.

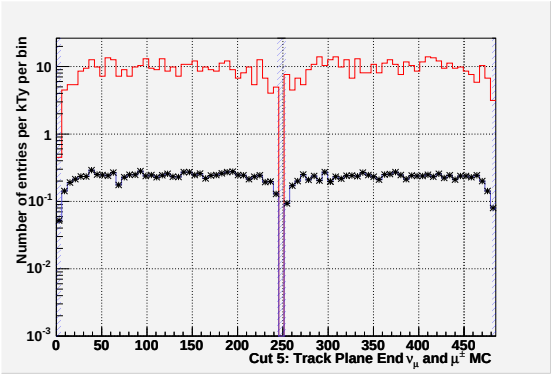

Figure G.11: The last plane in the track for MC cosmic background μ and MC ν is shown. The cosmic MC background is shown with the red histogram and the ν MC is shown with the blue histogram with the marker. The area with the cross hash is cut from the sample. Both the cosmic background μ and ν are scaled to events per kTy. No statistical error bars are drawn. Both 0 and 1 shower data is shown together.

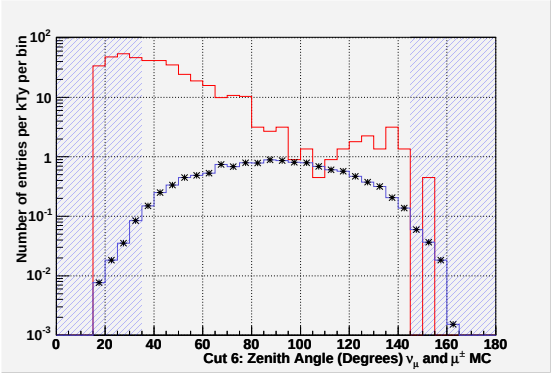

Figure G.12: The track zenith angle in degrees for MC cosmic background μ and MC ν is shown. The cosmic MC background is shown with the red histogram and the ν MC is shown with the blue histogram with the marker. The area with the cross hash is cut from the sample. Both the cosmic background μ and ν are scaled to events per kTy. No statistical error bars are drawn. Both 0 and 1 shower data is shown together.

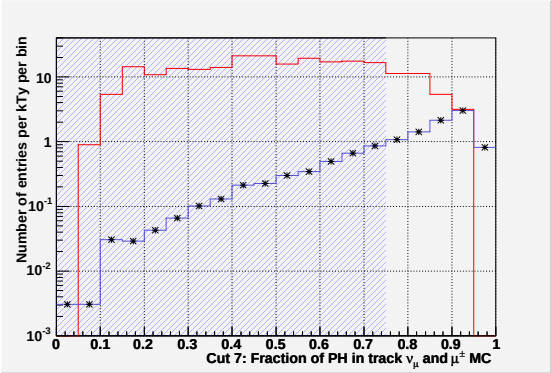

Figure G.13: The fraction of ph in the track for MC cosmic background μ and MC ν is shown. The cosmic MC background is shown with the red histogram and the ν MC is shown with the blue histogram with the marker. The area with the cross hash is cut from the sample. Both the cosmic background μ and ν are scaled to events per kTy. No statistical error bars are drawn. Both 0 and 1 shower data is shown together.

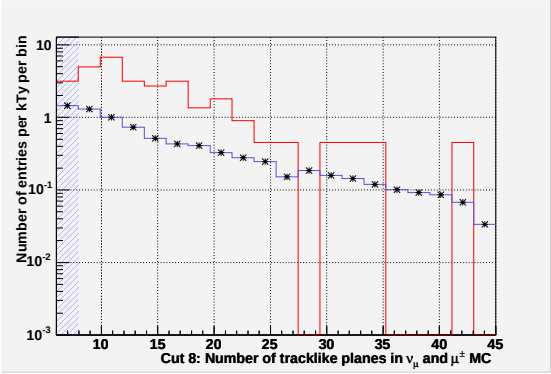

Figure G.14: The number of tracklike planes in a track for MC cosmic background μ and MC ν is shown. The cosmic MC background is shown with the red histogram and the ν MC is shown with the blue histogram with the marker. The area with the cross hash is cut from the sample. Both the cosmic background μ and ν are scaled to events per kTy. No statistical error bars are drawn. Both 0 and 1 shower data is shown together.

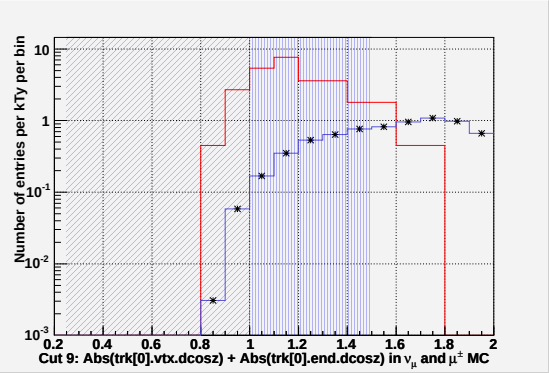

Figure G.15: The track directional cosine in the z-direction for MC cosmic background μ and MC ν is shown. The cosmic MC background is shown with the red histogram and the ν MC is shown with the blue histogram with the marker. The area with the cross hash is cut from the sample. The second cross hash to the right of the first cross hash cuts events when there vertex is more than 3.0 m from the center of the detector. Both the cosmic background μ and ν are scaled to events per kTy. No statistical error bars are drawn. Both 0 and 1 shower data is shown together.

References

[1] C.L.F Howcroft, Atmospheric Neutrinos in the MINOS Far Detector, Ph.D Thesis, 2004

[2] The orignal reference to this is in a letter Pauli wrote is not published. The references in the MINOS TDR discuss this.

[3] F.Reines and C.L. Cowan, Jr., Phys. Rev. 92, 830-831, 1953

[4] G. Danby et al., Phys. Rev. Lett. 9, 36-44, 1962

[5] K. Kodama et al., Phys. Lett. B, 504,218-224, 2001

[6] D.J. Gross and F. Wiczek, Phys. Rev. Lett. 30, 1343-1346, 1973

[7] H.D. Politzer, Phys. Rev. Lett. 30, 1346-1349, 1973

[8] S. Glashow, Nucl. Phys., 22, 579-588, 1961

[9] A. Salam and J.C. Ward, Phys. Lett. 13, 168-171, 1964

[10] S. Weinberg, Phys. Rev. Lett. 19, 1264-1266, 1967

[11] G.'t Hooft, Nucl. Phys.B 33, 173-199, 1971 and G 't Hooft, Nucl. Phys. B 35, 167-188, 1971

[12] B.R. Martin and G. Shaw, Particle Physics, John Wiley and Sons, 1992

[13] F.J. Yndurain, Quantum Chromomdynamics: An Introduction to the theory of Quarks and Gluons, Springer- Verlag, 1983

[14] J.J. Sakurai, Nuovo Cim. 7, 649, 1958

[15] E.C.G Sudarshan and R.E. Marshak, Phys. Rev. 109, 1860-1862, 1958

[16] R.P. Feymann and M. Gell-Mann, Phys. Rev. 109, 193-198, 1958

[17] Review of Particle Physics, The European Physical Journal Vol. 15 1-4, 2000

[18] M. Acciarri et al., Phys. Lett. B, 470, 268-280, 1999

[19] I.J.R Aitchinson and A.J.G Hey, Gauge Theories in Particle Physics, Second Edition, Institute of Physics Publishing Bristol and Philadelphia, 1996

[20] R.N. Mohapatra and P.B. Pal, Massive Neutrinos in Physics and Astrophysics, World Scientific, 1998

[21] B.W Lee and R.E. Shrock, Phys. Rev. D 16, 1444-1473, 1977

[22] J.F. Beacom and P. Vogel, Phys. Rev. Lett. 83, 5222-5225, 1999

[23] E. Majorana, Nuovo Cim. 14, 171-184, 1937

[24] W.H. Furry, Phys. Rev. 56, 1184-1193, 1939

[25] H.V. Klapdor-Kleingrothaus et al., Mod. Phys. Lett. A16,2409-2420, 2001

[26] C.E. Alaseth et al., Mod. Phys. Lett. A17, 1475-1487, 2002

[27] J. Schechter and J.W.F. Valle, Phys. Rev. D 24, 1883-1889, 1981

[28] J.F. Nieves and P.B. Pal, Phys. Rev. D 40, 1693-1696, 1989

[29] W. Greiner and B.Muller, Gauge Theory of Weak Interactions, Springer, 1995

[30] F.J Hasert et al., Phys. Lett. B46, 138-140, 1973

[31] S.M Bilenky, J. Hosek and S.T. Petcov, Phys. Lett. B 94, 495-498, 1980

[32] B. Pontecorvo, Sov. Phys. JTEP. 6, 429, 1957

[33] M. Doi et al., Phys. Lett. B 102, 323-326, 1981

[34] Z. Maki,M. Nakagawa and S. Sakata, Prog. Theor. Phys. 28 870, 1962

[35] L. Wolfenstein, Phys. Rev. D 17, 2369-2374, 1978

[36] S. Mikheev and A. Smirnov, Nuovo Cim. C9, 17-26, 1986

[37] Y. Fukuda et al., Phys. Lett. B 433,9-18,1998

[38] H. Gallagher, Neutrino Oscillation searches with the Soudan2 detector, Ph.D Thesis, April 1996, There are many other places this information can be found including many other Soudan2 theses.

[39] Y. Fukuda et al. Phys. Rev. Lett. 81, 1562-1567, 1998

[40] M. Sanchez et al., Phys. Rev. D 68, 113004, 2003

[41] M. Ambrosio et al., Phys. Rev. D 59, 012003, 1999

[42] J. N. Bachall, Phys. Rev. Lett. 12, 300-302, 1964

[43] R. Davis Jr., Phys. Rev. Lett. 12 ,303-305, 1964

[44] H. A. Bethe, Phys. Rev. 55,434-456,1939

[45] Davis et al., Phys. Rev. Lett. 20, 1205-1209, 1968

[46] Q. R. Ahmad, Phys. Rev. Lett. 87, 1071301-1-1071301-6, 2001

[47] Q.R. Ahmad, Phys. Rev. Lett. 89, 011301-1-011301-6, 2002

[48] K. Eguchi et al. Phys. Rev. Lett 90, 021802 (2003)

[49] S.H. Ahn et al., Phys. Lett. B 511,178-184, 2001

[50] M. Maltoni et al., Phys. Rev. D 68, 113010, 2003

[51] NuMI Technical Design Handbook, 2002-2004 (different revisions)

[52] M.Diwan et al., NuMI-Note-0846, 2002

[53] M. Diwan et al., NuMI-Note-0847, 2002

[54] D. Indurthry et al., NuMI-Note-1027, 2004

[55] MINOS Collaboration,NuMI-Note-0930, 2003 (unpublished)

[56] The CHOOZ Collaboration, M. Apollonio, et al., Eur.Phys.J.C27:331-374, 2003. Also hep-ex/0301017.

[57] P.B Pal and L. Wolfenstein, Phys. Rev. D, 25, 766-773, 1982

[58] R.F. Streater and A.S. Wightman, PCT, Spin and Statistics, and all that,The Benjamin/Cummings Publishing Company, Inc., 1964 And references therin

[59] V. Barger, K. Whitsnant and R.J.N Phillips, Phys. Rev. Lett.45,2084-2088, 1980

[60] N. Cabibbo, Phys. Lett 72B, 333, 1978

[61] R. Bluhm, V.A. Kostelecky and N. Russell, Presented at Orbis Scientiac: Physics of Mass, Miami, Florida, December 1997 and also in hep-ph/9809597

[62] O.W. Greenberg, Phys. Rev. Lett. 89, 231602, 2002

[63] J.S. Bell, Proc. Roy. Soc. A231, 497, 1955

[64] Sandip Pakvasa,Second Meeting on CPT and Lorentz Symmetry CPT'Ol, August 15-18, 2001 Bloomington, Indiana, hep-ph/0110175 v2.

[65] Barger et al., Phys. Rev. Lett. 85, 5055, 2000

[66] V.A. Kostelecky and M. Mews, hep-ph/0309025, 2003

[67] T.D Lee and C.N. Yang Phys. Rev. 104, 254, 1956

[68] C.S. Wu, E. Ambler, R.W. Hayward, D. Hoppes and R.P Hudson, Phys. Rev. 105, 1413, 1957

[69] Quang Ho-Kim and Pham Xuan Yem, Elementary Particles and Their Interactions, Springer- Verlag Berlin Heidelberg, 1998

[70] Micheal E. Peskin and Daniel V. Schroeder, An Introduction to Quantum Field Theory, Persus Books, Reading Massachusetts, 1995

[71] Franz Gross, Relativistic Quantum Mechanics and Field Theory, Wiley Science Paperback Series,1999

[72] J.H. Christenson, J.W. Cronin, V.L. Fitch and R.Turlay, Phys. Rev. Lett. 13, 138,1964

[73] A. Angelopoulos et al., Phys. Lett. B 444, 43, 1998

[74] K. Abe et al., Phys. Rev. Lett. 87, 091802, 2001

[75] B. Aubert et al., Phys. Rev. Lett. 87, 091801, 2001

[76] M.S. Fee et al., Phys. Rev. A 48, 192, 1993

[77] H.A. Torii et al., Phys. Rev. A 59, 223, 1999

[78] D.S. Aryes et al., Phys. Rev. D 3, 1051, 1971

[79] L.K. Gibbons et al., Phys. Rev. D 55, 6625, 1997

[80] R.S. Van Dyck Jr., P.B. Schwinberg and H.G. Dehmelt, Phys. Rev. Lett.,59,26 1987

[81] MINOS Collaboration, The MINOS Technical Design Report-NuMI-Note-0337, 1998

[82] MINOS Collaboration, The MINOS Detectors Design Parameter Book 1.3, 2001

[83] R. Opsanov and K. Lang, NuMI-Note-1101, 2005

[84] N. Tagg et al., NIM A 539 668-678, 2005

[85] D. Reyna, NuMI-Note-0757, 2001

[86] P. Shannan and N. Tobien, NuMI-Note-0838, 2002

[87] A.S Clark et al., Phys. Rev. D 9, 533, 1974

[88] M.A. Kordosky, Hadronic interactions in the MINOS Detectors, Ph.D Thesis

[89] P.L. Vahle, Electromagnetic interactions in the MINOS Detectors, Ph.D Thesis

[90] R. Nichol, Calibration in the MINOS Detctors, Ph.D Thesis

[91] T.K. Gaisser, Cosmic Rays and Particle Physics, Cambridge University Press, 1990

[92] L. Jenner, NuMI-Note-0975, 2003

[93] P. Adamson et al., Nuclear Instrumentation and Methods in Physics Research A 492, 325-343, 2002 also NuMI-NOTE-0743

[94] P. Harris, NuMI-NOTE-0550,1999

[95] P. Harris, NuMI-NOTE-0692,2000

[96] P. Harris, NuMI-NOTE-0693,2000

[97] P. Adamson et al., NuMI-NOTE-0793, 2001

[98] MINOS NIM article to be published

[99] S. Kasahara, A Study of Cosmic Ray Composition in the Knee Region using Multiple Muon Events in the Soudan 2 Detector, Ph.D Thesis, 1997

[100] F. Yumiceva and B. Wands, Email communication

[101] B. Becker, NuMI-NOTE-0856, 2002

[102] B.Viren, NuMI-NOTE-0876, 2002

[103] B. Becker and D. Boehnlein, NuMI-NOTE-1047,2004

[104] R.P. Feynman, M. Kislinger and F. Ravndal, Phys. Rev. D3, 2706, 1971

[105] M. Honda et al., Phys. Rev. D 70, 043008, 2004

[106] G.D. Barr et al., Phys. Rev. D 70, 023006, 2004

[107] J. Favier et al., Phys. Rev. D 68, 093006, 2003

[108] G. Battistoni et al., Astropart. Phys.19:269-290,2003 also hep-ph/0207035

[109] G. Barr, Private communication

[110] H. Gallagher, Nucl. Phys. Proc. Suppl. 112:188-194, 2002

[111] K. Ruddick, PDK-784 and PDK-704

[112] R.P. Feynman and M. Gell-Mann, Phys. Rev. 109, 193, 1958

[113] D. Rein and L. Sehgal, Annals Phys. 133: 79

[114] H. Gallagher,Nucl. Phys. B (Proc. Suppl.) 112, 188, 2002

[115] A. Bodek and U.K Yang, AIP Conf. Proc. 721: 358-362, 2004

[116] Hugh Gallagher-Private communication

[117] K. Lang, NuMI-NOTE-0664, 2000

[118] M. Kordosky and K. Lang, NuMI-NOTE-0748, 2001

[119] J.Day and K. Lang, NuMI-NOTE-0749, 2001

[120] J.Liu et al., NuMI-NOTE-0797, 2001

[121] K. Lang et al., NuMI-NOTE-0928, 2001

[122] N. Felt et al., NuMI-NOTE-0901, 2003

[123] D. Boehnlein, NuMI-NOTE-0784, 2001

[124] D. Boehnlein, NuMI-NOTE-0868,2002

[125] B. Rebel and S. Mufson, NuMI-NOTE-0725

[126] B. Rebel and S. Mufson, NuMI-NOTE-0834

[127] B. Becker and A. Godley, NuMI-NOTE-868,2002

[128] B. Becker, R. Piteria and A. Sousa, NuMI-NOTE-964, 2003

[129] H.M. Gallagher and M.C. Goodman, NuMI-NOTE-112, 1995

[130] D. Boehnlein, NuMI-NOTE-913, 2003

[131] C.P. Ward, NuMI-Note-1085, 2005

[132] D. Boehnlein et al., NuMI-Note-1061. 2004

[133] S.L. Mufson and B. Rebel, NuMI-Note-1099, 2005

[134] E. Beall, Cosmic ray charge ratio in the MINOS far detector, Ph.D Thesis, 2005

[135] A. Blake, A study of Atmospheric Neutrino Oscillations in the MINOS Far Detector, Ph.D Thesis, 2005

[136] P.Adamson et al., To be submitted to Phys. Rev. D, also-hep-ex/0512036